GENERATING PERIODIC ORBITS IN THE CIRCULAR RESTRICTED THREE-BODY PROBLEM WITH APPLICATIONS TO LUNAR SOUTH POLE COVERAGE

A Thesis
Submitted to the Faculty

of

Purdue University

by

Daniel J. Grebow

In Partial Fulfillment of the
Requirements for the Degree

of

Master of Science in Aeronautics and Astronautics

May 2006
Purdue University
West Lafayette, Indiana

"Happy is the man that findeth wisdom; and the man that getteth understanding. For the merchandise of it is better than the merchandise of silver, and the gain thereof than fine gold. She is more precious than rubies: and all the things thou canst desire are not to be compared unto her. Length of days is in her right hand; and in her left hand riches and honour. Her ways are ways of pleasantness, and all her paths are peace. She is a tree of life to them that lay hold upon her: and happy is every one that retaineth her. The LORD by wisdom hath founded the earth; by understanding hath he established the heavens. By his knowledge the depths are broken up, and the clouds drop down the dew."

(Proverbs 3:13-20) *KJV*

ACKNOWLEDGEMENTS

Socrates pursued wisdom, knowledge, and understanding. However, in Plato's *Meno*, Socrates paradoxically argues for the existence of knowledge *a priori*. That is, he argues that knowledge does not come from experience but rather originates from a "spontaneous recovery" through recollection. He proves this by posing basic geometry questions to a young uneducated slave. The boy answers Socrates' geometry questions correctly! Since the boy is uneducated, his knowledge of geometry must have come from within. Therefore, knowledge *a priori* must exist.

There is a flaw in the argument, of course. Socrates has failed to realize that the nature of his own questioning has led the boy to the correct answers. That is, Socrates has asked the questions in such a way that the uneducated boy has become educated. The knowledge did not originate from recollection, but rather was passed from Socrates to the boy through Socrates' own subtle questioning.

Let me not make the same mistake. The knowledge imparted by this work did not simply originate from within, but came from others. For this reason, I have many people that need to be thanked.

Most definitely, Dr. Kathleen Howell has provided a strong foundation for my knowledge in orbital mechanics. If there is value in this work, she is the creditor. She is the Socrates and I am the uneducated young boy. It is by her subtle questioning that I have become educated. It is my privilege to work for her.

It is also my privilege to work with Dave Folta at NASA Goddard Spaceflight Center. In fact, Dave is a great counterexample to Socrates' argument. Nobody possesses more knowledge of orbits based on experience than Dave. It was his idea to investigate lunar south pole coverage, not mine.

Much credit must also be given to Marty Ozimek. Marty and I literally worked side-by-side at Goddard and Purdue in designing the architectures for lunar south pole coverage. In fact, many of the ideas conveyed in Chapter 4 come directly from him. I hope to work more with him in the future.

Some of my other colleagues must also be thanked. Chris Patterson has helped me understand so many things; there is no way I can list them all. For example, he taught me how to use GENERATOR. Furthermore, Lucia Irrgang and I initially worked together on computing periodic orbits near L_4 and L_5. I hope also to work more with Lucia in the future.

Others also need to be thanked. Belinda Marchand initially instructed me with modifications of the two-level corrector to include constraints. The STK® three-body scenarios originally came from Frank Vaughn at Goddard. Analytical Graphics, Inc. representative Paul Black has been an immediate help whenever problems were encountered with STK.

I would also like to thank Purdue University and NASA Goddard Spaceflight Center under Contract Number NNG04GP69G, for providing the support necessary to complete this work.

TABLE OF CONTENTS

Page

LIST OF TABLES viii
LIST OF FIGURES x
ABSTRACT xiii
1. INTRODUCTION 1
    1.1 Problem Definition 2
        1.1.1 The Circular Restricted Three-Body Problem 2
        1.1.2 Lunar South Pole Coverage 2
    1.2 Previous Contributors 3
        1.2.1 Quasi-Periodic and Periodic Solutions 4
        1.2.2 Application to Lunar South Pole Coverage and Station-Keeping Strategies 6
    1.3 Current Work 7
2. BACKGROUND 10
    2.1 The Circular Restricted Three-Body Problem 10
    2.2 The Equilibrium Points 13
    2.3 First-Order Analytic Approximations for Variations Relative to the Collinear Points 15
        2.3.1 Quasi-Periodic, First-Order Approximations Near the Collinear Libration Points 18
        2.3.2 Periodic, First-Order Approximations Near the Collinear Libration Points 19
    2.4 Fundamental Variational Relationships 21
        2.4.1 The State-Transition Matrix 21
        2.4.2 Contemporaneous and Non-Contemporaneous Variations in the State 23

Page
2.4.3 An Introduction to Invariant Manifold Theory 25
3. GENERATING ORBITS IN THE CIRCULAR RESTRICTED THREE-BODY PROBLEM 27
3.1 The Two-Level Differential Corrections Process 27
3.1.1 The "First Level" of the Corrections Process 28
3.1.2 The "Second Level" of the Corrections Process 30
3.1.3 Numerical Example: Lissajous Trajectories 34
3.2 A Simple Corrector 35
3.2.1 The Algorithm 35
3.2.2 Numerical Results: L_1, L_2, and L_3 Lyapunov Families of Orbits 38
3.2.3 The Stability Index and Bifurcations 45
3.3 Targeting Orbits in Three-Dimensional Space Using Symmetry 48
3.3.1 Strategies to Compute Periodic Orbits 48
3.3.2 Numerical Results: L_1, L_2, L_3 Halo, Axial, and Vertical Families of Orbits 53
3.4 Asymmetric Corrections Schemes 75
3.4.1 Strategies to Compute Periodic Orbits 75
3.4.2 Numerical Results: L_4/L_5 Planar, Axial, and Vertical Families of Orbits 83
3.5 Alternative Methods 90
3.5.1 Sequential Quadratic Programming: Completing the L_3 Halo Orbit Family 90
3.5.2 Two-Level Corrections with Constraints: Completing the L_4 Vertical Orbit Family 93
4. ORBIT SELECTION FOR LUNAR SOUTH POLE COVERAGE AND THE TRANSITION TO A FULL EPHEMERIS MODEL 101
4.1 Orbit Selection for Lunar South Pole Coverage 101
4.1.1 Period and Stability Index 105
4.1.2 Potential Orbits for Coverage of the Lunar South Pole 108

Page
4.2 Transition to a Full Ephemeris Model 110
4.2.1 Obtaining Results with the Purdue Software Package GENERATOR 110
4.2.2 A Preliminary Coverage Analysis 112
4.2.3 Architectures for Lunar South Pole Coverage 113
5. COVERAGE AND STATION-KEEPING ANALYSES FOR LUNAR SOUTH POLE COVERAGE 120
5.1 Coverage Analysis 120
5.1.1 Defining the Ground Stations and Establishing the Links 120
5.1.2 Results for Architectures Supporting Lunar South Pole Coverage 127
5.2 Station-Keeping Analysis 139
5.2.1 The Station-Keeping Algorithm 139
5.2.2 Station-Keeping Results 141
6. RESULTS AND RECOMMENDATIONS 142
6.1 Summary of Results 142
6.2 Recommendations for Future Work 143
LIST OF REFERENCES 146
VITA 152

LIST OF TABLES

Table Page

2.1 Locating the Collinear Libration Points 14

3.1 L_1 Lyapunov Family Initial Conditions 40

3.2 L_2 Lyapunov Family Initial Conditions 42

3.3 L_3 Lyapunov Family Initial Conditions 44

3.4 Northern L_1 Halo Family Initial Conditions 56

3.5 Northern L_2 Halo Family Initial Conditions 58

3.6 Northern L_3 Halo Family Initial Conditions 60

3.7 Northeast L_1 Axial Family Initial Conditions 62

3.8 Northwest L_2 Axial Family Initial Conditions 64

3.9 Northeast L_3 Axial Family Initial Conditions 66

3.10 L_1 Vertical Family Initial Conditions 68

3.11 L_2 Vertical Family Initial Conditions 70

3.12 L_3 Vertical Family Initial Conditions 72

3.13 Northern L_2 Butterfly Family Initial Conditions 74

3.14 L_4 Planar Family Initial Conditions with $y_0 = \frac{\sqrt{3}}{2}$ 85

3.15 Northern L_4 Axial Family Initial Conditions with $z_0 = 0.1$ 87

3.16 L_4 Vertical Family Initial Conditions with $y_0 = 0.42545$ 89

3.17 Northern L_3 Family Initial Conditions Using SQP (Orange) 92

3.18 L_4 Vertical Family Initial Conditions Using Two-Level Corrector with Constraints (Green) 100

4.1 Potential Orbits for Coverage of the Lunar South Pole 109

5.1 Percent Access Times for 12-Day L_1 Halo Orbits and Ground Station at the Shackleton Crater 122

Table Page

5.2 Percent Access Times for 12-Day L_1 Halo Orbits and Ground Station at the White Sands Test Facility 125

5.3 Percent Access Times for 7-Day L_1 Halo Orbits 130

5.4 Percent Access Times for 8-Day L_1 and L_2 Halo Orbits 132

5.5 Percent Access Times for 16-Day L_1 and L_2 Vertical Orbits 134

5.6 Percent Access Times for 14-Day L_2 Butterfly Orbits 136

5.7 Percent Access Times for 7-Day L_2 Halo Orbit and 14-Day L_2 Butterfly Orbit 138

5.8 Station-Keeping Results for One Year (~ 24 Revs) 141

LIST OF FIGURES

Figure Page

2.1 Formulation of the Restricted Three-Body Problem 11

2.2 Equilibrium or Libration Points (Magenta) in the CR3BP 14

2.3 First-Order Approximation to a Lissajous Trajectory 19

2.4 First-Order Approximation to a Lyapunov Orbit 20

2.5 Representation of Contemporaneous and Non-Contemporaneous Variations in the State 24

3.1 Path Before (Red) and After (Black) First Level is Applied 29

3.2 Path Before Second Level is Applied (Black) and Final Continuous Path (Blue) 33

3.3 Differentially Corrected L_1 Lissajous Trajectory 34

3.4 Initial and Final Path for Simple Corrector 36

3.5 The L_1 Lyapunov Family 39

3.6 The L_2 Lyapunov Family 41

3.7 The L_3 Lyapunov Family 43

3.8 Characteristic Multipliers Associated with Center Subspace for L_1 Lyapunov Orbits 47

3.9 The Northern L_1 Halo Family 55

3.10 The Northern L_2 Halo Family 57

3.11 The Northern L_3 Halo Family 59

3.12 The Northeast L_1 Axial Family 61

3.13 The Northwest L_2 Axial Family 63

3.14 The Northeast L_3 Axial Family 65

3.15 The L_1 Vertical Family 67

3.16 The L_2 Vertical Family 69

3.17 The L_3 Vertical Family 71

Figure Page

3.18 The Northern L_2 Butterfly Family 73

3.19 The L_4 Planar Family 84

3.20 The Northern L_4 Axial Family 86

3.21 The L_4 Vertical Family 88

3.22 Path Before Second Level is Applied (Black) and Final Periodic Solution (Blue) 96

3.23 The L_4 Vertical Orbits Using a Two-Level Corrector with Constraints 99

4.1 Southern Halo Orbit Family: Earth-Moon L_1 (Orange) and L_2 (Blue) 102

4.2 Vertical Orbit Families of Interest: Earth-Moon L_1 (Red) and L_2 (Cyan) 103

4.3 Southern L_2 Butterfly Orbit Family 104

4.4 Definition of Maximum x^m -Distance 106

4.5 Period versus Maximum x^m -Distance from the Moon 106

4.6 Stability Index versus Maximum x^m-Distance from the Moon 107

4.7 12-Day L_1 Orbit (Orange) and Patch Points (Black) CR3BP 109

4.8 Two Phased Spacecraft in 12-Day L_1 Halo Orbits from GENERATOR 111

4.9 z^m-Displacement in the Rotating Reference Frame for Two Spacecraft in 12-Day L_1 Halo Orbits 112

4.10 Two Phased Spacecraft in 7-Day L_2 Halo Orbits from GENERATOR 115

4.11 Two Phased Spacecraft in 8-Day L_1 and L_2 Halo Orbits from GENERATOR 116

4.12 Two Phased Spacecraft in 16-Day L_1 and L_2 Vertical Orbits from GENERATOR 117

4.13 Two Phased Spacecraft in 14-Day L_2 Butterfly Orbits from GENERATOR . 118

4.14 Two Phased Spacecraft in a 7-Day L_2 Halo Orbit and a 14-Day L_2 Butterfly Orbit 119

5.1 STK 12-Day L_1 Halo Orbits 121

5.2 A Facility is Placed on the Moon at the Shackleton Crater (89.9°S, 0.0°E) ... 122

5.3 Line-of-Sight Access Beams (Green) with Lunar Facility 123

Figure Page

5.4 Elevation of Each Satellite Above the Horizon as Viewed from the Shackleton Crater Facility for 12-Day L_1 Halo Orbit Scenario 124

5.5 An STK Facility is Placed at the White Sands Test Facility (32.3°N, 106.8°W) 125

5.6 Possible Communications Relay Between the White Sands Test Facility and the Lunar Ground Station at the Shackleton Crater 126

5.7 STK 7-Day L_2 Halo Orbits 129

5.8 Elevation of Each Satellite Above the Horizon as Viewed from the Shackleton Crater Facility for 7-Day L_2 Halo Orbit Scenario 130

5.9 STK 8-Day L_1 and L_2 Halo Orbits 131

5.10 Elevation of Each Satellite Above the Horizon as Viewed from the Shackleton Crater Facility for 8-Day L_1 and L_2 Halo Orbit Scenario 132

5.11 STK 16-Day L_1 and L_2 Vertical Orbits 133

5.12 Elevation of Each Satellite Above the Horizon as Viewed from the Shackleton Crater Facility for 16-Day L_1 and L_2 Vertical Orbit Scenario 134

5.13 STK 14-Day L_2 Butterfly Orbits 135

5.14 Elevation of Each Satellite Above the Horizon as Viewed from the Shackleton Crater Facility for 14-Day L_2 Butterfly Orbit Scenario 136

5.15 STK 7-Day L_2 Halo and 14-Day L_2 Butterfly Orbits 137

5.16 Elevation of Each Satellite Above the Horizon as Viewed from the Shackleton Crater Facility for 7-Day L_2 Halo and 14-Day L_2 Butterfly Orbit Scenario 138

5.17 Schematic for Station-Keeping Algorithm 140

6.1 Earth-Moon L_1 Vertical Orbit Associated Unstable (Red) and Stable (Blue) Manifolds 144

ABSTRACT

Grebow, Daniel J. M.S.A.A., Purdue University, May 2006. Generating Periodic Orbits in the Circular Restricted Three-Body Problem with Applications to Lunar South Pole Coverage. Major Professor: Dr. Kathleen C. Howell.

A potential ground station at the lunar south pole has prompted studies of orbit architectures that ensure adequate coverage. The creation of multi-body orbit constellations begins with a thorough investigation of periodic orbits in the Circular Restricted Three-Body Problem (CR3BP). Strategies for the determination of periodic solutions in the CR3BP enhance capabilities and define boundaries. Families of planar, vertical, and axial orbits are computed that are associated with all five libration points. Additional periodic solutions in the vicinity of the collinear libration points suggest favorable geometries for lunar south pole coverage.

A detailed analysis of halo and vertical families, as well as other orbits near the libration points in the vicinity of the Moon, suggests that constant communications can be achieved with two spacecraft in combinations of Earth-Moon libration point orbits. In particular, the investigation focuses on nine different orbits from these families with periods ranging from 7 to 16 days. Natural solutions are generated in a full ephemeris model including solar perturbations. Possible ground stations on the Moon and on the Earth are established for coverage results and verification of communications capabilities. Preliminary station-keeping costs are also computed for long term communications with the ground stations.

1. INTRODUCTION

Current limitations in a number of technical areas, including mission design capabilities, inhibit a thorough exploration of space. Thus, a demand exists for more innovative ideas in orbital design and more sophisticated computational tools. Increased complexity of the dynamical model, including additional gravity forces acting on the spacecraft, offers an infinite variety of trajectories. A thorough investigation of these trajectories aids the discovery process and facilitates space exploration.

Modeling the motion of the spacecraft by including the gravitational forces associated with the Sun, Earth, and Moon has historically proven effective in obtaining new scientific knowledge about the Sun. For example, NASA's Third International Sun/Earth Explorer (ISEE-3) mission supplied valuable information regarding solar flares and gamma-ray bursts [1]. Furthermore, the recent Genesis spacecraft retrieved solar wind particles over a span of two years [2] that are now being analyzed. The shapes of the trajectory arcs used by ISEE-3 and Genesis spacecraft are advantageous for gathering scientific data and for a communications relay with the Earth. The basic models for both missions include the gravitational forces of the Sun, Earth, and Moon in the analysis.

Since the President's Vision for Space Exploration [3] announcement in January 2004, preparations are underway for autonomous and manned activities on the lunar surface. For the development of the trajectory design options for a return to the Moon, incorporation of the gravity effects for not only the Moon, but also the Earth and Sun, offers very useful information for spacecraft motion in the vicinity of the Moon. The results allow flexibility for mission design and ultimately facilitate exploration of Mars.

1.1 Problem Definition

1.1.1 The Circular Restricted Three-Body Problem

The motion of a less massive body about an additional body with significantly larger mass is formulated as a two-body problem in orbital mechanics. Closed form analytical solutions exist and are conic in nature. However, the inclusion of an additional (third) body in the gravity model, that is, the general three-body problem, is not solvable analytically in closed form.

The general three-body model can be simplified to greatly reduce the complexity of the problem, however. The third body, or spacecraft, is assumed to possess infinitesimal mass in comparison with the other two bodies, or primaries. Furthermore, it is assumed that the motion of the two primaries is Keplerian. Additional assumptions require that the distance between the two primaries remain constant, thereby restricting the motion of the primaries to be circular relative to the system barycenter. The motion of the third body is described relative to a rotating reference frame determined by the motion of the primaries. This, of course, is the classical formulation of the Circular Restricted Three-Body Problem (CR3BP).

Even with the simplifying assumptions, the CR3BP is still not solvable in closed form. Particular solutions do, however, exist in the three-body problem. For example, it is known that five equilibrium solutions or libration points exist in the rotating frame. Furthermore, approximate analytical solutions are available for motion in the vicinity of the equilibrium points by analyzing variations with respect to the equilibrium solutions. These solutions serve as a basis for numerical computation. Moreover, due to the sensitivities inherent in the CR3BP, the development of numerical procedures is challenging. Nevertheless, the solution space can be explored thereby leading to the discovery of new types of trajectories.

1.1.2 Lunar South Pole Coverage

Current interest in autonomous and manned exploration studies is focused primarily on the south pole of the Moon due to constant exposure to sunlight and the Shackleton Crater site located nearby. NASA has also indicated that water ice at the lunar poles may help facilitate exploration of the solar system [3]. A ground station on the Moon requires a system of satellites that is always in view of the Earth such that constant communications between the lunar surface and the Earth is available.

Rather than adjusting current mission objectives due to limitations inherent in the original constellations, a libration point orbit can be considered such that current mission design requirements are fully satisfied. However, many orbit families remain unknown and the practical application of most known families of trajectories has not yet been thoroughly investigated. In addition, an optimal design may involve combinations of trajectories from various families – some yet to be exposed. Identification of the best libration point orbit or combinations of orbits that fulfill the primary mission objectives as the first step in the design process requires an extensive study of the dynamical theory regarding periodic orbits in the CR3BP.

From the characteristics of the various types of periodic solutions, some useful architectures for lunar south pole coverage exist within the context of the three-body problem. A thorough investigation of a wide range of libration point orbits offers many different coverage options. Of course, long term mission requirements demand that station-keeping costs also be computed.

1.2 Previous Contributors

Much of the dynamical analysis in mechanics for the three-body problem was developed by Sir Isaac Newton (1643-1727) in 1687 with the *Principia*. Newton's predecessor, Leonhard Euler (1707-1783), was the first to simplify the problem by assuming an infinitesimal mass for the third body, thereby introducing the "restricted" three-body problem. Euler was also the first to model the dynamics in a rotating reference frame. Meanwhile, Joseph-Louis Lagrange (1736-1813), a contemporary of Euler, identified the five equilibrium solutions, or libration points, in the CR3BP. His solutions correctly predicted the existence of the Sun-Jupiter Trojan Asteroids. Nearly a hundred years after Euler and Lagrange, Jules Henri Poincaré (1854-1912) demonstrated the non-integrability of the three-body problem. His work ultimately became the foundation of modern dynamical systems theory.

1.2.1 Quasi-Periodic and Periodic Solutions

One of many significant contributions, Poincaré proved that periodic orbits exist in the three-body problem. Moreover, Poincaré claimed that there are an *infinite* variety of periodic solutions [4]. In 1920, Moulton [5] published *Periodic Orbits*, a collection of studies from more than five authors; the book is solely devoted to analytical methods for approximating periodic motion near all five equilibrium points. In the fourth chapter of this work, Buck employs a power series method to develop third-order approximations for solutions near the triangular equilibrium points. His solutions resemble what are now known as vertical orbits.

Due to the increasing speed and accuracy of modern computers, numerical methods for the computation of many different types of periodic solutions have evolved in the last fifty years. In 1965, Hénon [6] published a series of treatises on stability and bifurcations for in-plane periodic solutions. His work established an important link between families of solutions in the restricted three-body problem. Near this same time, Goodrich [7] obtained numerical solutions for in-plane periodic motion in the vicinity of the triangular equilibrium points in the Earth-Moon system. Bray and Goudas [8] obtained numerical results for vertical orbits near the collinear libration points in 1966. Furthermore, the results by Goodrich were confirmed a year later (1967) when Deprit, Henrard, Palmore, and Price [9] computed similar motion in the vicinity of the triangular points. In this same year, Szebehely [10] published *Theory of Orbits: The Restricted Problem of Three Bodies*. Included in his study is an extensive compilation of both analytical and numerical analyses in the restricted three-body problem.

In 1973, Hénon [11] expanded his analysis to include vertical stability of periodic solutions in the restricted three-body problem. Meanwhile, Farquhar and Kamel [12] obtained third-order approximations for quasi-periodic motion near the trans-lunar libration point in the Earth-Moon system using a Linstedt-Poincaré method. A few years later, Richardson and Cary [13] developed, via a method of successive approximations truncated to the fourth-order, a model for quasi-periodic motion in the vicinity of the interior libration point for the Sun-Earth/Moon system.

Markellos and Halioulias [14] created a corrections scheme in 1977 that quickly computes asymmetric periodic solutions for the Störmer problem. The scheme proves invaluable for obtaining solutions with no visible symmetries. Furthermore, Markellos successfully applied the corrections scheme to the CR3BP and the stability of the solutions was assessed using the methods developed by Hénon [15]. In 1979, Zagouras and Kazantzis [16] numerically determined halo, axial, and vertical families near the collinear points in the Sun-Jupiter system. Furthermore, Breakwell and Brown [17] obtained numerical results in the Earth-Moon system for halo orbits near the collinear points while Robin and Markellos [18] catalogued eight different families of orbits for the Sun-Jupiter case in the vicinity of Jupiter. In 1984, using a three-dimensional method of regularization originally developed by Kusstenheimo and Stiefel, Howell and Breakwell [19] applied it in the restricted problem and developed approximations for "almost rectilinear" halo orbits near the collinear points. A thorough numerical investigation of halo orbits was also completed [20]. A year after Howell and Breakwell developed their approximations, Zagouras [21] improved Buck's approximations to include fourth-order terms. He also developed a corrections scheme to obtain numerical results for vertical and axial orbits near the triangular equilibrium points.

A method for obtaining numerical results for quasi-periodic solutions in the CR3BP was accomplished by Howell and Pernicka [22] in 1988. The method is adaptable for multiple flight regimes and easily modified for constrained motion [23-24]. For example, periodic solutions are available from a more general arc simply by constraining periodicity [25]. In general, the method remains one of the most powerful tools in transitioning quasi-periodic and periodic solutions from the CR3BP to a full ephemeris model with only small variations in shape.

More recently, Papadakis and Zagouras [26] studied bifurcations of families near the triangular libration points. In 1999, Howell and Campbell [27] completed an extensive investigation of periodic solutions and bifurcations in the Sun-Earth/Moon system for the collinear libration points in the Earth/Moon vicinity. Dichmann, Doedel, and Paffenroth [28] have obtained numerical results for connections between the Lyapunov, halo, axial, and vertical orbits in the vicinity of the collinear points in the Earth-Moon system using the software AUTO. In 2003, Doedel, Paffenroth, Keller, Dichmann, Galán-Vioque, and Vanderbauwhede [29] further applied AUTO to successfully map periodic solutions near the collinear points to those in the vicinity of the triangular points. Their study also includes numerical results for axial and vertical orbits in the vicinity of the triangular points.

1.2.2 Application to Lunar South Pole Coverage and Station-Keeping Strategies

In 1971, Farquhar [30] initially examined the use of 'halo' orbits to maintain a communications link between the far side of the Moon and the Earth. His study includes a communications architecture and station-keeping costs. Later, extensive work on optimal station-keeping strategies using Floquet modes for halo orbits in the Earth-Moon system was completed by Simó, Gómez, Libre, Martínez, and Rodríguez [31-32]. In this approach, the unstable subspace that is available from dynamical systems theory is used to develop a station-keeping strategy. Station-keeping analyses for the Earth-Moon halo orbits were also completed by Howell and Pernicka [33], Howell and Keeter [34], and Gómez et al. [35]. Most recently, Scheeres, Han, and Hou [36] as well as Renault and Scheeres [37] have investigated the generalized optimal placement of statistical control maneuvers applied to orbits in the Earth-Moon restricted three-body problem. The orbits in these studies are typical of those that might be used for lunar coverage and also provide an additional benchmark for the station-keeping costs.

The potential use of libration point orbits for lunar south pole coverage has not yet been fully investigated. Ely and Lieb [38-39] have investigated the placement of a system of satellites to support a south pole station and global orbital constellations, but their analysis is based on a two-body model with the third body effects modeled as gravitational perturbations. They also incorporate solar radiation pressure. On a broader scale, NASA's Living with a Star (LWS) program was created to learn more about the Sun-Earth system. The initiative included the possible investigation of north and south "pole-sitters" for constant Earth atmospheric monitoring and surveillance [40]. Such ideas may be adaptable to the Moon for feasible south pole architectures. Studies of satellite constellations in Earth orbit are also being examined for application to the Moon.

1.3 Current Work

For application to the lunar south pole coverage problem, the initial design begins with the CR3BP for the Earth-Moon system. First-order linear approximations for small amplitude Lyapunov orbits near the collinear points are used to obtain families of Lyapunov, halo, axial, and vertical orbits. In addition, a family of orbits that may be described as a butterfy shape are computed. The exact bifurcation points along a family of periodic orbits are available by applying a method of bisections. Furthermore, strategies for computing and expanding the solution space are presented. The strategies ultimately lead to a mapping of planar, axial, and vertical orbits in the vicinity of the triangular points.

The southern halo families, small amplitude vertical families, and a butterfly family in the vicinity of the cis- or trans-lunar libration points are conducive to lunar south pole coverage. Orbits from these families are selected based on (i) feasibility for lunar south pole coverage, (ii) predetermined altitude constraints; and, (iii) time to complete one full period. Once a specific architecture is selected, the orbit is discretized into a series of patch points. With modifications to a corrections scheme posed by Marchand, Howell, and Wilson [25], the patch points are then differentially corrected to meet both the desired time-of-flight and the orbit periodicity requirements. The solutions are transitioned to a full ephemeris model, including solar perturbations, using the Purdue Software Package GENERATOR [41]. Adapting models created by Folta and Vaughn [42], the patch points that define a libration point orbit from GENERATOR are targeted in Satellite Tool Kit®. A facility is placed at the Shackleton Crater near the south pole of the Moon and access times between the facility and the spacecraft constellation are analyzed. Access times with the Earth, specifically the White Sands Test Facility, are also computed. Finally, a preliminary station-keeping analysis using invariant manifold theory is accomplished.

This study is organized in the following manner:

Chapter 2:

In this chapter, the equations of motion are derived. The differential equations are formulated within the context of the CR3BP. A method for computation of the system equilibrium points is included. First-order analytical approximations are summarized for quasi-periodic and periodic motion near the system equilibrium points and the state-transition matrix is defined. Contemporaneous and non-contemporaneous variations along the path are described and invariant manifold theory is introduced.

Chapter 3:

A two-level differential corrections scheme is derived to numerically determine quasi-periodic motion near the system equilibrium points. Analytical approximations serve as the initial guess. Various methods and strategies for numercially computing periodic orbits and the associated families of solutions in the CR3BP are explored. Many different families are represented, including the planar, axial, and vertical families in the vicinity of all five equilibrium points.

Chapter 4:

Orbits with characteristics that support lunar south pole communications coverage are identified for mission applications. Criteria for evaluation include feasibility of coverage, period, and certain stability parameters. Nine different orbits from five different families with periods ranging from 7 to 16 days are transferred to a full ephemeris model. Five different coverage scenarios for two spacecraft are selected and preliminary coverage analyses are summarized.

Chapter 5:

Line-of-sight access times between a lunar ground station at the Shackleton Crater (89.9°S, 0.0°E) and dual spacecraft constellations that correspond to five coverage scenarios are analyzed with advanced commercial software. General line-of-sight access between the spacecraft constellation and the Earth is summarized. More specifically, line-of-sight access between a spacecraft constellation and a possible transmitting site located at the White Sands Test Facility, in New Mexico (32.3°N, 106.8°W) is computed. Preliminary station-keeping results for the nine orbits are also developed by application of invariant manifold theory.

Chapter 6:

The results are summarized and recommendations for future work are offered.

2. BACKGROUND

The differential equations describing the motion of a body of infinitesimal mass subject to the gravity of two much more massive primaries are nonlinear and cannot be solved analytically in closed form. However, numerical integration yields unexpected solutions: non-planar, periodic orbits in the vicinity of the two primaries but orbiting neither one, three-dimensional "figure-eight" trajectories, and an infinite variety of other shapes. The differential equations describing the motion of the small body are formulated in terms of the classical Circular Restricted Three-Body Problem (CR3BP) in this chapter. The equilibrium points in this system are easily computed. First-order analytical approximations are derived from the variational equations relative to the equilibrium points and the state transition matrix is introduced. Contemporaneous and non-contemporaneous variations in the state are defined; invariant manifold theory is introduced.

2.1 The Circular Restricted Three-Body Problem

The position of a small body (P_3 with mass m_3) relative to two primaries (P_1 with mass m_1 and P_2 with mass m_2) is depicted in Figure 2.1. Let $\vec{R}_i$ be the position of P_i with respect to the system barycenter B. Using Newton's Law of Gravity, the equations describing the motion of P_3 are governed by the vector differential equation,

$$m_3 \frac{{}^{\mathbf{I}}d^2\vec{R}_3}{dt^2} = -\frac{Gm_3m_1}{\left\|\vec{R}_{13}\right\|^3}\vec{R}_{13} - \frac{Gm_3m_2}{\left\|\vec{R}_{23}\right\|^3}\vec{R}_{23}, \tag{2.1}$$

where G is the universal gravitational constant. Then, $\vec{R}_{13}$ and $\vec{R}_{23}$ are the relative positions of P_3 with respect to P_1 and P_2. The superscript **I** represents differentiation in the inertial frame. The mass is *restricted* such that $m_1 > m_2 >> m_3$. This implies that m_3 is "infinitesimal," i.e., P_3 cannot impact the motion of m_1 and m_2. Thus, the motion of P_1 and P_2 is Keplerian. Further, the motion of P_2 relative to P_1 is assumed to be *circular*.

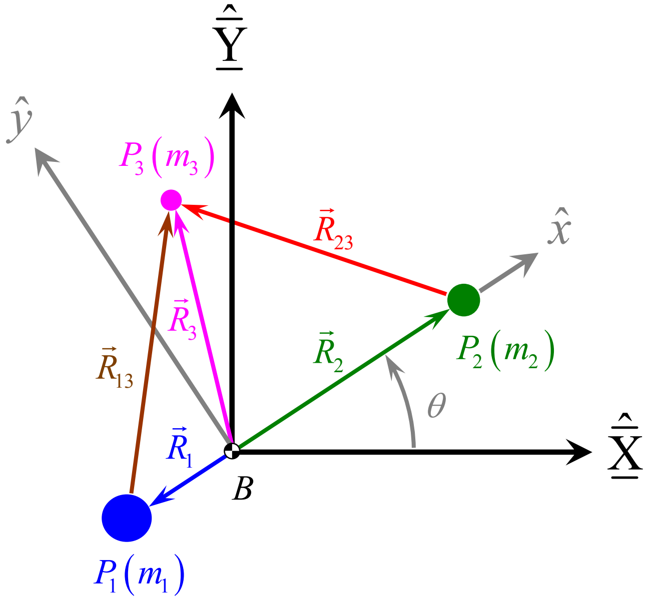

Figure 2.1 Formulation for the Restricted Three-Body Problem

Equation (2.1) can be generalized by introducing characteristic quantities. Let the characteristic length l^* be defined such that

$$l^* = \left\|\vec{R}_1\right\| + \left\|\vec{R}_2\right\|. \tag{2.2}$$

Then, the characteristic mass m^* is the sum of the primary masses, i.e.,

$$m^* = m_1 + m_2, \tag{2.3}$$

and the characteristic time t^* is computed as

$$t^* = \sqrt{\frac{l^{*3}}{Gm^*}}. \tag{2.4}$$

Since the motion of P_2 about P_1 is assumed to be circular, l^* is constant. Using equations (2.2)-(2.4) to non-dimensionalize equation (2.1) yields

$$\frac{{}^{I}d^2\vec{r}_3}{d\tau^2} = -\frac{1-\mu}{\left\|\vec{r}_{13}\right\|^3}\vec{r}_{13} - \frac{\mu}{\left\|\vec{r}_{23}\right\|^3}\vec{r}_{23}, \tag{2.5}$$

where $\vec{r}_3 = \frac{\vec{R}_3}{l^*}$, $\vec{r}_{13} = \frac{\vec{R}_{13}}{l^*}$, $\vec{r}_{23} = \frac{\vec{R}_{23}}{l^*}$, the mass ratio $\mu = \frac{m_2}{m^*}$, and the non-dimensional time $\tau = \frac{t}{t^*}$. Thus, the right side of equation (2.5) is fully defined.

The left side of equation (2.5) can be expanded kinematically. For convenience, the motion of P_3 is described in terms of the barycentric, rotating frame **S** where $\hat{x}$ is parallel to $\vec{r}_2$, $\hat{z}$ is parallel to the angular velocity vector associated with the Keplerian primary orbits, and $\hat{y}$ completes the right-handed set. (The unit vectors associated with the **S** frame are denoted as grey in Figure 2.1.) Therefore,

$$\vec{r}_3 = x\hat{x} + y\hat{y} + z\hat{z}, \tag{2.6}$$

where x, y, and z are the components of position of P_3 relative to B, defined in terms of the rotating frame. The angular velocity of the rotating frame with respect to the inertial frame is written ${}^{\mathbf{I}}\vec{\omega}^{\mathbf{S}} = n\hat{z}$, where the non-dimensional mean motion is unity, i.e., $n = 1$. Therefore, twice differentiating equation (2.6) with respect to an inertial observer yields the kinematic expression,

$${}^{\mathbf{I}}\ddot{\vec{r}}_3 = \left(\ddot{x} - 2\dot{y} - x\right)\hat{x} + \left(\ddot{y} + 2\dot{x} - y\right)\hat{y} + z\hat{z}. \tag{2.7}$$

The dots in equation (2.7) represent differentiation with respect to τ. Furthermore, expressing $\vec{r}_{13}$ and $\vec{r}_{23}$ in terms of μ, x, y, and z yields

$$\vec{r}_{13} = \vec{r}_3 - \vec{r}_1 = \left(x + \mu\right)\hat{x} + y\hat{y} + z\hat{z}, \tag{2.8}$$

$$\vec{r}_{23} = \vec{r}_3 - \vec{r}_2 = \left(x - \left(1 - \mu\right)\right)\hat{x} + y\hat{y} + z\hat{z}. \tag{2.9}$$

Finally, the vector equation (2.5) can be rewritten in scalar form as

$$\ddot{x} - 2\dot{y} - x = -\frac{\left(1-\mu\right)\left(x+\mu\right)}{\left\|\vec{r}_{13}\right\|^3} - \frac{\mu\left(x - \left(1-\mu\right)\right)}{\left\|\vec{r}_{23}\right\|^3}, \tag{2.10}$$

$$\ddot{y} + 2\dot{x} - y = -\frac{\left(1-\mu\right)y}{\left\|\vec{r}_{13}\right\|^3} - \frac{\mu y}{\left\|\vec{r}_{23}\right\|^3}, \tag{2.11}$$

$$\ddot{z} = -\frac{\left(1-\mu\right)z}{\left\|\vec{r}_{13}\right\|^3} - \frac{\mu z}{\left\|\vec{r}_{23}\right\|^3}. \tag{2.12}$$

The motion of P_3 relative to B in the rotating frame is determined by numerically integrating equations (2.10)-(2.12).

2.2 The Equilibrium Points

The system equilibrium points, also called the Lagrange or libration points, are determined from equations (2.10)-(2.12). The relationships that yield the constant equilibrium solutions are the following,

$$-x_{eq} = -\frac{(1-\mu)(x_{eq}+\mu)}{\|\vec{r}_{13}\|_{eq}^{3}} - \frac{\mu(x_{eq}-(1-\mu))}{\|\vec{r}_{23}\|_{eq}^{3}}, \tag{2.13}$$

$$-y_{eq} = -\frac{(1-\mu)y_{eq}}{\|\vec{r}_{13}\|_{eq}^{3}} - \frac{\mu y_{eq}}{\|\vec{r}_{23}\|_{eq}^{3}}, \tag{2.14}$$

$$0 = -\frac{(1-\mu)z_{eq}}{\|\vec{r}_{13}\|_{eq}^{3}} - \frac{\mu z_{eq}}{\|\vec{r}_{23}\|_{eq}^{3}}, \tag{2.15}$$

where $\|\vec{r}_{ij}\|_{eq}$ indicates the norm of a position vector evaluated at the equilibrium point. Five equilibrium points satisfy equations (2.13)-(2.15). From equation (2.15), it is evident that each equilibrium point possesses an out-of-plane component, $z_{eq}=0$. Furthermore, if $\|\vec{r}_{13}\|_{eq}=\|\vec{r}_{23}\|_{eq}=1$, then $y_{eq}\neq 0$, as is evident from equations (2.13)-(2.14). Using equations (2.8)-(2.9) to solve $\|\vec{r}_{13}\|_{eq}=\|\vec{r}_{23}\|_{eq}=1$ renders the solution $x_{eq}=\frac{1}{2}-\mu$ and $y_{eq}=\pm\frac{\sqrt{3}}{2}$. These equilibrium points, i.e., L_4 and L_5, are the triangular or equilateral points since the points exist at the vertices of two equilateral triangles with a common side, i.e., the straight line adjoining P_1 to P_2. (See Figure 2.2.) The remaining three equilibrium points, i.e., L_1, L_2, and L_3, are computed by defining $y_{eq}=0$ in equations (2.13)-(2.14). Since these three equilibrium points all lie on the *x*-axis, they are commonly labeled the collinear points. The form of the resulting equation is

$$x_{eq} + A\frac{1-\mu}{x_{eq}+\mu} + B\frac{\mu}{x_{eq}-1+\mu} = 0, \tag{2.16}$$

where the values of *A* and *B* are ±1 depending on the location of the equilibrium point. The values are summarized in Table 2.1. An iterative method to solve equation (2.16) for x_{eq} is straightforward and, thus, locates the positions of L_1, L_2, and L_3 along the *x*-axis.

Table 2.1

Locating the Collinear Libration Points

Libration Point	Location	A	B
L_1	$-\mu < x_{eq} < 1-\mu$	-1	1
L_2	$x_{eq} > 1-\mu$	-1	-1
L_3	$x_{eq} < -\mu$	1	1

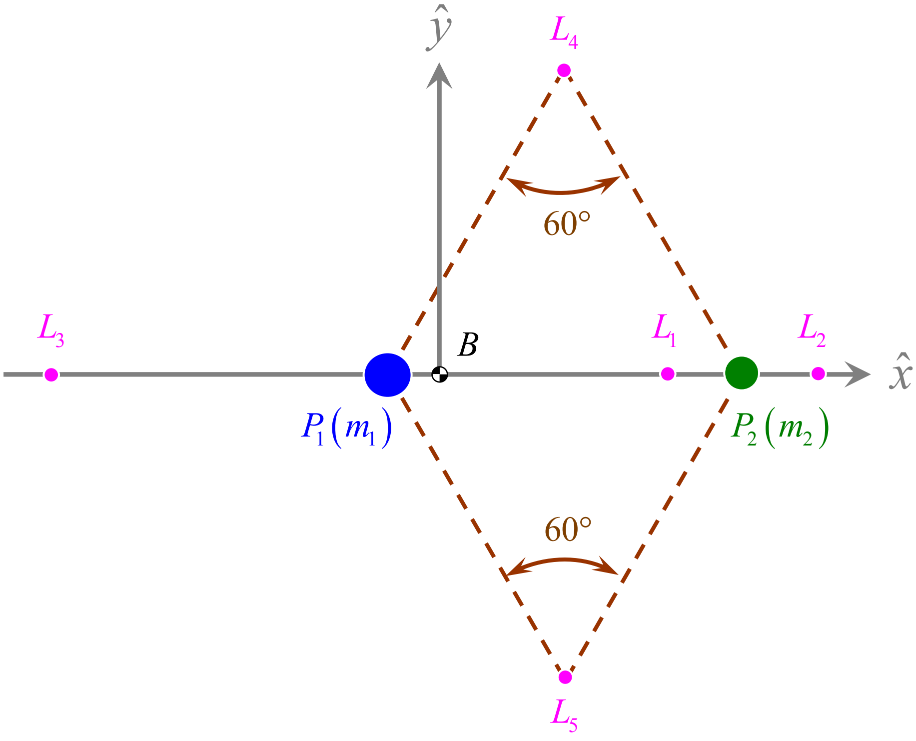

Figure 2.2 Equilibrium or Libration Points (Magenta) in the CR3BP

2.3 First-Order Analytical Approximations for Variations Relative to the Collinear Libration Points

The first-order analytical approximations for motion relative to the collinear points are derived via linearization with respect to the equilibrium point. The first-order variational equations can be solved to yield a useful approximation. As an initial step, introduce the following symbols,

$$\xi = x - x_{eq}, \tag{2.17}$$

$$\eta = y - y_{eq}, \tag{2.18}$$

$$\zeta = z - z_{eq}. \tag{2.19}$$

Therefore ξ, η, and ζ are the variations relative to the equilibrium point defined in terms of its measure numbers x_{eq}, y_{eq}, and z_{eq}. Then, linearizing equations (2.10)-(2.12) about the equilibrium solution yields

$$\ddot{\xi} - 2\dot{\eta} = U_{xx}\big|_{eq}\,\xi + U_{xy}\big|_{eq}\,\eta + U_{xz}\big|_{eq}\,\zeta, \tag{2.20}$$

$$\ddot{\eta} + 2\dot{\xi} = U_{yx}\big|_{eq}\,\xi + U_{yy}\big|_{eq}\,\eta + U_{yz}\big|_{eq}\,\zeta, \tag{2.21}$$

$$\ddot{\zeta} = U_{zx}\big|_{eq}\,\xi + U_{zy}\big|_{eq}\,\eta + U_{zz}\big|_{eq}\,\zeta, \tag{2.22}$$

where U_{ij} is the second partial defined by $\dfrac{\partial^2 U}{\partial j \partial i}$. The symbol $U_{ij}\big|_{eq}$ indicates that the partials are evaluated at the equilibrium point of interest. Since $z_{eq} = 0$ for all the equilibrium points, $U_{xz}\big|_{eq} = U_{yz}\big|_{eq} = U_{zx}\big|_{eq} = U_{zy}\big|_{eq} = 0$ and $U_{zz}\big|_{eq} < 0$. Also, for the collinear points, the equilibrium point is always on the *x*-axis, i.e., $y_{eq} = 0$, and, therefore, $U_{xy}\big|_{eq} = U_{yx}\big|_{eq} = 0$, $U_{xx}\big|_{eq} > 0$, and $U_{yy}\big|_{eq} < 0$. Then, for the collinear points, equations (2.20)-(2.22) are simplified to

$$\ddot{\xi} - 2\dot{\eta} = U_{xx}\big|_{eq}\,\xi, \tag{2.23}$$

$$\ddot{\eta} + 2\dot{\xi} = U_{yy}\big|_{eq}\,\eta, \tag{2.24}$$

$$\ddot{\zeta} = U_{zz}\big|_{eq}\,\zeta. \tag{2.25}$$

Notice that equation (2.25), i.e., the out-of-plane motion, is simple harmonic with frequency $v = \sqrt{\left| U_{zz}\big|_{eq} \right|}$ and independent of the in-plane motion. Therefore, the general solution for ζ can be written in the following form,

$$\zeta = \mathrm{C}_1 \cos v\tau + \mathrm{C}_2 \sin v\tau, \tag{2.26}$$

where C_1 and C_2 are constants. Correspondingly, ξ and η are coupled for the in-plane motion. Thus, the characteristic equation associated with equations (2.23)-(2.24) is of the form

$$\Lambda^2 + 2\beta_1 \Lambda - \beta_2{}^2 = 0, \tag{2.27}$$

where

$$\beta_1 = 2 - \frac{U_{xx}\big|_{eq} + U_{yy}\big|_{eq}}{2}, \tag{2.28}$$

$$\beta_2{}^2 = -U_{xx}\big|_{eq} U_{yy}\big|_{eq} > 0, \tag{2.29}$$

$$\lambda = \pm\sqrt{\Lambda}. \tag{2.30}$$

Then, λ represents the eigenvalues associated with the coupled equations (2.23)-(2.24). The general solutions for ξ and η are

$$\xi = \sum_{i=1}^{4} \mathrm{A}_i e^{\lambda_i \tau}, \tag{2.31}$$

$$\eta = \sum_{i=1}^{4} \mathrm{B}_i e^{\lambda_i \tau}, \tag{2.32}$$

where A_i and B_i are constants, but not independent. Direct substitution of equations (2.31)-(3.32) into equations (2.23)-(2.24) results in the following relationship between A_i and B_i, that is,

$$\mathrm{B}_i = \frac{\lambda_i - U_{xx}\big|_{eq}}{2\lambda_i} \mathrm{A}_i. \tag{2.33}$$

Differentiation of equations (2.31)-(2.32) with respect to τ, substitution of equation (2.33), and evaluation of the result at the initial time, $\tau = \tau_0 = 0,$ yields

$$\xi_0 = \sum_{i=1}^{4} \mathrm{A}_i, \tag{2.34}$$

$$\dot{\xi}_0 = \sum_{i=1}^{4} \mathrm{A}_i \lambda_i, \tag{2.35}$$

$$\eta_0 = \sum_{i=1}^{4} \frac{\lambda_i - U_{xx}\big|_{eq}}{2\lambda_i} \mathrm{A}_i, \tag{2.36}$$

$$\dot{\eta}_0 = \sum_{i=1}^{4} \frac{\lambda_i - U_{xx}\big|_{eq}}{2\lambda_i} \mathrm{A}_i \lambda_i. \tag{2.37}$$

Expressions for A$_i$ in terms of ξ_0, $\dot{\xi}_0$, η_0, $\dot{\eta}_0$, λ_i, and $U_{xx}\big|_{eq}$ are obtained by inversion of equation (2.34)-(2.37). In general, as evidenced by equation (2.30), the system possesses one unstable mode, one stable mode, and two center modes. Therefore, if A$_1$ and A$_2$ correspond to the stable and unstable modes, then by specifying ξ_0 and η_0, $\dot{\xi}_0$ and $\dot{\eta}_0$ can be specified such that $\mathrm{A}_1 = \mathrm{A}_2 = 0$. Then ξ, η, and ζ can be written in the form,

$$\xi = \xi_0 \cos s\tau + \frac{\eta_0}{\beta_3} \sin s\tau, \tag{2.38}$$

$$\eta = \eta_0 \cos s\tau + \xi_0 \beta_3 \sin s\tau, \tag{2.39}$$

$$\zeta = \zeta_0 \cos v\tau + \frac{\zeta_0}{v} \sin v\tau, \tag{2.40}$$

where

$$s = \sqrt{\beta_1 + \left(\beta_1^2 + \beta_2^2\right)^{1/2}}, \tag{2.41}$$

$$\beta_3 = \frac{s^2 - U_{xx}\big|_{eq}}{2s}. \tag{2.42}$$

Notice that the period of the motion is simply $\frac{2\pi}{s}$. From the linear approximation, the three-dimensional motion of P_3 is not periodic since the in-plane and out-of-plane frequencies are not commensurate. However, s and v are relatively close in value for the problem of interest. This suggests that quasi-periodic motion can be approximated.

2.3.1 Quasi-Periodic, First-Order Approximations Near the Collinear Libration Points

Equations (2.38)-(2.40) can be further simplified to produce approximate conditions for quasi-periodic, Lissajous motion in terms of discrete points along the path. The conditions are determined simply by specifying an amplitude A_ξ in the ξ direction or an amplitude A_η in the η direction; then, an amplitude A_ζ is specified in the ζ direction. If it is desired to specify A_ξ and A_ζ, then equations (2.38)-(2.40) can be simplified to the following form,

$$\xi = -A_\xi \cos\left(s\tau + \phi\right), \tag{2.43}$$

$$\eta = \beta_3 A_\xi \sin\left(s\tau + \phi\right), \tag{2.44}$$

$$\zeta = A_\zeta \sin\left(v\tau + \psi\right). \tag{2.45}$$

Alternatively, if it is desired that A_η and A_ζ are inputs, then equations (2.38)-(2.40) can be simplified to

$$\xi = -\frac{A_\eta}{\beta_3} \cos\left(s\tau + \phi\right), \tag{2.46}$$

$$\eta = A_\eta \sin\left(s\tau + \phi\right), \tag{2.47}$$

$$\zeta = A_\zeta \sin\left(v\tau + \psi\right). \tag{2.48}$$

The phase angles ϕ and ψ define the starting point along the Lissajous trajectory. Discretizing τ and differentiating equations (2.43)-(2.45) or (2.46)-(2.48) produces approximate positions and velocities at discrete points, or patch points, along the path. Ten revolutions of a first-order approximation to a Lissajous trajectory near L_1 appear in Figure 2.3 as plotted in the Earth-Moon system; $\phi = 180°$, $\psi = 90°$, A_η= 15,000 km, and $A_\zeta = 20,000$ km are input with four patch points per revolution. The period corresponding to each revolution is approximately 11.7471 days.

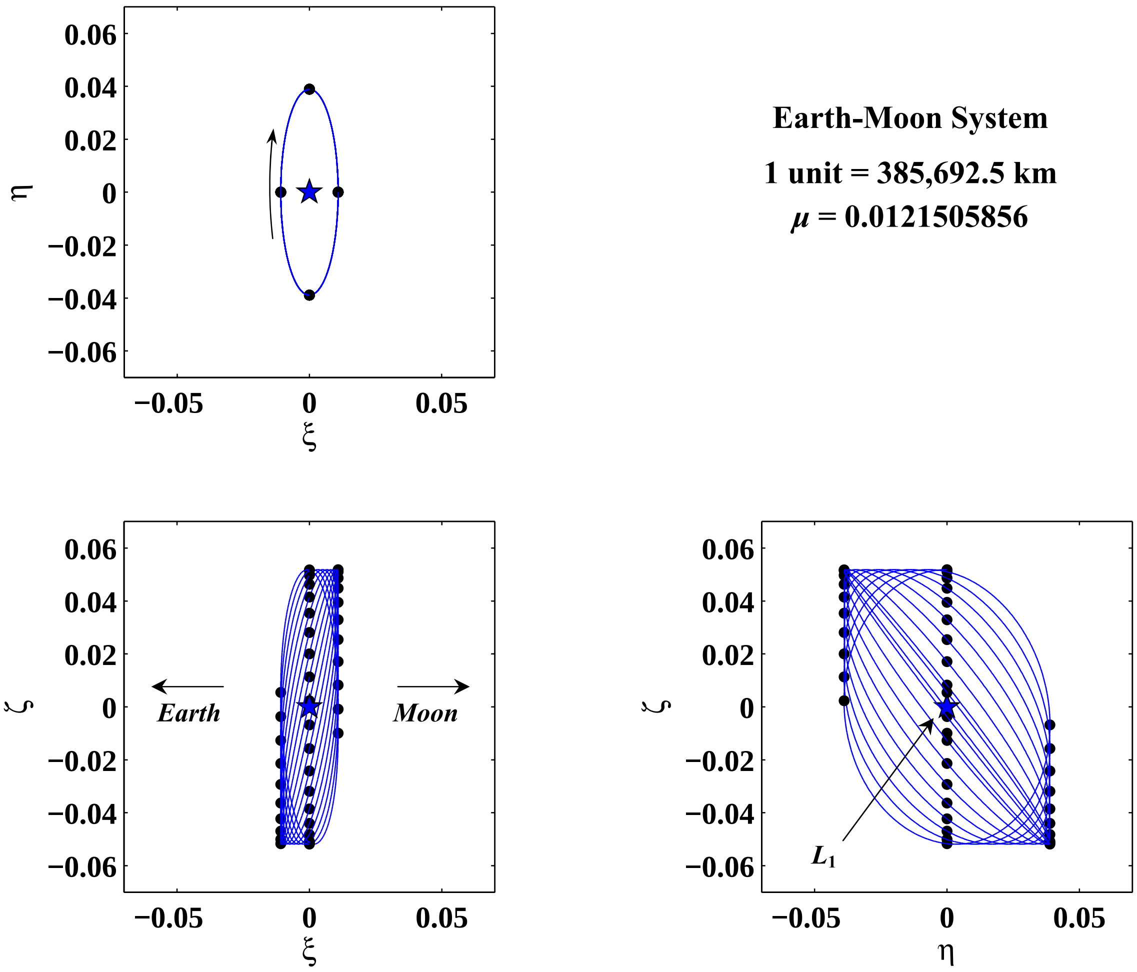

Figure 2.3 First-Order Approximation to a Lissajous Trajectory

2.3.2 Periodic, First-Order Approximations Near the Collinear Libration Points

According to Poincaré [4], an infinite variety of periodic solutions exist in the three-body problem. Because equations (2.10)-(2.12) are not solvable in closed form, computation of the periodic solution is challenging. Many of these solutions have been studied by various researchers [7-10, 15-21, 26-29]. Most of these studies are based on particular solutions obtained using different approaches. One way to obtain a particular periodic solution in the nonlinear problem is to first generate a particular periodic solution in the linear system.

Even planar periodic orbits in the nonlinear system are a challenge to compute without an initial guess. A first-order, planar linear approximation is available, however. Restricting the motion to be planar in the linear system, i.e., when $A_\zeta = 0$ in equations (2.45) and (2.48), provides accurate approximations for small amplitude A_ξ and A_η. A single patch point is positioned on the x-axis corresponding to the angles $\phi = 180°$, $\psi = 90°$. For the approximation in Figure 2.4, A_η = 15,000 km for a period of 11.7471 days. The resulting planar orbit is the approximation to a finite Lyapunov orbit. Other linear approximations for particular solutions that are three-dimensional are available by specifying the in-plane and out-of-plane frequencies to be commensurate.

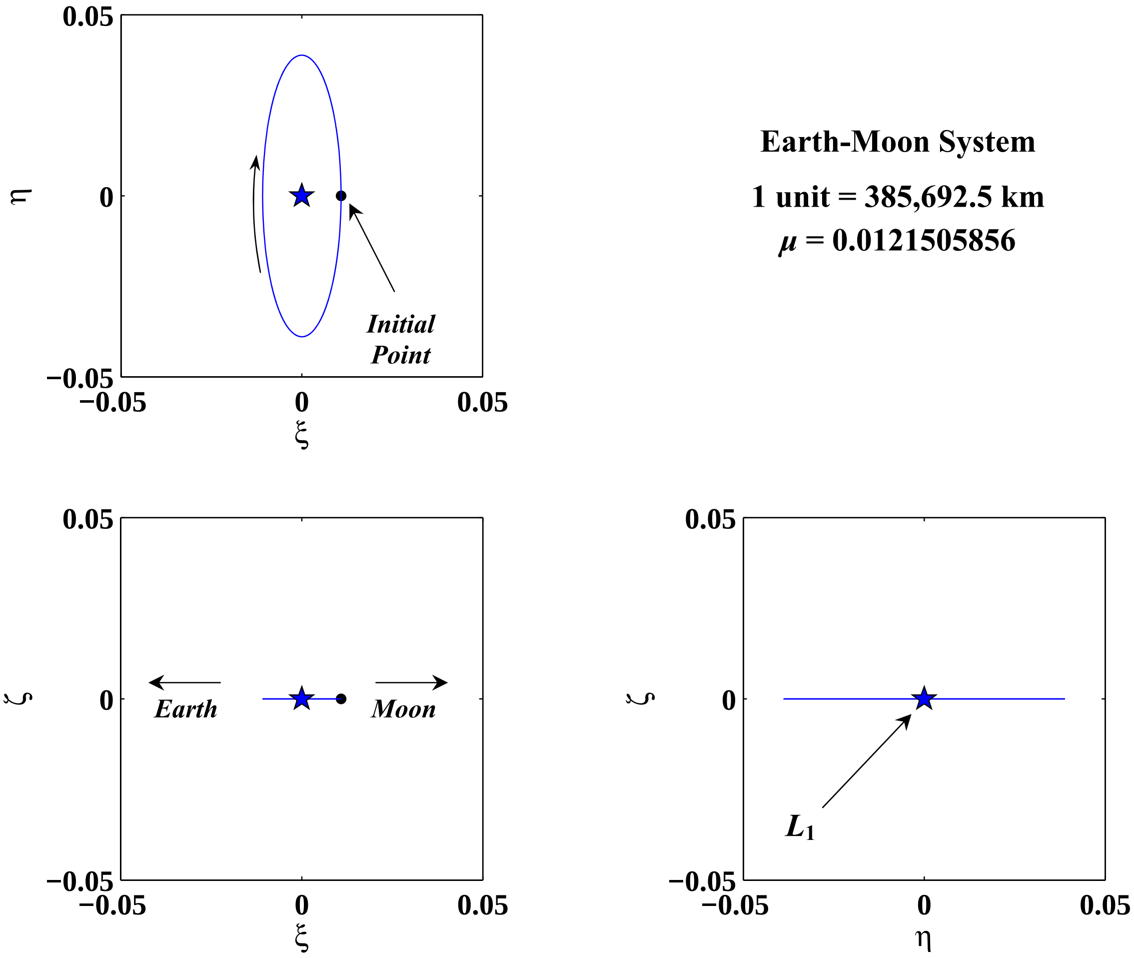

Figure 2.4 First-Order Approximation to a Lyapunov Orbit

2.4 Fundamental Variational Relationships

The analytical approximations are only accurate for motion close to the equilibrium point. However, other particular, numerical solutions exist for periodic motion not in the vicinity of the equilibrium point. For example, families of large amplitude halo orbits have been computed that originate in the vicinity of the collinear points [16, 17, 19-20, 27, 28]. Furthermore, families of solutions have been determined that 'connect' the motion near the collinear points to motion in the vicinity of triangular points [7, 9, 21, 26, 29]. The stability of the solutions provides information regarding the phase space, and the phase space is manipulated to determine other bounded motion as well as the flow to and from periodic orbits.

2.4.1 The State-Transition Matrix

The state-transition matrix is a linear map between state variations along the path. Since the system is conservative, a pseudo-potential function U can be defined, that is,

$$U = \frac{1-\mu}{\left\|\vec{r}_{13}\right\|} + \frac{\mu}{\left\|\vec{r}_{23}\right\|} + \frac{1}{2}\left(x^2 + y^2\right), \tag{2.49}$$

such that

$$\ddot{x} - 2\dot{y} - x = U_x, \tag{2.50}$$

$$\ddot{y} + 2\dot{x} - y = U_y, \tag{2.51}$$

$$\ddot{z} = U_z, \tag{2.52}$$

where $U_x = \frac{\partial U}{\partial x}$, $U_y = \frac{\partial U}{\partial y}$, and $U_z = \frac{\partial U}{\partial z}$. Let the associated six element state vector $\vec{q}$ be defined as $\vec{q} = \left\{x \quad y \quad z \quad \dot{x} \quad \dot{y} \quad \dot{z}\right\}^T$. The first-order variational equations are derived and result in the vector differential equation,

$$\delta\dot{\vec{q}} = \mathbf{A}\left(\tau\right)\delta\vec{q}. \tag{2.53}$$

Since the matrix $\mathbf{A}\left(\tau\right)$ is evaluated along the reference solution, it is generally not constant for an arbitrary trajectory as a reference solution. However, if the reference is a periodic solution, then $\mathbf{A}(\tau)$ is periodic as well. The general form of the 6×6 matrix $\mathbf{A}(\tau)$ is summarized in terms of four 3×3 submatrices,

$$\mathbf{A}(\tau) = \left[\begin{array}{c:c} \mathbf{0}_{3\times 3} & \mathbf{I}_{3\times 3} \\ \hdashline \mathbf{U}_{\underline{\mathbf{XX}}} & \mathbf{\Omega} \end{array}\right], \tag{2.54}$$

where submatrices $\mathbf{U}_{\underline{\mathbf{XX}}}$ and $\mathbf{\Omega}$ are defined as $\mathbf{U}_{\underline{\mathbf{XX}}} = \begin{bmatrix} U_{xx} & U_{xy} & U_{xz} \\ U_{yx} & U_{yy} & U_{yz} \\ U_{zx} & U_{zy} & U_{zz} \end{bmatrix}$ and $\mathbf{\Omega} = \begin{bmatrix} 0 & 2 & 0 \\ -2 & 0 & 0 \\ 0 & 0 & 0 \end{bmatrix}$, respectively. The components of $\mathbf{U}_{\underline{\mathbf{XX}}}$ are expressed as functions of the states such that $U_{ij} = \dfrac{\partial^2 U}{\partial j \partial i}$. The 6×6 state-transition matrix results in the following partials,

$$\mathbf{\Phi}(\tau + \tau_0, \tau_0) = \begin{bmatrix} \frac{\partial x}{\partial x_0} & \frac{\partial x}{\partial y_0} & \frac{\partial x}{\partial z_0} & \frac{\partial x}{\partial \dot{x}_0} & \frac{\partial x}{\partial \dot{y}_0} & \frac{\partial x}{\partial \dot{z}_0} \\ \frac{\partial y}{\partial x_0} & \frac{\partial y}{\partial y_0} & \frac{\partial y}{\partial z_0} & \frac{\partial y}{\partial \dot{x}_0} & \frac{\partial y}{\partial \dot{y}_0} & \frac{\partial y}{\partial \dot{z}_0} \\ \frac{\partial z}{\partial x_0} & \frac{\partial z}{\partial y_0} & \frac{\partial z}{\partial z_0} & \frac{\partial z}{\partial \dot{x}_0} & \frac{\partial z}{\partial \dot{y}_0} & \frac{\partial z}{\partial \dot{z}_0} \\ \frac{\partial \dot{x}}{\partial x_0} & \frac{\partial \dot{x}}{\partial y_0} & \frac{\partial \dot{x}}{\partial z_0} & \frac{\partial \dot{x}}{\partial \dot{x}_0} & \frac{\partial \dot{x}}{\partial \dot{y}_0} & \frac{\partial \dot{x}}{\partial \dot{z}_0} \\ \frac{\partial \dot{y}}{\partial x_0} & \frac{\partial \dot{y}}{\partial y_0} & \frac{\partial \dot{y}}{\partial z_0} & \frac{\partial \dot{y}}{\partial \dot{x}_0} & \frac{\partial \dot{y}}{\partial \dot{y}_0} & \frac{\partial \dot{y}}{\partial \dot{z}_0} \\ \frac{\partial \dot{z}}{\partial x_0} & \frac{\partial \dot{z}}{\partial y_0} & \frac{\partial \dot{z}}{\partial z_0} & \frac{\partial \dot{z}}{\partial \dot{x}_0} & \frac{\partial \dot{z}}{\partial \dot{y}_0} & \frac{\partial \dot{z}}{\partial \dot{z}_0} \end{bmatrix}, \tag{2.55}$$

and can be evaluated from the governing matrix differential equation such that

$$\dot{\mathbf{\Phi}}(\tau + \tau_0, \tau_0) = \mathbf{A}(\tau)\mathbf{\Phi}(\tau + \tau_0, \tau_0). \tag{2.56}$$

The well-known form of the solution to equations (2.56) is

$$\delta\vec{q} = \mathbf{\Phi}(\tau + \tau_0, \tau_0)\delta\vec{q}_0, \tag{2.57}$$

where $\delta\vec{q}_0$ is the vector of initial variations at τ_0 and the elements of the vector $\delta\vec{q}$ represent the variations at $\tau+\tau_0$. Simultaneous numerical integration of equation (2.56) and the equations of motion, i.e., equations (2.10)-(2.12), produces the evolving components of $\mathbf{\Phi}\left(\tau+\tau_0,\tau_0\right)$. Furthermore, from equation (2.57) it is evident that $\mathbf{\Phi}\left(\tau_0,\tau_0\right)=\mathbf{I}_{6\times 6}$. The state-transition matrix supplies valuable information regarding both the stability of the system and predictions for variations along the path.

2.4.2 Contemporaneous and Non-Contemporaneous Variations in the State

Predictions of future variations along the path are critical for the development of targeting schemes to obtain periodic orbits. To predict variations along the path, let $\vec{q}_i$ be a six-element state vector that denotes the position and velocity states associated with the i^{th} point along the path as seen in Figure 2.5. If *f* represents a mapping via numerical integration from point *i* to the next point $i+1$, then

$$\vec{q}_{i+1}=f\left(\vec{q}_i,\Delta\tau\right), \tag{2.58}$$

where $\Delta\tau=\tau_{i+1}-\tau_i$. Then, the non-contemporaneous state variation corresponding to the $i^{th}+1$ point, i.e., $\delta\vec{q}_{i+1}$, must satisfy

$$\vec{q}_{i+1}+\delta\vec{q}_{i+1}=f\left(\vec{q}_i+\delta\vec{Q}_i,\Delta\tau+\delta\tau_{i+1}\right), \tag{2.59}$$

where $\delta\vec{Q}_i$ represents a contemporaneous variation in the state for the i^{th} point along the path. (See Figure 2.5.) Using a first-order Taylor series expansion, equation (2.58) becomes

$$\vec{q}_{i+1}+\delta\vec{q}_{i+1}=f\left(\vec{q}_i,\Delta\tau\right)+\left.\frac{\partial f}{\partial\vec{q}_i}\right|_{\vec{q}_i,\Delta\tau}\delta\vec{Q}_i+\left.\frac{\partial f}{\partial\tau}\right|_{\vec{q}_i,\Delta\tau}\delta\tau_{i+1}. \tag{2.60}$$

It is apparent that $\left.\frac{\partial f}{\partial\vec{q}_i}\right|_{\vec{q}_i,\Delta\tau}=\mathbf{\Phi}\left(\tau_{i+1},\tau_i\right)$ and $\left.\frac{\partial f}{\partial\tau}\right|_{\vec{q}_i,\Delta\tau}=\dot{\vec{q}}_{i+1}$. Thus, in substituting equation (2.58) into equation (2.60), the first-order approximation for the variations $\delta\vec{q}_{i+1}$ is rewritten as

$$\delta\vec{q}_{i+1} = \left[\mathbf{\Phi}\left(\tau_{i+1},\tau_i\right) \quad \dot{\vec{q}}_{i+1}\right]\begin{Bmatrix}\delta\vec{Q}_i \\ \delta\tau_{i+1}\end{Bmatrix}. \tag{2.61}$$

Equation (2.61) and equation (2.57) together comprise an important fundamental relationship between non-contemporaneous and contemporaneous variations in a state vector, i.e.,

$$\delta\vec{Q}_i = \delta\vec{q}_i - \dot{\vec{q}}_i\delta\tau_i. \tag{2.62}$$

This vector relationship is also apparent in Figure 2.5. Furthermore, substituting equation (2.61) into equation (2.60) and rearranging results in the following useful expression,

$$\delta\vec{q}_{i+1} - \dot{\vec{q}}_{i+1}\delta\tau_{i+1} = \mathbf{\Phi}\left(\tau_{i+1},\tau_i\right)\left(\delta\vec{q}_i - \dot{\vec{q}}_i\delta\tau_i\right). \tag{2.63}$$

Equation (2.61) is the foundation of any targeting scheme when the problem is independent of the time associated with the initial state, i.e., τ_i. Equation (2.63) serves as the basis for more complex targeting schemes where there exists a more specific dependence on τ_i, e.g., simultaneously predicting variations in position and time for a series of discrete patch point states along the path.

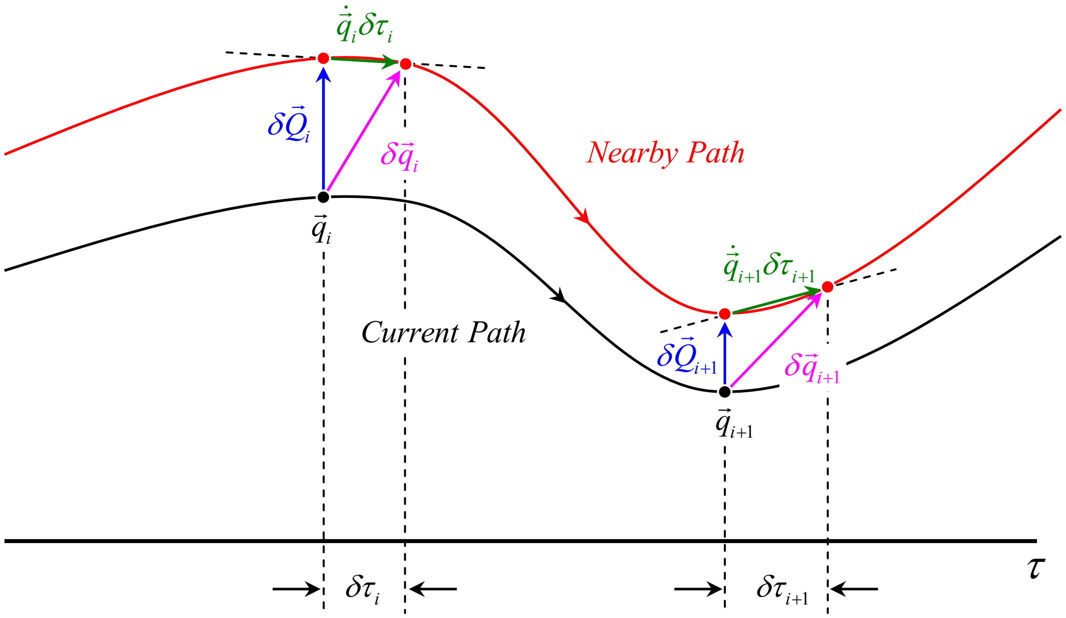

Figure 2.5 Representation of Contemporaneous and Non-Contemporaneous Variations in the State

2.4.3 An Introduction to Invariant Manifold Theory

The phase space offers information regarding the characteristic flow near particular solutions. The center, unstable, and stable subspaces are available from analysis of the phase space and are useful in obtaining various types of trajectory arcs. The invariant manifolds associated with the unstable and stable subspaces of periodic and quasi-periodic solutions, in particular, are key factors in understanding and designing transfers toward and away from these orbits. Perko [43] includes a thorough investigation of invariant manifold theory as it applies to equilibrium points and periodic orbits.

For a periodic orbit, the monodromy matrix is defined as the state-transition matrix after one full period T, i.e., $\Phi\left(T+\tau_i,\tau_i\right)$. Since the orbit is periodic, any point along the path can be represented by one six-element state vector along the path. Such a representative point is labeled as the "fixed point." Then, the initial time τ_i corresponds to the i^{th} fixed point along the path of a periodic solution. Of course, information concerning the phase space relative to this fixed point is available from the eigenstructure of $\Phi\left(T+\tau_i,\tau_i\right)$. If the eigenstructure is such that the periodic orbit possesses an unstable and a stable mode, then the eigenvalues and eigenvectors can be used to develop linear approximations to the unstable subspace W_u and stable subspace W_s. If W_u and W_s are available, they are further exploited to generate the global unstable and stable manifolds. Then, let the six-dimensional vector $\hat{Y}_i^{W_u}$ represent the eigenvector associated with the unstable mode of $\Phi\left(T+\tau_i,\tau_i\right)$ such that it can be decomposed in terms of three-dimensional components $\vec{R}_i^{W_u}$ and $\vec{V}_i^{W_u}$ as follows,

$$\hat{Y}_i^{W_u}=\begin{Bmatrix}\vec{R}_i^{W_u}\\ \vec{V}_i^{W_u}\end{Bmatrix}. \tag{2.64}$$

Then, the unstable direction is represented by

$$\vec{X}_i^{W_u}=\frac{\hat{Y}_i^{W_u}}{\left\|\vec{R}_i^{W_u}\right\|}. \tag{2.65}$$

A small perturbation in the unstable direction, $\vec{X}_i^{W_u}$, places the spacecraft on an unstable manifold departing the vicinity of the reference solution. The perturbing terms are represented by

$$\begin{Bmatrix} \delta\vec{R}_i^{W_u} \\ \delta\vec{V}_i^{W_u} \end{Bmatrix} = d \cdot \vec{X}_i^{W_u}, \tag{2.66}$$

where *d* is an initial displacement in the unstable direction. The unstable manifold for the i^{th} point along path of a periodic solution is obtained by perturbing the corresponding states by $\pm\left\{\delta\vec{R}_i^{W_u T} \quad \delta\vec{V}_i^{W_u T}\right\}^T$ and integrating forward in time. The stable manifold is obtained using the same analysis but with the stable subspace and integrating backward in time.

3. GENERATING ORBITS IN THE CIRCULAR RESTRICTED THREE-BODY PROBLEM

In 1892, Poincaré showed that an infinite number of periodic solutions exist in the three-body problem. Many of the solutions remain unknown and the practical application of most of the known periodic solutions has not yet been thoroughly investigated. However, due to the nature of the solutions, perhaps the most useful orbit architectures can be pieced together within the context of the three-body problem. Therefore, generating orbits in the CR3BP is a critical step in constructing a useful trajectory for the mission design process. A thorough investigation of orbits in the CR3PB is useful in generating a trajectory such that the current mission design requirements are fully satisfied. Due to the sensitivities of the problem, the acquisition of many different algorithms for convergence aids the discovery process. Furthermore, an understanding of the stability of the solutions and their bifurcations yields knowledge about the geometry and intersection of invariant manifolds.

The determination of quasi-periodic motion in the CR3BP is based upon a general two-level corrections scheme. Additional periodic solutions can be computed. Five different methods for generating periodic solutions are included in this chapter. Strategies for predicting initial guesses for solutions and locating bifurcations along a manifold are offered. Many different types of orbit families are generated, including planar, axial, and vertical families of orbits near all five libration points. A general assessment of the stability of these solutions is also summarized.

3.1 The Two-Level Differential Corrections Process

The two-level corrector was first applied to the CR3BP in 1986, by Howell and Pernicka [22]. The corrections scheme locates a natural solution in the vicinity of an initial guess comprised of multiple segments and is therefore a powerful tool in the computation of quasi-periodic solutions in the CR3BP; it is also a significant aid in bringing highly sensitive solutions to a full ephemeris model with only small variations in characteristics. The quasi-periodic solutions of interest here are denoted as Lissajous trajectories, a type of motion named after the French physicist Jules Antoine Lissajous (1822-1880) who discovered similar motions when optically studying vibrations. The two-level corrections scheme is also easily modified for constrained motion and adaptable for multiple flight regimes [23-25].

3.1.1 The "First Level" of the Corrections Process

The goal of a two-level corrections scheme is the determination of a trajectory with specified characteristics. The "first level" of the process is focused on position continuity. Velocity discontinuities are inserted to ensure a continuous path. Figure 3.1 illustrates this first step in the process. In the figure, a path is represented as a set of individual segments numbered $1, 2, \ldots, n$. Recall that the points that eventually connect the segments are termed patch points. The red curves reflect initial approximations for each segment. These "initial guesses" can be obtained analytically or numerically.

The first level of the two-level corrector allows variations in initial velocity on a segment such that endpoint positions available from the approximations are exactly targeted. (See the black path in Figure 3.1.) For each segment, i.e., between every i^{th} and $i^{th}+1$ patch point, equation (2.61) is used in an iterative process to solve for variations in initial velocity and time that reduce the final point variations in position to zero. Then, let $\vec{V}_i$ be the velocity vector associated with the i^{th} patch point and τ_{i+1} the initial time for integration to the $i^{th}+1$ patch point. Then, $\vec{V}_i$ and τ_{i+1} are iteratively updated using

$$\delta\vec{R}_{i+1} = \underbrace{\left[\begin{array}{ccc:c} \dfrac{\partial x}{\partial \dot{x}_0} & \dfrac{\partial x}{\partial \dot{y}_0} & \dfrac{\partial x}{\partial \dot{z}_0} & \\ \dfrac{\partial y}{\partial \dot{x}_0} & \dfrac{\partial y}{\partial \dot{y}_0} & \dfrac{\partial y}{\partial \dot{z}_0} & \vec{V}_{i+1} \\ \dfrac{\partial z}{\partial \dot{x}_0} & \dfrac{\partial z}{\partial \dot{y}_0} & \dfrac{\partial z}{\partial \dot{z}_0} & \end{array}\right]}_{\mathbf{L}} \begin{Bmatrix} \delta\vec{V}_i \\ \delta\tau_{i+1} \end{Bmatrix}, \tag{3.7}$$

where the smallest Euclidean norm yields

$$\begin{Bmatrix} \delta\vec{V}_i \\ \delta\tau_{i+1} \end{Bmatrix} = \mathbf{L}^T\left[\mathbf{L}\mathbf{L}^T\right]^{-1}\delta\vec{R}_{i+1}, \tag{3.8}$$

until $\delta\vec{R}_{i+1} < \varepsilon$. As a result, for *n* patch points, there will exist new velocities for the first *n* – 1 patch point states (all nodes but the final patch point *n*). Since time is tagged at the endpoint along each segment, new times associated with the last *n* – 1 patch points will be determined. Of course, time continuity is preserved across the entire path and each point is fully targeted. There will also exist velocity discontinuities, or $\Delta\vec{V}$'s, at each internal patch points, i.e.,

$$\Delta\vec{V}_i = \vec{V}_i^+ - \vec{V}_i^-, \tag{3.9}$$

where '+' and '–' denote characteristic quantities associated with outgoing and incoming segments. In Figure 3.1, the final continuous path across all segments is black.

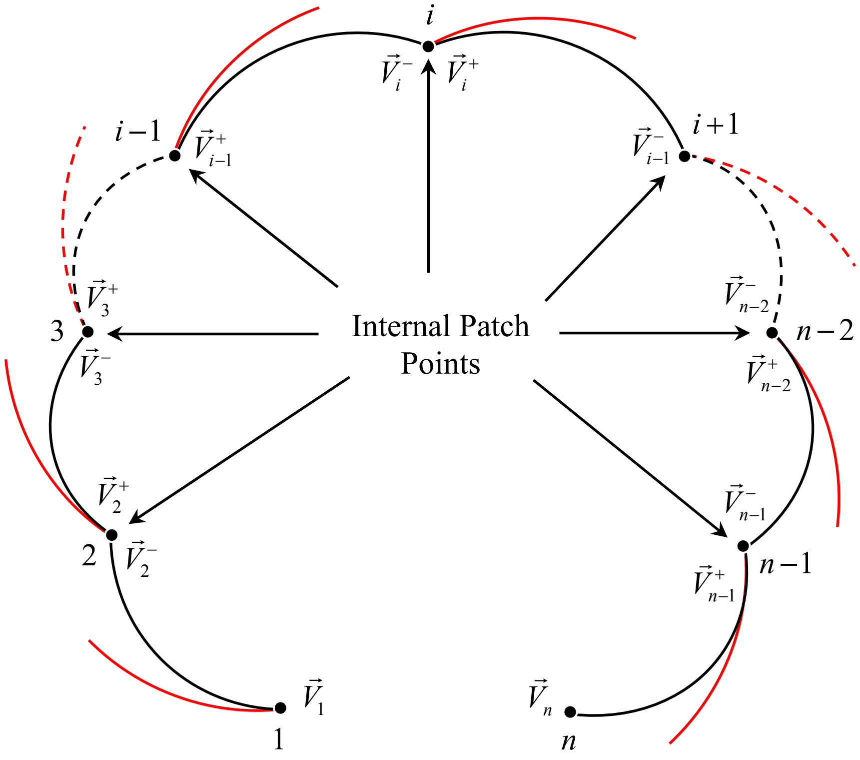

Figure 3.1 Path Before (Red) and After (Black) First Level is Applied

3.1.2 The "Second Level" of the Corrections Process

The "second level" of the corrections process focuses on minimizing the $\Delta\vec{V}$'s associated with the first level, thereby locating a natural solution in the vicinity of the initial guess. That is, the second level simultaneously shifts each patch point position and time, i.e., $\delta\vec{R}_i$ and $\delta\tau_i$, to minimize the $\Delta\vec{V}$'s inserted in the first level. To accomplish the task, it is necessary to express variations in $\Delta\vec{V}_i$ as functions of $\delta\vec{R}_i$ and $\delta\tau_i$. From equation (3.9), the velocity discontinuity identified with the i^{th} patch point depends on both the outgoing $i^{th}-1$ and incoming $i^{th}+1$ states. (See Figure 3.1) Therefore, the relationship between $\delta\vec{R}_i$, $\delta\tau_i$, and $\Delta\vec{V}_i$ can be written as

$$\delta\Delta\vec{V}_i = \underbrace{\begin{bmatrix} M_{\vec{R}_i}^- & M_{\tau_i}^- & M_{\vec{R}_i} & M_{\tau_i} & M_{\vec{R}_i}^+ & M_{\tau_i}^+ \end{bmatrix}}_{\mathbf{M}_i} \begin{Bmatrix} \delta\vec{R}_{i-1} \\ \delta\tau_{i-1} \\ \delta\vec{R}_i \\ \delta\tau_i \\ \delta\vec{R}_{i+1} \\ \delta\tau_{i+1} \end{Bmatrix}. \tag{3.10}$$

The state-relationship matrix $\mathbf{M}_i$ is identified via the partials of equation (3.9) with respect to position and time such that

$$M_{\vec{R}_i}^- = \frac{\partial\Delta\vec{V}_i}{\partial\vec{R}_{i-1}} = \frac{\partial\Delta\vec{V}_i}{\partial\vec{V}_i^-}\frac{\partial\vec{V}_i^-}{\partial\vec{R}_{i-1}} = -\frac{\partial\vec{V}_i^-}{\partial\vec{R}_{i-1}}, \tag{3.11}$$

$$M_{\tau_i}^- = \frac{\partial\Delta\vec{V}_i}{\partial\tau_{i-1}} = \frac{\partial\Delta\vec{V}_i}{\partial\vec{V}_i^-}\frac{\partial\vec{V}_i^-}{\partial\tau_{i-1}} = -\frac{\partial\vec{V}_i^-}{\partial\tau_{i-1}}, \tag{3.12}$$

$$M_{\vec{R}_i} = \frac{\partial\Delta\vec{V}_i}{\partial\vec{R}_i} = \frac{\partial\Delta\vec{V}_i}{\partial\vec{V}_i^-}\frac{\partial\vec{V}_i^-}{\partial\vec{R}_i} + \frac{\partial\Delta\vec{V}_i}{\partial\vec{V}_i^+}\frac{\partial\vec{V}_i^+}{\partial\vec{R}_i} = -\frac{\partial\vec{V}_i^-}{\partial\vec{R}_i} + \frac{\partial\vec{V}_i^+}{\partial\vec{R}_i}, \tag{3.13}$$

$$M_{\tau_i} = \frac{\partial\Delta\vec{V}_i}{\partial\tau_i} = \frac{\partial\Delta\vec{V}_i}{\partial\vec{V}_i^-}\frac{\partial\vec{V}_i^-}{\partial\tau_i} + \frac{\partial\Delta\vec{V}_i}{\partial\vec{V}_i^+}\frac{\partial\vec{V}_i^+}{\partial\tau_i} = -\frac{\partial\vec{V}_i^-}{\partial\tau_i} + \frac{\partial\vec{V}_i^+}{\partial\tau_i}, \tag{3.14}$$

$$M_{\vec{R}_i}^+ = \frac{\partial\Delta\vec{V}_i}{\partial\vec{R}_{i+1}} = \frac{\partial\Delta\vec{V}_i}{\partial\vec{V}_i^+}\frac{\partial\vec{V}_i^+}{\partial\vec{R}_{i+1}} = \frac{\partial\vec{V}_i^+}{\partial\vec{R}_{i+1}}, \tag{3.15}$$

$$M_{\tau_i}^+ = \frac{\partial\Delta\vec{V}_i}{\partial\tau_{i+1}} = \frac{\partial\Delta\vec{V}_i}{\partial\vec{V}_i^+}\frac{\partial\vec{V}_i^+}{\partial\tau_{i+1}} = \frac{\partial\vec{V}_i^+}{\partial\tau_{i+1}}. \tag{3.16}$$

Each of the resulting partials in equation (3.11)-(3.16) must be further reduced for evaluation. The partials of $\vec{V}_i^-$ and $\vec{V}_i^+$ with respect to the $i^{th}-1$, i^{th}, $i^{th}+1$ positions and times are derived from the linear variational equations. Using equation (2.63), the linear variational equations are written,

$$\begin{Bmatrix} \delta\vec{R}_{i-1} - \vec{V}_{i-1}^+ \delta\tau_{i-1} \\ \delta\vec{V}_{i-1}^+ - \dot{\vec{V}}_{i-1}^+ \delta\tau_{i-1} \end{Bmatrix} = \begin{bmatrix} \mathbf{A}_{i-1,i} & \mathbf{B}_{i-1,i} \\ \mathbf{C}_{i-1,i} & \mathbf{D}_{i-1,i} \end{bmatrix} \begin{Bmatrix} \delta\vec{R}_i - \vec{V}_i^- \delta\tau_{i+1} \\ \delta\vec{V}_i^- - \dot{\vec{V}}_i^- \delta\tau_{i+1} \end{Bmatrix}, \tag{3.11}$$

and

$$\begin{Bmatrix} \delta\vec{R}_{i+1} - \vec{V}_{i+1}^- \delta\tau_{i+1} \\ \delta\vec{V}_{i+1}^- - \dot{\vec{V}}_{i+1}^- \delta\tau_{i+1} \end{Bmatrix} = \begin{bmatrix} \mathbf{A}_{i+1,i} & \mathbf{B}_{i+1,i} \\ \mathbf{C}_{i+1,i} & \mathbf{D}_{i+1,i} \end{bmatrix} \begin{Bmatrix} \delta\vec{R}_i - \vec{V}_i^+ \delta\tau_{i+1} \\ \delta\vec{V}_i^+ - \dot{\vec{V}}_i^+ \delta\tau_{i+1} \end{Bmatrix}, \tag{3.12}$$

where $\mathbf{\Phi}\left(\tau_{i-1},\tau_i\right) = \begin{bmatrix} \mathbf{A}_{i-1,i} & \mathbf{B}_{i-1,i} \\ \mathbf{C}_{i-1,i} & \mathbf{D}_{i-1,i} \end{bmatrix}$ and $\mathbf{\Phi}\left(\tau_{i+1},\tau_i\right) = \begin{bmatrix} \mathbf{A}_{i+1,i} & \mathbf{B}_{i+1,i} \\ \mathbf{C}_{i+1,i} & \mathbf{D}_{i+1,i} \end{bmatrix}$. Notice that determination of $\mathbf{\Phi}\left(\tau_{i-1},\tau_i\right)$ requires integrating backwards in time. This numerical step can be avoided simply by recognizing that $\mathbf{\Phi}\left(\tau_{i-1},\tau_i\right) = \mathbf{\Phi}\left(\tau_i,\tau_{i-1}\right)^{-1}$. Isolating the state variations of interest in equations (3.11) and (3.12) results in the following expressions,

$$\frac{\partial\vec{V}_i^-}{\partial\vec{R}_{i-1}} = \mathbf{B}_{i-1,i}^{-1}, \tag{3.13}$$

$$\frac{\partial\vec{V}_i^-}{\partial\tau_{i-1}} = -\mathbf{B}_{i-1,i}^{-1}\vec{V}_{i-1}^+, \tag{3.14}$$

$$\frac{\partial\vec{V}_i^-}{\partial\vec{R}_i} = -\mathbf{B}_{i-1,i}^{-1}\mathbf{A}_{i-1,i}, \tag{3.15}$$

$$\frac{\partial\vec{V}_i^-}{\partial\tau_i} = \dot{\vec{V}}_i^- + \mathbf{B}_{i-1,i}^{-1}\mathbf{A}_{i-1,i}\vec{V}_i^-, \tag{3.16}$$

$$\frac{\partial\vec{V}_i^+}{\partial\vec{R}_i} = -\mathbf{B}_{i+1,i}^{-1}\mathbf{A}_{i+1,i}, \tag{3.17}$$

$$\frac{\partial\vec{V}_i^+}{\partial\tau_i} = \dot{\vec{V}}_i^+ + \mathbf{B}_{i+1,i}^{-1}\mathbf{A}_{i+1,i}\vec{V}_i^+, \tag{3.18}$$

$$\frac{\partial\vec{V}_i^+}{\partial\vec{R}_{i+1}} = \mathbf{B}_{i+1,i}^{-1}, \tag{3.19}$$

$$\frac{\partial \vec{V}_i^+}{\partial \tau_{i+1}} = -\mathbf{B}_{i+1,i}^{-1} \vec{V}_{i+1}^- . \tag{3.20}$$

Additional scalar variational relationships are added to equation (3.10) such that the variations in the $\Delta\vec{V}$'s are clearly expressed in terms of position and time variations along incoming and outgoing segments, i.e.,

$$\begin{Bmatrix} \delta\Delta\vec{V}_2 \\ \delta\Delta\vec{V}_3 \\ \vdots \\ \delta\Delta\vec{V}_{n-2} \\ \delta\Delta\vec{V}_{n-1} \end{Bmatrix} = \left[\mathbf{M}\right] \begin{Bmatrix} \delta\vec{R}_1 \\ \delta\tau_1 \\ \delta\vec{R}_2 \\ \delta\tau_2 \\ \delta\vec{R}_3 \\ \delta\tau_3 \\ \vdots \\ \delta\vec{R}_{n-2} \\ \delta\tau_{n-2} \\ \delta\vec{R}_{n-1} \\ \delta\tau_{n-1} \\ \delta\vec{R}_n \\ \delta\tau_n \end{Bmatrix}, \tag{3.21}$$

where

$$\mathbf{M} = \left[\begin{array}{ccccccccccccc} M_{\vec{R}_1}^- & M_{\tau_1}^- & M_{\vec{R}_1} & M_{\tau_1} & M_{\vec{R}_1}^+ & M_{\tau_1}^+ & \cdots & & & & & \mathbf{0} & \\ \mathbf{0}_{3\times3} & \vec{0}_{3\times1} & M_{\vec{R}_2}^- & M_{\tau_2}^- & M_{\vec{R}_2} & M_{\tau_2} & & & & & & & \\ & \vdots & & & & & \ddots & & & & & \vdots & \\ & & & & & & & M_{\vec{R}_{n-1}} & M_{\tau_{n-1}} & M_{\vec{R}_{n-1}}^+ & M_{\tau_{n-1}}^+ & \mathbf{0}_{3\times3} & \vec{0}_{3\times1} \\ & \mathbf{0} & & & & & \cdots & M_{\vec{R}_n}^- & M_{\tau_n}^- & M_{\vec{R}_n} & M_{\tau_n} & M_{\vec{R}_n}^+ & M_{\tau_n}^+ \end{array}\right]. \tag{3.22}$$

Note that **M** is a banded matrix. Such a form lends tractability to the solution of equation (3.21). Furthermore, since there are more variables than equations for the linear system described by equation (3.21), an infinite number of solutions are available. However, the objective is to locate a natural solution in the vicinity of the initial guess. (See Figure 3.2.) Therefore, the smallest Euclidean norm of **M** is used to compute the variations in position and time, i.e., $\delta\vec{R}_i$ and $\delta\tau_i$, for every patch point. A new set of patch point positions and times are determined by subtracting these $\delta\vec{R}_i$ and $\delta\tau_i$ from the current set of patch point positions and times. Re-targeting the new patch points again, using the first level, results in smaller $\Delta\vec{V}$'s at the internal points. (Recall Figure 3.1.) Then, $\delta\vec{R}_i$ and $\delta\tau_i$ are again recomputed using the second level to locate different, new patch point positions and times. The $\Delta\vec{V}$'s associated with the internal points will be reduced even further when the first level is reapplied. The process is repeated, ending with the first level, until $\left\|\Delta\vec{V}_i\right\| < \varepsilon$ for $i = 2,\ldots,n-1$, thereby resulting in a continuous path. (See Figure 3.2.)

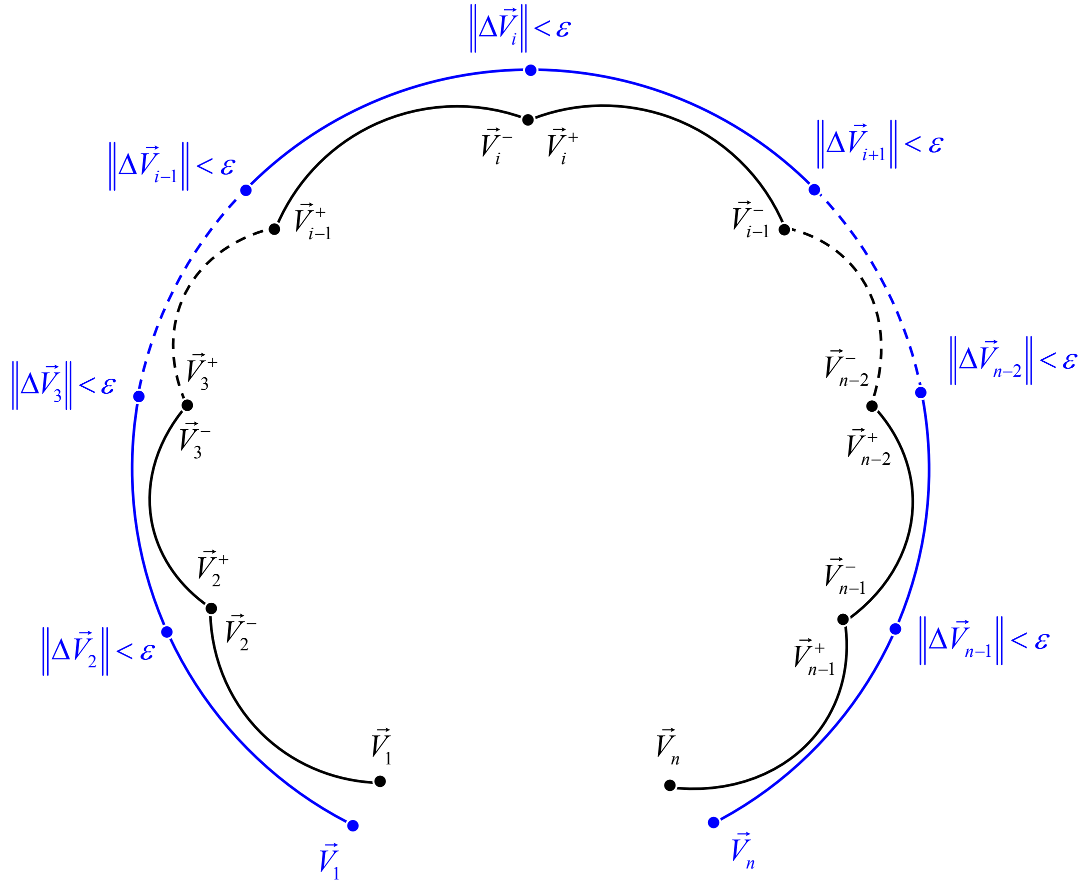

Figure 3.2 Path Before Second Level is Applied (Black)
and Final Continuous Path (Blue)

3.1.3 Numerical Example: Lissajous Trajectories

The two-level corrections process can be used to determine particular solutions to the nonlinear differential equations in the CR3BP. The analytical solutions to the linear equations of motion can be used as an approximation for quasi-periodic motion, and, thus, initiate the numerical process. The corrector is applied to the Lissajous trajectory approximation in the Earth-Moon system near L_1 (see Figure 2.3). The result appears in Figure 3.3. In summary, $\sum_{i=2}^{n-1}\left\|\Delta\vec{V}_i\right\|$ for $n = 41$ patch points is reduced from an initial value of 1.20319112 to $2.54715766 \times 10^{-13}$ non-dimensional units, i.e., 13 orders of magnitude, in just six iterations.

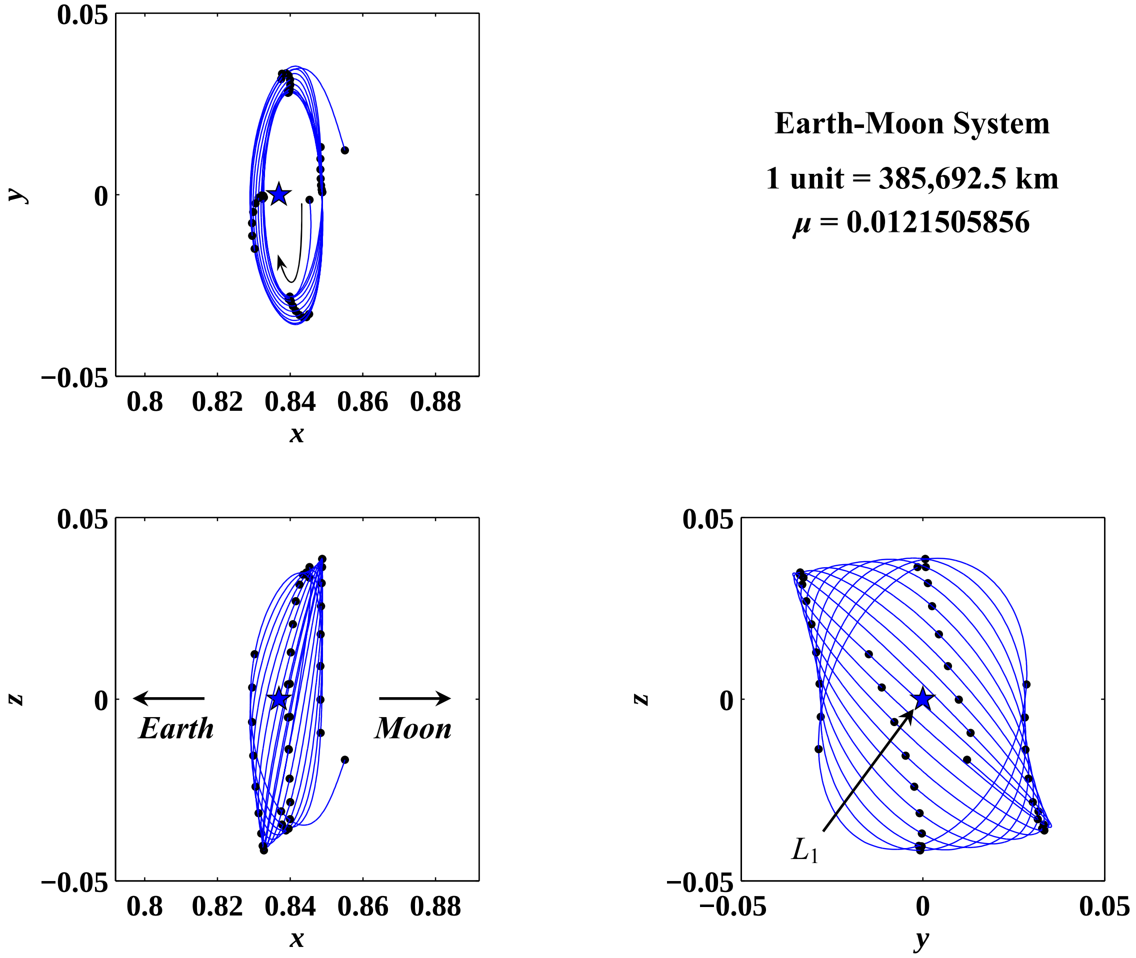

Figure 3.3 Differentially Corrected L_1 Lissajous Trajectory

Note the nonlinear effects of the natural solution depicted in Figure 3.3. For example, the motion is not as uniform as the initial motion computed from the first-order analytical approximation. (See Figure 2.3.) The amplitude in the y direction, A_y, and the amplitude in the z direction, A_z, are not exactly the same for each revolution. Furthermore, A_y is now approximately 13,500 km and A_z is approximately 16,000 km. However, although the orbit is slightly smaller than the initial first-order approximation, the characteristic shape is still maintained. Considering the sensitivities associated with the CR3BP, the ability to compute a natural solution and maintain the characteristic shape for multiple revolutions lends tractability to the two-level differential corrections process.

3.2 A Simple Corrector

A *simple* targeting scheme uses symmetry about the x-z plane to determine periodic planar solutions in the vicinity of the collinear libration points. The resulting solutions are termed Lyapunov orbits, named after the Russian mathematician Aleksandr Mikhailovich Lyapunov (1857-1918) for his work on ordered differential equations, stability theory, and non-linear analysis. First-order analytical approximations for the solutions are available in equations (2.43)-(2.44) or (2.46)-(2.47). Small amplitude Lyapunov orbits are expanded from these analytical approximations to obtain a manifold family of solutions. A general assessment of the stability and the locations of bifurcation points that signal intersections with other families of solutions are detailed below for the L_1 Lyapunov family.

3.2.1 The Algorithm

The algorithm can be used to numerically compute Lyapunov orbits in the vicinity of the collinear points. In general, exploitation of any symmetry greatly reduces the complexity of the three-body problem. Furthermore, restricting the motion of P_3 to the x-y plane, a required characteristic of the Lyapunov orbits, further reduces the degrees of freedom. For convenience, the initial state vector associated with a Lyapunov orbit is usually located on the x-axis and possesses only two non-zero components. Thus, a targeting scheme for computation of Lyapunov orbits is triggered with an initial state vector of the form

$$\vec{q}_0 = \left\{ x_0 \quad 0 \quad 0 \quad 0 \quad \dot{y}_0 \quad 0 \right\}^T, \tag{3.23}$$

where initial values x_0 and $\dot{y}_0$ are available for the first iteration from the analytical approximations. Therefore, the objective is to adjust the nonzero components of the initial state such that a perpendicular crossing is achieved at the endpoint. (See Figure 3.4.) Though not necessary for convergence, fixing either x_0 or $\dot{y}_0$ allows for an expansion of solution space once the current solution is obtained. A scheme for constraining x_0 is based on the mapping

$$\delta \dot{x} = F\left(\dot{y}_0\right), \tag{3.24}$$

where F represents a mapping of $\dot{y}_0$ from $y_0 = 0$ to the next crossing $y = 0$. This mapping is therefore independent of the integration time, τ. (See Figure 3.4 for a representation of F.) The variation of $\delta \dot{x}$ with respect to $\delta \dot{y}_0$ is available from the state-transition matrix. Therefore, using equation (2.61), a targeter for convergence is simply

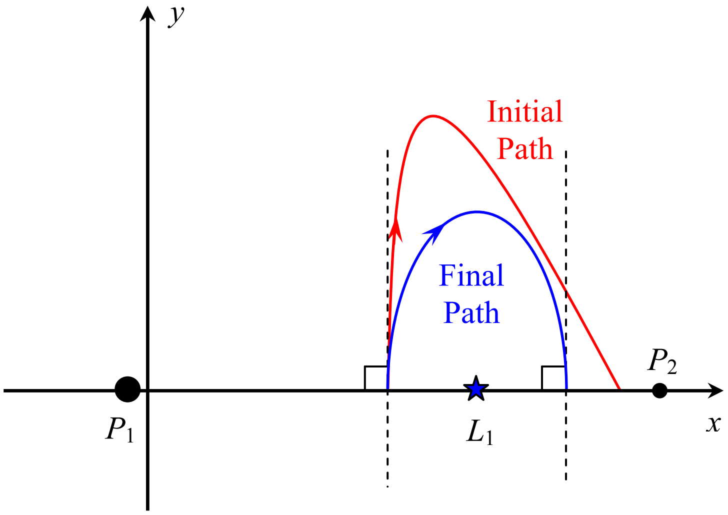

Figure 3.4 Initial and Final Path for Simple Corrector

$$\delta\dot{x} = \frac{\partial\dot{x}}{\partial\dot{y}_0}\delta\dot{y}_0. \tag{3.25}$$

Since a perpendicular crossing is targeted when F is applied to $\dot{y}_0$, the desired value of $\delta\dot{x}$ at the second crossing is zero. Solving for $\delta\dot{y}_0$ in equation (3.25), subtracting this from $\dot{y}_0$, and re-integrating yields a smaller $\delta\dot{x}$. The process is repeated until $\delta\dot{x} < \varepsilon$ and a perpendicular crossing is achieved.

Notice that an additional mapping can be written such that

$$\delta y = G(\dot{y}_0), \tag{3.26}$$

where G takes $\dot{y}_0$ to δy when $y = 0$ at the next crossing. Therefore, $\delta y = 0$. Using equation (2.61) the targeter defined by the variational relationships then becomes

$$\begin{Bmatrix} 0 \\ \delta\dot{x} \end{Bmatrix} = \left[\begin{array}{c|c} \dfrac{\partial y}{\partial\dot{y}_0} & \dot{y} \\ \dfrac{\partial\dot{x}}{\partial\dot{y}_0} & \ddot{y} \end{array}\right] \begin{Bmatrix} \delta\dot{y}_0 \\ \delta\tau \end{Bmatrix}. \tag{3.27}$$

The additional equation greatly increases the speed of convergence. Similar to equation (3.25), solving for $\delta\dot{y}_0$ in equation (3.27), subtracting this from $\dot{y}_0$, and re-integrating produces a smaller value for $\delta\dot{x}$. Notice that, given the definitions for F and G, it is unnecessary to also subtract $\delta\tau$ from τ. As in the prior case, the process is repeated until $\delta\dot{x} < \varepsilon$. Therefore, predictions in the endpoint variations are available from equation (2.61) and are used in an iterative procedure to update the control parameter $\delta\dot{y}_0$ until the desired final point variation $\delta\dot{x}$ is reduced to zero. The goal is to eliminate the endpoint variations and, thus, these are the constraint parameters, while the initial variations in the state are the control parameters. For example, in equation (3.27), $\delta\dot{y}_0$ is the control parameter and the constraint parameter is $\delta\dot{x}$, with a goal or target $\delta\dot{x} = 0$.

The final Lyapunov orbit is obtained by integrating the converged values in $\vec{q}_0$ (with updated $\dot{y}_0$) over the period $T = 2\tau$. A method of continuation is then employed to expand the solution space. In applying continuation, a prediction for the neighboring n^{th} solution is obtained from the current result such that,

$$\vec{q}_0^{\,n} = \vec{q}_0^{\,n-1} + S \cdot \Delta\vec{q}_0^{\,n-1}, \tag{3.28}$$

where $\vec{q}_0^{\,n-1}$ is the initial condition corresponding to the previously converged solution. The step size S is usually simply a fixed value Δx_0. Since it is desired to step along the x-axis,

$$\Delta\vec{q}_0^{\,n-1} = \{1 \quad 0 \quad 0 \quad 0 \quad 0 \quad 0\}^T. \tag{3.29}$$

The process is repeated until the manifold family of solutions is obtained.

3.2.2 Numerical Results: L_1, L_2, and L_3 Lyapunov Families of Orbits

The algorithm in the previous section is used to obtain families of Lyapunov orbits in the vicinity of the collinear points in the Earth-Moon system. (See Figures 3.5-3.7.) The black orbits appearing in Figures 3.5-3.7 correspond to intersections, or bifurcations, between the Lyapunov orbit families and other families of periodic orbits. For example, depicted in Figure 3.5 are two distinct bifurcations. Note that the smaller amplitude bifurcation corresponds to the intersection between the L_1 Lyapunov orbits and the L_1 halo orbit family. Furthermore, the larger amplitude bifurcation is associated with the intersection between the L_1 Lyapunov orbits and the L_1 axial orbit family. Unlike the Lyapunov orbits, both the axial and halo orbit families are three-dimensional. (See Section 3.3 for a more detailed discussion of the halo and axial orbit families.) Further, since closest approach for the Lyapunov orbits near the collinear points occurs along the x-axis, and both the initial and final point of the targeting scheme are also located on the x-axis, the algorithm breaks down when passage by either primary is close. However, reducing the step-size and saving the states associated with every 10 or 20 orbits yields an appropriate representation for the shape of the solution space. The initial conditions, period T, and stability index υ are also provided in Tables 3.1-3.3. The stability index is further discussed in Section 3.2.3. Notice that the initial conditions, periods, and stability indices are computed for the bifurcating orbits. Also, recall that the period T can be dimensionalized simply by multiplying by the characteristic time t^* available from equation (2.4). For example, in the Earth-Moon system $t^* \cong 4.3644$ days.

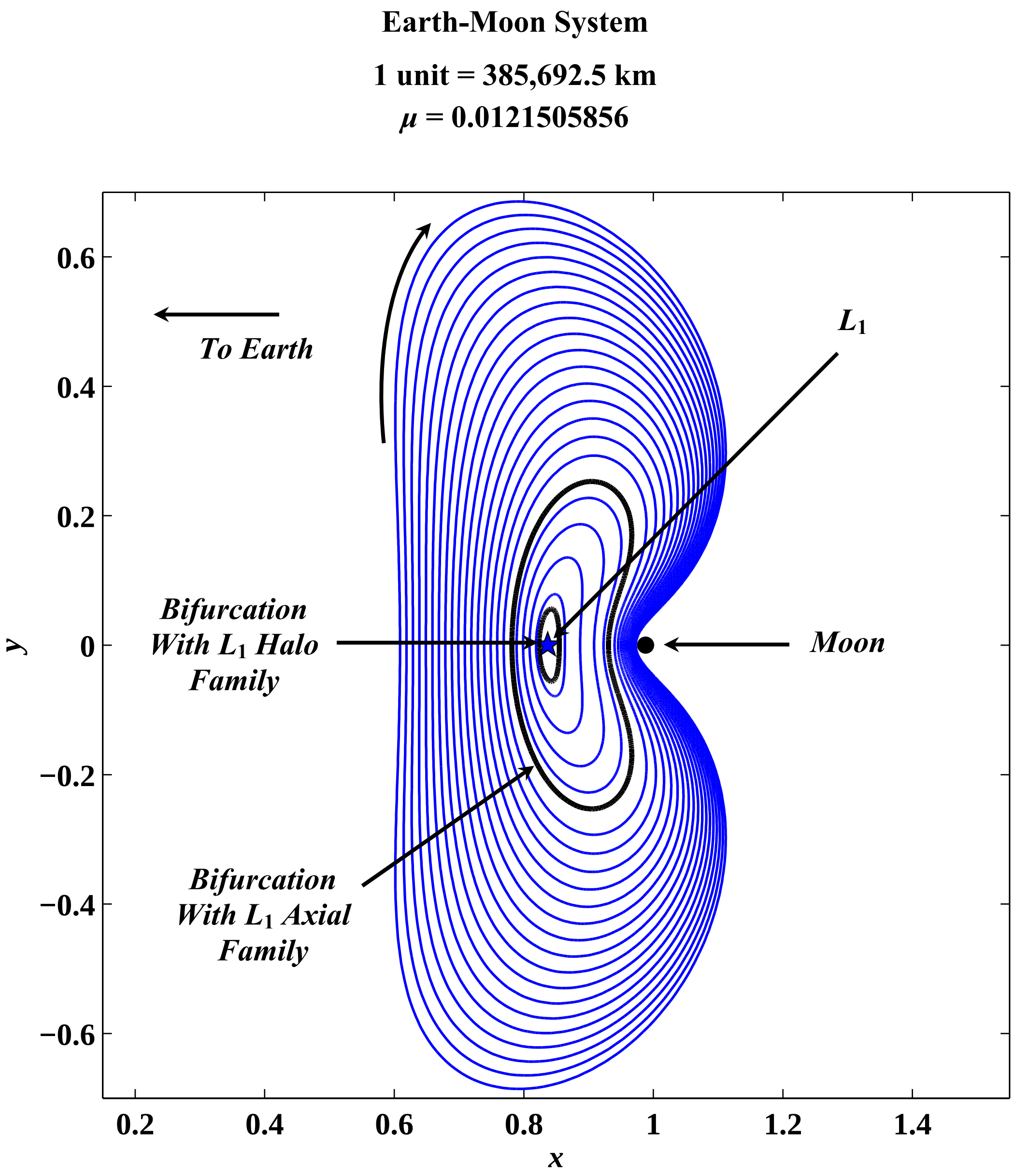

Figure 3.5 The L_1 Lyapunov Family

Table 3.1

L_1 Lyapunov Family Initial Conditions

x_0	$\dot{y}_0$	T	υ	
0.8234	0.1263	2.7430	1180.5771	L_1 Halos
0.8189	0.1750	2.7959	1045.0317	
0.8089	0.2838	3.0224	662.3978	
0.7989	0.3649	3.3638	387.9805	
0.7889	0.4159	3.7121	254.6194	
0.7816	0.4432	3.9500	200.3471	L_1 Axials
0.7689	0.4813	4.3317	144.2199	
0.7589	0.5068	4.6052	117.6505	
0.7489	0.5305	4.8579	99.3896	
0.7389	0.5531	5.0915	86.3560	
0.7289	0.5752	5.3071	76.8352	
0.7189	0.5971	5.5060	69.7938	
0.7089	0.6189	5.6891	64.5687	
0.6989	0.6409	5.8575	60.7141	
0.6889	0.6631	6.0121	57.9192	
0.6789	0.6855	6.1538	55.9615	
0.6689	0.7082	6.2836	54.6777	
0.6589	0.7313	6.4023	53.9465	
0.6489	0.7548	6.5107	53.6761	
0.6389	0.7786	6.6097	53.7965	
0.6289	0.8028	6.7001	54.2536	
0.6189	0.8275	6.7824	55.0055	
0.6089	0.8526	6.8573	56.0195	

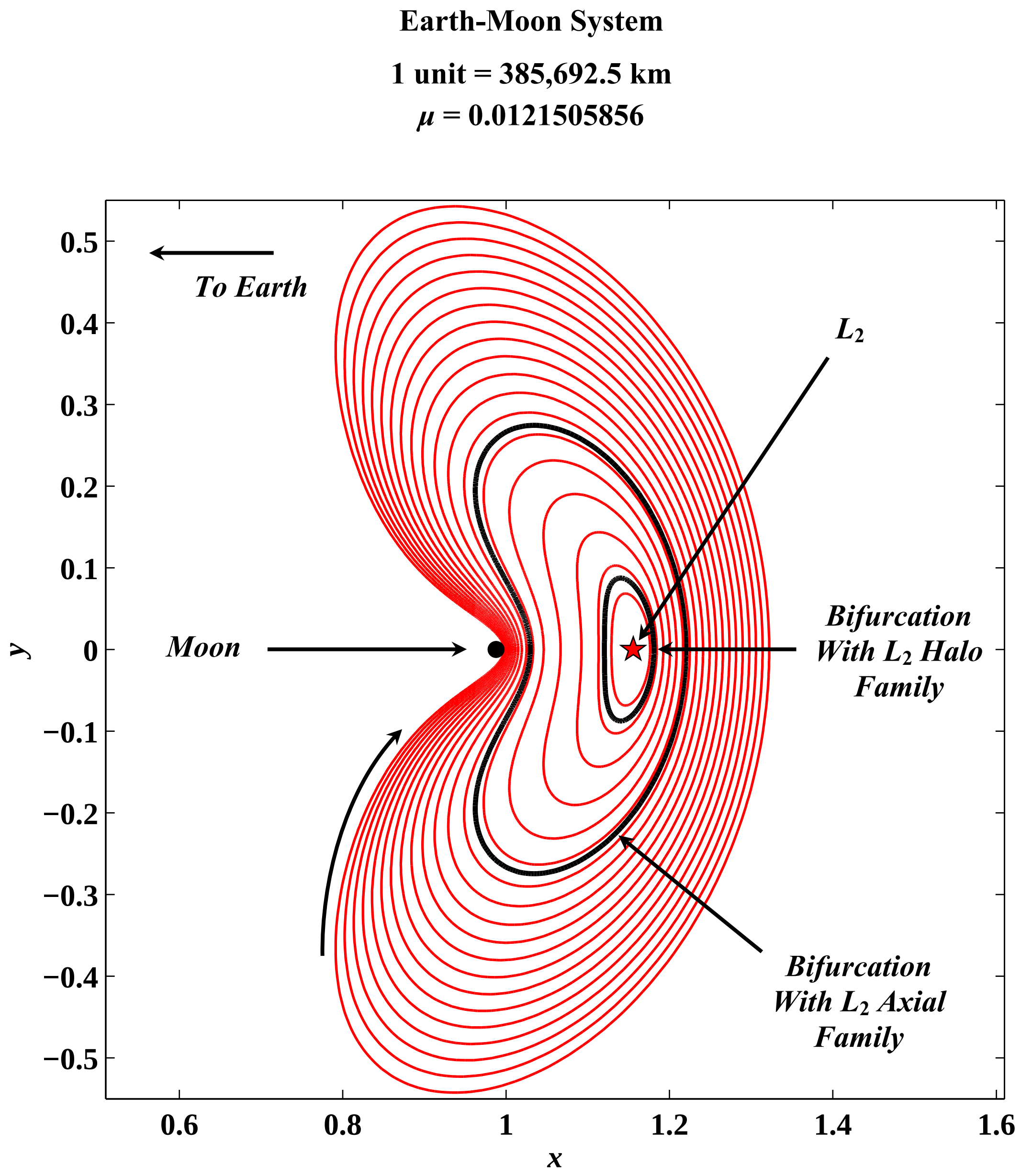

Figure 3.6 The L_2 Lyapunov Family

Table 3.2

L_2 Lyapunov Family Initial Conditions

x_0	$\dot{y}_0$	T	υ	
1.1762	-0.1231	3.3981	651.0097	
1.1809	-0.1559	3.4155	606.1130	L_2 Halos
1.1843	-0.1818	3.4341	564.4278	
1.1924	-0.2502	3.5128	435.7722	
1.2005	-0.3239	3.6841	288.4590	
1.2086	-0.3804	3.9421	189.9619	
1.2167	-0.4164	4.2083	140.5503	
1.2200	-0.4275	4.3105	127.8850	L_2 Axials
1.2248	-0.4419	4.4584	113.2251	
1.2329	-0.4621	4.6923	96.0231	
1.2410	-0.4794	4.9123	84.1910	
1.2491	-0.4948	5.1204	75.5738	
1.2572	-0.5092	5.3180	69.0655	
1.2653	-0.5227	5.5062	64.0400	
1.2734	-0.5357	5.6856	60.1148	
1.2815	-0.5484	5.8568	57.0416	
1.2896	-0.5607	6.0203	54.6507	
1.2977	-0.5729	6.1765	52.8217	
1.3058	-0.5849	6.3258	51.4659	
1.3139	-0.5968	6.4685	50.5160	
1.3220	-0.6087	6.6049	49.9203	

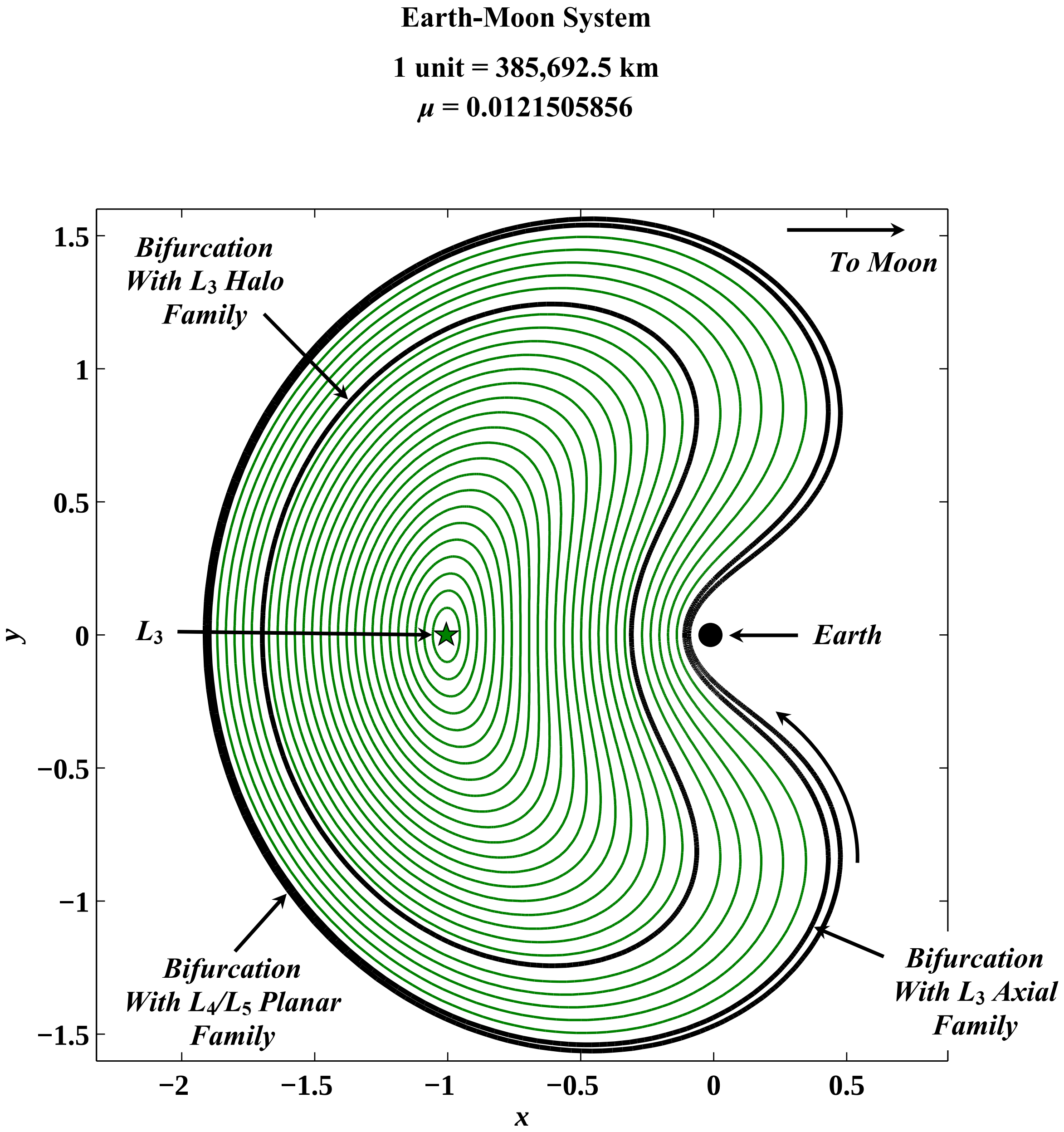

Figure 3.7 The L_3 Lyapunov Family

Table 3.3

L_3 Lyapunov Family Initial Conditions

x_0	$\dot{y}_0$	T	υ	
-1.0560	0.1017	6.2185	1.6753	
-1.0884	0.1652	6.2186	1.6729	
-1.1208	0.2280	6.2189	1.6694	
-1.1532	0.2899	6.2192	1.6647	
-1.1856	0.3512	6.2196	1.6589	
-1.2180	0.4119	6.2201	1.6519	
-1.2504	0.4721	6.2207	1.6437	
-1.2828	0.5318	6.2213	1.6343	
-1.3152	0.5911	6.2221	1.6236	
-1.3476	0.6500	6.2229	1.6117	
-1.3800	0.7086	6.2238	1.5985	
-1.4124	0.7670	6.2248	1.5840	
-1.4448	0.8252	6.2260	1.5680	
-1.4772	0.8833	6.2272	1.5506	
-1.5096	0.9414	6.2285	1.5316	
-1.5420	0.9994	6.2300	1.5110	
-1.5744	1.0576	6.2316	1.4885	
-1.6068	1.1159	6.2334	1.4640	
-1.6392	1.1745	6.2353	1.4372	
-1.6716	1.2335	6.2374	1.4078	
-1.6967	1.2795	6.2391	1.3828	L_3 Halos
-1.7364	1.3531	6.2423	1.3390	
-1.7688	1.4142	6.2451	1.2981	
-1.8012	1.4765	6.2484	1.2511	
-1.8336	1.5405	6.2522	1.1959	
-1.8663	1.6072	6.2566	1.1283	
-1.8963	1.6715	6.2616	1.0499	L_3 Axials
-1.9118	1.70633	6.2647	1.0000	L_4/L_5 Planar

3.2.3 The Stability Index and Bifurcations

Information offered by analysis of the phase space includes stability and bifurcation points. The eigenvalues and/or characteristic multipliers associated with the monodromy matrix are used to evaluate the stability of the solutions, and to isolate intersections with other families of orbits in the solution space. All of the solutions examined in this study possess six characteristic multipliers in reciprocal pairs. Since the solution is periodic, two of the six multipliers are equal to one. The other four include a pair associated with the stable/unstable subspace and the final pair represents the center subspace. Since there is one stable and one unstable mode, the average of the (reciprocal) pair of multipliers associated with the stable subspace ($\left|\lambda^{W_s}\right| < 1$) and unstable subspace ($\left|\lambda^{W_u}\right| > 1$), or

$$\upsilon = \frac{1}{2}\left(\left|\lambda^{W_s}\right| + \left|\lambda^{W_u}\right|\right), \tag{3.30}$$

is defined as the stability index υ. The value of the index is a single numerical quantity to assess the stability of the system [20].

If $\lambda^{W_s} = \lambda^{W_u} = \pm 1$, the reference trajectory defines the exact intersection between two different families. Thus, the orbit is a subset of both families and identifies a bifurcation point. Furthermore, if both characteristic multipliers associated with the center subspace, i.e., λ^{Γ} and λ^{Γ^*}, are such that $\lambda^{\Gamma} = \lambda^{\Gamma^*} = \pm 1$, the solution or orbit also defines the intersection point between two different families. When $\lambda^{W_s} = \lambda^{W_u} = \pm 1$ and $\lambda^{\Gamma} = \lambda^{\Gamma^*} = \pm 1$ simultaneously, the trajectory solution belongs to three different families. Thus, three families intersect resulting in a trifurcation [26]. Other types of bifurcations also exist that are not included in this analysis. For example, the point at which two complex conjugate multipliers leave the unit circle in the complex plane is a special type of bifurcation known as a Krien collision [27]. In short, valuable information is gained by analyzing the characteristic multipliers.

The exact location of the bifurcation orbits can be computed using continuation and a method of bisections [44]. A distinct change in the eigenstructure, i.e., when the characteristic multipliers leave the unit circle to occupy the real axis or vice versa, triggers the location of the bifurcation point. If a distinct change in the eigenstructure occurs between two successive solutions during a continuation process, then a bifurcating orbit is clearly located between the current and previous solution. Therefore, let $\vec{q}_0^{\,n-1}$ and $\vec{q}_0^{\,n-2}$ be the initial states associated with the current and previous solutions as prescribed by equation (3.28). Then

$$\vec{q}_0^{\,lower} = \vec{q}_0^{\,n-2}, \tag{3.31}$$

$$\vec{q}_0^{\,upper} = \vec{q}_0^{\,n-1}. \tag{3.32}$$

Also, let $\vec{q}_0^{\,mid}$ be the initial state associated with the prediction for a solution midway between the previous two trajectories,

$$\vec{q}_0^{\,mid} = \vec{q}_0^{\,lower} + \frac{S}{2} \cdot \Delta\vec{q}_0^{\,lower}. \tag{3.33}$$

Then, as before, the location of the bifurcation is available from the eigenstructure and is either between $\vec{q}_0^{\,lower}$ and $\vec{q}_0^{\,mid}$ or between $\vec{q}_0^{\,mid}$ and $\vec{q}_0^{\,upper}$. If it is evident from the eigenstructure that the bifurcating orbit is located between $\vec{q}_0^{\,lower}$ and $\vec{q}_0^{\,mid}$, then

$$\vec{q}_0^{\,upper} = \vec{q}_0^{\,mid}. \tag{3.34}$$

Alternatively, if it is evident that the bifurcation occurs between $\vec{q}_0^{\,mid}$ and $\vec{q}_0^{\,upper}$, then

$$\vec{q}_0^{\,lower} = \vec{q}_0^{\,mid}. \tag{3.35}$$

Let the initial state $\vec{q}_0^{\,mid}$ associated with the bisecting solution be redefined by using the prediction,

$$\vec{q}_0^{\,mid} = \vec{q}_0^{\,lower} + \frac{S}{4} \cdot \Delta\vec{q}_0^{\,lower}, \tag{3.36}$$

to converge the new solution. Notice that the step size for the prediction of $\vec{q}_0^{\,mid}$ is reduced by a factor of two with every new prediction of $\vec{q}_0^{\,mid}$. New $\vec{q}_0^{\,upper}$ or $\vec{q}_0^{\,lower}$ are again redefined and the process is continued until $\lambda^{W_s} = \lambda^{W_u} = \pm 1$ or $\lambda^{\Gamma} = \lambda^{\Gamma^*} = \pm 1$ thereby obtaining the exact initial state (within numerical precision) for the bifurcating orbit.

The stability indices in Tables 3.1-3.3 are calculated using equation (3.30) and the bifurcations are located using the method of bisections. (Recall the bifurcation trajectories are plotted as black orbits in Figures 3.5-3.7.) Notice that for orbits corresponding to the initial conditions represented in Tables 3.1-3.3, the stability index is positive, i.e., $\upsilon > 1$, with the exception of the last initial condition provided for the L_3 Lyapunov orbits. Therefore, the first two bifurcations, located when expanding the solution space for all three Lyapunov families, are associated with the condition $\lambda^{\Gamma} = \lambda^{\Gamma^*} = \pm 1$. Initially, the multipliers in the center subspace for all three families are located on the unit circle, as expected. Expanding the solutions reveals bifurcations with the halo orbit families, where the center multipliers become real. The multipliers return to the unit circle at the intersection of the Lyapunov and the axial orbit families. The third bifurcation along the L_3 family, the bifurcation with the L_4/L_5 planar orbits, is associated with $\lambda^{W_s} = \lambda^{W_u} = \pm 1$, as evidenced by a stability index of one. (See Figure 3.8 for the propagation of the characterstic multipliers associated with the center subspace for the L_1 Lyapunov orbits represented in Figure 3.5 and Table 3.1.)

The strategies for locating the intersections between families are also used to obtain the family of solutions for the intersecting families, i.e., the halo, the axial, and the L_4/L_5 planar families. Strategies for computing the halo, axial, and L_4/L_5 planar families are further discussed in the following sections. Bifurcations within these families are located using the same method, and the solutions are expanded to locate additional families.

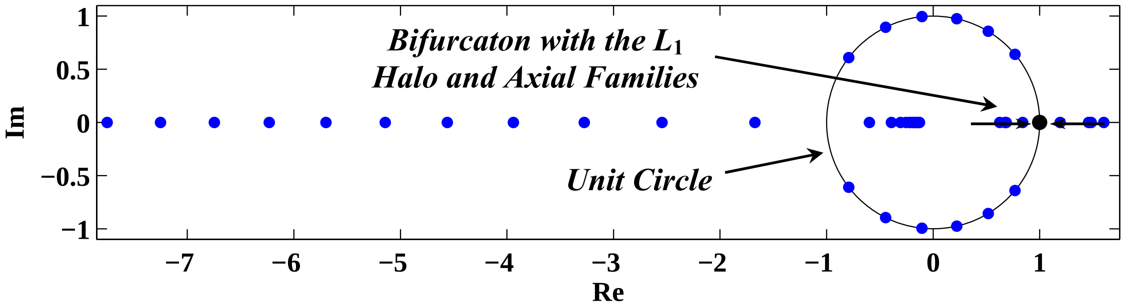

Figure 3.8 Characteristic Multipliers Associated with Center Subspace
for L_1 Lyapunov Orbits.

3.3 Targeting Orbits in Thee-Dimensional Space Using Symmetry

The simple targeter is also generalized to compute periodic orbits in three-dimensional space. The periodic solutions bifurcating from the small amplitude Lyapunovs, as seen in Figures 3.5-3.7, are denoted halo orbits, as first coined by Farquhar [45] who noticed that a spacecraft in an L_2 halo orbit on the far side of the Moon appears to resemble a halo about the Moon when viewed from the Earth. A spacecraft in such an orbit maintains continuous communications with the Earth. The axial orbits are so named because the family appears to rotate about the x-axis from the bifurcating Lyapunov orbit, as will be apparent later in Section 3.3. The most "vertical" member of the axial family marks the bifurcating orbit between the axial and vertical families. The vertical orbits resemble a "figure-8," and are labeled vertical since the motion of small amplitude members of the family is primarily in the z direction. Numerical results for the halo, axial, and vertical families of orbits are available in the literature [8, 16-17, 19-20, 27-28]. A number of algorithms can be employed successfully to compute these families in the vicinity of the collinear libration points by exploiting symmetry.

3.3.1 Strategies to Compute Periodic Orbits

Symmetric with respect to x-z plane. Periodic halo orbits as well as the vertical orbits are symmetric about the x-z plane. Therefore, the initial state vector is strategically positioned in the x-y plane such that only three nonzero components exist. Similar to the construction of the planar Lyapunov orbits, one of these parameters is held fixed while a differential corrections procedure is applied to the remaining two initial states until a perpendicular crossing is achieved at the endpoint. Thus, the initial state vector takes the form

$$\vec{q}_0 = \left\{ x_0 \quad 0 \quad z_0 \quad 0 \quad \dot{y}_0 \quad 0 \right\}^T, \tag{3.37}$$

where, if it is desired to fix x_0, the following mappings can be defined

$$\delta y = F\left(z_0, \dot{y}_0\right), \tag{3.38}$$

$$\delta \dot{x} = G\left(z_0, \dot{y}_0\right), \tag{3.39}$$

$$\delta \dot{z} = H\left(z_0, \dot{y}_0\right). \tag{3.40}$$

By definition *F*, *G*, and *H* bring z_0 and $\dot{y}_0$ to δy, $\delta \dot{x}$, and $\delta \dot{z}$ when $y = 0$, i.e., when the solution crosses the *x*-*y* plane at $\tau = \frac{1}{2}T$. (Recall that *T* is the period.) Therefore, the control parameters δz_0 and $\delta \dot{y}_0$ are iteratively updated until the constraints, $\delta \dot{x} = \delta \dot{z} \cong 0$, are satisfied. Specifically, using equation (2.61), the targeter is defined as

$$\begin{Bmatrix} 0 \\ \delta \dot{x} \\ \delta \dot{z} \end{Bmatrix} = \left[\begin{array}{cc|c} \dfrac{\partial y}{\partial z_0} & \dfrac{\partial y}{\partial \dot{y}_0} & \dot{y} \\ \dfrac{\partial \dot{x}}{\partial z_0} & \dfrac{\partial \dot{x}}{\partial \dot{y}_0} & \ddot{x} \\ \dfrac{\partial \dot{z}}{\partial z_0} & \dfrac{\partial \dot{z}}{\partial \dot{y}_0} & \ddot{z} \end{array}\right] \begin{Bmatrix} \delta z_0 \\ \delta \dot{y}_0 \\ \delta \tau \end{Bmatrix}. \tag{3.41}$$

Solving for δz_0 and $\delta \dot{y}_0$ in equation (3.41) and updating the initial state by subtracting these from z_0 and $\dot{y}_0$, respectively, yields smaller values of $\delta \dot{x}$ and $\delta \dot{z}$ in the next iteration. The process is repeated until $\delta \dot{x} < \varepsilon$ and $\delta \dot{z} < \varepsilon$, thereby constraining the motion to be perpendicular to the *x*-*y* plane at the endpoint.

Alternatively, if it is desired to fix z_0, the following mappings can be defined

$$\delta y = F\left(x_0, \dot{y}_0\right), \tag{3.42}$$

$$\delta \dot{x} = G\left(x_0, \dot{y}_0\right), \tag{3.43}$$

$$\delta \dot{z} = H\left(x_0, \dot{y}_0\right), \tag{3.44}$$

where *F*, *G*, and *H* bring x_0 and $\dot{y}_0$ to δy, $\delta \dot{x}$, and $\delta \dot{z}$ when $y = 0$. As such, δx_0 and $\delta \dot{y}_0$ are the control parameters with the same constraints $\delta \dot{x} = \delta \dot{z} \cong 0$. The corresponding targeter is written as

$$\begin{Bmatrix} 0 \\ \delta\dot{x} \\ \delta\dot{z} \end{Bmatrix} = \left[\begin{array}{cc|c} \dfrac{\partial y}{\partial x_0} & \dfrac{\partial y}{\partial \dot{y}_0} & \dot{y} \\ \dfrac{\partial \dot{x}}{\partial x_0} & \dfrac{\partial \dot{x}}{\partial \dot{y}_0} & \ddot{x} \\ \dfrac{\partial \dot{z}}{\partial x_0} & \dfrac{\partial \dot{z}}{\partial \dot{y}_0} & \ddot{z} \end{array}\right] \begin{Bmatrix} \delta x_0 \\ \delta \dot{y}_0 \\ \delta\tau \end{Bmatrix}, \tag{3.45}$$

where the controls are iteratively updated until the constraints are satisfied within the specified tolerance.

One full revolution along the halo or vertical orbit is obtained by integrating the converged initial state vector $\vec{q}_0$ over the period $T = 2\tau$. To obtain families of halo orbits, via continuation, fix z_0 in regions where z_0 is changing more rapidly than x_0, and fix x_0 in regions where x_0 is changing more rapidly than z_0. Since the halo orbit family originates with the bifurcating Lyapunov orbit from Section 3.2.1 (Figures 3.5-3.7), z_0 is initially fixed. Predictions for the next orbit in the family are obtained by using equation (3.28), where the step size *S* is simply a fixed value Δz_0. The southern orbits result for $\Delta z_0 < 0,$ whereas for the northern family of halo orbits is acquired when $\Delta z_0 > 0$. Also, since it is desired to step through values of z_0,

$$\Delta\vec{q}_0^{\,n-1} = \{0 \quad 0 \quad 1 \quad 0 \quad 0 \quad 0\}^T. \tag{3.46}$$

The prediction is converged to a new periodic orbit (at the specified value of z_0), using equation (3.45). The process is repeated for a fixed value Δz_0 until

$$\left|x_0^n - x_0^{n-1}\right| > \left|z_0^n - z_0^{n-1}\right|. \tag{3.47}$$

The fixed parameter is changed to x_0, and $\Delta\vec{q}_0^{\,n-1}$ is defined from equation (3.29). Predictions for the initial state corresponding to the next orbit in the family are computed from equation (3.28) assuming x_0 is fixed. The states converge to a periodic orbit. The procedure steps in x_0 until equation (3.47) fails to be true. The fixed parameter is then switched back to z_0 with $\Delta\vec{q}_0^{\,n-1}$ again defined by equation (3.46) and the process is continued. For some cases, e.g., in the L_2 halo orbit family and all the vertical orbit families, it is necessary to change the sign of Δz_0 when the fixed parameter is switched from x_0 to z_0.

Symmetric with respect to x-axis. The axial and vertical orbits are symmetric about the *x*-axis. Exploiting symmetry results in an initial state vector of the form

$$\vec{q}_0 = \{x_0 \quad 0 \quad 0 \quad 0 \quad \dot{y}_0 \quad \dot{z}_0\}^T . \tag{3.48}$$

For the axial orbits, two sets of mappings are necessary. When the motion of the orbit is primarily horizontal, the mappings for a fixed $\dot{y}_0$ are defined as,

$$\delta y = F\left(x_0, \dot{z}_0\right), \tag{3.49}$$

$$\delta z = G\left(x_0, \dot{z}_0\right), \tag{3.50}$$

$$\delta \dot{x} = H\left(x_0, \dot{z}_0\right), \tag{3.51}$$

where *F*, *G*, and *H* bring x_0 and $\dot{z}_0$ to δy, δz, and $\delta \dot{x}$ when $y = 0$. However, when the motion becomes more vertical the following mappings are more useful,

$$\delta y = P\left(x_0, \dot{z}_0\right), \tag{3.52}$$

$$\delta z = Q\left(x_0, \dot{z}_0\right), \tag{3.53}$$

$$\delta \dot{x} = R\left(x_0, \dot{z}_0\right), \tag{3.54}$$

where *P*, *Q*, and *R* bring x_0 and $\dot{z}_0$ to δy, δz, and $\delta \dot{x}$ when $z = 0$, i.e., the next crossing with the *x*-*y* plane. Therefore, using equation (2.61), the targeter is simply written as,

$$\begin{Bmatrix} \delta y \\ \delta z \\ \delta \dot{x} \end{Bmatrix} = \left[\begin{array}{cc|c} \dfrac{\partial y}{\partial x_0} & \dfrac{\partial y}{\partial \dot{z}_0} & \dot{y} \\ \dfrac{\partial z}{\partial x_0} & \dfrac{\partial z}{\partial \dot{z}_0} & \dot{z} \\ \dfrac{\partial \dot{x}}{\partial x_0} & \dfrac{\partial \dot{x}}{\partial \dot{z}_0} & \ddot{x} \end{array}\right] \begin{Bmatrix} \delta x_0 \\ \delta \dot{z}_0 \\ \delta \tau \end{Bmatrix} . \tag{3.55}$$

If the mappings *F*, *G*, and *H* are used, then $\delta y = 0$ in equation (3.55), whereas if the mappings *P*, *Q*, and *R* are used, then $\delta z = 0$ in equation (3.55). The control parameters,

δx_0 and $\delta \dot{z}_0$, are adjusted until the final endpoint constraints $\delta z = \delta \dot{x} \cong 0$ are satisfied, within a specified tolerance. Similarly, if it is desired to fix $\dot{z}_0$ the targeter is written

$$\begin{Bmatrix} \delta y \\ \delta z \\ \delta \dot{x} \end{Bmatrix} = \left[\begin{array}{cc:c} \dfrac{\partial y}{\partial x_0} & \dfrac{\partial y}{\partial \dot{y}_0} & \dot{y} \\ \dfrac{\partial z}{\partial x_0} & \dfrac{\partial z}{\partial \dot{y}_0} & \dot{z} \\ \dfrac{\partial \dot{x}}{\partial x_0} & \dfrac{\partial \dot{x}}{\partial \dot{y}_0} & \ddot{x} \end{array}\right] \begin{Bmatrix} \delta x_0 \\ \delta \dot{y}_0 \\ \delta \tau \end{Bmatrix}, \tag{3.56}$$

where $\delta y = 0$ or $\delta z = 0$ depending on the mapping. Again, the parameters δx_0 and $\delta \dot{y}_0$ are adjusted until $\delta z, \delta \dot{x} < \varepsilon$, and a perpendicular crossing with the *x*-axis at the endpoint is achieved.

The complete axial or vertical orbit is obtained by integrating the converged value of $\vec{q}_0$ over the period $T = 2\tau$. Since the axial family originates with a bifurcating Lyapunov orbit, it is desirable to initially fix $\dot{z}_0$ and use mappings corresponding to $y = 0$. Once an out-of-plane axial orbit is established, a method of continuation can be used by applying equation (3.28) with some fixed step size, $\Delta \dot{y}_0$ or $\Delta \dot{z}_0$, and corresponding adjustment $\Delta \vec{q}_0^{\,n-1}$ determined by the fixed parameter. As the solutions become more vertical, the mappings associated with $y = 0$ break down and it is necessary to switch to the mappings associated with $z = 0$.

Symmetry relative to two planes. The vertical orbits are symmetric about both the *x-z* and *x-y* planes. Therefore, any of the targeting schemes can, in theory, be employed to obtain the vertical family of orbits once the bifurcating solution from the axial family is obtained. However, an additional targeter can be constructed that exploits both types of symmetry. Using the mappings defined in equations (3.49)-(3.51), the targeter uses the control variables δx_0 and $\delta \dot{z}_0$ to force the endpoint parameters $\delta \dot{x}$ and $\delta \dot{z}$ to zero, thereby targeting a perpendicular crossing at the *x-z* plane. Using equation (2.61), this type of targeter is written in the form

$$\begin{Bmatrix} 0 \\ \delta\dot{x} \\ \delta\dot{z} \end{Bmatrix} = \left[\begin{array}{cc|c} \dfrac{\partial y}{\partial x_0} & \dfrac{\partial y}{\partial \dot{z}_0} & \dot{y} \\ \dfrac{\partial \dot{x}}{\partial x_0} & \dfrac{\partial \dot{x}}{\partial \dot{z}_0} & \ddot{x} \\ \dfrac{\partial \dot{z}}{\partial x_0} & \dfrac{\partial \dot{z}}{\partial \dot{z}_0} & \ddot{z} \end{array}\right] \begin{Bmatrix} \delta x_0 \\ \delta \dot{z}_0 \\ \delta\tau \end{Bmatrix}. \tag{3.57}$$

The complete vertical orbit is acquired by integrating the converged initial state vector $\vec{q}_0$ over the period $T = 4\tau$. A method of continuation over $\dot{x}_0$, as previously described, can be used to obtain the vertical family of orbits.

3.3.2 Numerical Results: L_1, L_2, and L_3 Halo, Axial, and Vertical Families of Orbits

The algorithms summarized in Section 3.3.1 are used to numerically compute the halo, axial, and vertical orbit families in the vicinity of the collinear points in the Earth-Moon system. The families with bifurcating orbits (black) are provided in Figures 3.9-3.18 with corresponding initial conditions, periods, and stability indices in Tables 3.4-3.13. Bifurcating orbits in each of these families are located using a method of bisections. The bifurcating orbits from the Lyapunov families are the basis to acquire the northern families of halo orbits. The southern orbit family is obtained by reflecting the northern orbit family across the *x-y* plane. For example, the northern L_1 halo orbit family is depicted in Figure 3.9. The corresponding initial conditions, periods, and stability indices are presented in Table 3.4. The initial orbit used to compute the halo orbit family, i.e., the Lyapunov orbit, is available from Table 3.1. A method of continuation generates the orbit family and a method of bisections computes a bifurcation between the L_1 halo orbit family and the L_4/L_5 axial orbit families. (See the near-rectilinear black orbit in Figure 3.9.) Then, as mentioned previously, the southern L_1 halo orbits are computed by reflecting the orbits represented in Figure 3.9 across the *x-y* plane. The algorithms fail to converge for large amplitude L_3 halo orbits since the endpoints pass very close to the Earth, as depicted in Figure 3.11. Similarly, bifurcating orbits from the Lyapunov orbit families are used to compute the "northeast" or "northwest" axial families (see Figures 3.12-3.14 and Tables 3.7-3.9). The remaining part of the axial family is computed by reflecting the orbits across the *x-z* plane. The most vertical member of the axial orbit family corresponds to a bifurcation with the vertical orbit family. The vertical orbit families are found using the above strategies and are represented in Figures 3.15-3.17 with corresponding initial conditions, periods, and stability indices available in Tables 3.10-3.12. Since the hodographs corresponding to the L_1 and L_2 vertical orbit families intersect, it is advantageous to use the final targeting scheme from the previous section when obtaining the L_2 vertical orbit family. A family of orbits that bifurcate from a near-rectilinear L_2 halo orbit and might be described as representing a "butterfly" in shape is also generated. (See Figure 3.18 and Table 3.13.)

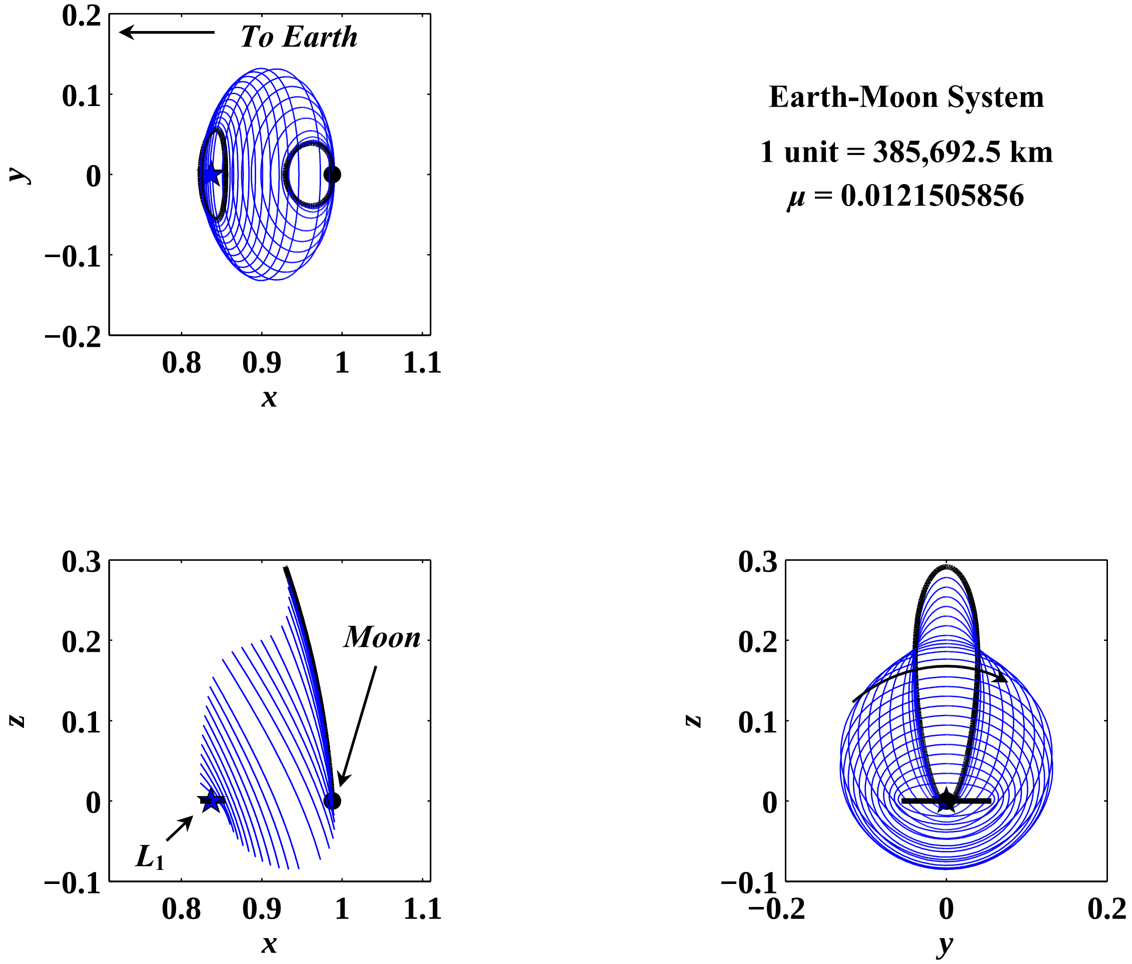

Figure 3.9 The Northern L_1 Halo Family

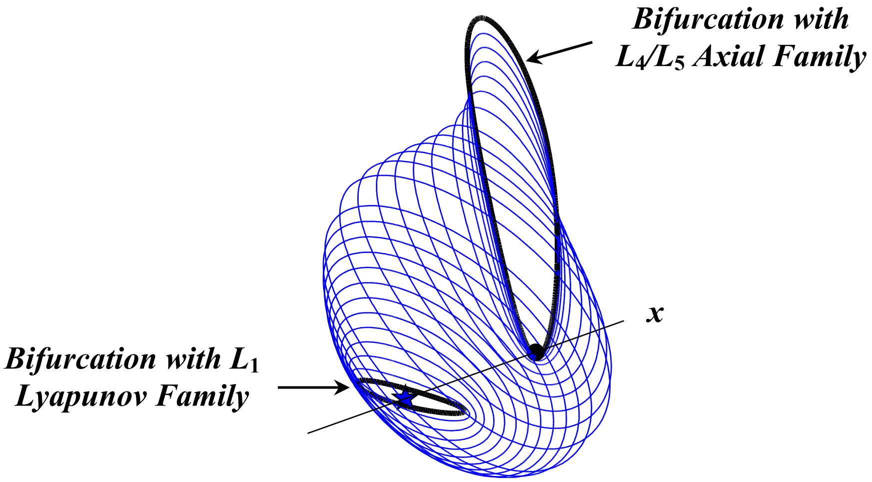

Table 3.4

Northern L_1 Halo Family Initial Conditions

x_0	z_0	$\dot{y}_0$	T	υ	
0.8234	0.0000	0.1263	2.7430	1180.5771	L_1 Lyapunovs
0.8234	0.0224	0.1343	2.7464	1096.9329	
0.8235	0.0344	0.1439	2.7507	993.7530	
0.8237	0.0464	0.1558	2.7566	865.0564	
0.8242	0.0584	0.1690	2.7634	724.4702	
0.8250	0.0704	0.1827	2.7707	584.3385	
0.8260	0.0824	0.1964	2.7778	454.2552	
0.8273	0.0944	0.2095	2.7838	340.4499	
0.8289	0.1064	0.2219	2.7872	245.8832	
0.8307	0.1184	0.2334	2.7864	170.8261	
0.8329	0.1304	0.2437	2.7785	113.6730	
0.8355	0.1424	0.2527	2.7594	71.7704	
0.8389	0.1544	0.2599	2.7215	42.1098	
0.8509	0.1765	0.2624	2.5402	10.2024	
0.8629	0.1858	0.2504	2.3567	3.0145	
0.8749	0.1914	0.2325	2.1914	1.0000	
0.8869	0.1957	0.2110	2.0477	1.4145	
0.8989	0.2002	0.1865	1.9289	1.9886	
0.9109	0.2060	0.1590	1.8417	2.2935	
0.9246	0.2180	0.1232	1.8050	2.5615	
0.9305	0.2300	0.1043	1.8397	2.7481	
0.9330	0.2420	0.0936	1.8959	2.8581	
0.9335	0.2540	0.0874	1.9586	2.8438	
0.9329	0.2660	0.0839	2.0222	2.6473	
0.9315	0.2780	0.0822	2.0845	2.1802	
0.9292	0.2914	0.0817	2.1509	1.0000	L_4/L_5 Axials

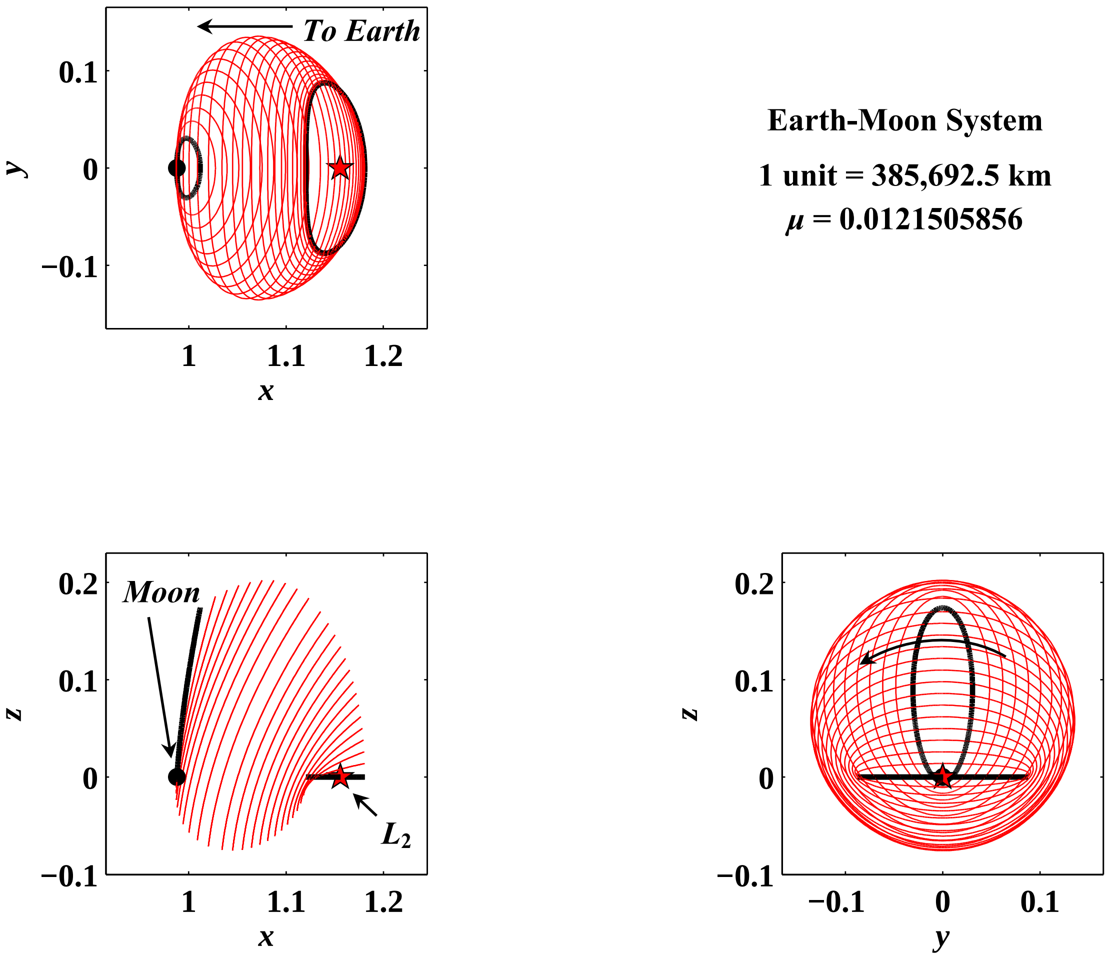

Figure 3.10 The Northern L_2 Halo Family

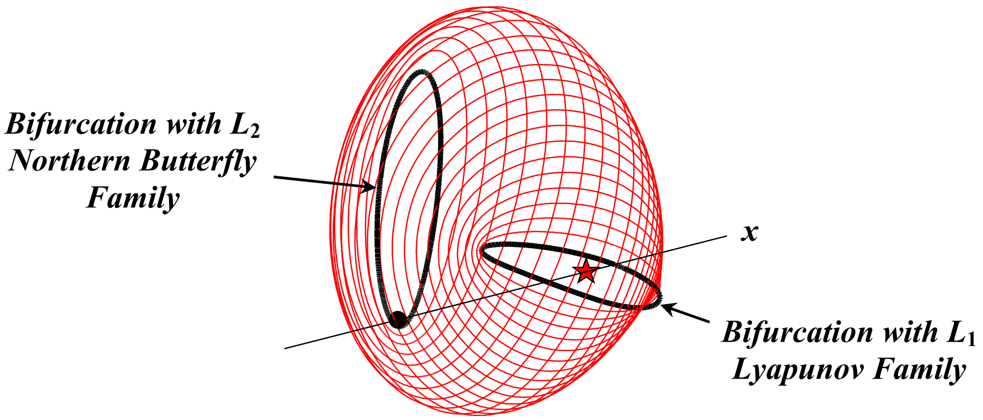

Table 3.5

Northern L_2 Halo Family Initial Conditions

x_0	z_0	$\dot{y}_0$	T	υ	
1.1809	0.0000	-0.1559	3.4155	606.1130	L_2 Lyapunovs
1.1807	0.0139	-0.1570	3.4139	597.2650	
1.1802	0.0259	-0.1596	3.4100	576.0367	
1.1794	0.0379	-0.1637	3.4037	543.6409	
1.1782	0.0499	-0.1688	3.3949	502.0654	
1.1767	0.0619	-0.1747	3.3835	453.6604	
1.1746	0.0739	-0.1812	3.3694	400.9064	
1.1721	0.0859	-0.1879	3.3521	346.2209	
1.1690	0.0979	-0.1946	3.3314	291.8115	
1.1654	0.1099	-0.2011	3.3066	239.5741	
1.1611	0.1219	-0.2073	3.2768	191.0295	
1.1561	0.1339	-0.2130	3.2406	147.2915	
1.1503	0.1459	-0.2180	3.1959	109.0641	
1.1435	0.1579	-0.2220	3.1393	76.6589	
1.1354	0.1699	-0.2247	3.0645	50.0298	
1.1234	0.1837	-0.2253	2.9374	26.0252	
1.1114	0.1934	-0.2220	2.7903	12.8967	
1.0994	0.1993	-0.2153	2.6259	5.7514	
1.0874	0.2020	-0.2054	2.4499	1.9040	
1.0754	0.2022	-0.1926	2.2689	1.0000	
1.0634	0.2003	-0.1770	2.0883	1.2995	
1.0514	0.1968	-0.1589	1.9123	1.6540	
1.0394	0.1919	-0.1381	1.7434	1.6636	
1.0274	0.1856	-0.1146	1.5818	1.4595	
1.0118	0.1739	-0.0799	1.3743	1.0000	L_2 Butterflies

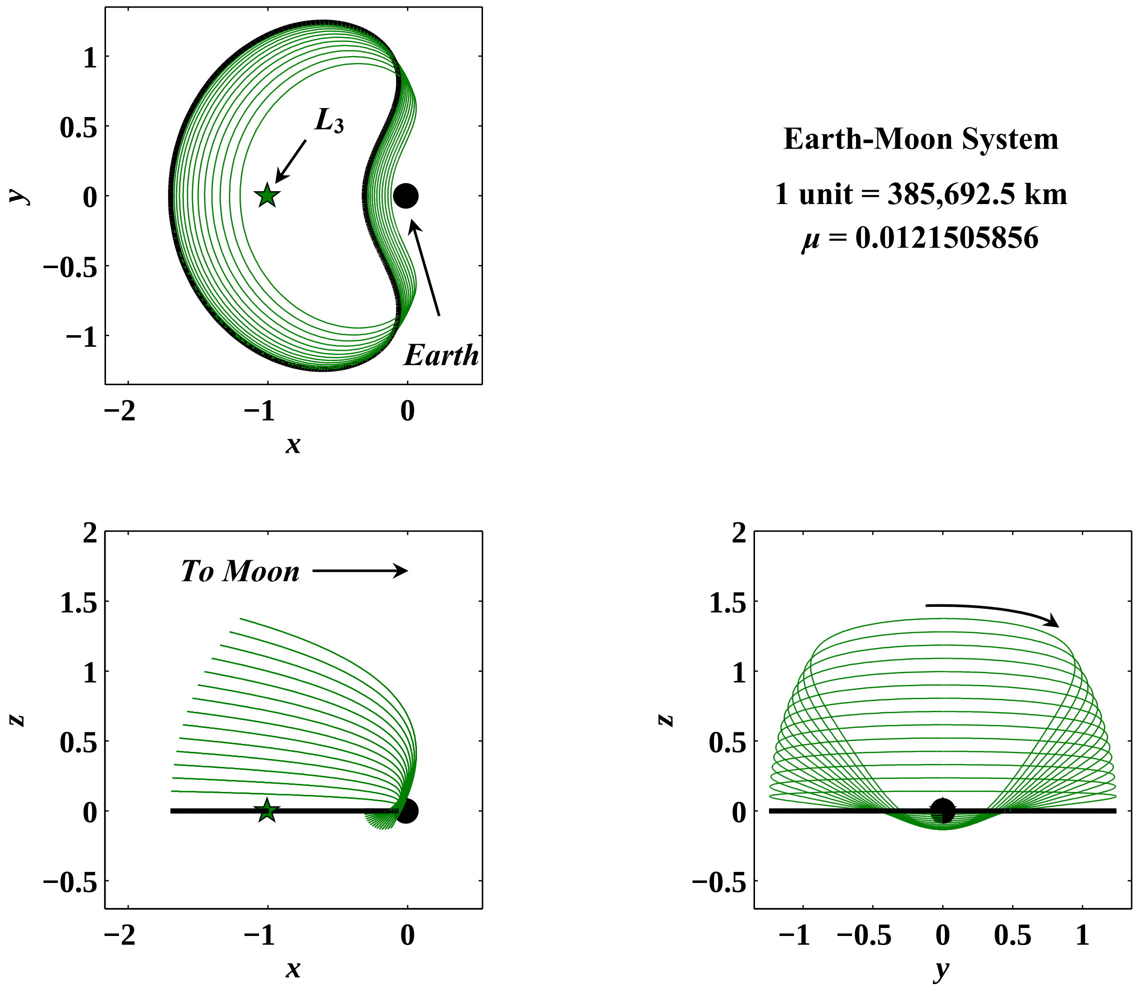

Figure 3.11 The Northern L_3 Halo Family

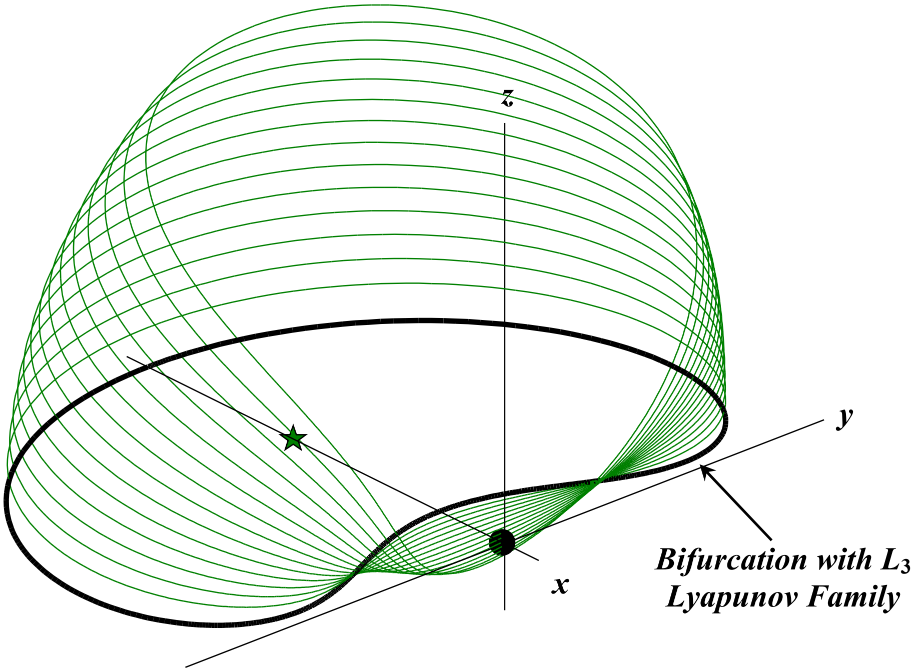

Table 3.6

Northern L_3 Halo Family Initial Conditions

x_0	z_0	$\dot{y}_0$	T	υ	
-1.6967	0.0000	1.2796	6.2391	1.3828	L_3 Lyapunovs
-1.6921	0.1408	1.2760	6.2391	1.3811	
-1.6838	0.2358	1.2696	6.2389	1.3779	
-1.6712	0.3308	1.2600	6.2387	1.3731	
-1.6543	0.4258	1.2470	6.2384	1.3667	
-1.6329	0.5208	1.2307	6.2381	1.3589	
-1.6069	0.6158	1.2108	6.2376	1.3495	
-1.5762	0.7108	1.1874	6.2370	1.3386	
-1.5405	0.8058	1.1602	6.2363	1.3264	
-1.4996	0.9008	1.1291	6.2353	1.3129	
-1.4530	0.9958	1.0938	6.2342	1.2983	
-1.4004	1.0908	1.0539	6.2328	1.2826	
-1.3411	1.1858	1.0091	6.2311	1.2660	
-1.2743	1.2808	0.9588	6.2289	1.2488	
-1.1989	1.3758	0.9021	6.2261	1.2310	

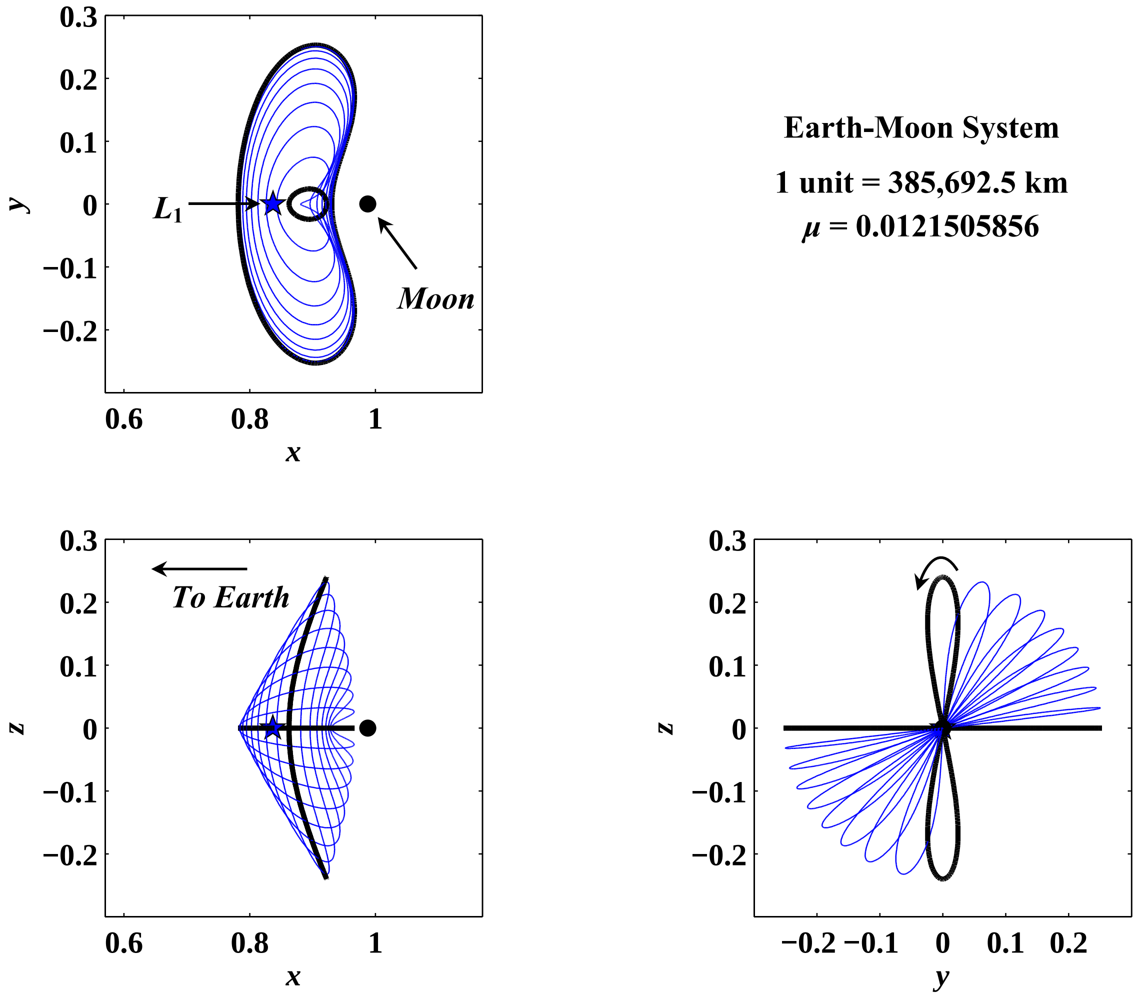

Figure 3.12 The Northeast L_1 Axial Family

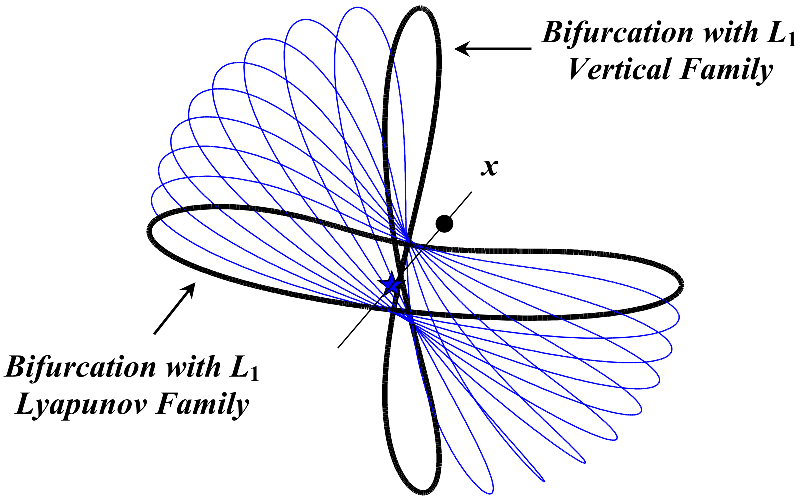

Table 3.7

Northeast L_1 Axial Family Initial Conditions

x_0	$\dot{y}_0$	$\dot{z}_0$	T	υ	
0.7816	0.4432	0.0000	3.9500	200.3471	L_1 Lyapunovs
0.7824	0.4401	0.0500	3.9520	201.2840	
0.7848	0.4307	0.1000	3.9579	204.0837	
0.7888	0.4146	0.1500	3.9677	208.7091	
0.7947	0.3912	0.2000	3.9814	215.0815	
0.8027	0.3594	0.2500	3.9984	223.0401	
0.8130	0.3176	0.3000	4.0182	232.2452	
0.8262	0.2625	0.3500	4.0390	241.9622	
0.8431	0.1874	0.4000	4.0574	250.5755	
0.8625	0.0907	0.4434	4.0652	254.2398	L_1 Verticals

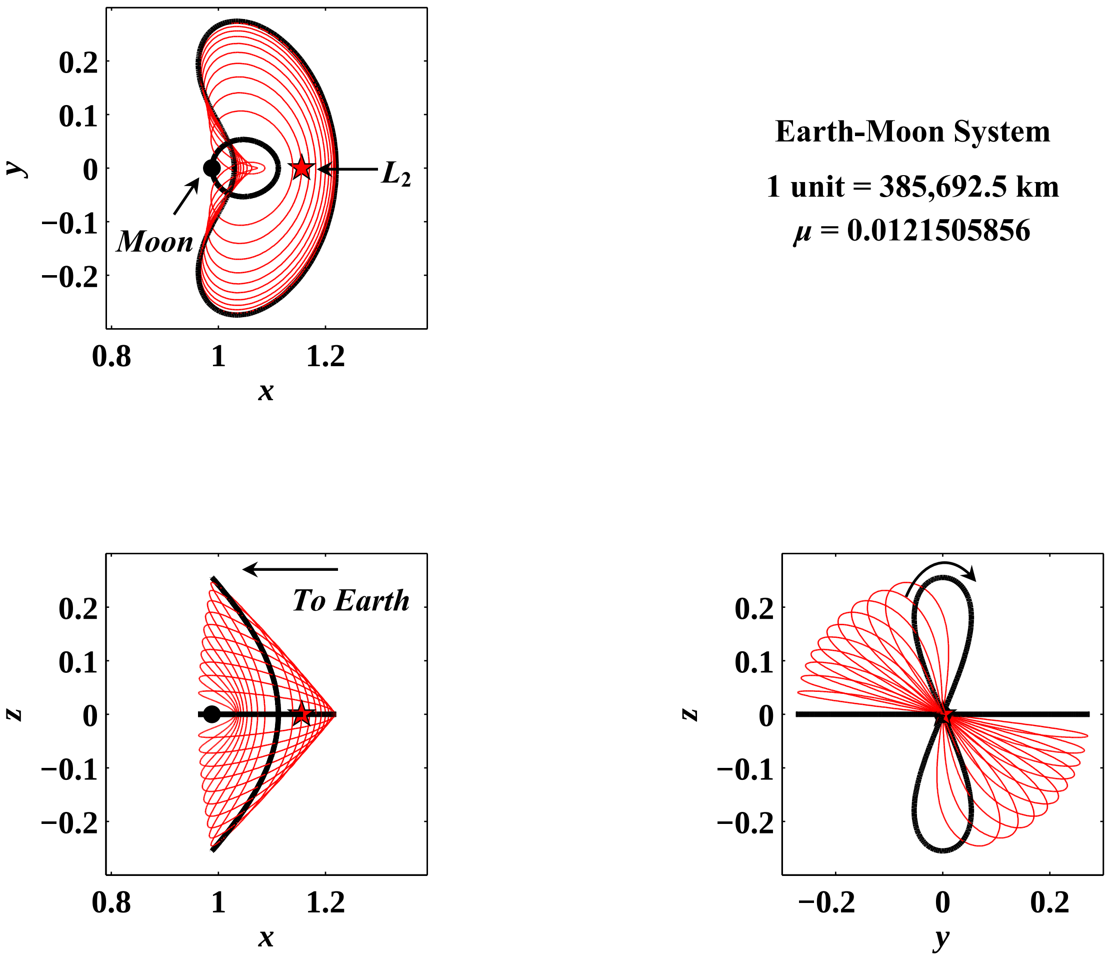

Figure 3.13 The Northwest L_2 Axial Family

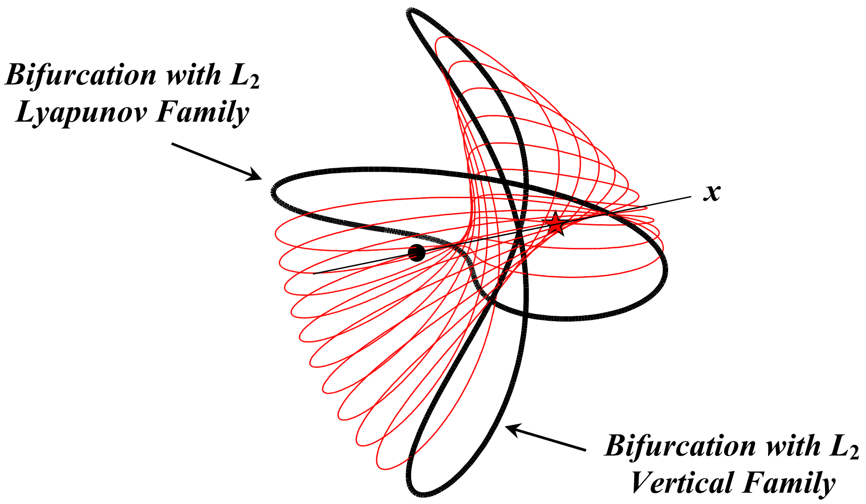

Table 3.8

Northwest L_2 Axial Family Initial Conditions

x_0	$\dot{y}_0$	$\dot{z}_0$	T	υ	
1.2200	-0.4275	0.0000	4.3105	127.8850	L_2 Lyapunovs
1.2183	-0.4248	0.0500	4.3133	129.1383	
1.2152	-0.4198	0.0841	4.3183	131.3556	
1.2112	-0.4133	0.1139	4.3247	134.0770	
1.2062	-0.4048	0.1434	4.3326	137.3638	
1.1998	-0.3938	0.1740	4.3425	141.2513	
1.1918	-0.3796	0.2067	4.3544	145.7239	
1.1818	-0.3610	0.2419	4.3684	150.6775	
1.1697	-0.3369	0.2800	4.3838	155.8679	
1.1554	-0.3055	0.3214	4.3995	160.8533	
1.1389	-0.2647	0.3659	4.4130	164.9638	
1.1119	-0.1812	0.4358	4.4222	167.6717	L_2 Verticals

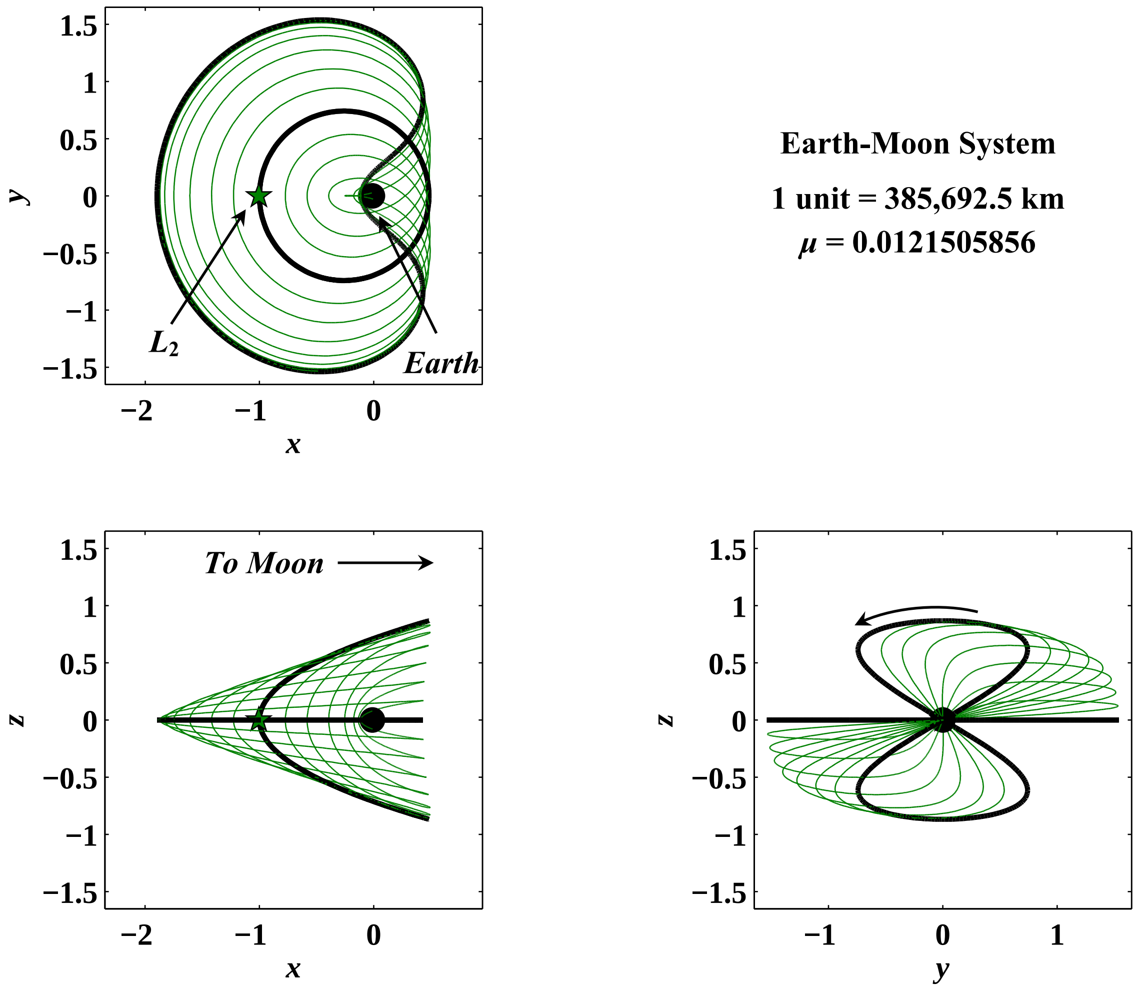

Figure 3.14 The Northeast L_3 Axial Family

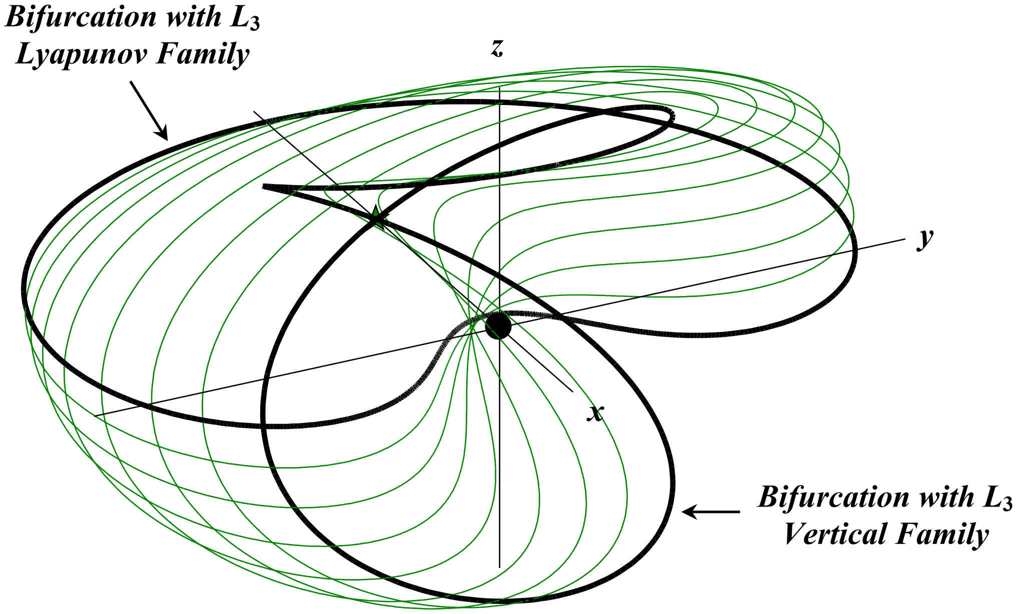

Table 3.9

Northeast L_3 Axial Family Initial Conditions

x_0	$\dot{y}_0$	$\dot{z}_0$	T	υ	
-1.8963	1.6715	0.0000	6.2616	1.0499	L_3 Lyapunovs
-1.8902	1.6761	0.0900	6.2617	1.0604	
-1.8705	1.6893	0.1800	6.2621	1.0889	
-1.8291	1.7093	0.2745	6.2628	1.1273	
-1.7488	1.7269	0.3737	6.2638	1.1567	
-1.6081	1.7186	0.4779	6.2651	1.1567	
-1.4186	1.6683	0.5873	6.2660	1.1370	
-1.2271	1.5950	0.7022	6.2664	1.1211	
-1.0003	1.4900	0.8726	6.2666	1.1142	L_3 Verticals

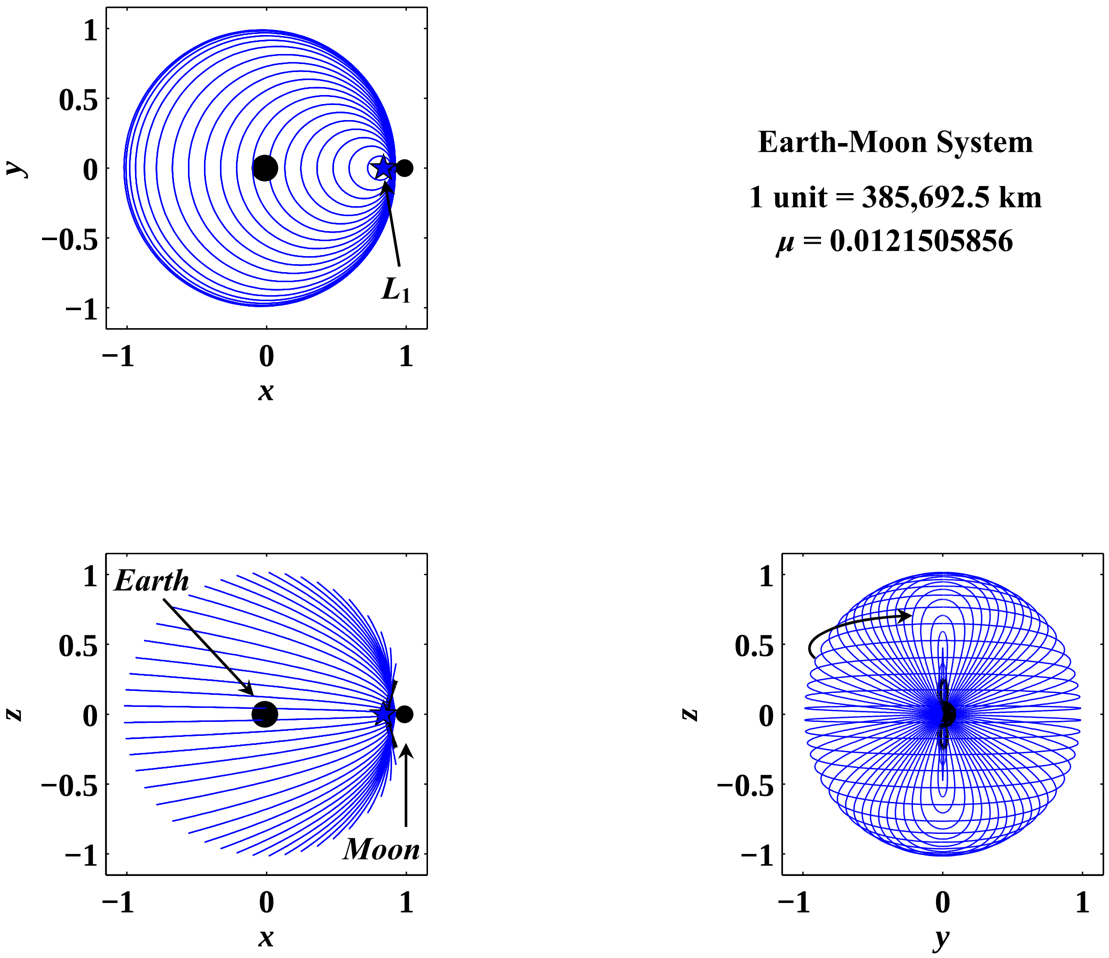

Earth-Moon System

1 unit = 385,692.5 km

μ = 0.0121505856

Figure 3.15 The L_1 Vertical Family

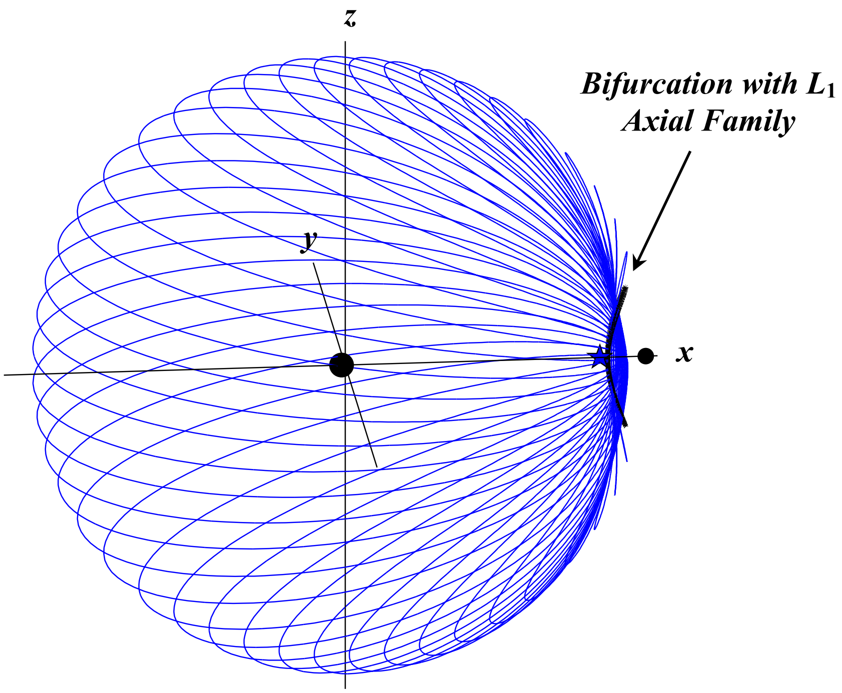

Table 3.10

L_1 Vertical Family Initial Conditions

x_0	z_0	$\dot{y}_0$	T	υ	
1.0118	0.1739	-0.0799	4.0652	254.2398	L_1 Axials
0.9261	0.3616	-0.0544	5.0950	168.7846	
0.8860	0.4766	-0.0009	5.6180	178.5819	
0.8184	0.5916	0.0776	5.8965	191.1137	
0.7233	0.7066	0.1817	6.0552	193.8062	
0.5906	0.8216	0.3221	6.1527	184.7102	
0.4756	0.8936	0.4416	6.1963	171.8511	
0.3606	0.9465	0.5601	6.2235	157.0654	
0.2456	0.9833	0.6780	6.2419	141.4589	
0.1306	1.0057	0.7953	6.2551	125.6070	
0.0156	1.0148	0.9123	6.2650	109.8492	
-0.0994	1.0108	1.0291	6.2726	94.4116	
-0.2144	0.9937	1.1457	6.2786	79.4644	
-0.3294	0.9626	1.2621	6.2834	65.1508	
-0.4444	0.9162	1.3783	6.2874	51.6049	
-0.5594	0.8520	1.4945	6.2908	38.9630	
-0.6744	0.7654	1.6105	6.2936	27.3749	
-0.7894	0.6477	1.7265	6.2960	17.0201	
-0.8756	0.5267	1.8134	6.2976	10.2053	
-0.9389	0.4047	1.8772	6.2987	5.8212	
-0.9809	0.2897	1.9195	6.2994	3.2509	
-1.0080	0.1747	1.9468	6.2998	1.7631	
-1.0214	0.0597	1.9603	6.3000	1.0856	

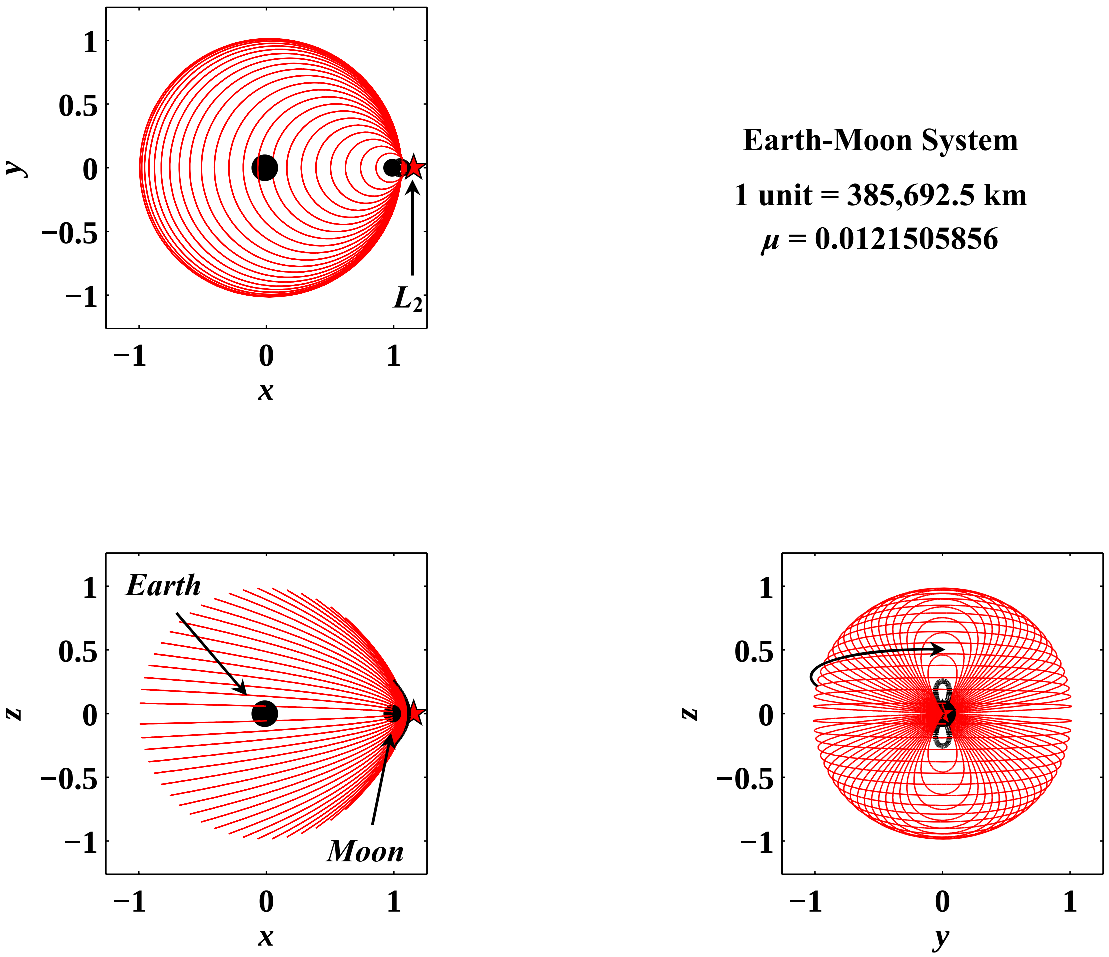

Figure 3.16 The L_2 Vertical Family

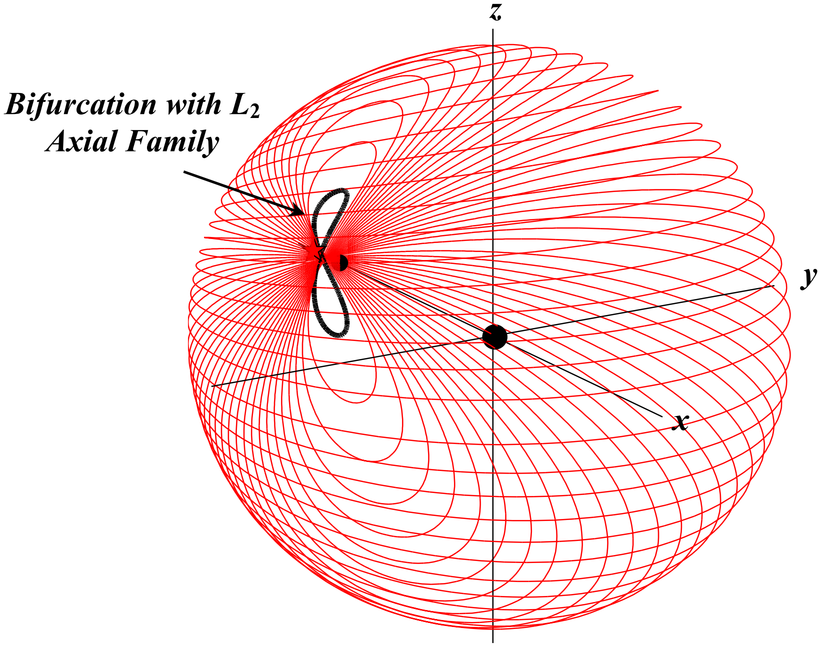

Table 3.11

L_2 Vertical Family Initial Conditions

x_0	$\dot{y}_0$	$\dot{z}_0$	T	υ	
1.1119	-0.1812	0.4358	4.4222	167.6717	L_2 Axials
1.1003	-0.3217	0.5973	5.6753	204.3084	
1.0906	-0.4317	0.7416	6.0172	240.7419	
1.0842	-0.5417	0.8415	6.1305	236.0384	
1.0796	-0.6517	0.9128	6.1848	217.8085	
1.0762	-0.7617	0.9635	6.2162	194.9734	
1.0735	-0.8717	0.9978	6.2366	170.9369	
1.0713	-0.9817	1.0179	6.2508	147.2392	
1.0694	-1.0917	1.0248	6.2613	124.6527	
1.0679	-1.2017	1.0192	6.2692	103.5866	
1.0665	-1.3117	1.0009	6.2754	84.2596	
1.0654	-1.4217	0.9694	6.2804	66.7829	
1.0644	-1.5317	0.9234	6.2845	51.2053	
1.0636	-1.6307	0.8677	6.2876	38.8193	
1.0629	-1.7198	0.8038	6.2900	28.9912	
1.0624	-1.8000	0.7321	6.2919	21.2089	
1.0619	-1.8721	0.6525	6.2935	15.0634	
1.0616	-1.9371	0.5634	6.2947	10.2310	
1.0613	-1.9891	0.4740	6.2957	6.8491	
1.0611	-2.0306	0.3827	6.2964	4.4628	
1.0609	-2.0639	0.2853	6.2969	2.7679	
1.0608	-2.0860	0.1920	6.2973	1.7530	
1.0608	-2.1007	0.0820	6.2975	1.1314	

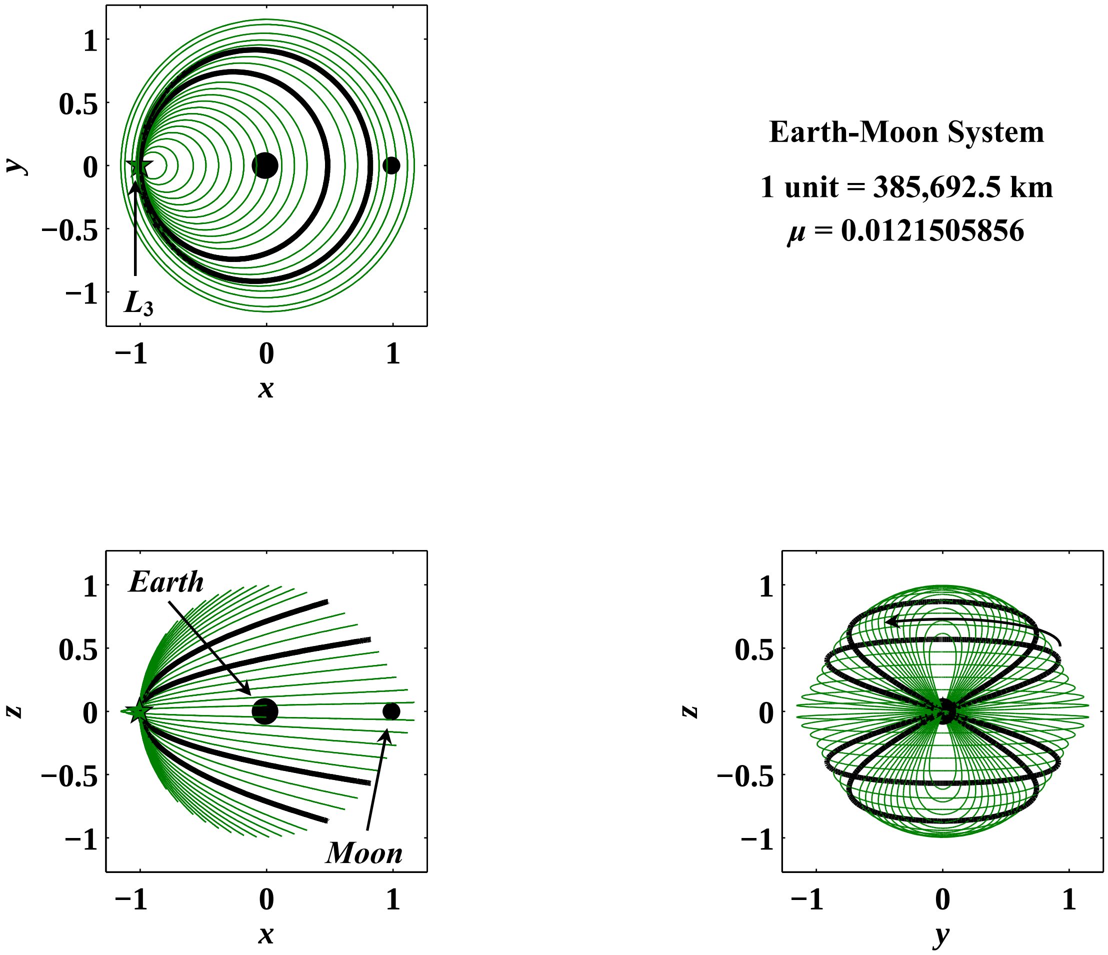

Figure 3.17 The L_3 Vertical Family

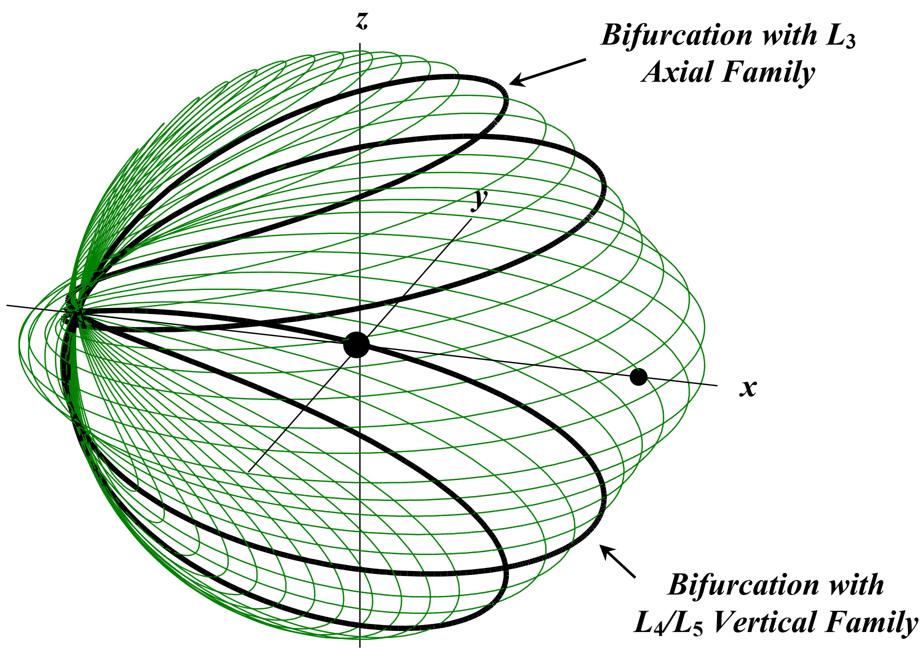

Bifurcation with L_3 Axial Family

Bifurcation with L_4/L_5 Vertical Family

Table 3.12

L_3 Vertical Family Initial Conditions

x_0	z_0	$\dot{y}_0$	T	υ	
-0.7916	0.6160	-0.2129	6.2505	1.5968	
-0.7012	0.7160	-0.3031	6.2508	1.5604	
-0.5798	0.8160	-0.4241	6.2513	1.5119	
-0.4798	0.8775	-0.5239	6.2518	1.4724	
-0.3798	0.9242	-0.6236	6.2523	1.4334	
-0.2798	0.9583	-0.7234	6.2529	1.3947	
-0.1798	0.9811	-0.8232	6.2537	1.3565	
-0.0798	0.9934	-0.9229	6.2546	1.3186	
0.0202	0.9956	-1.0227	6.2557	1.2812	
0.1202	0.9878	-1.1225	6.2570	1.2443	
0.2202	0.9697	-1.2223	6.2588	1.2078	
0.3202	0.9408	-1.3221	6.2610	1.1718	
0.4830	0.8679	-1.4846	6.2666	1.1142	L_3 Axials
0.6202	0.7763	-1.6214	6.2752	1.0670	
0.7202	0.6866	-1.7211	6.2868	1.0334	
0.8213	0.5690	-1.8214	6.3111	1.0021	L_4/L_5 Verticals
0.8897	0.4705	-1.8880	6.3474	1.0038	
0.9527	0.3705	-1.9468	6.4196	1.0071	
1.0259	0.2705	-2.0078	6.5791	1.0072	
1.1147	0.1705	-2.0751	6.8165	1.0000	
1.1678	0.0705	-2.1154	6.9476	1.0000	

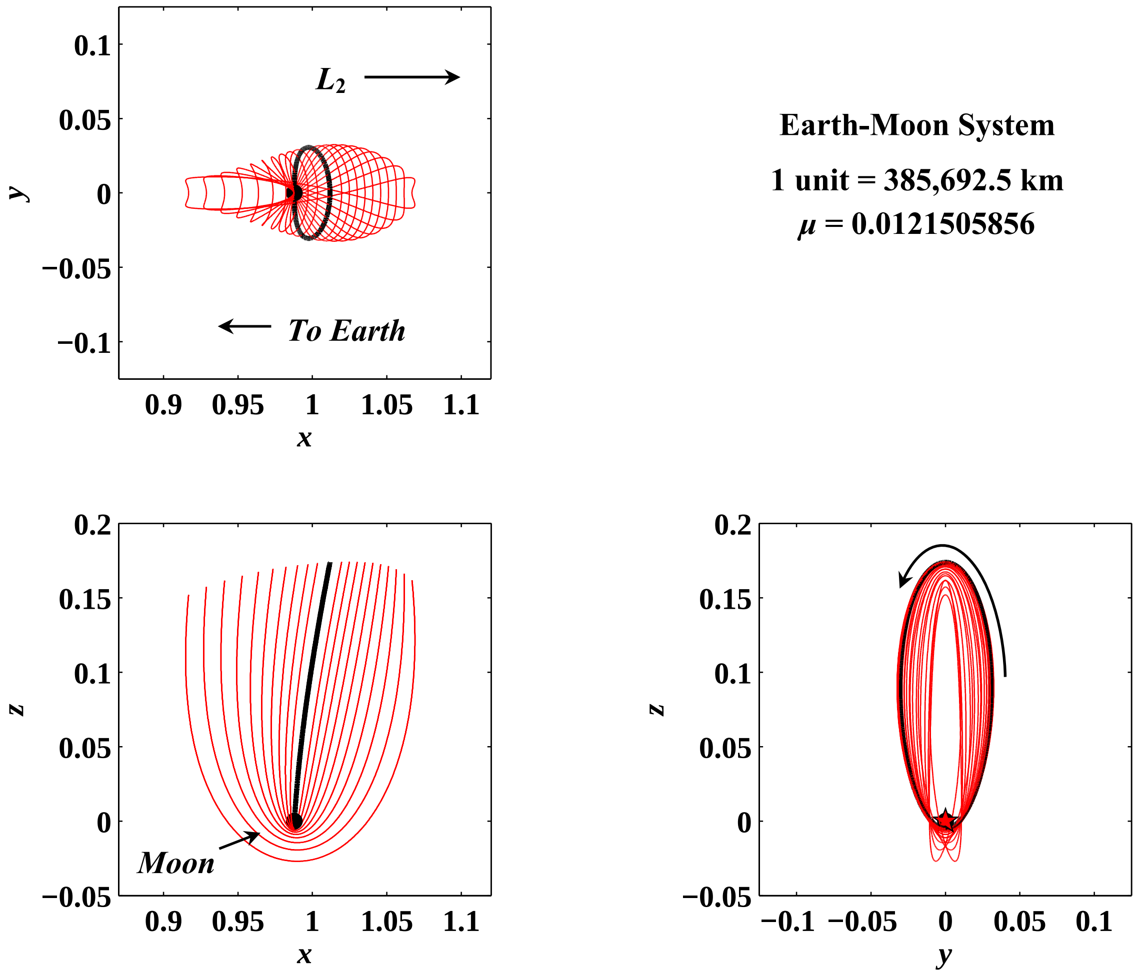

Earth-Moon System

1 unit = 385,692.5 km

$\mu = 0.0121505856$

Figure 3.18 The Northern L_2 Butterfly Family

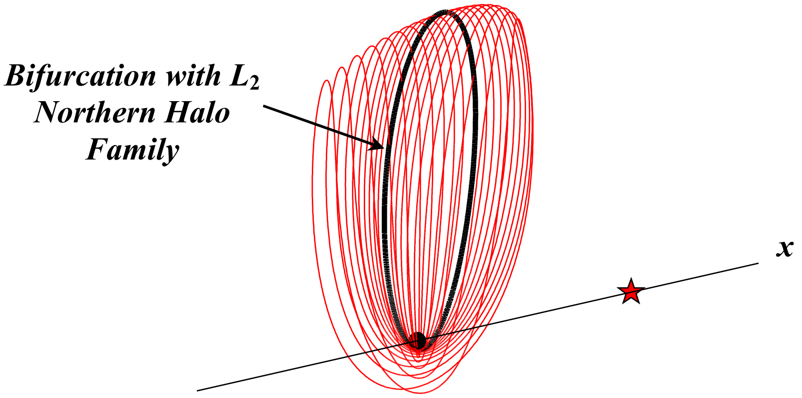

Table 3.13

Northern L_2 Butterfly Family Initial Conditions

x_0	z_0	$\dot{y}_0$	T	υ	
1.0118	0.1739	-0.0799	1.3743	1.0000	L_2 Halos
1.0196	0.1742	-0.0817	2.7519	1.0589	
1.0249	0.1743	-0.0821	2.7582	1.1762	
1.0301	0.1742	-0.0816	2.7687	1.3772	
1.0354	0.1740	-0.0801	2.7845	1.6932	
1.0406	0.1735	-0.0770	2.8077	2.1774	
1.0459	0.1727	-0.0721	2.8409	2.9191	
1.0511	0.1713	-0.0646	2.8891	4.0650	
1.0564	0.1693	-0.0539	2.9596	5.8298	
1.0616	0.1662	-0.0392	3.0637	8.4171	
1.0669	0.1619	-0.0189	3.2255	11.5767	

3.4 Asymmetric Correction Schemes

An asymmetric corrections scheme is a powerful tool for converging to any periodic solution. The targeting schemes in Sections 3.2-3.3 use symmetry to adjust the control parameters such that endpoint constraints are fully satisfied. However, there exist asymmetric periodic solutions as well, in particular, the periodic solutions near the triangular equilibrium points. Near L_4 or L_5, the planes of symmetry are either not easily defined or are not consistently defined along the family. In such cases, equation (2.61) cannot be used to adjust the control variables at the initial time that minimize the endpoint variations. A more sophisticated algorithm is necessary. An algorithm introduced by Markellos and Halioulias [14-15] successfully produces periodic solutions of this type. A continuation method for predicting elements of future initial state vectors by shifting along the tangent to the family is also developed. The algorithms and continuation methods are used to locate the L_4 planar, axial, and vertical families of orbits. Similar orbits have been computed by various researchers [7, 9, 21, 26, 29].

3.4.1 Strategies to Compute Periodic Orbits

The planar case. The initial condition, associated with the planar case, that produces asymmetric periodic orbits, e.g., planar orbits in the vicinity of L_4, is of the form

$$\vec{q}_0 = \{x_0 \quad y_0 \quad 0 \quad \dot{x}_0 \quad \dot{y}_0 \quad 0\}^T. \tag{3.58}$$

To later expand the solution space, one of the four nonzero components are fixed during the integration process. Furthermore, one of the nonzero components also serves as a reference for defining mappings. Assuming $\dot{y}_0$ is fixed, then,

$$x = F\left(x_0, \dot{x}_0, \dot{y}_0\right), \tag{3.59}$$

$$\dot{x} = G\left(x_0, \dot{x}_0, \dot{y}_0\right), \tag{3.60}$$

where the mappings bring $x_0, \dot{x}_0,$ and $\dot{y}_0$ to x for F and to $\dot{x}$ for G from the reference y_0 to $y = y_0$. The reference value remains consistent throughout the entire family. Therefore, a reference value is determined that is common to all orbits in the family, i.e., each orbit in the family crosses the reference. Therefore, for periodic motion, the goal is determination of the variations δx_0 and $\delta \dot{x}_0$ such that $x = x_0 + \delta x_0$ and $\dot{x} = \dot{x}_0 + \delta \dot{x}_0$, i.e.,

$$x = F\left(x_0 + \delta x_0, \dot{x}_0 + \delta \dot{x}_0, \dot{y}_0 + \delta \dot{y}_0\right) = x_0 + \delta x_0, \tag{3.61}$$

$$\dot{x} = G\left(x_0 + \delta x_0, \dot{x}_0 + \delta \dot{x}_0, \dot{y}_0 + \delta \dot{y}_0\right) = \dot{x}_0 + \delta \dot{x}_0. \tag{3.62}$$

From the first-order Taylor series expansion for equation (3.61)-(3.62),

$$F\left(x, \dot{x}\right) = x_0 + \delta x_0 = F\left(x_0, \dot{x}_0\right) + \frac{\partial F}{\partial x_0}\delta x_0 + \frac{\partial F}{\partial \dot{x}_0}\delta \dot{x}_0, \tag{3.63}$$

$$G\left(x, \dot{x}\right) = \dot{x}_0 + \delta \dot{x}_0 = G\left(x_0, \dot{x}_0\right) + \frac{\partial G}{\partial x_0}\delta x_0 + \frac{\partial G}{\partial \dot{x}_0}\delta \dot{x}_0. \tag{3.64}$$

Rearranging equations (3.63)-(3.64) results in targeter relationships,

$$\begin{Bmatrix} \delta x \\ \delta \dot{x} \end{Bmatrix} = \begin{bmatrix} \left(\dfrac{\partial F}{\partial x_0} - 1\right) & \dfrac{\partial F}{\partial \dot{x}_0} \\ \dfrac{\partial G}{\partial x_0} & \left(\dfrac{\partial G}{\partial \dot{x}_0} - 1\right) \end{bmatrix} \begin{Bmatrix} \delta x_0 \\ \delta \dot{x}_0 \end{Bmatrix}, \tag{3.65}$$

where the partials of *F* and *G* with respect to $x_0, \dot{x}_0, \text{and}\, \dot{y}_0$ are available from the linear variational equations. To obtain these partials, use equation (2.61) and isolate the appropriate sensitivity partials

$$\frac{\partial F}{\partial x_0} = \frac{\delta x}{\delta x_0} = \frac{\partial x}{\partial x_0} - \frac{\partial y}{\partial x_0}\frac{\dot{x}}{\dot{y}}, \tag{3.66}$$

$$\frac{\partial F}{\partial \dot{x}_0} = \frac{\delta x}{\delta \dot{x}_0} = \frac{\partial x}{\partial \dot{x}_0} - \frac{\partial y}{\partial \dot{x}_0}\frac{\dot{x}}{\dot{y}}, \tag{3.67}$$

$$\frac{\partial F}{\partial \dot{y}_0} = \frac{\delta x}{\delta \dot{y}_0} = \frac{\partial x}{\partial \dot{y}_0} - \frac{\partial y}{\partial \dot{y}_0}\frac{\dot{x}}{\dot{y}}, \tag{3.68}$$

$$\frac{\partial G}{\partial x_0} = \frac{\delta y}{\delta x_0} = \frac{\partial \dot{x}}{\partial x_0} - \frac{\partial y}{\partial x_0}\frac{\ddot{x}}{\dot{y}}, \tag{3.69}$$

$$\frac{\partial G}{\partial \dot{x}_0} = \frac{\delta y}{\delta \dot{x}_0} = \frac{\partial \dot{x}}{\partial \dot{x}_0} - \frac{\partial y}{\partial \dot{x}_0}\frac{\ddot{x}}{\dot{y}}, \tag{3.70}$$

$$\frac{\partial G}{\partial \dot{y}_0} = \frac{\delta y}{\delta \dot{y}_0} = \frac{\partial \dot{x}}{\partial \dot{y}_0} - \frac{\partial y}{\partial \dot{y}_0}\frac{\ddot{x}}{\dot{y}}. \tag{3.71}$$

The solution for the variations in δx_0 and $\delta \dot{x}_0$ is obtained from equation (3.65). Then, δx_0 and $\delta \dot{x}_0$ are subtracted from the states x_0 and $\dot{x}_0$, respectively. The process is repeated until $\delta x, \delta \dot{x} < \varepsilon$, and the periodic orbit is obtained.

Equations (3.66)-(3.71) are also employed for predictions, that is, an initial guess for the next initial state $\vec{q}_0^{\,n}$ along the tangent subspace *Γ* corresponding to the family. Let $\Delta\vec{q}_0^{\,n-1}$ be defined as

$$\Delta\vec{q}_0^{\,n-1} = \left\{ \Delta x_0^{n-1} \quad 0 \quad 0 \quad \Delta\dot{x}_0^{n-1} \quad \Delta\dot{y}_0^{n-1} \quad 0 \right\}^T, \tag{3.72}$$

where the following equations must be satisfied

$$\Delta x_0^{n-1} = \frac{\partial F}{\partial x_0}\Delta x_0^{n-1} + \frac{\partial F}{\partial \dot{x}_0}\Delta\dot{x}_0^{n-1} + \frac{\partial F}{\partial \dot{y}_0}\Delta\dot{y}_0^{n-1}, \tag{3.73}$$

$$\Delta\dot{x}_0^{n-1} = \frac{\partial G}{\partial x_0}\Delta x_0^{n-1} + \frac{\partial G}{\partial \dot{x}_0}\Delta\dot{x}_0^{n-1} + \frac{\partial G}{\partial \dot{y}_0}\Delta\dot{y}_0^{n-1}, \tag{3.74}$$

such that the components of $\Delta\vec{q}_0^{\,n-1}$ are normalized,

$$1 = \left(\Delta x_0^{n-1}\right)^2 + \left(\Delta\dot{x}_0^{n-1}\right)^2 + \left(\Delta\dot{y}_0^{n-1}\right)^2. \tag{3.75}$$

The simultaneous solution of equations (3.73)-(3.75) yields values for the scalars Δx_0^{n-1}, $\Delta\dot{x}_0^{n-1}$, and $\Delta\dot{y}_0^{n-1}$. Then, equation (3.28) is used for some fixed step size *S*, and the prediction $\vec{q}_0^{\,n}$ initiates a new iteration process to locate a periodic orbit. To compute the entire family, it is necessary to change the sign of *S* when passing through the extremum of *Γ*. The switch time is apparent at the point when Δx_0^{n-1} and $\Delta\dot{x}_0^{n-1}$ simultaneously change signs, i.e.,

$$\Delta x_0^{n-2} \cdot \Delta x_0^{n-1} < 0, \tag{3.76}$$

$$\Delta\dot{x}_0^{n-2} \cdot \Delta\dot{x}_0^{n-1} < 0. \tag{3.77}$$

The entire process is repeated until the family of solutions is computed.

Motion in three-dimensional space with reference y_0. To calculate the L_4 vertical orbits, the targeting algorithm must be adapted to include out-of-plane motion. Successful computation of asymmetric periodic orbits in three-dimensional space depends upon the following mappings, i.e.,

$$x = F\left(x_0, z_0, \dot{x}_0, \dot{y}_0, \dot{z}_0\right), \tag{3.78}$$

$$z = G\left(x_0, z_0, \dot{x}_0, \dot{y}_0, \dot{z}_0\right), \tag{3.79}$$

$$\dot{x} = H\left(x_0, z_0, \dot{x}_0, \dot{y}_0, \dot{z}_0\right), \tag{3.80}$$

$$\dot{z} = I\left(x_0, z_0, \dot{x}_0, \dot{y}_0, \dot{z}_0\right), \tag{3.81}$$

such that each one maps from the reference y_0 to $y = y_0$, where y_0 is common for all orbits in the family. The goal is the determination of the variations $\delta x_0, \delta z_0, \delta \dot{x}_0$, and $\delta \dot{z}_0$ that result in this particular type of periodic orbit, i.e.,

$$x = F\left(x_0 + \delta x_0, z_0 + \delta z_0, \dot{x}_0 + \delta \dot{x}_0, \dot{y}_0 + \delta \dot{y}_0, \dot{z}_0 + \delta \dot{z}_0\right) = x_0 + \delta x_0, \tag{3.82}$$

$$z = G\left(x_0 + \delta x_0, z_0 + \delta z_0, \dot{x}_0 + \delta \dot{x}_0, \dot{y}_0 + \delta \dot{y}_0, \dot{z}_0 + \delta \dot{z}_0\right) = z_0 + \delta z_0, \tag{3.83}$$

$$\dot{x} = H\left(x_0 + \delta x_0, z_0 + \delta z_0, \dot{x}_0 + \delta \dot{x}_0, \dot{y}_0 + \delta \dot{y}_0, \dot{z}_0 + \delta \dot{z}_0\right) = \dot{x}_0 + \delta \dot{x}_0, \tag{3.84}$$

$$\dot{z} = I\left(x_0 + \delta x_0, z_0 + \delta z_0, \dot{x}_0 + \delta \dot{x}_0, \dot{y}_0 + \delta \dot{y}_0, \dot{z}_0 + \delta \dot{z}_0\right) = \dot{z}_0 + \delta \dot{z}_0. \tag{3.85}$$

Using a Taylor series to expand equations (3.82)-(3.85) about the reference, results in the following first-order targeter,

$$\begin{Bmatrix} \delta x \\ \delta z \\ \delta \dot{x} \\ \delta \dot{z} \end{Bmatrix} = \begin{bmatrix} \left(\dfrac{\partial F}{\partial x_0} - 1\right) & \dfrac{\partial F}{\partial z_0} & \dfrac{\partial F}{\partial \dot{x}_0} & \dfrac{\partial F}{\partial \dot{y}_0} & \dfrac{\partial F}{\partial \dot{z}_0} \\ \dfrac{\partial G}{\partial x_0} & \left(\dfrac{\partial G}{\partial z_0} - 1\right) & \dfrac{\partial G}{\partial \dot{x}_0} & \dfrac{\partial G}{\partial \dot{y}_0} & \dfrac{\partial G}{\partial \dot{z}_0} \\ \dfrac{\partial H}{\partial x_0} & \dfrac{\partial H}{\partial z_0} & \left(\dfrac{\partial H}{\partial \dot{x}_0} - 1\right) & \dfrac{\partial H}{\partial \dot{y}_0} & \dfrac{\partial H}{\partial \dot{z}_0} \\ \dfrac{\partial I}{\partial x_0} & \dfrac{\partial I}{\partial z_0} & \dfrac{\partial I}{\partial \dot{x}_0} & \dfrac{\partial I}{\partial \dot{y}_0} & \left(\dfrac{\partial I}{\partial \dot{z}_0} - 1\right) \end{bmatrix} \begin{Bmatrix} \delta x_0 \\ \delta z_0 \\ \delta \dot{x}_0 \\ \delta \dot{y}_0 \\ \delta \dot{z}_0 \end{Bmatrix}. \tag{3.86}$$

To determine the partials in equation (3.86), let **Q** be defined as

$$\mathbf{Q}=\begin{bmatrix} \frac{\partial F}{\partial x_0} & \frac{\partial F}{\partial z_0} & \frac{\partial F}{\partial \dot{x}_0} & \frac{\partial F}{\partial \dot{y}_0} & \frac{\partial F}{\partial \dot{z}_0} \\ \frac{\partial G}{\partial x_0} & \frac{\partial G}{\partial z_0} & \frac{\partial G}{\partial \dot{x}_0} & \frac{\partial G}{\partial \dot{y}_0} & \frac{\partial G}{\partial \dot{z}_0} \\ \frac{\partial H}{\partial x_0} & \frac{\partial H}{\partial z_0} & \frac{\partial H}{\partial \dot{x}_0} & \frac{\partial H}{\partial \dot{y}_0} & \frac{\partial H}{\partial \dot{z}_0} \\ \frac{\partial I}{\partial x_0} & \frac{\partial I}{\partial z_0} & \frac{\partial I}{\partial \dot{x}_0} & \frac{\partial I}{\partial \dot{y}_0} & \frac{\partial I}{\partial \dot{z}_0} \end{bmatrix}. \tag{3.87}$$

Then the partials in equation (3.86) are contained in **Q** such that the components of **Q** are found using equation (2.61) to isolate the appropriate sensitivity partials. Thus,

$$\mathbf{Q}=\begin{bmatrix} \frac{\partial x}{\partial x_0} & \frac{\partial x}{\partial z_0} & \frac{\partial x}{\partial \dot{x}_0} & \frac{\partial x}{\partial \dot{y}_0} & \frac{\partial x}{\partial \dot{z}_0} \\ \frac{\partial y}{\partial x_0} & \frac{\partial y}{\partial z_0} & \frac{\partial y}{\partial \dot{x}_0} & \frac{\partial y}{\partial \dot{y}_0} & \frac{\partial y}{\partial \dot{z}_0} \\ \frac{\partial \dot{x}}{\partial x_0} & \frac{\partial \dot{x}}{\partial z_0} & \frac{\partial \dot{x}}{\partial \dot{x}_0} & \frac{\partial \dot{x}}{\partial \dot{y}_0} & \frac{\partial \dot{x}}{\partial \dot{z}_0} \\ \frac{\partial \dot{y}}{\partial x_0} & \frac{\partial \dot{y}}{\partial z_0} & \frac{\partial \dot{y}}{\partial \dot{x}_0} & \frac{\partial \dot{y}}{\partial \dot{y}_0} & \frac{\partial \dot{y}}{\partial \dot{z}_0} \end{bmatrix} - \frac{1}{\dot{y}}\begin{Bmatrix} \dot{x} \\ \dot{z} \\ \ddot{x} \\ \ddot{z} \end{Bmatrix}\begin{Bmatrix} \frac{\partial y}{\partial x_0} & \frac{\partial y}{\partial z_0} & \frac{\partial y}{\partial \dot{x}_0} & \frac{\partial y}{\partial \dot{y}_0} & \frac{\partial y}{\partial \dot{z}_0} \end{Bmatrix}. \tag{3.88}$$

Given the form of this targeter, a constraint to fix $\delta \dot{y}_0$ is accomplished simply by equating $\delta \dot{y}_0$ to zero in equation (3.86). However, the additional equation increases the speed of convergence of the algorithm. Furthermore, the targeter is only differentially correcting the initial variations $\delta x_0, \delta z_0, \delta \dot{x}_0,$ and $\delta \dot{z}_0$ to compute a periodic solution, as defined by the mappings in equations (3.82)-(3.85). Therefore it is not necessary to fix $\delta \dot{y}_0$ when computing the family. Of course, four equations in equation (3.86) implies an infinite number of solutions. For this application, the solution with the smallest Euclidean norm is selected. The initial state vector is updated via $\delta x_0, \delta z_0, \delta \dot{x}_0, \delta \dot{y}_0,$ and $\delta \dot{z}_0$ in an iterative process until $\delta x, \delta z, \delta \dot{x}, \delta \dot{z} < \varepsilon,$ thereby obtaining a periodic orbit.

The predictions for $\vec{q}_0^{\,n}$ to uniformly move along the tangent subspace Γ associated with the family are available from equations (3.87) and (3.88). Let $\Delta\vec{q}_0^{\,n-1}$ be defined as

$$\Delta\vec{q}_0^{\,n-1} = \left\{ \Delta x_0^{n-1} \quad 0 \quad \Delta z_0^{n-1} \quad \Delta\dot{x}_0^{n-1} \quad \Delta\dot{y}_0^{n-1} \quad \Delta\dot{z}_0^{n-1} \right\}^T, \tag{3.89}$$

where the matrix equation

$$\begin{Bmatrix} \Delta x_0^{n-1} \\ \Delta z_0^{n-1} \\ \Delta\dot{x}_0^{n-1} \\ \Delta\dot{z}_0^{n-1} \end{Bmatrix} = [\mathbf{Q}] \begin{Bmatrix} \Delta x_0^{n-1} \\ \Delta z_0^{n-1} \\ \Delta\dot{x}_0^{n-1} \\ \Delta\dot{y}_0^{n-1} \\ \Delta\dot{z}_0^{n-1} \end{Bmatrix}, \tag{3.90}$$

must be satisfied such that for normalized $\Delta\vec{q}_0^{\,n-1}$,

$$1 = \left(\Delta x_0^{n-1}\right)^2 + \left(\Delta z_0^{n-1}\right)^2 + \left(\Delta\dot{x}_0^{n-1}\right)^2 + \left(\Delta\dot{y}_0^{n-1}\right)^2 + \left(\Delta\dot{z}_0^{n-1}\right)^2. \tag{3.91}$$

Solving equations (3.90) and (3.91) simultaneously produces the components of $\Delta\vec{q}_0^{\,n-1}$. To obtain the entire family, the sign of S is changed when the following conditions are simultaneously satisfied,

$$\Delta x_0^{n-2} \cdot \Delta x_0^{n-1} < 0, \tag{3.92}$$

$$\Delta z_0^{n-2} \cdot \Delta z_0^{n-1} < 0, \tag{3.93}$$

$$\Delta\dot{x}_0^{n-2} \cdot \Delta\dot{x}_0^{n-1} < 0, \tag{3.94}$$

$$\Delta\dot{z}_0^{n-2} \cdot \Delta\dot{z}_0^{n-1} < 0. \tag{3.95}$$

The process is continued until the desired family is obtained.

Motion in three-dimensional space with reference z_0. For some families of orbits, e.g., the L_4/L_5 axial orbits, no common reference y_0 can be defined for every orbit in the family. Therefore, it is necessary to change the reference to a different parameter. For example, to obtain an L_4 axial family let z_0 define the reference. Then, the mappings are defined as follows,

$$x = Q\left(x_0, y_0, \dot{x}_0, \dot{y}_0, \dot{z}_0\right), \tag{3.96}$$

$$y = R\left(x_0, y_0, \dot{x}_0, \dot{y}_0, \dot{z}_0\right), \tag{3.97}$$

$$\dot{x} = T\left(x_0, y_0, \dot{x}_0, \dot{y}_0, \dot{z}_0\right), \tag{3.98}$$

$$\dot{y} = V\left(x_0, y_0, \dot{x}_0, \dot{y}_0, \dot{z}_0\right), \tag{3.99}$$

such that each variable is mapped from the reference z_0 to $z = z_0$. Then, for a periodic orbit, equations (3.96)-(3.99) are rewritten in the following functional form,

$$x = Q\left(x_0 + \delta x_0, y_0 + \delta y_0, \dot{x}_0 + \delta \dot{x}_0, \dot{y}_0 + \delta \dot{y}_0, \dot{z}_0 + \delta \dot{z}_0\right) = x_0 + \delta x_0, \tag{3.100}$$

$$y = R\left(x_0 + \delta x_0, y_0 + \delta y_0, \dot{x}_0 + \delta \dot{x}_0, \dot{y}_0 + \delta \dot{y}_0, \dot{z}_0 + \delta \dot{z}_0\right) = y_0 + \delta y_0, \tag{3.101}$$

$$\dot{x} = T\left(x_0 + \delta x_0, y_0 + \delta y_0, \dot{x}_0 + \delta \dot{x}_0, \dot{y}_0 + \delta \dot{y}_0, \dot{z}_0 + \delta \dot{z}_0\right) = \dot{x}_0 + \delta \dot{x}_0, \tag{3.102}$$

$$\dot{y} = V\left(x_0 + \delta x_0, y_0 + \delta y_0, \dot{x}_0 + \delta \dot{x}_0, \dot{y}_0 + \delta \dot{y}_0, \dot{z}_0 + \delta \dot{z}_0\right) = \dot{y}_0 + \delta \dot{y}_0. \tag{3.103}$$

A Taylor series expansion about the reference solution to equations (3.100)-(3.103) results in the following variational relationships

$$\begin{Bmatrix} \delta x \\ \delta y \\ \delta \dot{x} \\ \delta \dot{y} \end{Bmatrix} = \begin{bmatrix} \left(\dfrac{\partial Q}{\partial x_0} - 1\right) & \dfrac{\partial Q}{\partial y_0} & \dfrac{\partial Q}{\partial \dot{x}_0} & \dfrac{\partial Q}{\partial \dot{y}_0} & \dfrac{\partial Q}{\partial \dot{z}_0} \\ \dfrac{\partial R}{\partial x_0} & \left(\dfrac{\partial R}{\partial y_0} - 1\right) & \dfrac{\partial R}{\partial \dot{x}_0} & \dfrac{\partial R}{\partial \dot{y}_0} & \dfrac{\partial R}{\partial \dot{z}_0} \\ \dfrac{\partial T}{\partial x_0} & \dfrac{\partial T}{\partial y_0} & \left(\dfrac{\partial T}{\partial \dot{x}_0} - 1\right) & \dfrac{\partial T}{\partial \dot{y}_0} & \dfrac{\partial T}{\partial \dot{z}_0} \\ \dfrac{\partial V}{\partial x_0} & \dfrac{\partial V}{\partial y_0} & \dfrac{\partial V}{\partial \dot{x}_0} & \left(\dfrac{\partial V}{\partial \dot{y}_0} - 1\right) & \dfrac{\partial V}{\partial \dot{z}_0} \end{bmatrix} \begin{Bmatrix} \delta x_0 \\ \delta y_0 \\ \delta \dot{x}_0 \\ \delta \dot{y}_0 \\ \delta \dot{z}_0 \end{Bmatrix}. \tag{3.104}$$

In order to obtain the partials in equation (3.104), let **P** be defined as

$$\mathbf{P} = \begin{bmatrix} \dfrac{\partial Q}{\partial x_0} & \dfrac{\partial Q}{\partial x_0} & \dfrac{\partial Q}{\partial \dot{x}_0} & \dfrac{\partial Q}{\partial \dot{y}_0} & \dfrac{\partial Q}{\partial \dot{z}_0} \\ \dfrac{\partial R}{\partial x_0} & \dfrac{\partial R}{\partial x_0} & \dfrac{\partial R}{\partial \dot{x}_0} & \dfrac{\partial R}{\partial \dot{y}_0} & \dfrac{\partial R}{\partial \dot{z}_0} \\ \dfrac{\partial T}{\partial x_0} & \dfrac{\partial T}{\partial x_0} & \dfrac{\partial T}{\partial \dot{x}_0} & \dfrac{\partial T}{\partial \dot{y}_0} & \dfrac{\partial T}{\partial \dot{z}_0} \\ \dfrac{\partial V}{\partial x_0} & \dfrac{\partial V}{\partial x_0} & \dfrac{\partial V}{\partial \dot{x}_0} & \dfrac{\partial V}{\partial \dot{y}_0} & \dfrac{\partial V}{\partial \dot{z}_0} \end{bmatrix}, \tag{3.105}$$

such that **P** is computed using equation (2.61) and isolating the appropriate sensitivity partials, i.e.,

$$\mathbf{P}=\begin{bmatrix} \frac{\partial x}{\partial x_0} & \frac{\partial x}{\partial y_0} & \frac{\partial x}{\partial \dot{x}_0} & \frac{\partial x}{\partial \dot{y}_0} & \frac{\partial x}{\partial \dot{z}_0} \\ \frac{\partial y}{\partial x_0} & \frac{\partial y}{\partial y_0} & \frac{\partial y}{\partial \dot{x}_0} & \frac{\partial y}{\partial \dot{y}_0} & \frac{\partial y}{\partial \dot{z}_0} \\ \frac{\partial \dot{x}}{\partial x_0} & \frac{\partial \dot{x}}{\partial y_0} & \frac{\partial \dot{x}}{\partial \dot{x}_0} & \frac{\partial \dot{x}}{\partial \dot{y}_0} & \frac{\partial \dot{x}}{\partial \dot{z}_0} \\ \frac{\partial \dot{y}}{\partial x_0} & \frac{\partial \dot{y}}{\partial y_0} & \frac{\partial \dot{y}}{\partial \dot{x}_0} & \frac{\partial \dot{y}}{\partial \dot{y}_0} & \frac{\partial \dot{y}}{\partial \dot{z}_0} \end{bmatrix} - \frac{1}{\dot{z}}\begin{Bmatrix} \dot{x} \\ \dot{y} \\ \ddot{x} \\ \ddot{y} \end{Bmatrix}\begin{Bmatrix} \frac{\partial z}{\partial x_0} & \frac{\partial z}{\partial y_0} & \frac{\partial z}{\partial \dot{x}_0} & \frac{\partial z}{\partial \dot{y}_0} & \frac{\partial z}{\partial \dot{z}_0} \end{Bmatrix}. \quad (3.106)$$

The solution for the variations $\delta x_0, \delta y_0, \delta \dot{x}_0, \delta \dot{y}_0,$ and $\delta \dot{z}_0$ in equations (3.104) is selected as that with the smallest Euclidean norm. The initial state vector is updated in an iterative process until $\delta x, \delta y, \delta \dot{x}, \delta \dot{y} < \varepsilon,$ thereby obtaining a periodic orbit.

For the predictions $\vec{q}_0^{\,n}$ to uniformly move along the tangent subspace *Γ*, let $\Delta\vec{q}_0^{\,n-1}$ be defined as

$$\Delta\vec{q}_0^{\,n-1} = \left\{\Delta x_0^{n-1} \quad \Delta y_0^{n-1} \quad 0 \quad \Delta\dot{x}_0^{n-1} \quad \Delta\dot{y}_0^{n-1} \quad \Delta\dot{z}_0^{n-1}\right\}^T, \quad (3.107)$$

where

$$\begin{Bmatrix} \Delta x_0^{n-1} \\ \Delta y_0^{n-1} \\ \Delta\dot{x}_0^{n-1} \\ \Delta\dot{y}_0^{n-1} \end{Bmatrix} = \left[\mathbf{P}\right]\begin{Bmatrix} \Delta x_0^{n-1} \\ \Delta y_0^{n-1} \\ \Delta\dot{x}_0^{n-1} \\ \Delta\dot{y}_0^{n-1} \\ \Delta\dot{z}_0^{n-1} \end{Bmatrix}. \quad (3.108)$$

Of course,

$$1 = \left(\Delta x_0^{n-1}\right)^2 + \left(\Delta y_0^{n-1}\right)^2 + \left(\Delta\dot{x}_0^{n-1}\right)^2 + \left(\Delta\dot{y}_0^{n-1}\right)^2 + \left(\Delta\dot{z}_0^{n-1}\right)^2, \quad (3.109)$$

must also be satisfied. Solving equations (3.108) and (3.109) simultaneously produces the components of $\Delta\vec{q}_0^{\,n-1}$. The sign of *S* is switched when the following conditions are all satisfied,

$$\Delta x_0^{n-2} \cdot \Delta x_0^{n-1} < 0, \quad (3.110)$$

$$\Delta y_0^{n-2} \cdot \Delta y_0^{n-1} < 0, \quad (3.111)$$

$$\Delta\dot{x}_0^{n-2} \cdot \Delta\dot{x}_0^{n-1} < 0, \quad (3.112)$$

$$\Delta\dot{y}_0^{n-2} \cdot \Delta\dot{y}_0^{n-1} < 0. \tag{3.113}$$

The process is repeated until the family of orbits is obtained.

3.4.2 Numerical Results: L_4/L_5 Planar, Axial, and Vertical Families of Orbits

The strategies and the corresponding algorithms from Section 3.4.1 are used to compute asymmetric periodic orbits in the vicinity of the triangular points in the Earth-Moon system. The orbit families with their bifurcating orbits are computed using a method of bisections and appear in Figures 3.19-3.21. The initial conditions, periods, and stability indices are provided in Tables 3.14-3.16. The largest amplitude L_3 Lyapunov orbit from Figure 3.7 corresponds to a bifurcation orbit intersecting the L_4/L_5 planar orbit family. The L_4 planar orbit family, as depicted in Figure 3.19, is computed using the reference $y = y_0 = \frac{\sqrt{3}}{2}$. The reference is selected such that all orbits in the family cross the reference. (See Table 3.14 for corresponding initial conditions, periods, and stability indices.) Furthermore, the bifurcation associated with the near-rectilinear L_1 halo orbits is a basis for computing the northern L_4 axial orbit family. (Recall Figure 3.9.) The reference $z = z_0 = 0.1$ is selected such that it is common to all orbits in the family but, also, not significantly close to the Moon. The northern L_4 axial orbit family is represented in Figure 3.20 with corresponding parameters presented in Table 3.15. The southern orbit family is determined by reflecting the northern orbit family across the *x-y* plane. The L_4 axial orbit families terminate with an L_4 vertical orbit. This orbit, with reference $y = y_0 = 0.42545$, is a basis to compute the L_4 vertical orbit family. (See Figures 3.21 and Table 3.16.) Then, the corresponding L_5 vertical and axial orbit families can be obtained by reflecting the L_4 orbit families across the *x-z* plane. Thus, a mapping between periodic orbits near L_1 to orbits in the vicinity of L_3 is available via the L_4/L_5 axial and vertical orbit families.

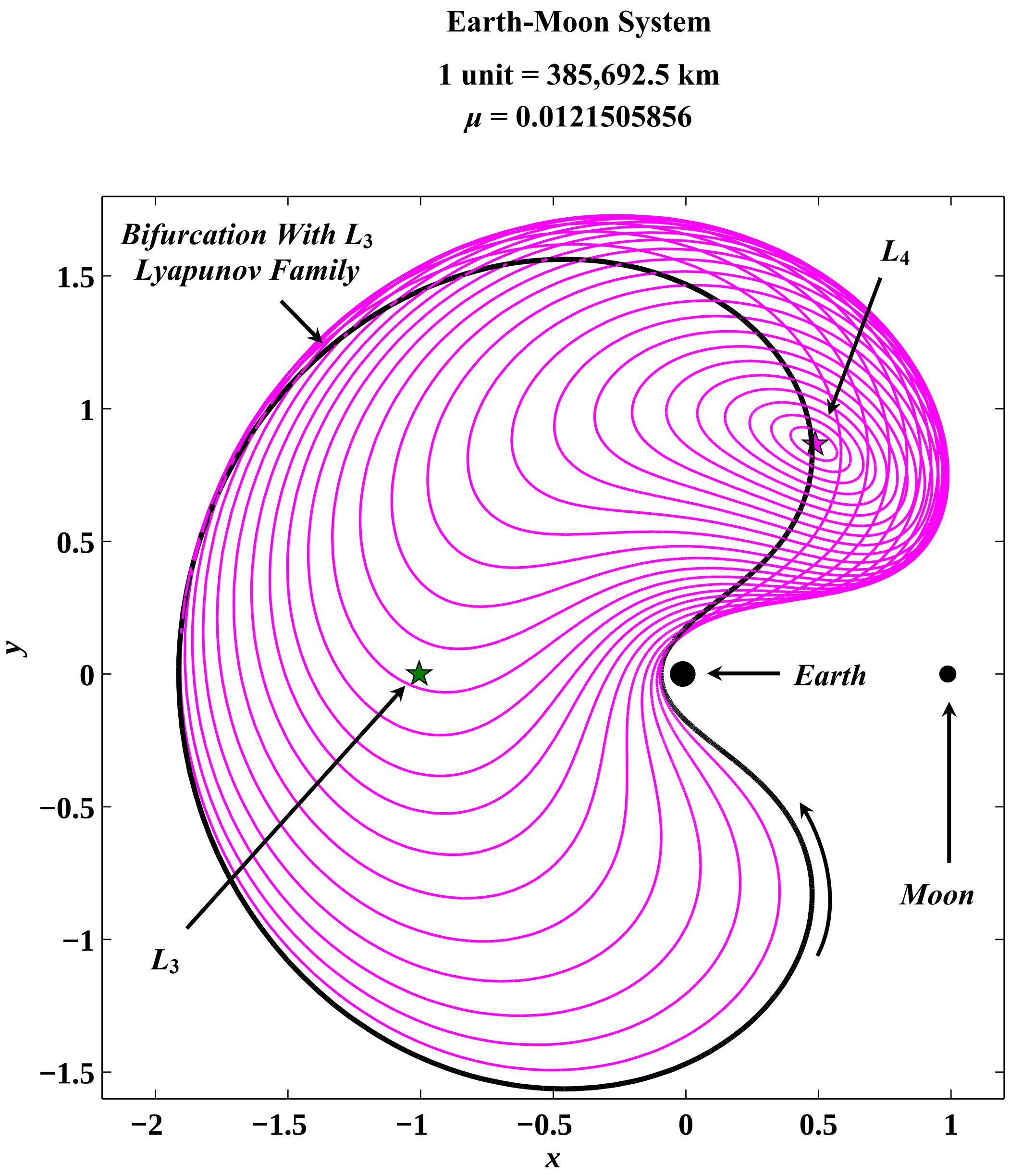

Figure 3.19 The L_4 Planar Family

Table 3.14

L_4 Planar Family Initial Conditions with $y_0 = \frac{\sqrt{3}}{2}$

x_0	$\dot{x}_0$	$\dot{y}_0$	T	υ	
0.4750	0.0697	-1.0915	6.2647	1.0000	L_3 Lyapunovs
0.5837	0.0606	-1.0896	6.2657	1.0000	
0.6853	0.0637	-1.0828	6.2691	1.0000	
0.7656	0.0726	-1.0703	6.2747	1.0000	
0.8312	0.0839	-1.0509	6.2829	1.0000	
0.8826	0.0959	-1.0245	6.2937	1.0000	
0.9203	0.1077	-0.9931	6.3064	1.0000	
0.9459	0.1183	-0.9595	6.3201	1.0000	
0.9621	0.1277	-0.9261	6.3338	1.0000	
0.9717	0.1356	-0.8943	6.3470	1.0000	
0.9775	0.1438	-0.8581	6.3621	1.0000	
0.9788	0.1518	-0.8174	6.3791	1.0000	
0.9753	0.1594	-0.7724	6.3977	1.0000	
0.9665	0.1661	-0.7229	6.4178	1.0000	
0.9520	0.1715	-0.6689	6.4391	1.0000	
0.9314	0.1748	-0.6102	6.4612	1.0000	
0.9043	0.1754	-0.5467	6.4836	1.0000	
0.8736	0.1728	-0.4850	6.5035	1.0000	
0.8401	0.1669	-0.4249	6.5210	1.0000	
0.8043	0.1579	-0.3667	6.5361	1.0000	
0.7667	0.1457	-0.3104	6.5488	1.0000	
0.7274	0.1306	-0.2562	6.5592	1.0000	
0.6867	0.1126	-0.2040	6.5675	1.0000	
0.6447	0.0918	-0.1542	6.5738	1.0000	
0.6015	0.0685	-0.1069	6.5783	1.0000	
0.5572	0.0428	-0.0622	6.5812	1.0000	

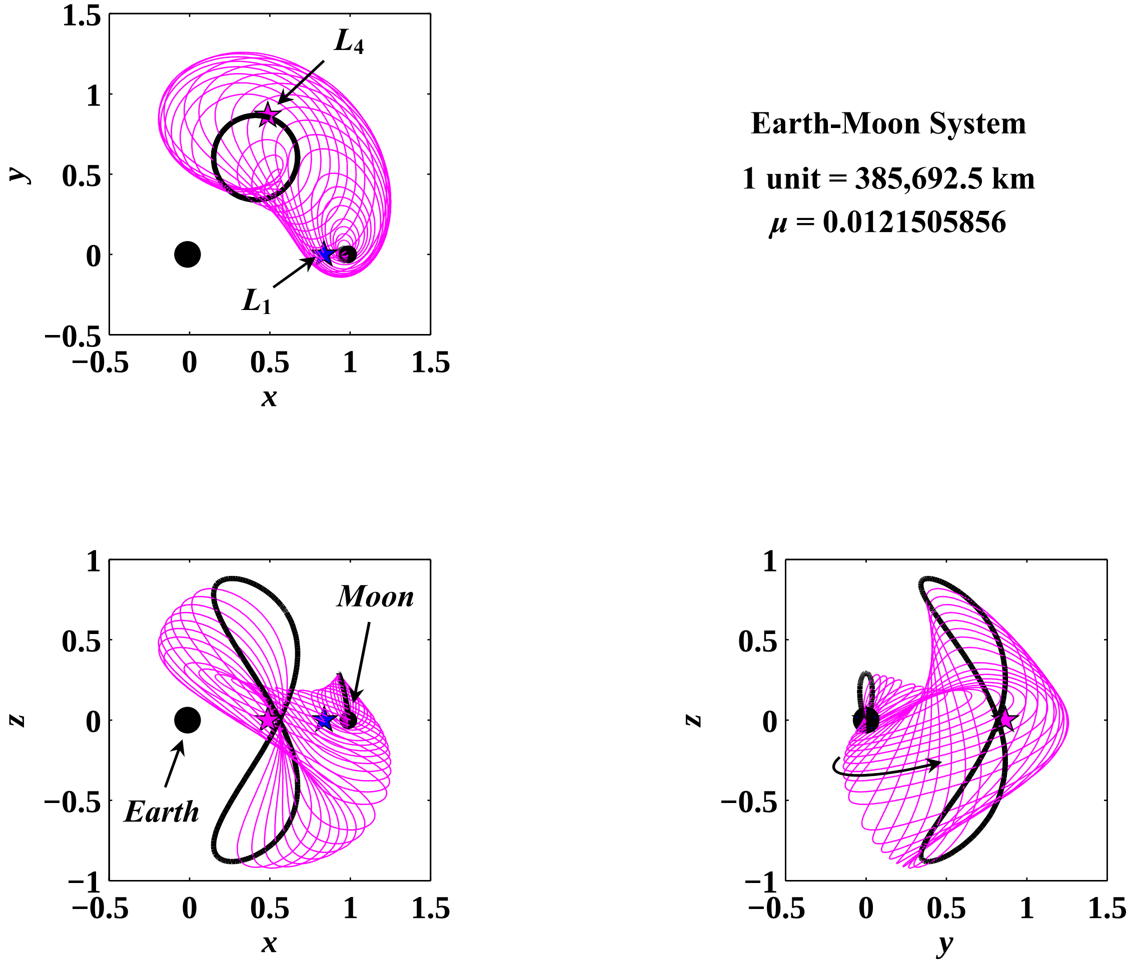

Earth-Moon System

1 unit = 385,692.5 km

μ = 0.0121505856

Figure 3.20 The Northern L_4 Axial Family

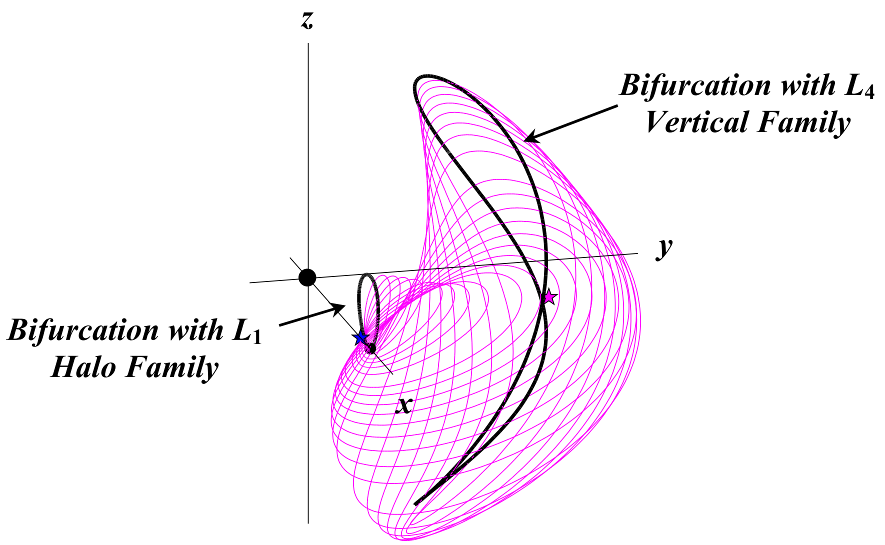

Table 3.15

Northern L_4 Axial Family Initial Conditions with $z_0 = 0.1$

x_0	y_0	$\dot{x}_0$	$\dot{y}_0$	$\dot{z}_0$	T	υ	
0.9767	-0.0334	-0.0737	-0.0626	0.4671	2.1509	1.0000	L_1 Halos
0.9522	-0.0146	-0.1089	0.0426	0.4599	2.1684	1.2665	
0.9353	-0.0019	-0.1254	0.1104	0.4375	2.2359	1.4014	
0.9167	0.0122	-0.1328	0.1753	0.4026	2.3433	1.9466	
0.8958	0.0292	-0.1297	0.2354	0.3601	2.4992	2.7963	
0.8580	0.0661	-0.1077	0.3173	0.2917	2.8625	4.3600	
0.8342	0.0949	-0.0924	0.3566	0.2589	3.1374	5.0376	
0.8067	0.1326	-0.0815	0.3939	0.2321	3.4831	5.3890	
0.7717	0.1819	-0.0838	0.4337	0.2144	3.9253	5.3009	
0.7080	0.2548	-0.1289	0.4969	0.2175	4.6214	4.5915	
0.6695	0.2848	-0.1739	0.5331	0.2351	4.9622	4.1337	
0.6301	0.3060	-0.2311	0.5692	0.2645	5.2632	3.6779	
0.5946	0.3174	-0.2918	0.5997	0.3028	5.4992	3.2707	
0.5620	0.3221	-0.3562	0.6244	0.3522	5.6920	2.8854	
0.5326	0.3217	-0.4220	0.6401	0.4148	5.8483	2.5153	
0.5074	0.3183	-0.4850	0.6421	0.4922	5.9719	2.1603	
0.4874	0.3140	-0.5394	0.6237	0.5849	6.0671	1.8235	
0.4740	0.3117	-0.5768	0.5776	0.6899	6.1379	1.5161	
0.4713	0.3236	-0.5690	0.3981	0.8913	6.2216	1.1156	
0.4848	0.3462	-0.5045	0.2472	0.9807	6.2495	1.0403	
0.5014	0.3731	-0.4279	0.1236	1.0239	6.2641	1.0202	
0.5208	0.4071	-0.3372	0.0078	1.0440	6.2743	1.0113	
0.5409	0.4472	-0.2392	-0.0943	1.0455	6.2816	1.0067	
0.5621	0.4981	-0.1267	-0.1894	1.0313	6.2873	1.0038	
0.5823	0.5617	-0.0005	-0.2722	1.0021	6.2917	1.0019	
0.5982	0.6402	0.1380	-0.3369	0.9591	6.2948	1.0007	
0.6035	0.7821	0.3538	-0.3843	0.8750	6.2966	1.0000	L_4 Verticals

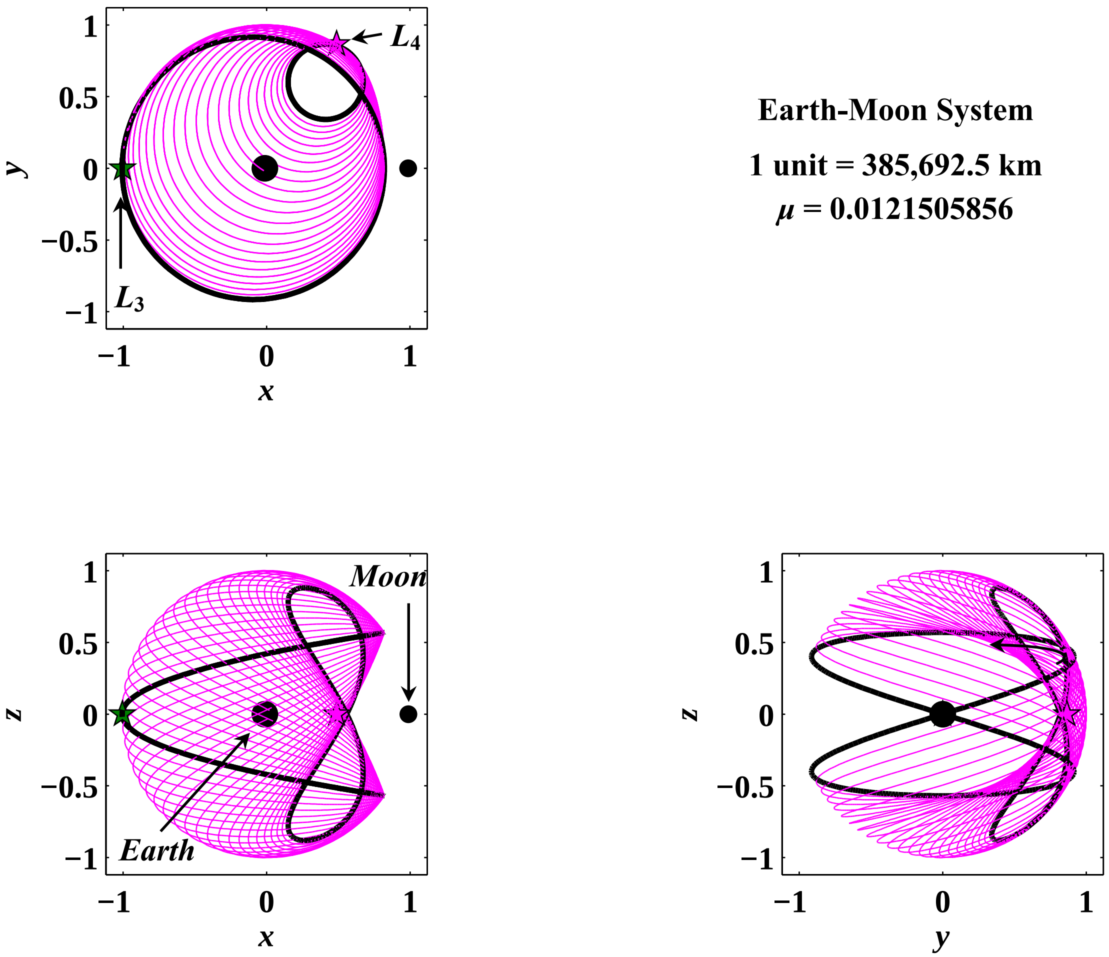

Figure 3.21 The L_4 Vertical Family

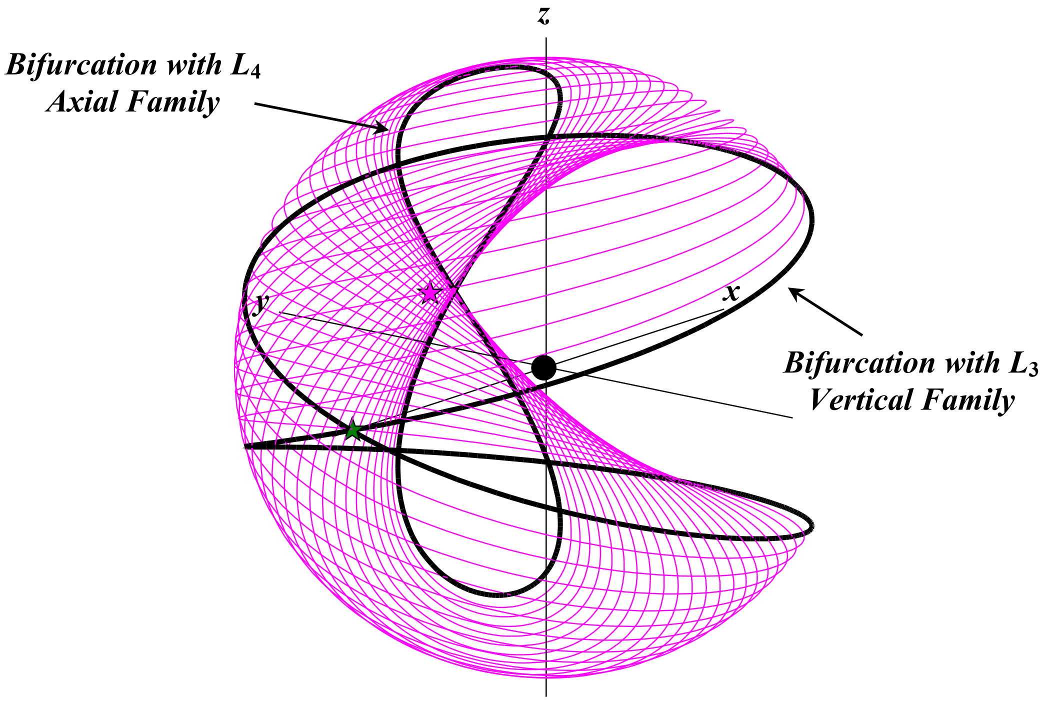

Table 3.16

L_4 Vertical Family Initial Conditions with $y_0 = 0.42545$

x_0	z_0	$\dot{x}_0$	$\dot{y}_0$	$\dot{z}_0$	T	υ	
0.6032	0.6678	-0.3544	-0.3857	0.5728	6.2966	1.0000	L_4 Axials
0.6390	0.6333	-0.3106	-0.4867	0.6482	6.2977	1.0012	
0.6617	0.6093	-0.2749	-0.5583	0.6967	6.2985	1.0020	
0.6825	0.5857	-0.2350	-0.6310	0.7410	6.2995	1.0028	
0.7013	0.5631	-0.1915	-0.7050	0.7803	6.3005	1.0035	
0.7180	0.5416	-0.1444	-0.7806	0.8138	6.3015	1.0040	
0.7325	0.5219	-0.0942	-0.8577	0.8407	6.3025	1.0044	
0.7450	0.5042	-0.0412	-0.9364	0.8600	6.3035	1.0047	
0.7553	0.4889	0.0143	-1.0162	0.8708	6.3045	1.0048	
0.7636	0.4763	0.0718	-1.0966	0.8722	6.3055	1.0048	
0.7700	0.4666	0.1311	-1.1767	0.8636	6.3064	1.0047	
0.7745	0.4598	0.1918	-1.2554	0.8443	6.3072	1.0045	
0.7773	0.4560	0.2537	-1.3314	0.8142	6.3080	1.0042	
0.7782	0.4552	0.3167	-1.4031	0.7731	6.3086	1.0039	
0.7775	0.4573	0.3806	-1.4691	0.7210	6.3092	1.0036	
0.7753	0.4620	0.4411	-1.5237	0.6631	6.3097	1.0032	
0.7718	0.4686	0.4981	-1.5674	0.6015	6.3101	1.0030	
0.7668	0.4773	0.5553	-1.6025	0.5335	6.3104	1.0027	
0.7604	0.4881	0.6127	-1.6278	0.4603	6.3106	1.0025	
0.7525	0.5009	0.6701	-1.6424	0.3832	6.3108	1.0023	
0.7428	0.5156	0.7271	-1.6453	0.3038	6.3110	1.0022	
0.7314	0.5321	0.7836	-1.6361	0.2238	6.3110	1.0021	
0.7167	0.5521	0.8442	-1.6120	0.1380	6.3111	1.0021	L_3 Verticals

3.5 Alternative Methods

Other approaches are also available for generating periodic orbits in the CR3BP. Due to the sensitivity of the problem, some computational methods converge better than others depending on the geometry of the solution. Ultimately, the most useful tool is one that employs an automated procedure to map all solutions of interest. Two alternatives offer different perspectives in approaching the problem of computing periodic orbits in the CR3BP. One approach formulates the search for periodic orbits in terms of an optimization problem. With parameter optimization, specifically Sequential Quadratic Programming (SQP), additional orbits in the L_3 halo family are determined. (See Figure 3.11.) Returning to the two-level corrector, the final convergence method to be implemented involves discretizing the path into a series of patch points and adding constraints in the two-level corrections algorithm to converge to a periodic orbit. For both methods it is not necessary to exploit symmetry. All approaches produce families that are, ultimately, entwined.

3.5.1 Sequential Quadratic Programming: Completing the L_3 Halo Orbit Family

The Sequential Quadratic Programming (SQP) algorithm employed here uses a method posed by Broydon, Fletcher, Shanno, and Goldfarb to approximate the Lagrangian and Hessian [46]. Bounding the problem effectively reduces the design space to within ±0.2 non-dimensional units of the initial guess. This increases the speed of convergence and maintains a directed search that will produce orbits with the desired characteristics. For the collinear halo orbits, a possible form for the initial state vector for integration is,

$$\vec{q}_0 = \{x_0 \quad 0 \quad z_0 \quad 0 \quad \dot{y}_0 \quad 0\}^T, \tag{3.114}$$

where $\vec{q}_0$ corresponds to the apse point along the orbit and perpendicular to the *x*-*z* plane. Then, for the endpoint state $\vec{q}$, the problem is simply formulated as least-squares minimization, i.e.,

$$\min f(\vec{v}) = \|\vec{q} - \vec{q}_0\|^2, \tag{3.115}$$

with design variables $\vec{v}$. If it is desired to fix x_0, the design variables are

$$\vec{v} = \{z_0 \quad \dot{y}_0 \quad \tau\}^T, \tag{3.116}$$

subject to the bounds

$$z_{0_i} - 0.2 \leq z_0 < z_{0_i} + 0.2, \tag{3.117}$$

$$\dot{y}_{0_i} - 0.2 \leq \dot{y}_0 < \dot{y}_{0_i} + 0.2, \tag{3.118}$$

$$\tau_{0_i} - 0.2 \leq \tau_0 < \tau_{0_i} + 0.2, \tag{3.119}$$

where $z_{0_i} = z_0$, $\dot{y}_{0_i} = \dot{y}_0$, and $\tau_{0_i} = \tau_0$ before the minimization of *f*. Similarly, if it is desired to fix z_0, the design variables are

$$\vec{v} = \{x_0 \quad \dot{y}_0 \quad \tau\}^T, \tag{3.120}$$

subject to the bounds

$$x_{0_i} - 0.2 \leq x_0 < x_{0_i} + 0.2, \tag{3.121}$$

$$\dot{y}_{0_i} - 0.2 \leq \dot{y}_0 < \dot{y}_{0_i} + 0.2, \tag{3.122}$$

$$\tau_{0_i} - 0.2 \leq \tau_0 < \tau_{0_i} + 0.2, \tag{3.123}$$

where $x_{0_i} = x_0$, $\dot{y}_{0_i} = \dot{y}_0$, and $\tau_{0_i} = \tau_0$ before the minimization of *f*. Notice that the formulation of equation (3.115) does not necessarily converge to a perpendicular crossing. If it is desired to achieve a perpendicular crossing at the endpoint, equation (3.115) is simply redefined to be

$$\min f(\vec{v}) = (x - x_0)^2 + (z - z_0)^2 + (\dot{y} - \dot{y}_0)^2. \tag{3.124}$$

If either equation (3.115) or (3.124) is used for the minimization, predictions for the next orbit along the family are detailed in Section 3.2.1, for motion perpendicular to the *x-y* plane.

The entire process is also easily adapted to obtain asymmetric periodic solutions. However, improvements to be made to the current design are recommended. For example, the current design uses numerical gradients to approximate the Lagrangian and Hessian. Modifying the process to include analytical gradients greatly increases the speed of convergence. Furthermore, better predictions for neighboring periodic solutions while expanding the solution space are available by exploiting the tangent *Γ* space along the family as presented in section 3.4.1. However, even without such modifications, the algorithm successfully determines periodic solutions and steps along x_0 or z_0 to produce an entire family of orbits. In fact, the L_3 halo family in the Earth-Moon system is further expanded using SQP in regions where the previous targeter scheme failed to converge. (See Table 3.17 and corresponding orbits in orange.) Another way to compute these orbits is to employ regularization [19].

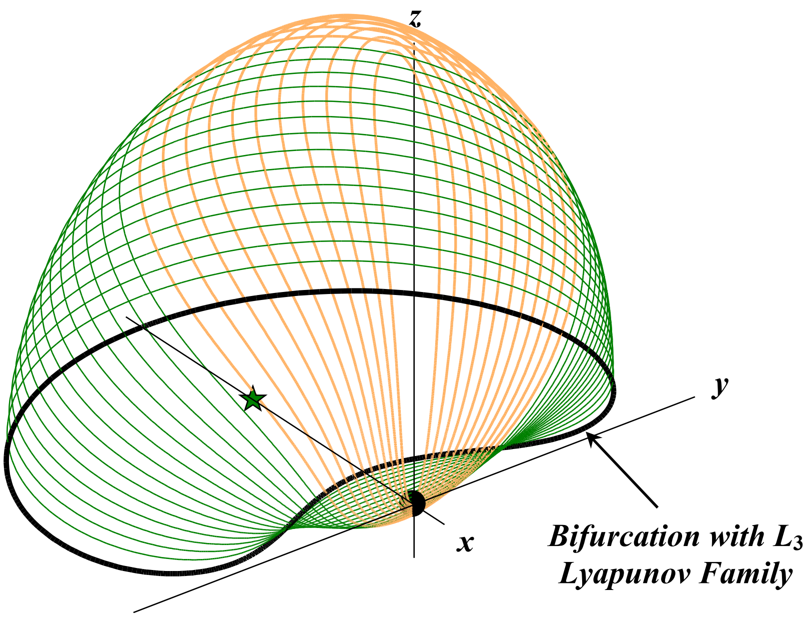

Table 3.17

Northern L_3 Halo Family Initial Conditions Using SQP (Orange)

x_0	z_0	$\dot{y}_0$	T	υ
-1.1131	1.4708	0.8376	6.2224	1.2129
-1.0145	1.5658	0.7636	6.2173	1.1941
-0.9195	1.6449	0.6923	6.2114	1.1776
-0.8245	1.7130	0.6208	6.2042	1.1618
-0.7295	1.7713	0.5491	6.1952	1.1461
-0.6345	1.8204	0.4772	6.1838	1.1297
-0.5395	1.8606	0.4051	6.1686	1.1119
-0.4445	1.8920	0.3329	6.1472	1.0921
-0.3495	1.9138	0.2607	6.1148	1.0688
-0.2545	1.9237	0.1887	6.0590	1.0385
-0.1595	1.9131	0.1169	5.9394	1.0000

3.5.2 Two-Level Corrections with Constraints: Completing the L_4 Vertical Orbit Family

The second level of the two-level differential corrector is easily adapted to accommodate constraints [25]. Periodicity can be modeled as a special type of constraint. This is accomplished by the addition of requirements on the patch points. To enforce periodicity, it is necessary to ensure that the patch point associated with the first state is exactly the same as the patch point, i.e., the elements of the state vector, associated with the last state. The convergence process is completely independent of any symmetries associated with the solutions, and therefore asymmetric periodic solutions can also be determined. Isolating a specific patch point in the orbit and constraining the point to be an extremum enables a method of continuation to expand the solution space and compute the family of orbits.

The periodicity constraint. For a periodic solution, in addition to minimizing the $\Delta\vec{V}$'s at the internal patch points (recall Figure 3.1), it is also necessary to minimize the values

$$\Delta\vec{R}_{1,n} = \vec{R}_1 - \vec{R}_n, \tag{3.125}$$

$$\Delta\vec{V}_{1,n} = \vec{V}_1 - \vec{V}_n, \tag{3.126}$$

where $\Delta\vec{R}_{1,n}$ and $\Delta\vec{V}_{1,n}$ are the discontinuities in position and velocity, respectively, between the first and last point, i.e., the n^{th} point. (See Figure 3.22.) Therefore, it is necessary to determine the variations in $\delta\vec{R}_i$ and $\delta\tau_i$ that also minimize the endpoint discontinuities. The endpoint discontinuities in position depend only on the first and n^{th} points. Therefore, using equation (3.125), the partial of $\Delta\vec{R}_{1,n}$ with respect to position and time can be evaluated as follows,

$$\frac{\partial\Delta\vec{R}_{1,n}}{\partial\vec{R}_n} = -\mathbf{I}_{3\times3}, \tag{3.127}$$

$$\frac{\partial\Delta\vec{R}_{1,n}}{\partial\tau_n} = \vec{0}_{3\times1}, \tag{3.128}$$

$$\frac{\partial \Delta \vec{R}_{1,n}}{\partial \vec{R}_1} = \mathbf{I}_{3\times 3}, \tag{3.129}$$

$$\frac{\partial \Delta \vec{R}_{1,n}}{\partial \tau_1} = \vec{0}_{3\times 1}. \tag{3.130}$$

However, the velocity discontinuity also depends on the outgoing state associated with the $n^{th} - 1$ patch point and the incoming state associated with the second patch point. Therefore, via equation (3.126) the partials of $\Delta \vec{V}_{1,n}$ with respect to position and time are computed from the following relationships,

$$\frac{\partial \Delta \vec{V}_{1,n}}{\partial \vec{R}_{n-1}} = \frac{\partial \Delta \vec{V}_{1,n}}{\partial \vec{V}_n^-}\frac{\partial \vec{V}_n^-}{\partial \vec{R}_{n-1}} = -\frac{\partial \vec{V}_n^-}{\partial \vec{R}_{n-1}}, \tag{3.131}$$

$$\frac{\partial \Delta \vec{V}_{1,n}}{\partial \tau_{n-1}} = \frac{\partial \Delta \vec{V}_{1,n}}{\partial \vec{V}_n^-}\frac{\partial \vec{V}_n^-}{\partial \tau_{n-1}} = -\frac{\partial \vec{V}_n^-}{\partial \tau_{n-1}}, \tag{3.132}$$

$$\frac{\partial \Delta \vec{V}_{1,n}}{\partial \vec{R}_n} = \frac{\partial \Delta \vec{V}_{1,n}}{\partial \vec{V}_n^-}\frac{\partial \vec{V}_n^-}{\partial \vec{R}_n} = -\frac{\partial \vec{V}_n^-}{\partial \vec{R}_n}, \tag{3.133}$$

$$\frac{\partial \Delta \vec{V}_{1,n}}{\partial \tau_n} = \frac{\partial \Delta \vec{V}_{1,n}}{\partial \vec{V}_n^-}\frac{\partial \vec{V}_i^-}{\partial \tau_n} = -\frac{\partial \vec{V}_n^-}{\partial \tau_n}, \tag{3.134}$$

$$\frac{\partial \Delta \vec{V}_{1,n}}{\partial \vec{R}_1} = \frac{\partial \Delta \vec{V}_{1,n}}{\partial \vec{V}_1^+}\frac{\partial \vec{V}_1^+}{\partial \vec{R}_1} = \frac{\partial \vec{V}_1^+}{\partial \vec{R}_1}, \tag{3.135}$$

$$\frac{\partial \Delta \vec{V}_{1,n}}{\partial \tau_1} = \frac{\partial \Delta \vec{V}_{1,n}}{\partial \vec{V}_1^+}\frac{\partial \vec{V}_1^+}{\partial \tau_1} = \frac{\partial \vec{V}_1^+}{\partial \tau_1}, \tag{3.136}$$

$$\frac{\partial \Delta \vec{V}_{1,n}}{\partial \vec{R}_2} = \frac{\partial \Delta \vec{V}_{1,n}}{\partial \vec{V}_1^+}\frac{\partial \vec{V}_1^+}{\partial \vec{R}_2} = \frac{\partial \vec{V}_1^+}{\partial \vec{R}_2}, \tag{3.137}$$

$$\frac{\partial \Delta \vec{V}_{1,n}}{\partial \tau_2} = \frac{\partial \Delta \vec{V}_{1,n}}{\partial \vec{V}_1^+}\frac{\partial \vec{V}_1^+}{\partial \tau_2} = \frac{\partial \vec{V}_1^+}{\partial \tau_2}, \tag{3.138}$$

where the partials of $\vec{V}_n^-$ and $\vec{V}_1^+$ with respect to the $n^{th} - 1$, n^{th}, 1^{st}, and 2^{nd} point positions and times are available from equations (3.13)-(3.20). Therefore, the new targeter that incorporates periodicity constraints takes the form

$$\left\{\begin{array}{c} \delta\Delta\vec{V}_2 \\ \delta\Delta\vec{V}_3 \\ \vdots \\ \delta\Delta\vec{V}_{n-2} \\ \delta\Delta\vec{V}_{n-1} \\ \hdashline \delta\Delta\vec{R}_{1,n} \\ \delta\Delta\vec{V}_{1,n} \end{array}\right\} = \left[\mathbf{M}^*\right]\left\{\begin{array}{c} \delta\vec{R}_1 \\ \delta\tau_1 \\ \delta\vec{R}_2 \\ \delta\tau_2 \\ \delta\vec{R}_3 \\ \vdots \\ \delta\tau_{n-2} \\ \delta\vec{R}_{n-1} \\ \delta\tau_{n-1} \\ \delta\vec{R}_n \\ \delta\tau_n \end{array}\right\}, \tag{3.139}$$

where

$$\mathbf{M}^* = \left[\begin{array}{ccccccccccc} \multicolumn{11}{c}{\mathbf{M}} \\ \hdashline \mathbf{I}_{3\times3} & \vec{0}_{3\times1} & \mathbf{0}_{3\times3} & \vec{0}_{3\times1} & \mathbf{0}_{3\times3} & \cdots & \vec{0}_{3\times1} & \mathbf{0}_{3\times3} & \vec{0}_{3\times1} & -\mathbf{I}_{3\times3} & \vec{0}_{3\times1} \\ \dfrac{\partial\vec{V}_1^+}{\partial\vec{R}_1} & \dfrac{\partial\vec{V}_1^+}{\partial\tau_1} & \dfrac{\partial\vec{V}_1^+}{\partial\vec{R}_2} & \dfrac{\partial\vec{V}_1^+}{\partial\tau_2} & \mathbf{0}_{3\times3} & \cdots & \vec{0}_{3\times1} & -\dfrac{\partial\vec{V}_n^-}{\partial\vec{R}_{n-1}} & -\dfrac{\partial\vec{V}_n^-}{\partial\tau_{n-1}} & -\dfrac{\partial\vec{V}_n^-}{\partial\vec{R}_n} & -\dfrac{\partial\vec{V}_n^-}{\partial\tau_n} \end{array}\right], \tag{3.140}$$

with **M** evaluated from the expressions in equation (3.22). Notice that the form of equation (3.140) requires at least four patch points be specified. Use the smallest Euclidian norm of **M** as the solution to equation (3.139) for the variations in position and time. Subtract these variations from the existing patch point positions and times to update the patch point states to reduce the internal $\Delta\vec{V}$'s and endpoint discontinuities in the next iteration. The process is continued until $\left\|\Delta\vec{V}_i\right\|, \left\|\Delta\vec{R}_{1,n}\right\|, \left\|\Delta\vec{V}_{1,n}\right\| < \varepsilon,$ thereby obtaining a periodic solution. (See Figure 3.22.)

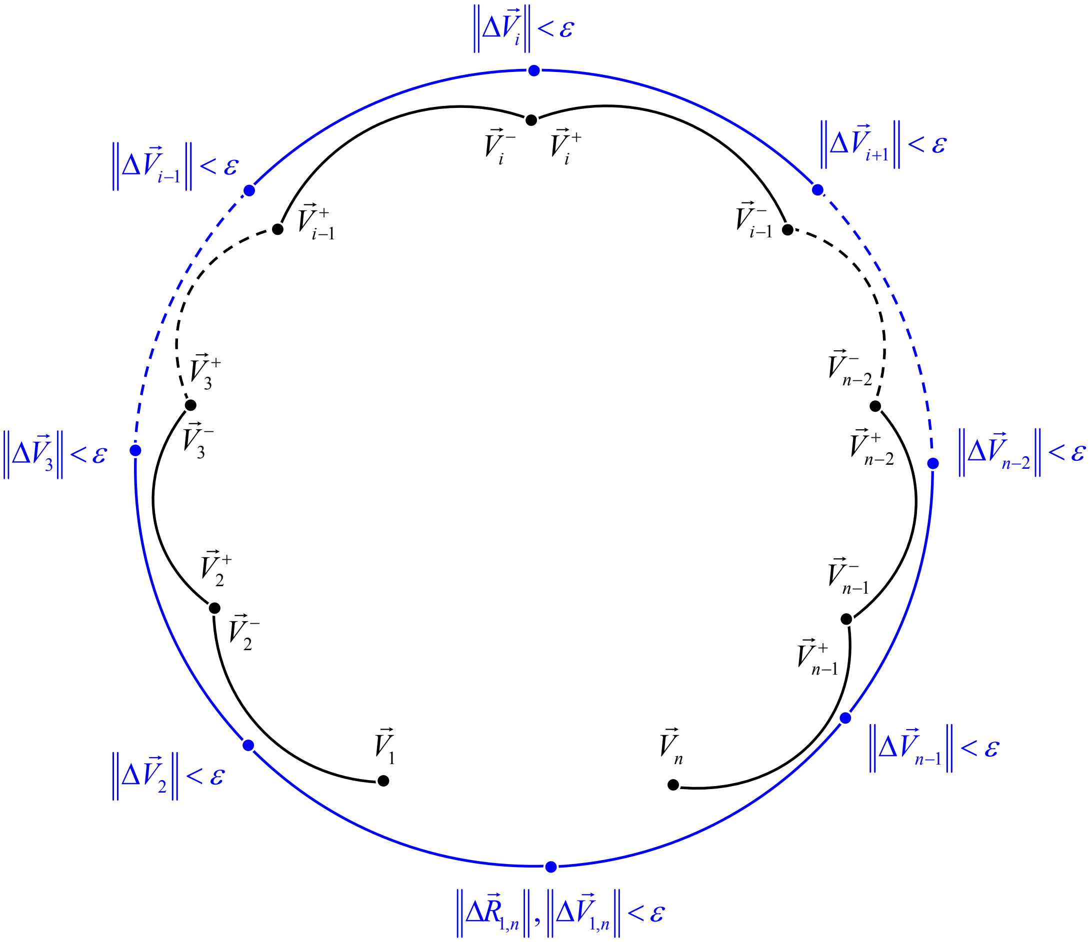

Figure 3.22 Path Before Second Level is Applied (Black)
and Final Periodic Solution (Blue)

Extrema constraints for continuation. To obtain a neighboring solution, it is necessary to control the extrema points of the converged solution. For example, a patch point to be associated with a neighboring solution can be predicted or estimated by fixing the step size Δz_0 and applying equations (3.28) and (3.46) to a point along the current solution. However, unless additional constraints are added, the corrections procedure will simply return to the same known periodic solution. Constraints are added to ensure that the patch point is associated with $z_{\max}$ and that variations $\delta z_{\max}$ are not applied during the new convergence process.

In general, adding constraints will eventually produce an over-constrained problem. However, this problem is easily avoided by specifying additional patch points along the path as well, thereby increasing the number of degrees of freedom. However, for only four patch points, there exist sixteen degrees of freedom. Reducing the $\Delta\vec{V}$'s associated with the internal state requires three equations of constraint. Adding the periodicity constraint and the extremum constraint with $\delta z_{\max} = 0$ implies eleven total equations of constraint. Since there are still more degrees of freedom than constraints, the problem possesses a solution.

Furthermore, since there are already six equations of constraint directly associated with first and last patch points, additional patch points are carefully selected when applying the extremum constraint. Therefore, to constrain the second patch point such that $z_0 = z_{\max}$, a constraint is also required to force $\dot{z}_0 = 0$. Since the incoming velocity associated with the second patch point is already being used to constrain periodicity, the outgoing velocity is employed to aid in satisfying the constraint $\dot{z}_0 = 0$. Notice that equations (3.17)-(3.20) can be rewritten for the second patch point in the form

$$\frac{\partial \vec{V}_2^+}{\partial \vec{R}_2} = \begin{bmatrix} \dfrac{\partial \dot{x}_2^+}{\partial \vec{R}_2} \\ \dfrac{\partial \dot{y}_2^+}{\partial \vec{R}_2} \\ \dfrac{\partial \dot{z}_2^+}{\partial \vec{R}_2} \end{bmatrix}, \quad \frac{\partial \vec{V}_2^+}{\partial \tau_2} = \begin{bmatrix} \dfrac{\partial \dot{x}_2^+}{\partial \tau_2} \\ \dfrac{\partial \dot{y}_2^+}{\partial \tau_2} \\ \dfrac{\partial \dot{z}_2^+}{\partial \tau_2} \end{bmatrix}, \quad \frac{\partial \vec{V}_2^+}{\partial \vec{R}_3} = \begin{bmatrix} \dfrac{\partial \dot{x}_2^+}{\partial \vec{R}_3} \\ \dfrac{\partial \dot{y}_2^+}{\partial \vec{R}_3} \\ \dfrac{\partial \dot{z}_2^+}{\partial \vec{R}_3} \end{bmatrix}, \quad \frac{\partial \vec{V}_2^+}{\partial \tau_3} = \begin{bmatrix} \dfrac{\partial \dot{x}_2^+}{\partial \tau_3} \\ \dfrac{\partial \dot{y}_2^+}{\partial \tau_3} \\ \dfrac{\partial \dot{z}_2^+}{\partial \tau_3} \end{bmatrix}. \quad (3.141)\text{ -}(3.144)$$

Then the targeter for the second level of the corrections process, including the constraint $\dot{z}_0 = 0$ is,

$$\begin{Bmatrix} \delta\Delta\vec{V}_2 \\ \delta\Delta\vec{V}_3 \\ \vdots \\ \delta\Delta\vec{V}_{n-2} \\ \delta\Delta\vec{V}_{n-1} \\ \delta\Delta\vec{R}_{1,n} \\ \delta\Delta\vec{V}_{1,n} \\ \hline \delta\dot{z}_2 \end{Bmatrix} = \left[\mathbf{M}^{**}\right] \begin{Bmatrix} \delta\vec{R}_1 \\ \delta\tau_1 \\ \delta\vec{R}_2 \\ \delta\tau_2 \\ \delta\vec{R}_3 \\ \delta\tau_3 \\ \delta\vec{R}_4 \\ \vdots \\ \delta\tau_n \end{Bmatrix}, \qquad (3.145)$$

for

$$\mathbf{M}^{**} = \left[\begin{array}{ccccccccc} \multicolumn{9}{c}{\mathbf{M}^{*}} \\ \hdashline \mathbf{0}_{3\times3} & \vec{0}_{3\times1} & \dfrac{\partial \dot{z}_2^{+}}{\partial \vec{R}_2} & \dfrac{\partial \dot{z}_2^{+}}{\partial \tau_2} & \dfrac{\partial \dot{z}_2^{+}}{\partial \vec{R}_3} & \dfrac{\partial \dot{z}_2^{+}}{\partial \tau_3} & \mathbf{0}_{3\times3} & \cdots & \vec{0}_{3\times1} \end{array}\right]. \tag{3.146}$$

Notationally, $\dot{z}_2$ is the z component of velocity for the second patch point. Also, the variation δz_2 is defined as zero in equation (3.145). The next solution in the family is determined using a fixed step Δz_0 and equations (3.28) and (3.46) are applied to the second patch point. The process is repeated until a family of solutions is obtained.

This process is used to complete the L_4 vertical orbit family originally seen in Figure 3.21 and Table 3.16. The initial conditions associated with the first orbit are listed in Table 3.16. These were numerically simulated over the period of motion and discretized into five patch points. Convergence is obtained using equation (3.145). The remaining portion of the family is computed using continuation and a fixed step Δz_0 where $\Delta z_0 < 0$. The converged orbits appear in Figure 3.23 and the initial conditions are listed in Table 3.18. Note that the family is determined by stepping through values of z for one patch point where the corresponding velocity $\dot{z}$ is forced to zero. This approach produces favorable results but, in general, is very dependent on the geometry of the solution. Furthermore, for some periodic solutions, a step through other parameters associated with different patch points may be superior. However, the constraints corresponding to the various other parameters must be derived and then applied to the patch point of interest. When considering all possible cases, the problem becomes very complicated, perhaps intractable. Alternatively, the continuation process can be enhanced by simultaneously predicting initial states for *all* the patch points. This is accomplished by shifting along the tangent Γ as discussed in Section 3.4.1. Such a scheme also aids in ‘following’ the solution through unpredictable twisting or curving paths as in the configuration space seen in the L_4 axial orbits.

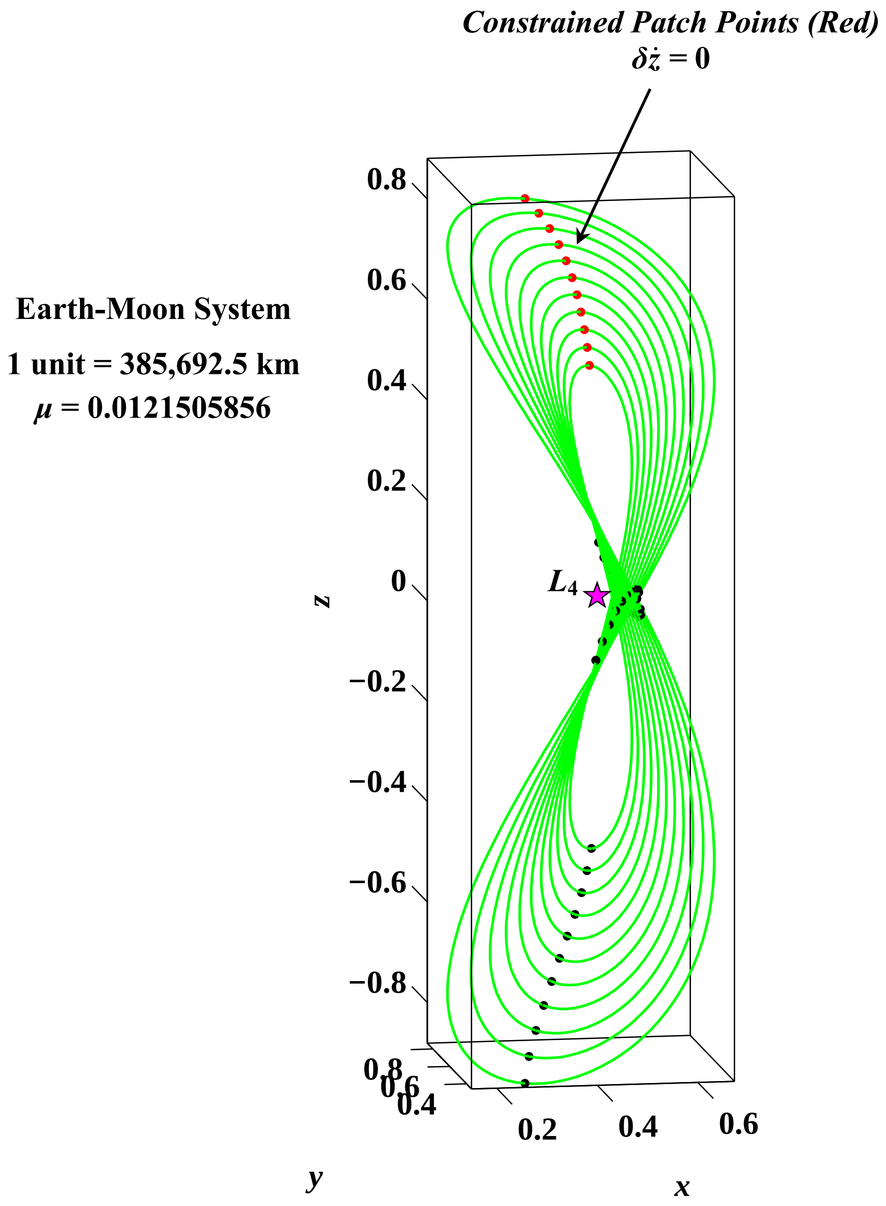

Figure 3.23 The L_4 Vertical Orbits Using a Two-Level Corrector with Constraints

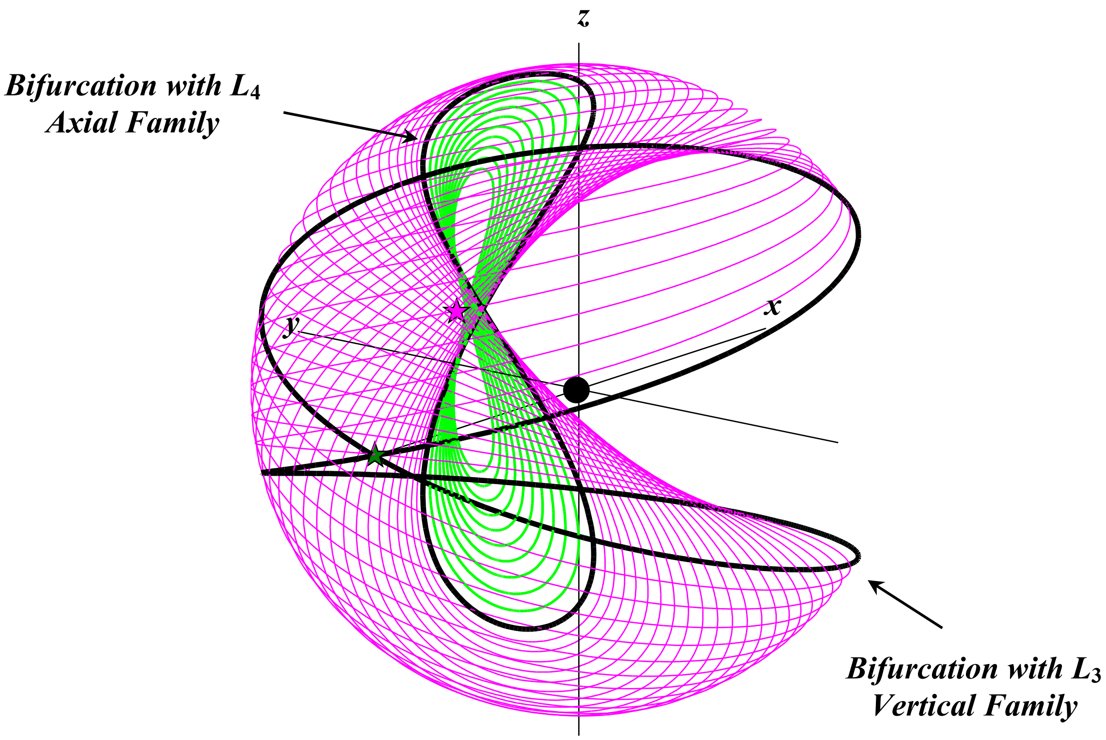

Table 3.18

L_4 Vertical Family Initial Conditions

Using Two-Level Corrector with Constraints (Green)

x_0	y_0	z_0	$\dot{x}_0$	$\dot{y}_0$	T	υ
0.3006	0.4431	0.8411	-0.3762	0.2559	6.2951	1.0000
0.3308	0.4921	0.8011	-0.3299	0.2221	6.2938	1.0000
0.3558	0.5355	0.7611	-0.2897	0.1927	6.2926	1.0000
0.3769	0.5745	0.7211	-0.2542	0.1669	6.2915	1.0000
0.3947	0.6097	0.6811	-0.2224	0.1441	6.2905	1.0000
0.4099	0.6418	0.6411	-0.1939	0.1238	6.2896	1.0000
0.4229	0.6711	0.6011	-0.1680	0.1059	6.2888	1.0000
0.4340	0.6978	0.5611	-0.1446	0.0900	6.2880	1.0000
0.4435	0.7222	0.5211	-0.1234	0.0758	6.2873	1.0000
0.4517	0.7444	0.4811	-0.1042	0.0632	6.2866	1.0000

4. ORBIT SELECTION FOR LUNAR SOUTH POLE COVERAGE AND THE TRANSITION TO A FULL EPHEMERIS MODEL

The various families of orbits and their connections to each other, as described in Chapter 3, can be key components for actual mission design. Many of the orbits computed possess geometries favorable for lunar south pole coverage. For example, spacecraft in L_1 and L_2 southern halo orbits are in direct view of the lunar south pole for nearly their entire period of motion, a favorable characteristic for lunar south pole coverage. Thus, the initial design begins in the CR3BP. The known families of orbits with their computed characteristics form a solid basis for selecting orbits to support lunar south pole coverage. The periods and stability indices associated with the orbits offer valuable information for initial design. Nine different orbits with periods ranging from 7 to 16 days are selected and transferred to a full ephemeris model, including solar perturbations. A preliminary coverage analysis is discussed for potential coverage architectures.

4.1 Orbit Selection for Lunar South Pole Coverage

Specific members of the known families of orbits in the Earth-Moon CR3BP are isolated based on communications instruments and subsurface constraints, bounding the useful range of orbits within a family to those with lunar altitudes between 50 km and 100,000 km. (See Figures 4.1–4.3.) Furthermore, it is useful to redefine the orbits in a Moon centered, rotating frame such that

$$x^m = x - (1-\mu), \tag{4.1}$$

$$y^m = y, \tag{4.2}$$

$$z^m = z, \tag{4.3}$$

where x^m, y^m, and z^m define the position of the spacecraft with respect to the Moon in the rotating frame and $\mu = 0.0121505856,$ the associated mass ratio.

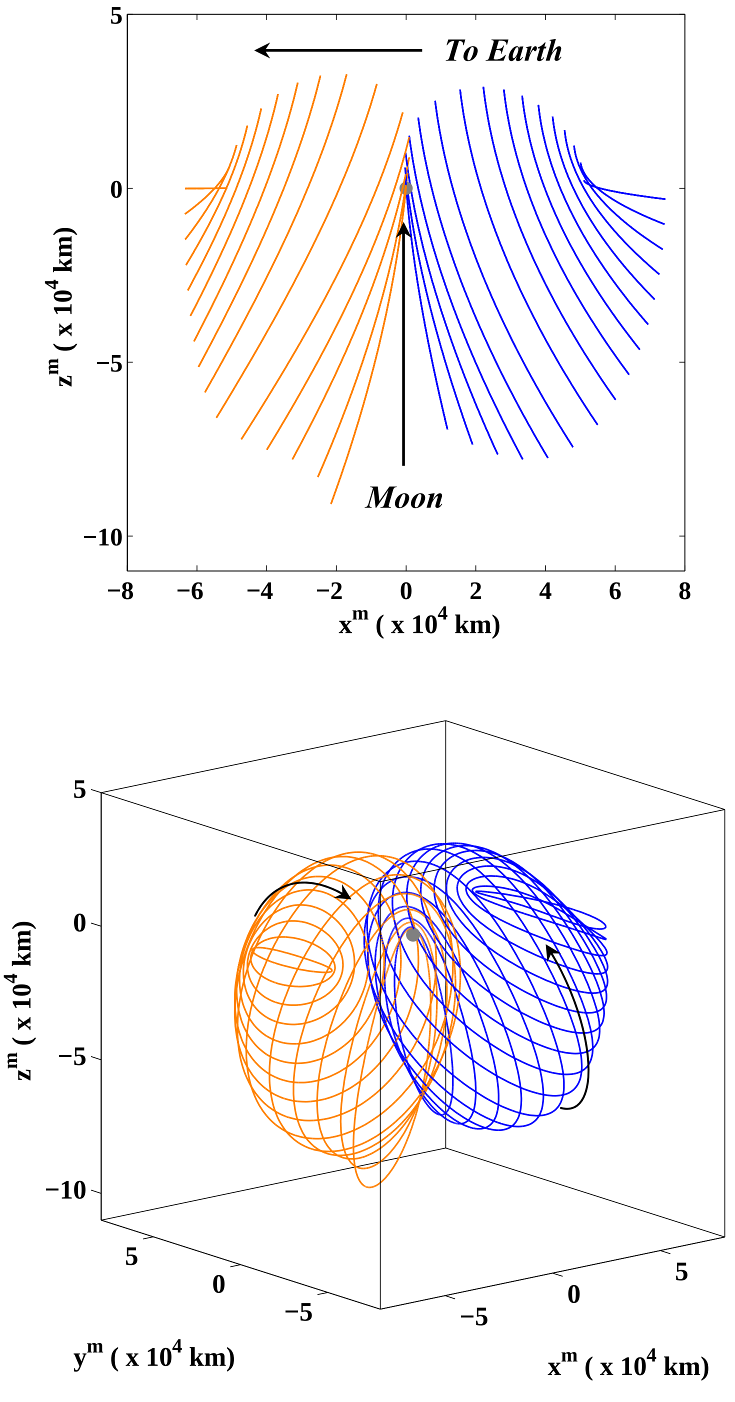

Figure 4.1 Southern Halo Orbit Families:
Earth-Moon L_1 (Orange) and L_2 (Blue).

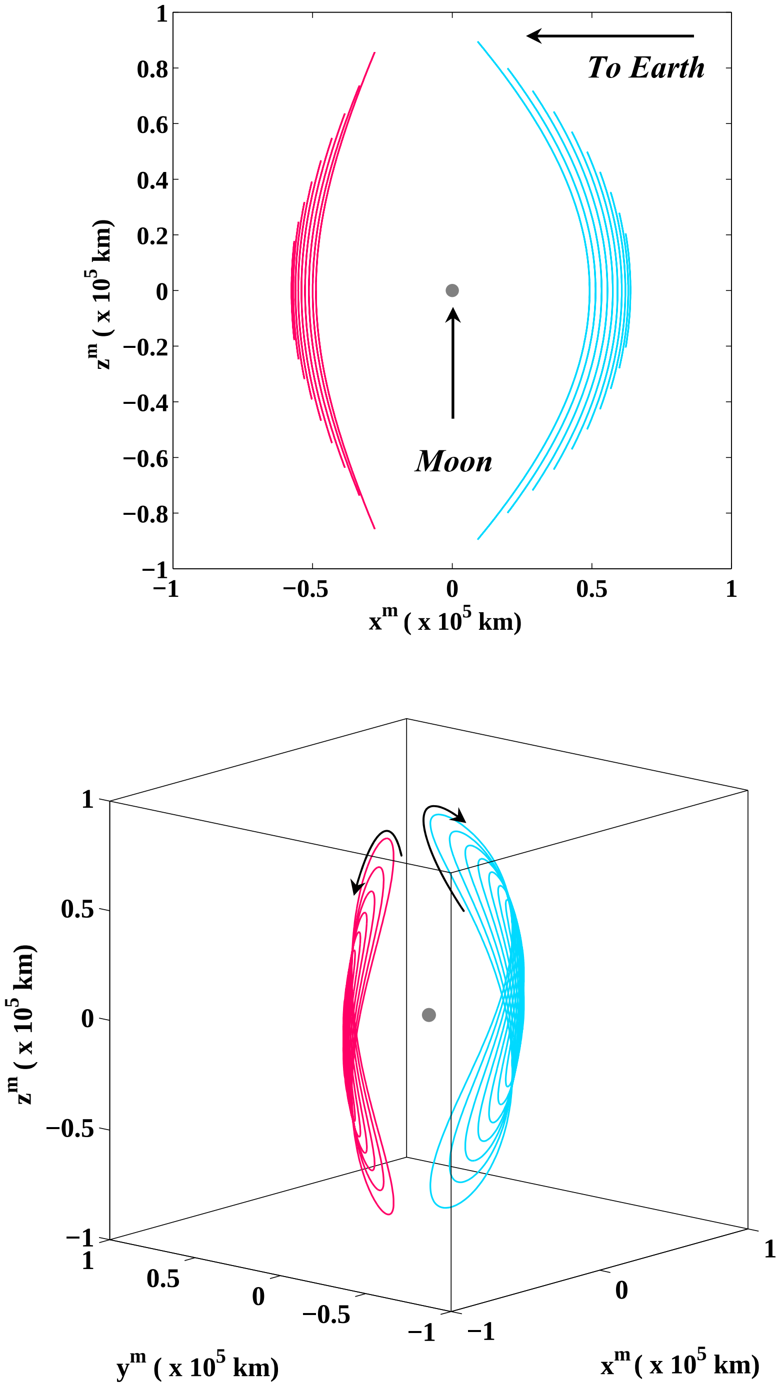

Figure 4.2 Vertical Orbit Families of Interest: Earth-Moon L_1 (Red) and L_2 (Cyan)

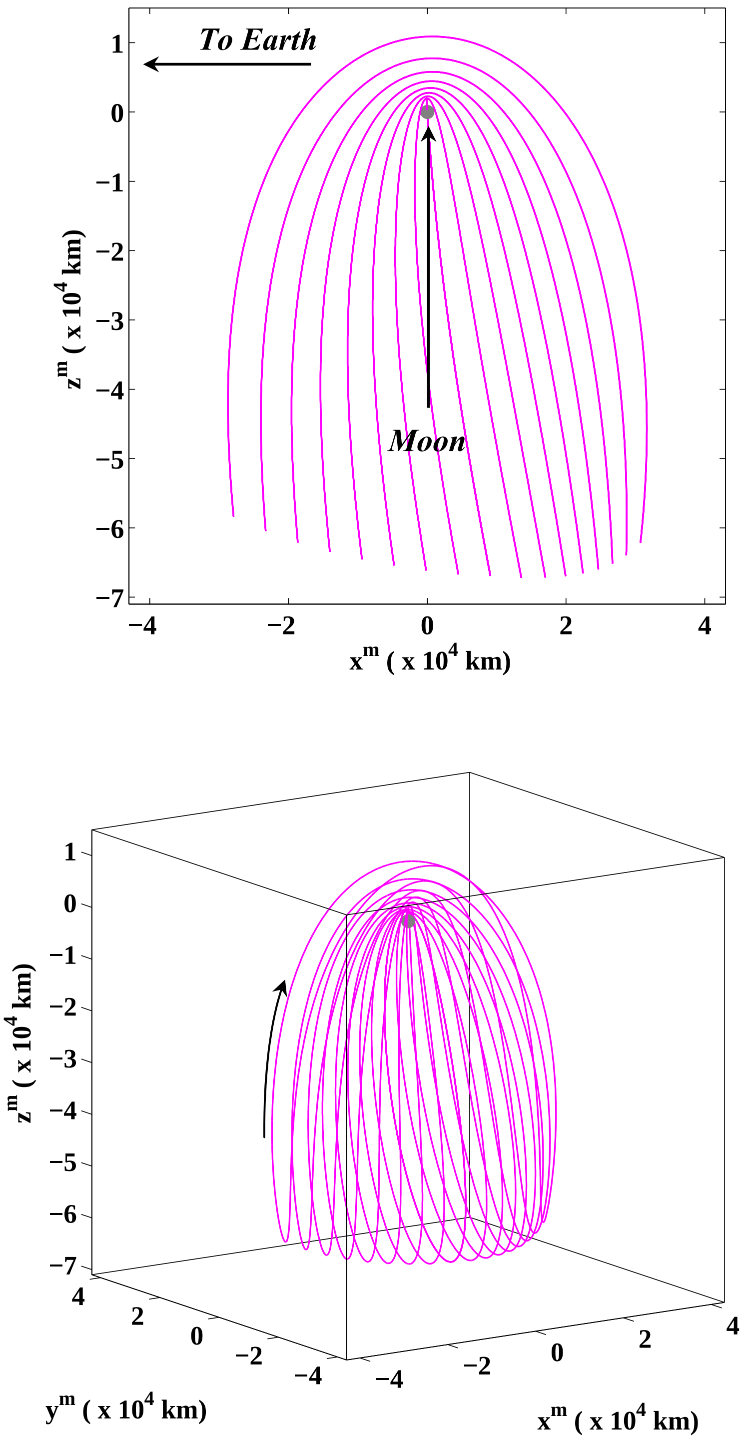

Figure 4.3 Southern L_2 Butterfly Orbit Family

A number of L_1 and L_2 southern halo orbits satisfying the altitude constraints appear in Figure 4.1. The L_1 and L_2 southern halo orbits are particularly effective in this problem since the motion is almost always within line-of-sight to the Earth. Many of the orbits pass very close to the Moon and are near-rectilinear in terms of the out-of-plane motion. The near-rectilinear orbits possess a line-of-sight to the lunar south pole for almost the entire period of the motion. Alternatively, the L_1 and L_2 vertical orbits with altitudes less than 100,000 km are also feasible for coverage of the lunar south pole. (See Figure 4.2.) These orbits bend toward both the north and south poles of the Moon, a favorable characteristic for polar coverage. Finally, the southern butterfly orbits are also effective for lunar south pole coverage. As evidenced in Figure 4.3, the butterfly orbits wrap around both the near and far side of the Moon such that a direct line-of-sight to the lunar south pole exists for nearly the entire orbital period. Of course, complete coverage is only achieved when at least two vehicles are placed in one or more of these orbits.

4.1.1 Period and Stability Index

The time to complete one full period is a useful selection parameter in the initial design phase. Let the maximum excursion distance, as it appears in the example halo orbit in Figure 4.4, be defined as the maximum x^m-distance for each orbit in the Moon centered, rotating frame. Orbital periods are plotted against maximum excursion distance during initial design selection, as indicated in Figure 4.5. Suitable regions for the production of feasible architectures occur when the orbital periods are commensurate. One such region consists of orbits in L_1 and L_2 halo families sharing periods between 7.9 and 12.2 days. An example that exhibits feasible south pole coverage consists of a 12-day L_1 and 12-day L_2 halo orbit combination, illustrated by the black dashed line in Figure 4.5. Another region with commensurate combinations consists of orbits with a ratio of periods that is 2:1, i.e., one period is exactly twice that of the other. An example from this region consists of a 14-day L_2 butterfly orbit and a 7-day L_2 halo orbit combination, as noted by the grey dashed lines in Figure 4.5. The information in Figure 4.5 serves as a basis for the determination of many other commensurate orbit combinations that lead to complete south pole coverage. Furthermore, orbits not investigated here may be added to Figure 4.5 without affecting the analysis.

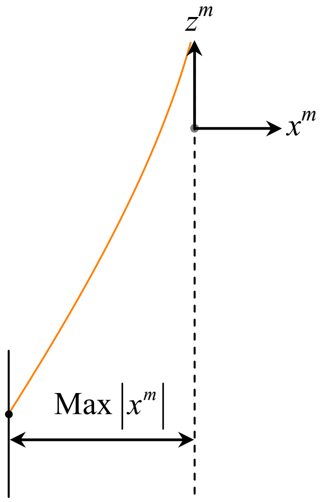

Figure 4.4 Definition of Maximum x^m-Distance

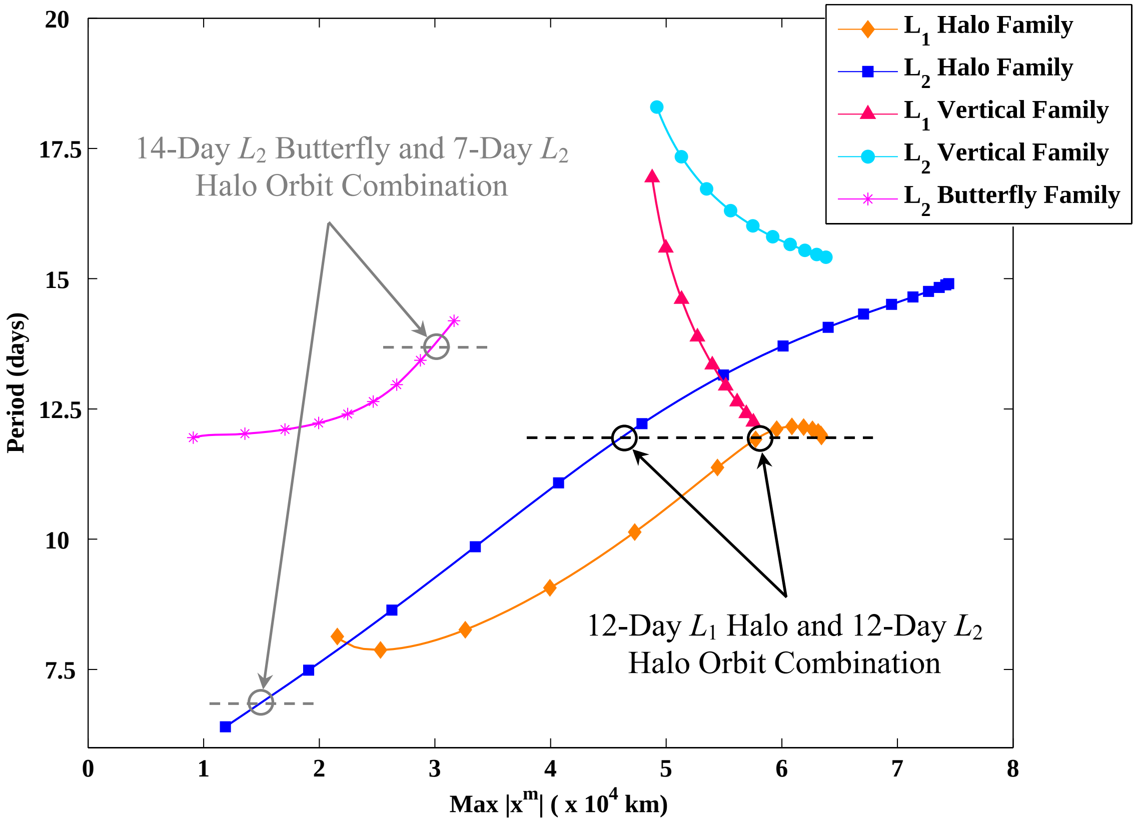

Figure 4.5 Period versus Maximum x^m-Distance from the Moon

Also useful for design purposes is the stability index, υ, as defined in Section 3.2.1. A stability index of one indicates a stable orbit, whereas stability indices greater than one reflect instability. Of course, a large stability index indicates a divergent mode that departs from the vicinity of the orbit very quickly. Generally, the stability index is directly correlated to the station-keeping costs and is inversely related to transfer costs. The stability indices for orbits from the various families appear in Figure 4.6 as functions of maximum excursion distance from the Moon. In general, the stability index increases with distance from the Moon.

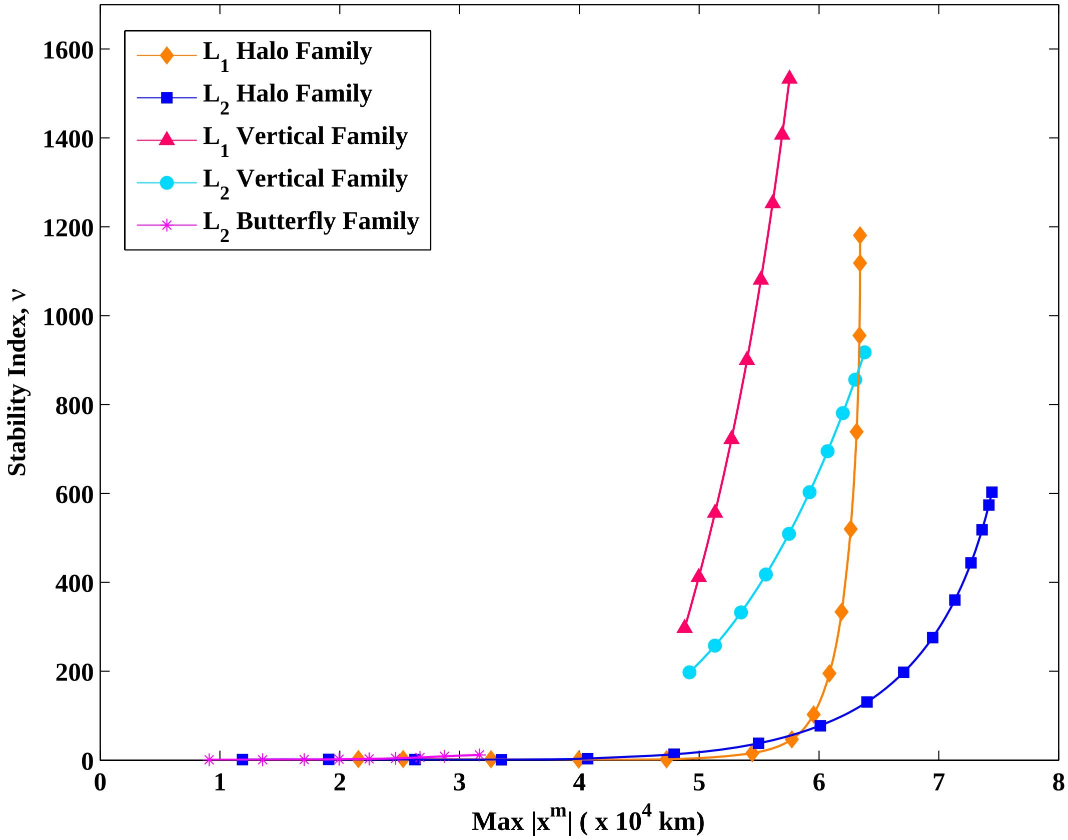

Figure 4.6 Stability Index versus Maximum x^m-Distance from the Moon

4.1.2 Potential Orbits for Coverage of the Lunar South Pole

Using periodicity and stability criteria, orbits from Figures 4.1–4.3 are selected for use in a coverage scenario. Either a single orbit is selected and two spacecraft are placed in the same orbit (but, out-of-phase), or a unique orbit is selected for each spacecraft such that their periods are commensurate. When an orbit with a precisely defined period is desired, the modified two-level differential corrections scheme accepts the patch points of a previously generated, neighboring orbit as an initial guess and generates a new orbit with the specified period. When this process is complete for all desired orbits, patch points are obtained; patch points for multiple revolutions are added to develop a baseline 180-day mission. Once the final trajectories are obtained, the initial time corresponding to one of the two spacecraft is phase shifted by a half-period, thus allowing the greatest chance for complete coverage of the lunar south pole.

For this investigation, nine different orbits from the families represented in Figures 4.1–4.3 are selected. Coverage can be adequately ensured with two spacecraft in just one of these nine orbits by phasing the vehicles appropriately. However, as already noted, selecting orbits with commensurate periods allows for architectures with combinations of two *different* orbits for complete lunar south pole coverage. For example, rather than placing two spacecraft in the same 7-day L_2 near-rectilinear halo orbit, one spacecraft is placed in a 7-day near-rectilinear halo and the other vehicle in a 14-day L_2 butterfly orbit. The combinations may provide more complete coverage. Possible orbits for use in combination to ensure lunar coverage are presented in Table 4.1.

For example, one possible solution to the coverage problem employs two spacecraft in the same 12-day L_1 halo orbit. The lunar periapsis for this orbit is approximately 36,500 km with corresponding apoapsis at 81,200 km. One spacecraft is phase shifted by a half-period, thus allowing the greatest chance for lunar south pole coverage, and the relative spacecraft positions appear in Figure 4.7. Fifteen revolutions are added for a baseline 180-day mission.

Table 4.1

Potential Orbits for Coverage of the Lunar South Pole

Orbit Type	Libration Point	Period (days)	Stability Index
Near-Rectilinear Halo	L_2	7.0	1.00
Near-Rectilinear Halo	L_1	8.0	1.25
Near-Rectilinear Halo	L_2	8.0	1.00
Halo	L_1	12.0	60
Halo	L_2	14.0	115
Vertical	L_1	14.0	690
Butterfly	L_2	14.0	11.3
Vertical	L_1	16.0	370
Vertical	L_2	16.0	515

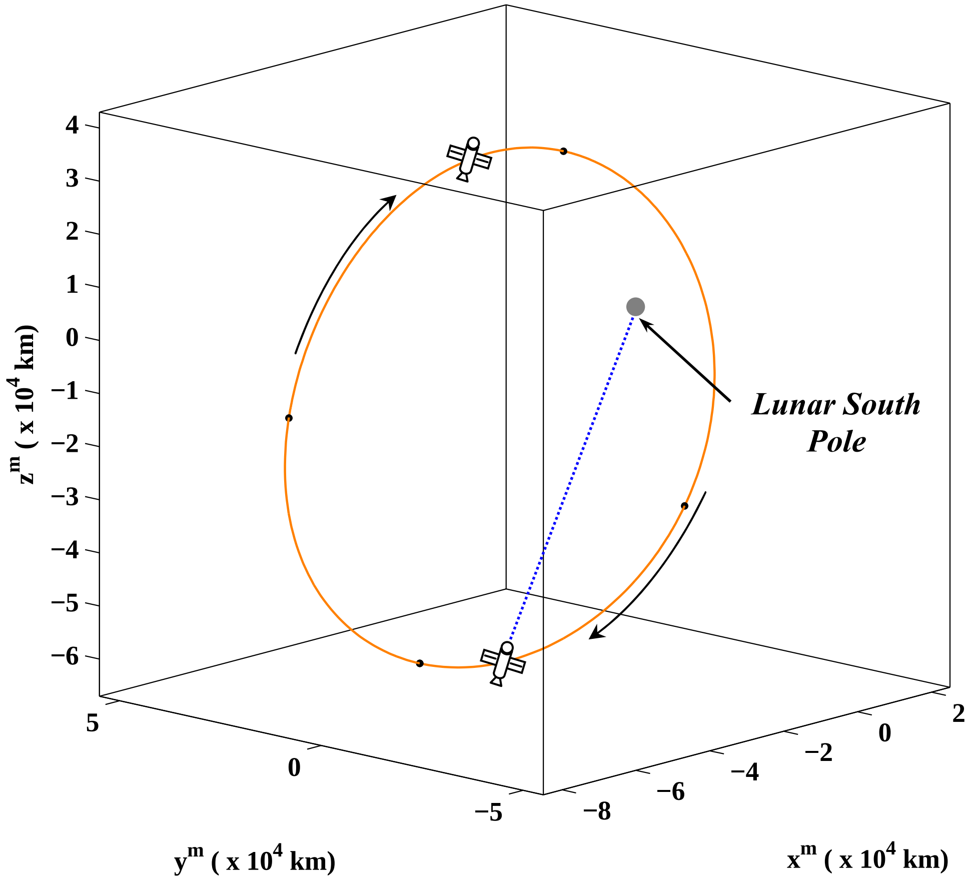

Figure 4.7 12-Day L_1 Orbit (Orange) and Patch Points (Black) from CR3BP

4.2 Transition to a Full Ephemeris Model

All orbits are initially designed under the assumption that a spacecraft is subject only to the gravitational force of the Earth and Moon in the CR3BP. The Purdue software package GENERATOR transitions trajectories computed in the CR3BP to a full ephemeris model, including solar perturbations, with only small variations in shape. Potential architectures for lunar south pole coverage are established and preliminary coverage analyses are completed.

4.2.1 Obtaining Results with the Purdue Software Package GENERATOR

The Purdue software package GENERATOR [41] is a mission design tool that is based on multi-body equations of motion including solar perturbations. Preliminary baseline trajectories can quickly be determined within the context of the two-, three- or four-body problem. Any number of bodies and the corresponding ephemeris information can be incorporated as desired (other forces, control schemes, and design components are available but not employed here). For this application, the 180-day baseline orbits acquired by using the modified two-level differential corrector in the CR3BP are transferred to the GENERATOR full ephemeris model. The patch point velocity discontinuities are minimized in a two-level corrections procedure within GENERATOR and a modified orbit emerges.

Recall that one possible scenario places two spacecraft in the same 12-day L_1 halo orbit. The orbits for the two spacecraft that result from GENERATOR appear in Figure 4.8 in both a Moon centered, rotating system of coordinates and the inertial Mean J2000 frame. Note that the trajectory of one spacecraft is plotted in blue; the motion of the other spacecraft appears in orange. The quasi-periodic motion of the spacecraft is most apparent in the Earth-Moon rotating frame where both orbit trajectories follow nearly the same path. Note that the patch point positions (black) have been adjusted for continuous motion in the full ephemeris model. In the Inertial Mean J2000 frame, the motion appears to “umbrella” around the Moon.

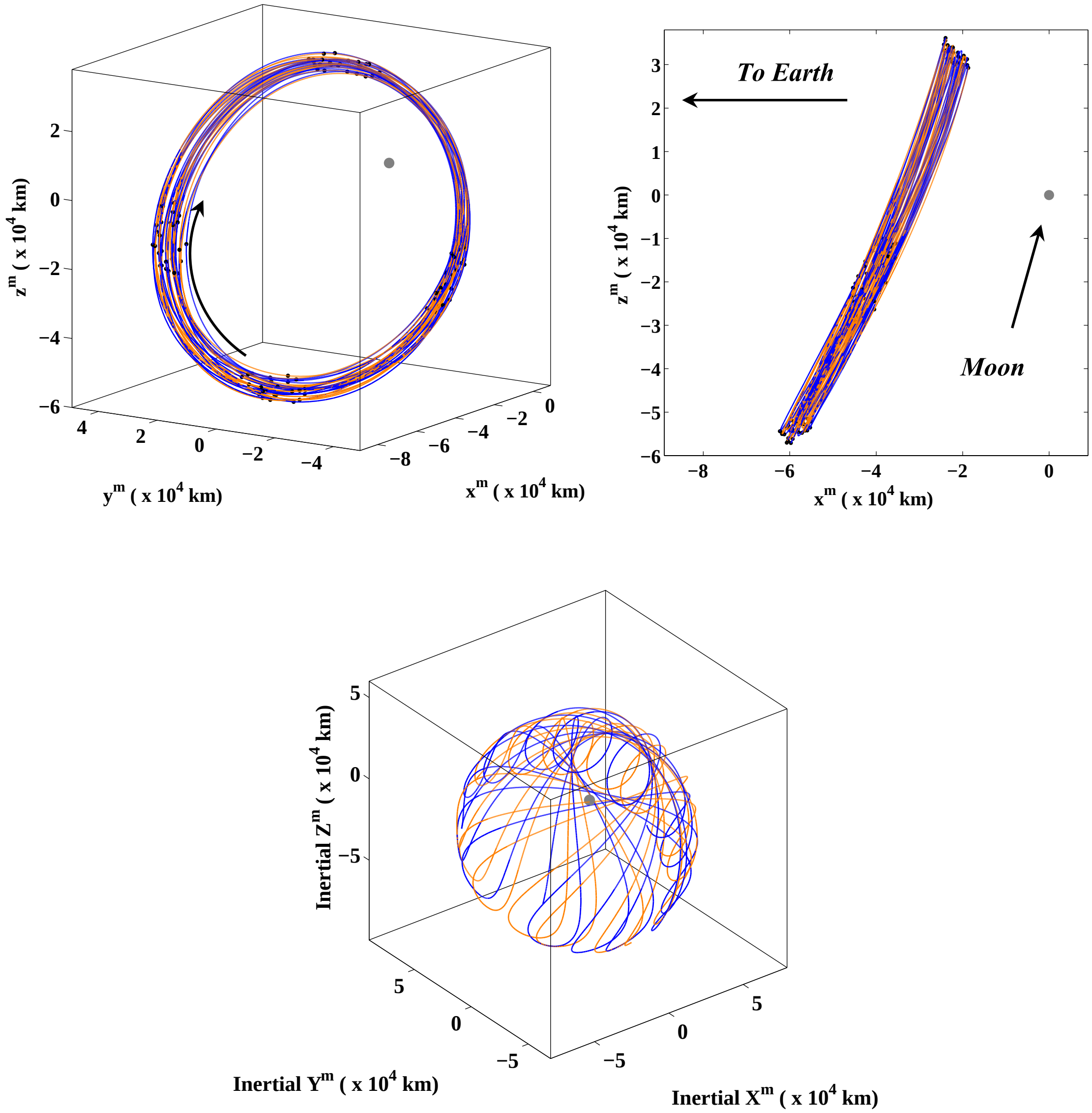

Figure 4.8 Two Phased Spacecraft in 12-Day L_1 Halo Orbits from GENERATOR; Moon Centered, Rotating Reference Frame (Top Left), x^m-z^m Projection (Top Right); Inertial Mean J2000 Reference Frame (Bottom)

4.2.2 A Preliminary Coverage Analysis

The resulting coverage schemes are initially analyzed by examination of the z^m-displacement of each of the spacecraft at the same instant of time. The z^m-displacement reflects the out-of-plane component of the position vector. The potential to maintain line-of-sight to the lunar south pole exists only if at least one of the spacecraft is below the Earth-Moon fundamental plane $z^m = 0$ at all times. Consider two spacecraft in a single L_1 halo orbit. A typical two-spacecraft coverage scheme is achieved by displacing the motion of each spacecraft by a half period. Thus, the two spacecraft are then phase shifted in the L_1 halo orbit and the z^m-displacement of each spacecraft as a function of time appears in Figure 4.9. The dashed line highlights the z^m-value at which the two spacecraft possess a common z^m-component but are moving in opposite directions along the orbit. The dashed line in Figure 4.9 also demonstrates that the z^m-crossing occurs 16,500 km below the fundamental plane, ensuring that at least one spacecraft is always within direct line-of-sight to the south pole. The first goal is to maximize the distance between the dashed line and the fundamental plane ($z^m = 0$). This initial step does not fully account for the actual position of the lunar south pole due to tilt and nutation of the rotation axes, but provides an estimate for the line-of-sight coverage behavior over time. Additionally, analyzing the z^m-displacement in this way also offers a visual confirmation that the proper periodicity constraint is implemented correctly, i.e., both spacecraft maintain the prescribed phasing over the entire mission time.

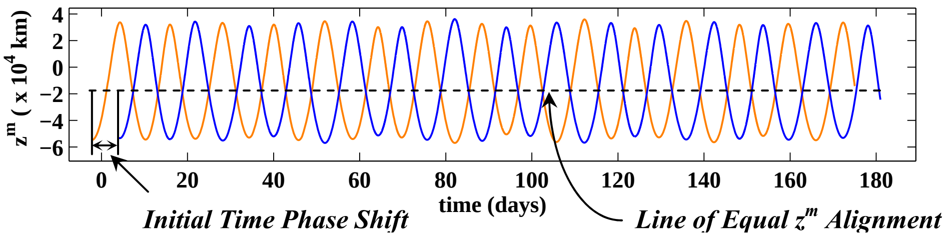

Figure 4.9 z^m-Displacement in the Rotating Reference Frame for Two Spacecraft in 12-Day L_1 Halo Orbits

4.2.3 Architectures for Lunar South Pole Coverage

Besides two spacecraft in the same 12-day L_1 halo orbit, other combinations of various orbits from Table 4.1 also yield viable coverage options. For example, the L_2 7-day halo orbit combination, with the orbits plotted in Figure 4.10, also utilizes only one halo orbit for both spacecraft. This near-rectilinear orbit passes approximately 2,750 km from the lunar surface at periapsis, 72,100 km at apoapsis altitude, and possesses a stability index of 1.00. Analyzing the GENERATOR z^m-displacement components, the scenario results in a distance between the dashed line for equal z^m alignment and the fundamental plane of 55,000 km. (See Figure 4.10.)

The 8-day L_1 and L_2 halo orbit scenario depicts an orbit combination that utilizes halo orbits in the vicinity of two distinct libration points (Figures 4.11). Like the 7-day scenario, the 8-day L_1 and L_2 halo orbits offer low minimum altitudes at approximately 1,400 km and 6,000 km, with apoapsis altitudes of 90,200 km and 76,900 km, and stability indices of 1.25 and 1.00, respectively. The GENERATOR analysis in Figure 4.11 demonstrates that the minimum distance between the dashed line for equal z^m alignment below the fundamental plane is 60,000 km.

The 16-day L_1 and L_2 vertical orbit scenario also utilizes multiple libration point orbits (Figure 4.12). The periapsis altitudes are much larger than the near-rectilinear halo orbits at 48,600 km and 55,800 km, respectively. The corresponding apoapsis altitudes are approximately 82,100 km for the L_1 vertical orbit and 69,600 km for the L_2 vertical orbit. The corresponding stability indices are 370 and 515 for the L_1 orbit and L_2 orbit, respectively. Due to the nature of the “figure-8” shape, the dashed line for equal z^m alignment occurs at the fundamental plane, suggesting brief intervals of time when both spacecraft are not within line-of-sight of the south pole. (See Figure 4.12.) An alternative scenario that employs the use of a vertical orbit for complete coverage is to place just one spacecraft in a 14-day L_1 vertical orbit and the other in a 14-day L_2 halo orbit.

The orbits for two spacecraft in a single 14-day L_2 butterfly orbit appear in Figure 4.13. The associated stability index of 11.3 is slightly higher than the near-rectilinear halo orbits. As evidenced by Figure 4.13, the GENERATOR minimum z^m-displacement crossing occurs 36,000 km below the fundamental plane. The orbit possesses a low periapsis altitude of 8,800 km. The corresponding apoapsis altitude for this orbit is approximately 67,900 km.

Finally, Figure 4.14 depicts a unique 14-day L_2 butterfly orbit and 7-day L_2 halo orbit scenario utilizing two different orbits from two different families. The scenario also exploits a 2:1 ratio between the periods. For this specific scenario, the minimum z^m-displacement crossing occurs 45,000 km below the fundamental plane (Figure 4.14).

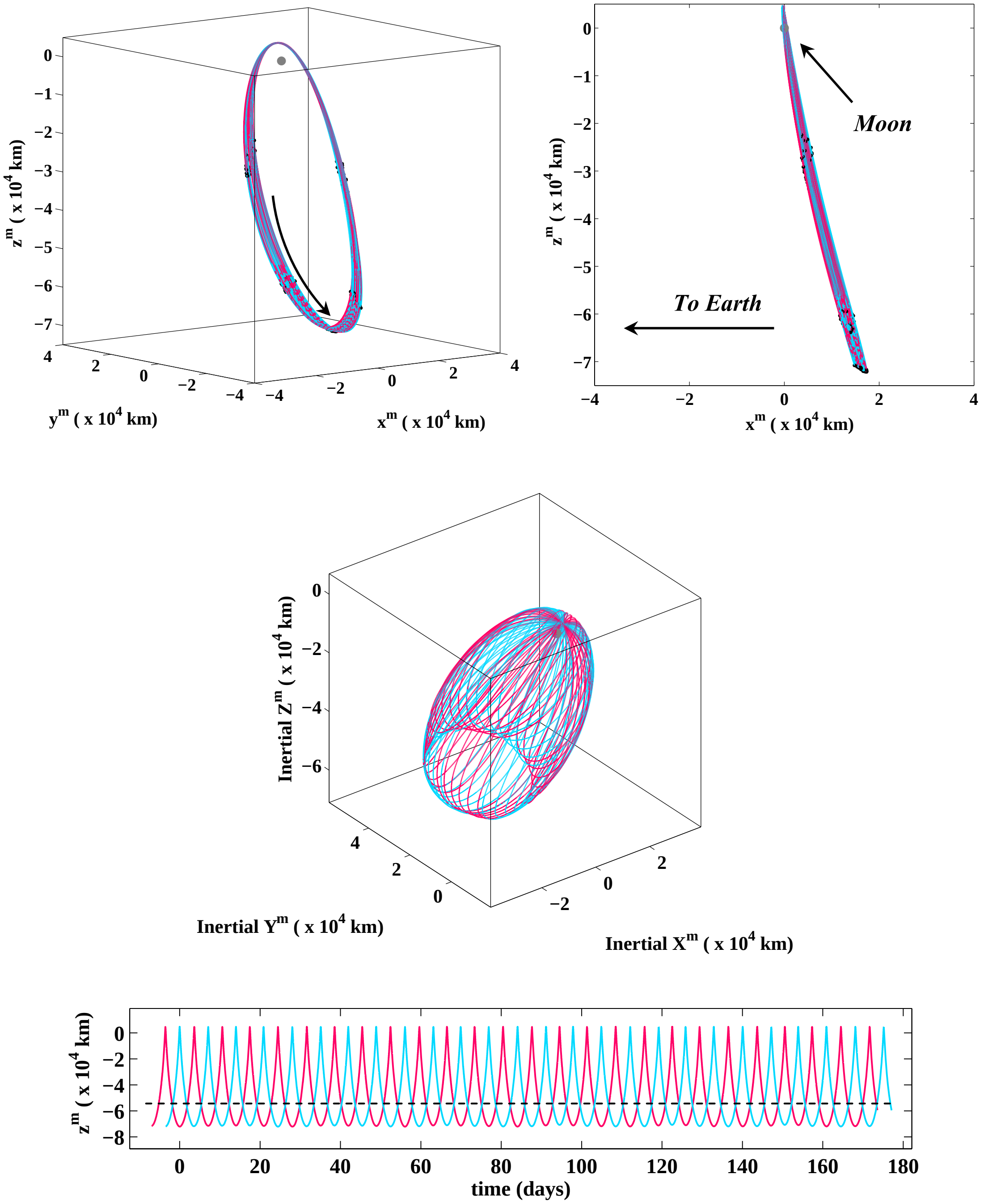

Figure 4.10 Two Phased Spacecraft in 7-Day L_2 Halo Orbits from GENERATOR; Moon Centered, Rotating Reference Frame (Top Left), x^m-z^m Projection (Top Right); Inertial Mean J2000 Reference Frame (Center); z^m-Displacement from Rotating Reference Frame (Bottom)

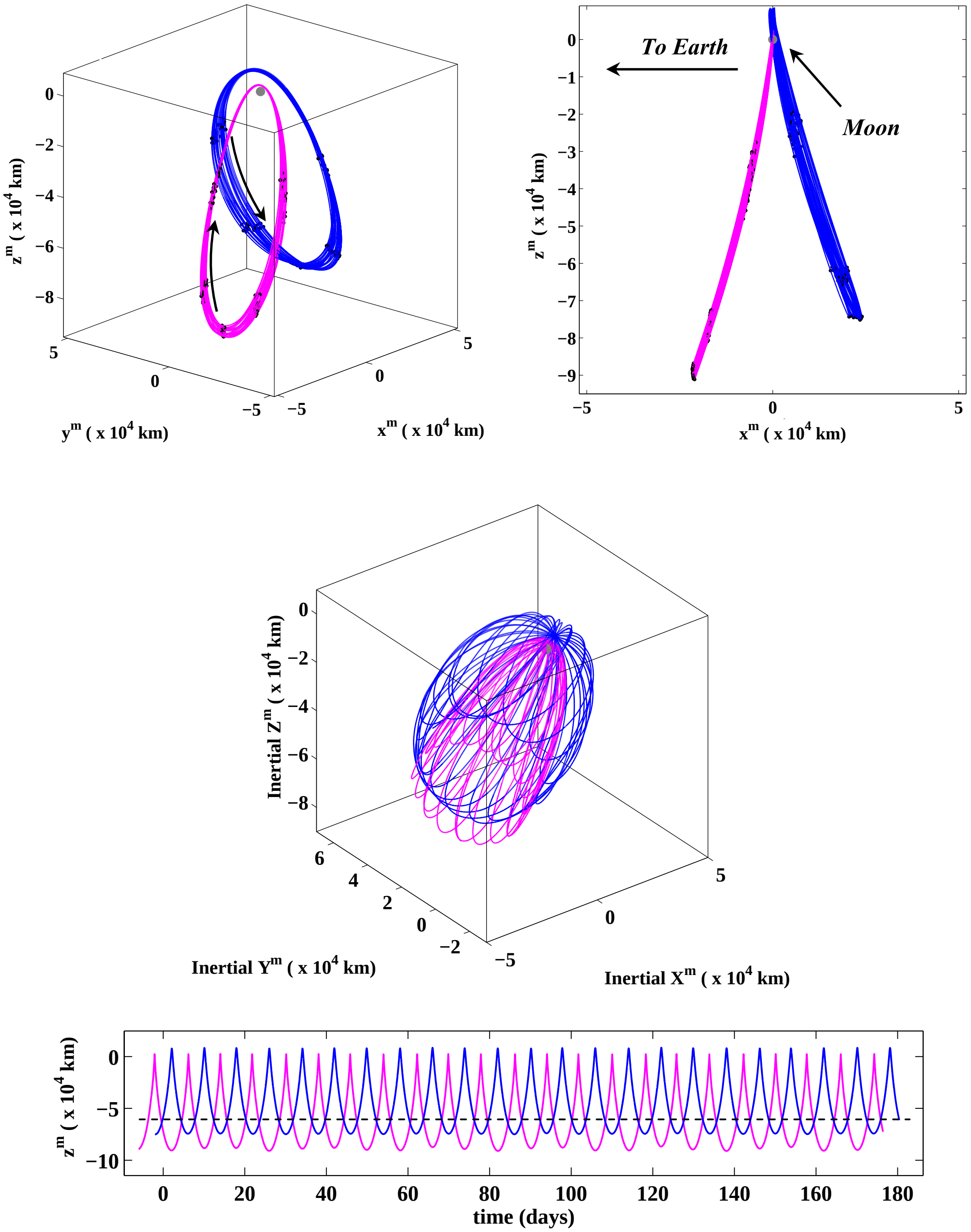

Figure 4.11 Two Phased Spacecraft in 8-Day L_1 and L_2 Halo Orbits from GENERATOR; Moon Centered, Rotating Reference Frame (Top Left), x^m-z^m Projection (Top Right); Inertial Mean J2000 Reference Frame (Center); z^m-Displacement from Rotating Reference Frame (Bottom)

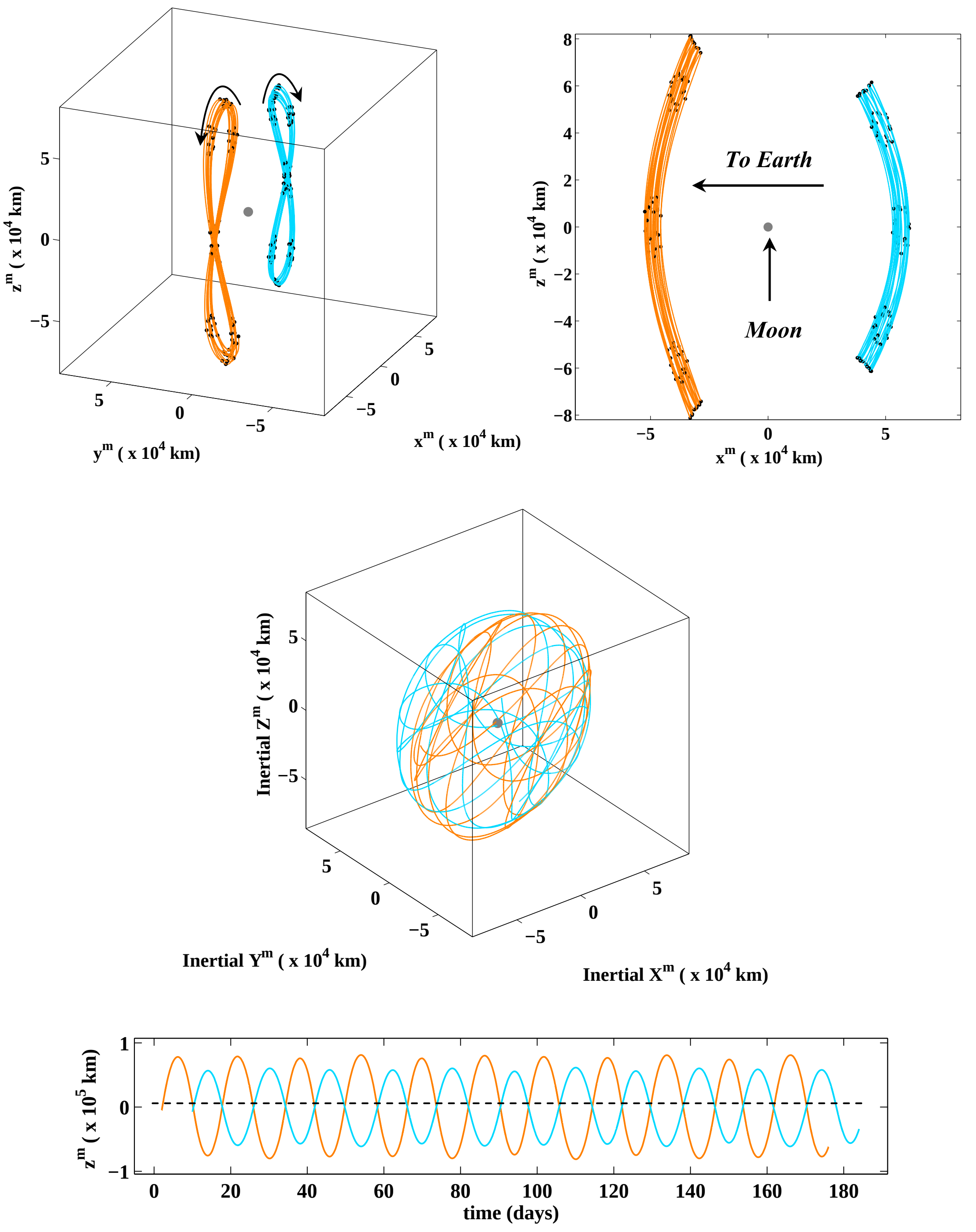

Figure 4.12 Two Phased Spacecraft in 16-Day L_1 and L_2 Vertical Orbits from GENERATOR; Moon Centered, Rotating Reference Frame (Top Left), x^m-z^m Projection (Top Right); Inertial Mean J2000 Reference Frame (Center); z^m-Displacement from Rotating Reference Frame (Bottom)

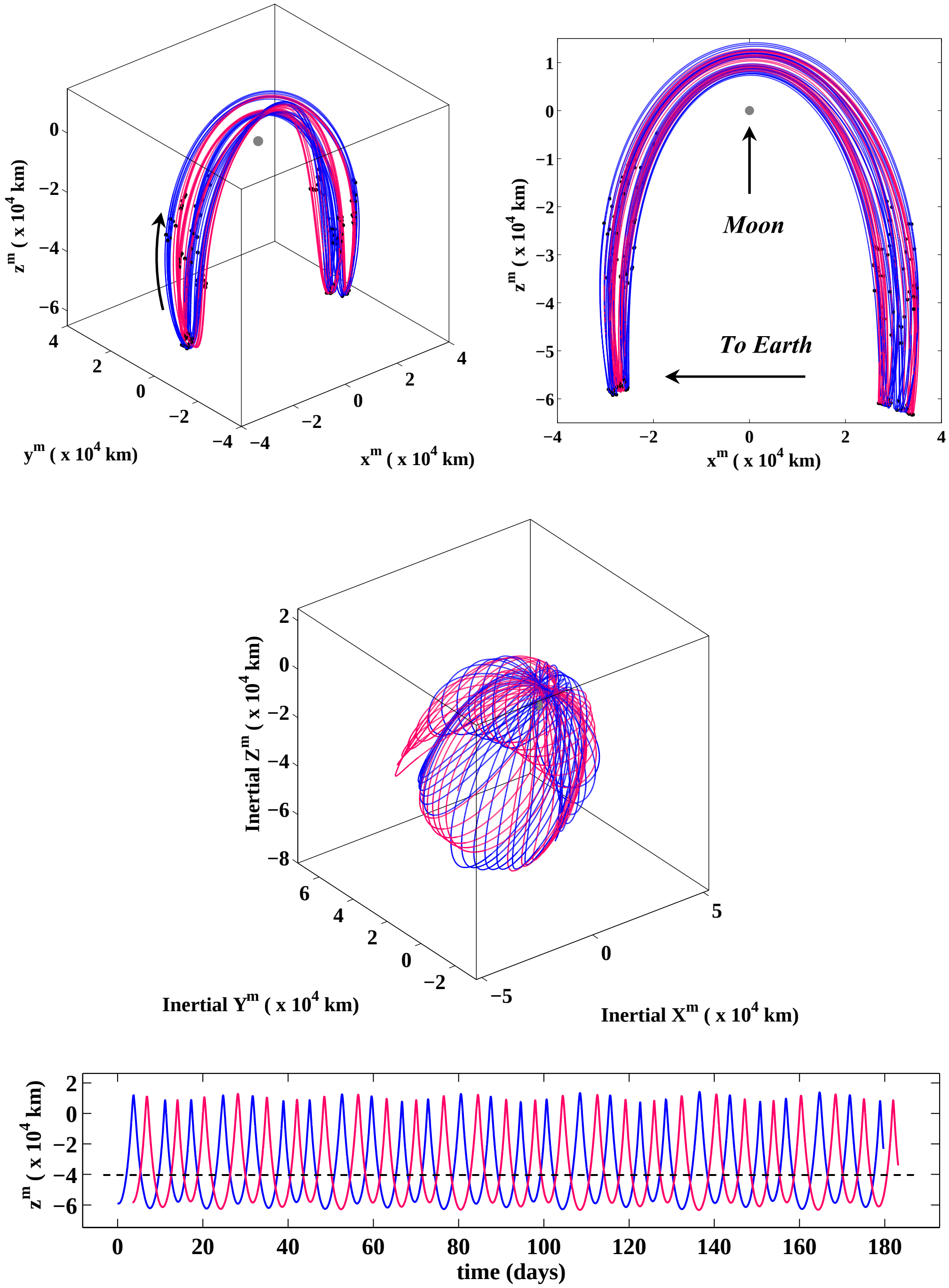

Figure 4.13 Two Phased Spacecraft in 14-Day L_2 Butterfly Orbits from GENERATOR; Moon Centered, Rotating Reference Frame (Top Left), x^m-z^m Projection (Top Right); Inertial Mean J2000 Reference Frame (Center); z^m-Displacement from Rotating Reference Frame (Bottom)

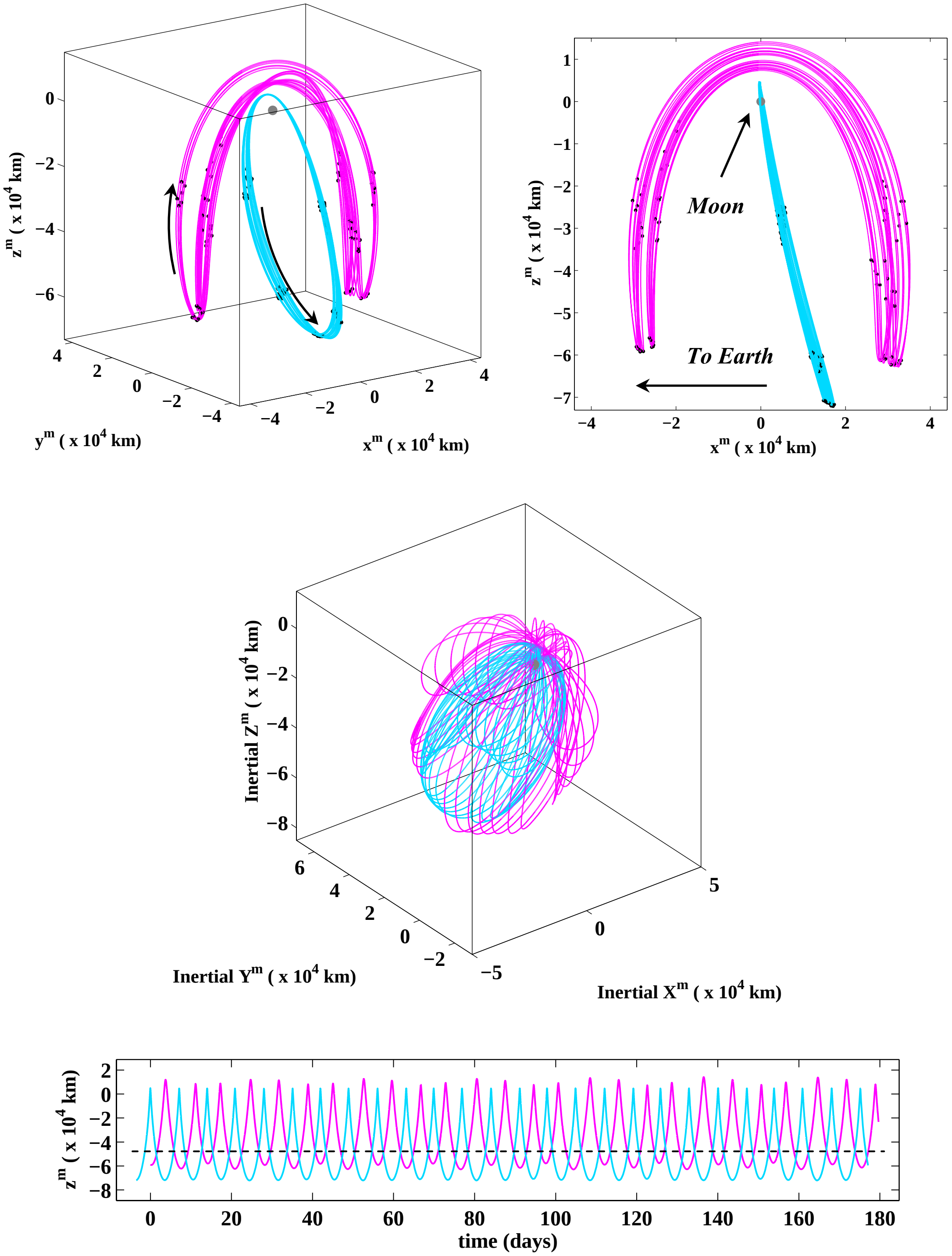

Figure 4.14 Two Phased Spacecraft in a 7-Day L_2 Halo Orbit and a 14-Day L_2 Butterfly Orbit; Moon Centered, Rotating Reference Frame (Top Left), x^m-z^m Projection (Top Right); Inertial Mean J2000 Reference Frame (Center); z^m-Displacement from Rotating Reference Frame (Bottom)

5. COVERAGE AND STATION-KEEPING ANALYSES FOR LUNAR SOUTH POLE COVERAGE

Mission scenarios for lunar south pole coverage have been developed in support of activities at NASA Goddard Spaceflight Center. Thus, trajectories designed in the Purdue software package GENERATOR are further evaluated in the NASA Goddard version of the Analytical Graphics, Inc. software package Satellite Tool Kit (STK®). To accomplish such a task, the solutions obtained from GENERATOR are confirmed by targeting GENERATOR patch points in STK using STK's Astrogator. The propagator in the STK targeting sequence is an eighth-order, full Runge-Kutta-Verner integrator with ninth-order error control including solar perturbations. In general, slight differences in modeling and numerical precision require only small corrections at each point. For example, transitioning from GENERATOR to STK using Astrogator Connect requires less than 1 m/s per year in corrections, an insignificant size in comparison with the costs necessary for station-keeping from other "real" errors. Obtaining the orbits in STK provides a complete coverage analysis for potential ground stations. Using invariant manifold theory, preliminary station-keeping analyses for the orbits in Table 4.1 are also available.

5.1 Coverage Analysis

Assuming an omni-directional communications link, the satellites are only accessible to the ground stations if they are within direct line-of-sight. Intervals when the ground stations are unable to access either satellite are recorded.

5.1.1 Defining the Ground Stations and Establishing the Links

Consider two satellites in a 12-day L_1 halo orbit as depicted in Figure 4.8. Using Astrogator Connect to target the converged GENERATOR patch point positions results in Figures 5.1. Due to constant exposure to sunlight and possibly the existence of frozen volatiles, the lunar south pole is a likely location for a ground station on the Moon. In addition, current interest is directed at exploration options expanding out from the south pole. One such location that is of scientific interest is the site of the Shackleton Crater [47]. Therefore, a facility is placed on the Moon with coordinates 89.9°S, 0.0°E corresponding to the Shackleton Crater. (See Figure 5.2.)

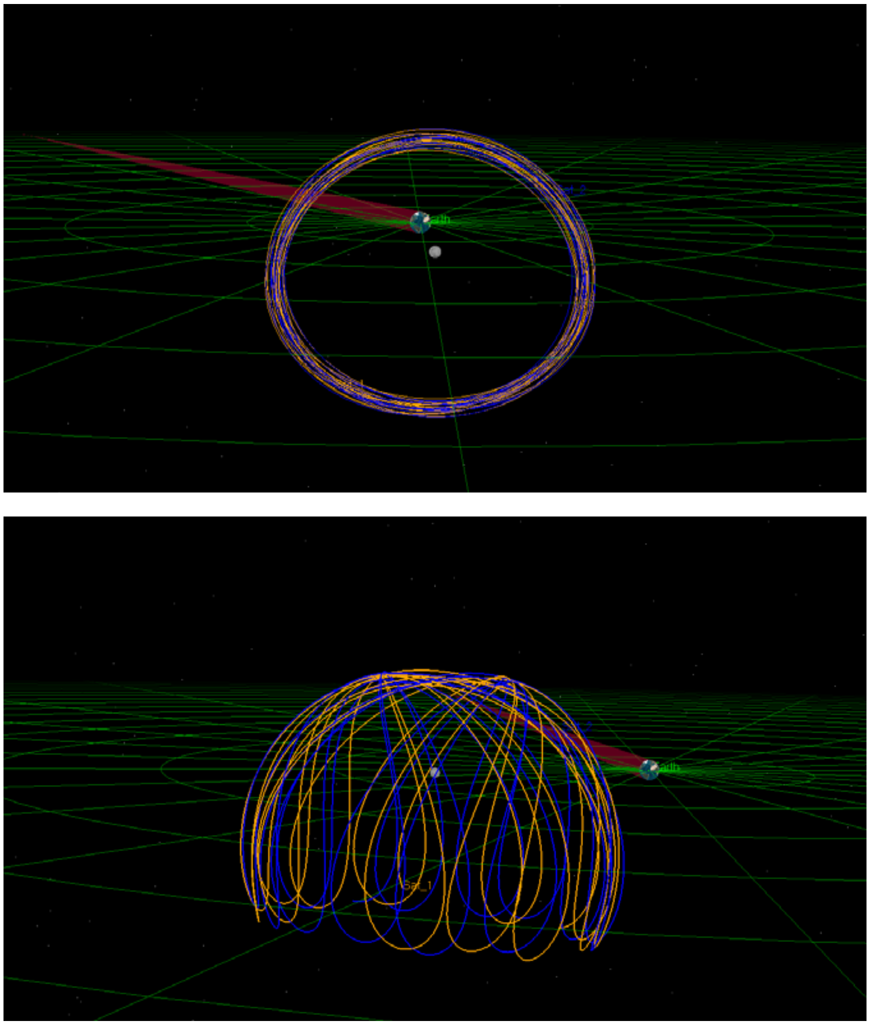

Figure 5.1 STK 12-Day L_1 Halo Orbits:
Moon Centered, Rotating Frame (Top);
Moon Centered, Inertial Mean J2000 Frame (Bottom)

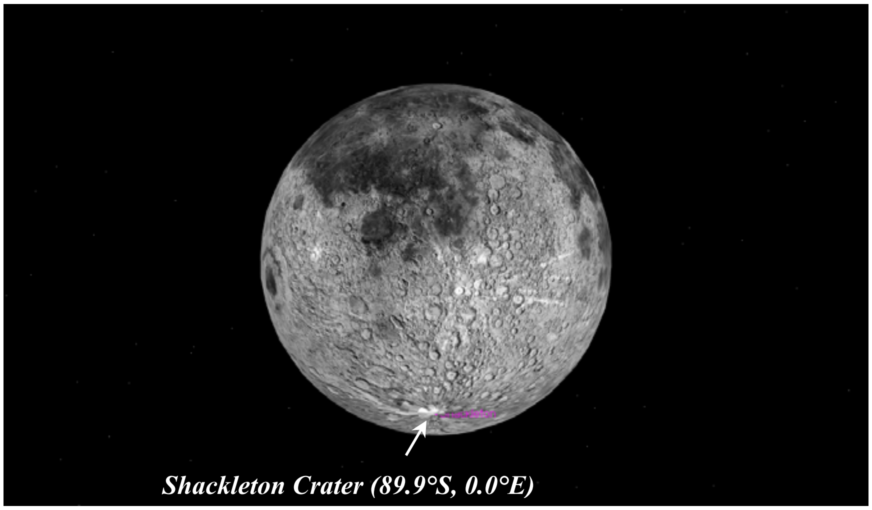

Figure 5.2 A Facility is Placed on Moon at the Shackleton Crater (89.9°S, 0.0°E)

Both satellites are placed in a constellation and the times when either satellite or both satellites have line-of-sight access with the facility is computed via an access chain. Furthermore, the line-of-sight access times between the lunar facility and each individual satellite is available. (See yellow access beams in Figure 5.3.) The results for the 12-day L_1 halo orbit scenario are available in Table 5.1 for a simulation time of 173.99 days. At least one satellite is always in direct line-of-sight of the Shackleton Crater.

Table 5.1

Percent Access Times for 12-Day L_1 Halo Orbits and

Ground Station at the Shackleton Crater

	Facility at Shackleton Crater
Only Satellite 1	63.51%
Only Satellite 2	63.92%
Both Satellites	27.42%
Either Satellite	100.00%
Simulation Time (days)	173.99

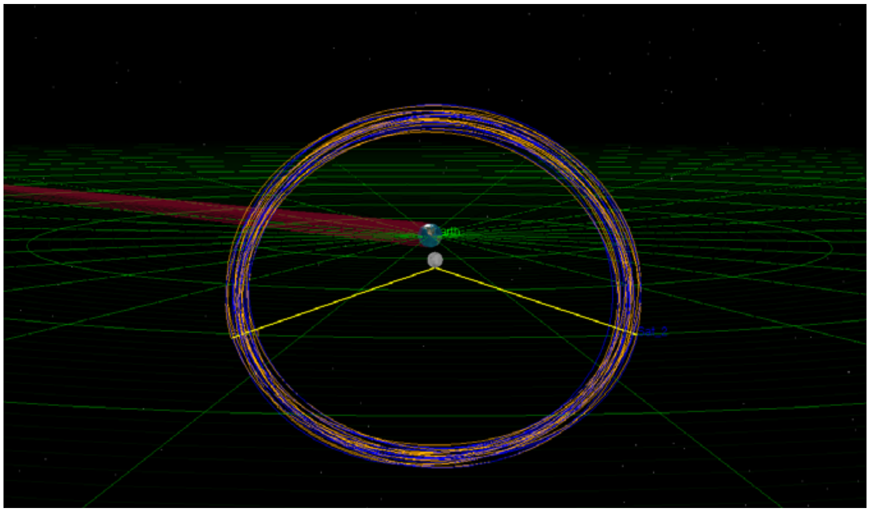

Figure 5.3 Line of Sight Access Beams (Yellow) with Lunar Facility

Information from the ground station regarding each satellite during access times is also available. For example, a plot of the elevation angle of each satellite relative to the facility as a function of time appears in Figure 5.4. As in Table 5.1, the plot demonstrates that the desired coverage is achieved. In fact, from Figure 5.4 it is apparent that at least one satellite is always 15° above the horizon as viewed from the facility (see black dashed line in Figure 5.4). That is, constant communications is achieved anywhere *inside* the Shackleton Crater only if the walls of the crater are inclined less than 15°. Furthermore, there is a satellite between the elevation angles 0° and 15°, 27.42% of the simulation time. Incorporated in Table 5.1 and Figure 5.4 is direct access with the true, exact location of the ground facility (89.9°S, 0.0°E) including lunar librations from wobble and nutation of the spin axis.

Alternatively, three fictional ground stations are placed in a new configuration along the Earth equator separated by 120°. The line-of-sight access between the ground-based Earth stations and the satellite constellation is computed via another access chain. The results are representative of access between the Earth and the satellites, i.e., times when Earth can communicate with either satellite. For two satellites in a 12-day L_1 halo orbit, each satellite always maintains line-of-sight with at least one ground station 100% of the simulation time. Of course, this is also evident from Figures 5.1 and 5.3 where each satellite is visibly always in direct line-of-sight with the Earth. Such a result is expected for satellites in Earth-Moon halo orbits [45]. It might be more accurate for actual mission analysis to specify a real transmitting site on the Earth for ground station communications with the lunar-based satellites. A probable location for this ground station is the White Sands Test Facility (WSTF) located in New Mexico (32.3°N, 106.8°W). (See Figure 5.5.) A chain is created for access between the satellite constellation and a facility located at WSTF. The times when each satellite, either satellite, or both satellites possess line-of-sight with the facility are computed. As evidenced from Table 5.2, each satellite maintains line-of-sight for nearly half the simulation time. Given Earth rotation, this is an excellent result.

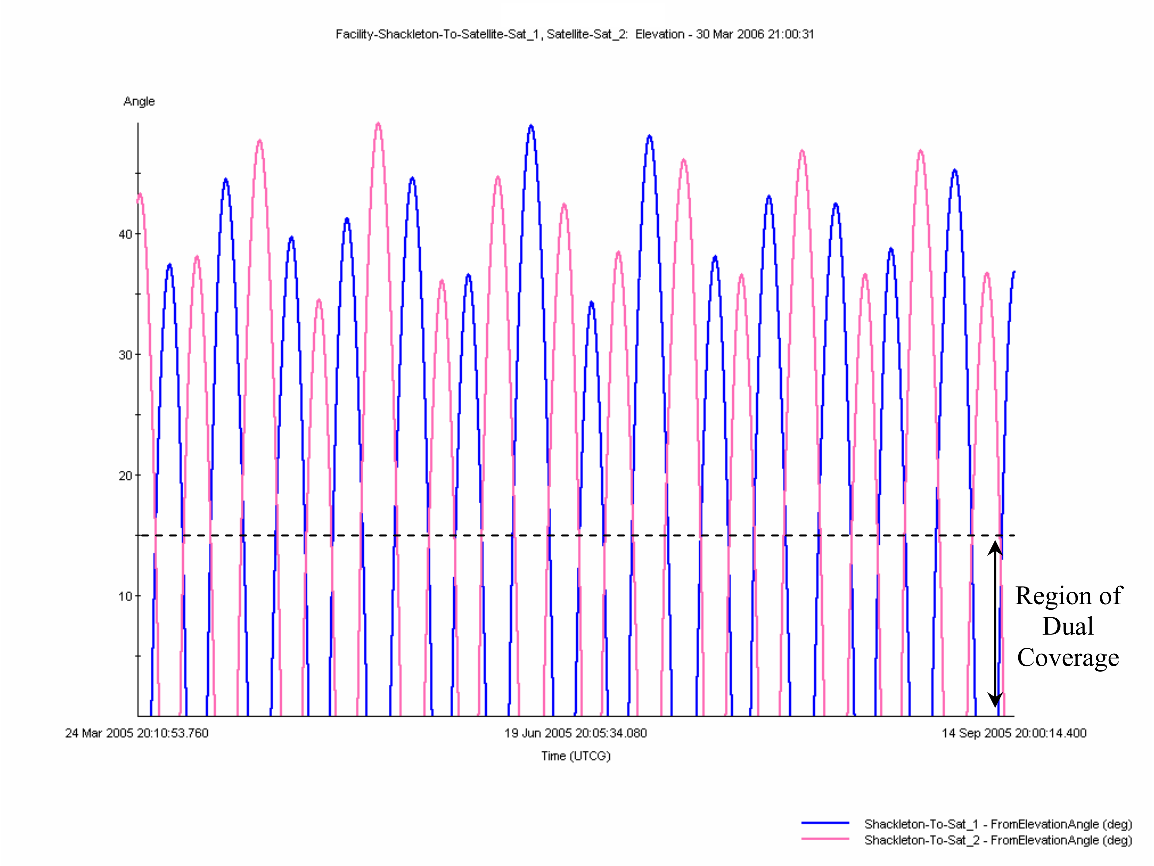

Figure 5.4 Elevation of Each Satellite Above the Horizon as Viewed from the Shackleton Crater Facility for 12-Day L_1 Halo Orbit Scenario

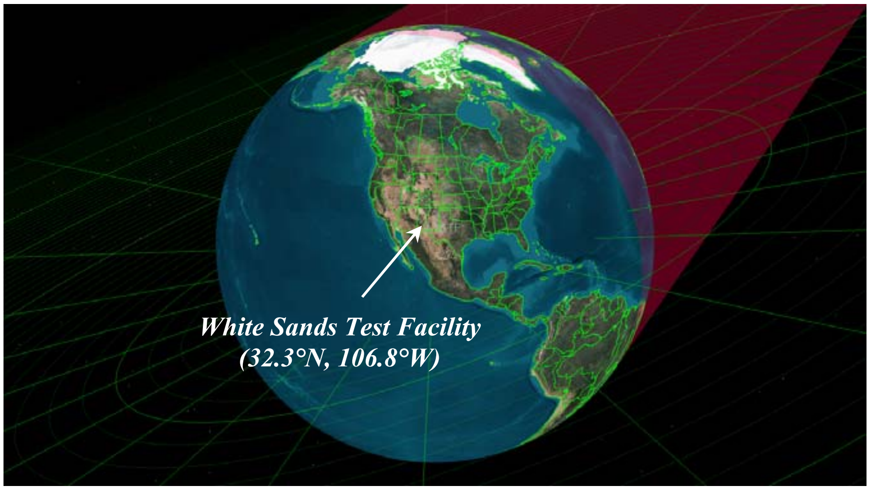

Figure 5.5 An STK Facility is Placed at the White Sands Test Facility (32.3°N, 106.8°W)

Table 5.2

Percent Access Times for 12-Day L_1 Halo Orbits and Ground Station at the White Sands Test Facility

	Facility at WSTF
Only Satellite 1	48.26%
Only Satellite 2	48.17%
Both Satellites	44.61%
Either Satellite	51.82%
Simulation Time (days)	173.99

An additional communications link between the satellites also provides valuable information. For example, a satellite in direct line-of-sight with the lunar facility may not, at the same time, possess line-of-sight with WSTF. However, if the other satellite possesses line-of-sight in direct communications with WSTF, then a communications link is established between the lunar facility and WSTF via a relay between the two satellites. (See Figure 5.6.) For some orbits, line-of-sight does not exist when the Moon is between the satellites, i.e., when one satellite is at periapsis and the other is at apoapsis. However, for the configuration of two satellites in 12-day L_1 halo orbits, there is line-of-sight between both satellites 100% of the simulation time.

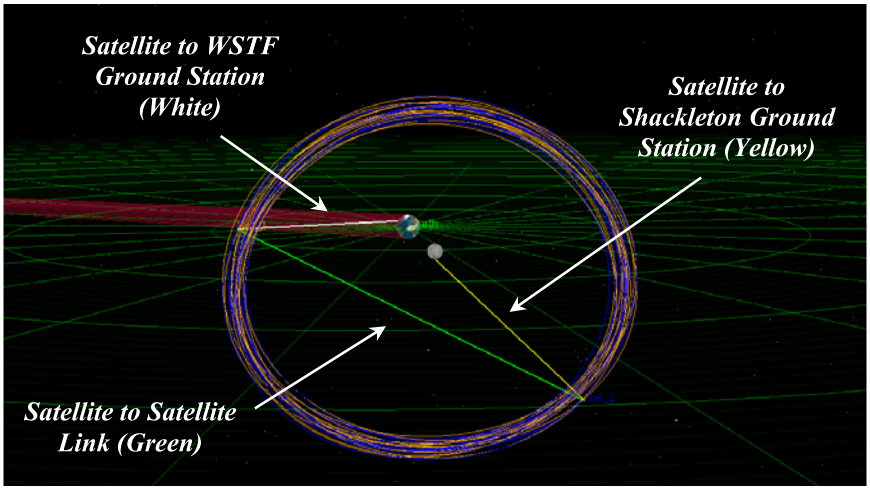

Figure 5.6 Possible Communications Relay Between the White Sands Test Facility and the Lunar Ground Station at the Shackleton Crater

5.1.2 Results for Architectures Supporting Lunar South Pole Coverage

Besides the 12-day L_2 halo orbit combination, the entire coverage analysis is easily repeated for the remaining architectures corresponding to Figures 4.10-4.14. The access and elevation results for all the remaining constellations in this study appear in Figures 5.7-5.16 and Tables 5.3-5.7. Recall the plots of the out-of-plane phasing between satellites in each figure. In general, smaller distances between the dashed line for equal z^m alignment and the fundamental plane, $z^m = 0$, as computed in GENERATOR, translate to smaller ranges over which the elevation angles of the two satellites allow simultaneous coverage scenarios in STK. A smaller range over the elevation angles reflects smaller time intervals over which the lunar facility has access with both satellites. Furthermore, nearly all the coverage scenarios possess nearly 50% access with WSTF. (See Tables 5.3-5.7.)

For the 7-day L_2 halo orbit combination (Figure 5.7), complete coverage of the facility occurs at all times, as observed from Figure 5.8. Both satellites simultaneously achieve access with the lunar facility for elevation angles from 0° to 65° for 92.78% of the simulation time. Therefore, if the walls of the Shackleton Crater are less than a 65° incline, constant communications can be maintained anywhere inside the crater. Also notable in Figure 5.7, is a time when both satellites are accessed by the Shackleton facility, i.e., both yellow access beams are active. Since the 7-day L_2 halo orbit is near-rectilinear, the motion is similar to a highly elliptical two-body orbit. Therefore, during the majority of the orbital period both satellites are within direct line-of-sight of the lunar facility, leading to large periods of redundant coverage. In fact, one satellite possesses line-of-sight with the Shackleton facility over 95% of the simulation time. Furthermore, the satellites are fully accessible from the Earth 100% of the time with only small intervals when one satellite cannot communicate with the other due to interference with the Moon. That is, for 99.21% of the simulation time, the satellites possess direct line-of-sight with each other.

The 8-day L_1 and L_2 halo orbit scenario shares many similarities with the 7-day L_2 halo orbit scenario (Figure 5.9). Simultaneous coverage of the lunar facility is achieved at approximately 0° to 60° in elevation angle, as apparent in Figure 5.10. That is, at least one satellite is always 60° above the horizon. The satellite configured in the 8-day L_1 halo orbit is in direct line-of-sight with the Shackleton facility nearly 99% of the simulation time. As with the previous scenarios utilizing halo orbits, satellites placed in the 8-day L_1 and L_2 halo orbits are always in direct access with the Earth. The satellites possess line-of-sight with one another 99.73% of the simulation time.

Due to the nature of the "figure-eight" shape, no two-satellite vertical orbit combination exhibits complete coverage of the lunar south pole, as evidenced with the 16-day L_1 and L_2 vertical orbit scenario. Neither satellite is within direct line-of-sight of the Shackleton facility when both satellites cross the fundamental plane at the same time. The elevation plot in Figure 5.12 confirms that there are, in fact, small intervals in time, i.e., 1.39% percent of the simulation time, when the lunar facility cannot access either satellite. At this same instant, the Moon passes directly between the satellites, and therefore the satellites are also not able to communicate with each other. In fact, the STK results in Figure 5.11 reveal an instant in time when no access beams (yellow) exist between the lunar facility and either satellite. At this same instant, an access beam (green) does not exist between the satellites either. Satellite-to-satellite line-of-sight occurs only 94.33% of the simulation time. Furthermore, due to passage behind the Moon, L_2 vertical orbits do not possesses 100% line-of-sight access with the Earth. However, since the out-of-plane motion for the vertical orbit is larger than the halo orbits, the verticals are able to communicate with WSTF nearly 52% of the time. (See Table 5.5.)

Two satellites in 14-day L_2 butterfly orbits, as depicted in Figure 5.13, exhibit the same properties as the near-rectilinear halo orbit scenarios. Figure 5.14 demonstrates that at least one satellite is always 45° above the horizon. That is, between 0° and 45° there is simultaneous coverage, and from Table 5.6 this occurs 78.25% of the time. For 0.39% of the simulation time, the Moon interferes with communication between the satellites. Similar to a satellite in an L_2 vertical orbit, a satellite in a 14-day L_2 butterfly orbit passes behind the Moon and therefore does not posses 100% line-of-sight with the Earth.

Finally, a constellation with one satellite in a 14-day L_2 butterfly orbit and another satellite placed in a 7-day L_2 halo orbits appears in Figure 5.15. Simultaneous coverage occurs for 85.57% of the time between elevations of 0° and 50° degrees. (See Figure 5.16 and Table 5.7.) Furthermore, the satellites are in direct line-of-sight with one another for 99.76% of the simulation time.

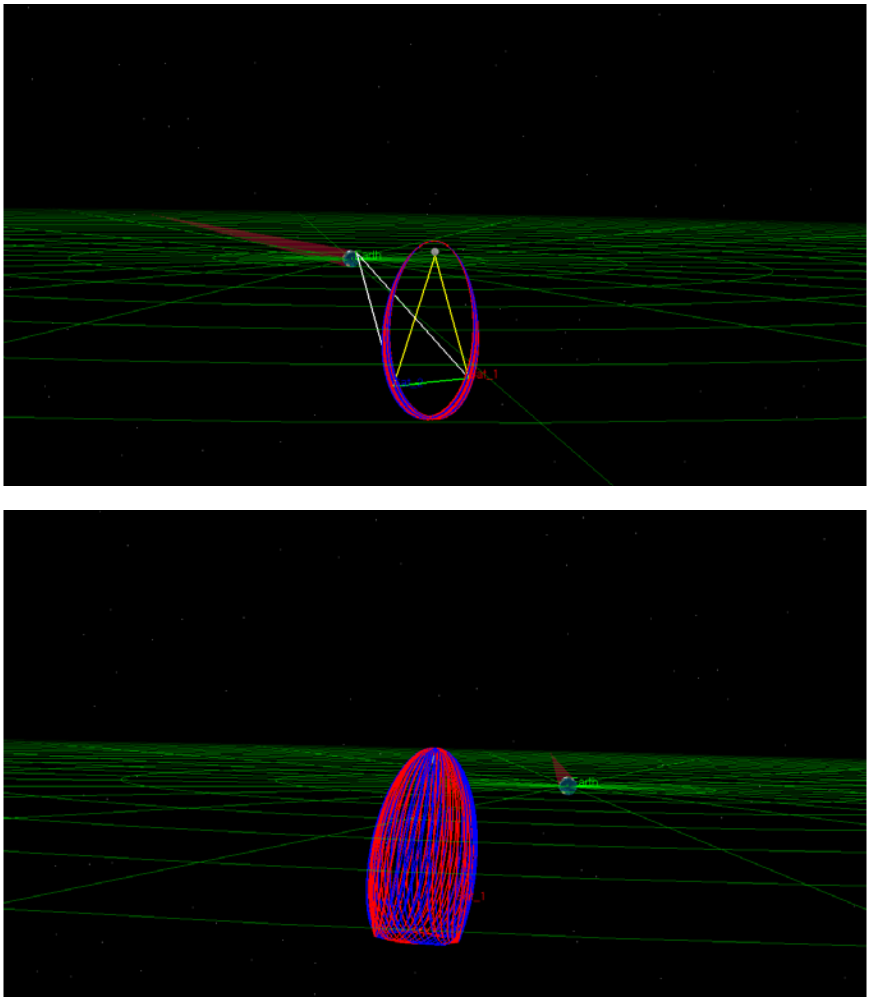

Figure 5.7 STK 7-Day L_2 Halo Orbits:
Moon Centered, Rotating Frame (Top);
Moon Centered, Inertial Frame (Bottom)

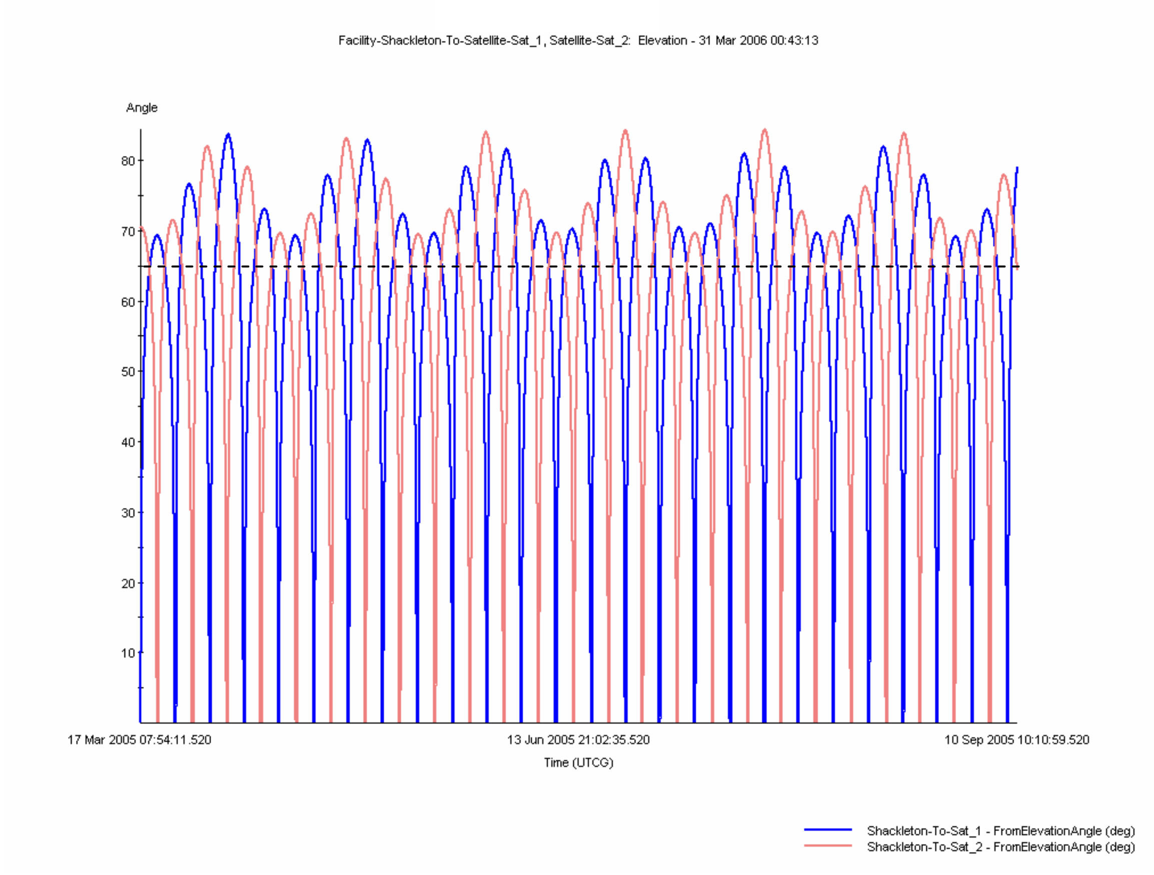

Figure 5.8 Elevation of Each Satellite Above the Horizon as Viewed from the Shackleton Crater Facility for 7-Day L_2 Halo Orbit Scenario

Table 5.3

Percent Access Times for 7-Day L_2 Halo Orbits

	Facility at Shackleton Crater	Earth	Facility at WSTF
Only Satellite 1	96.41%	100.00%	47.26%
Only Satellite 2	96.37%	100.00%	47.21%
Both Satellites	92.78%	100.00%	45.72%
Either Satellite	100.00%	100.00%	48.75%
Simulation Time (days)	177.10		

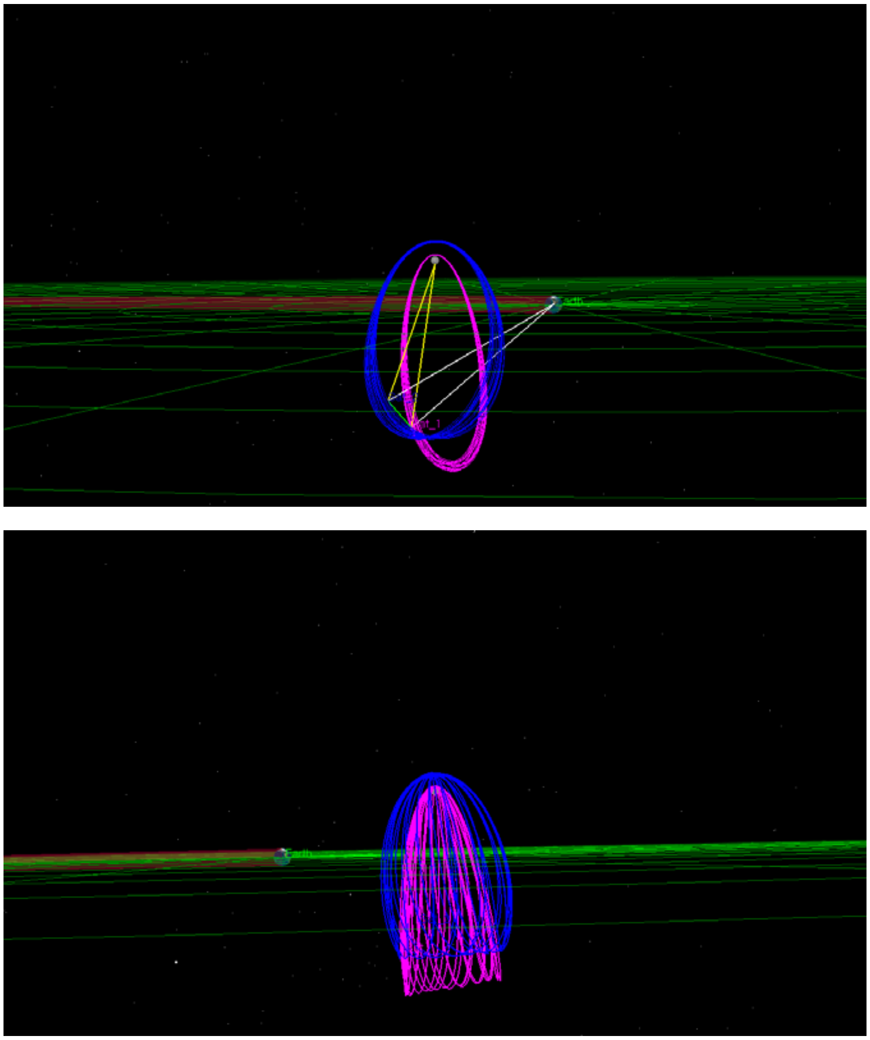

Figure 5.9 STK 8-Day L_1 and L_2 Halo Orbits:
Moon Centered, Rotating Frame (Top);
Moon Centered, Inertial Frame (Bottom)

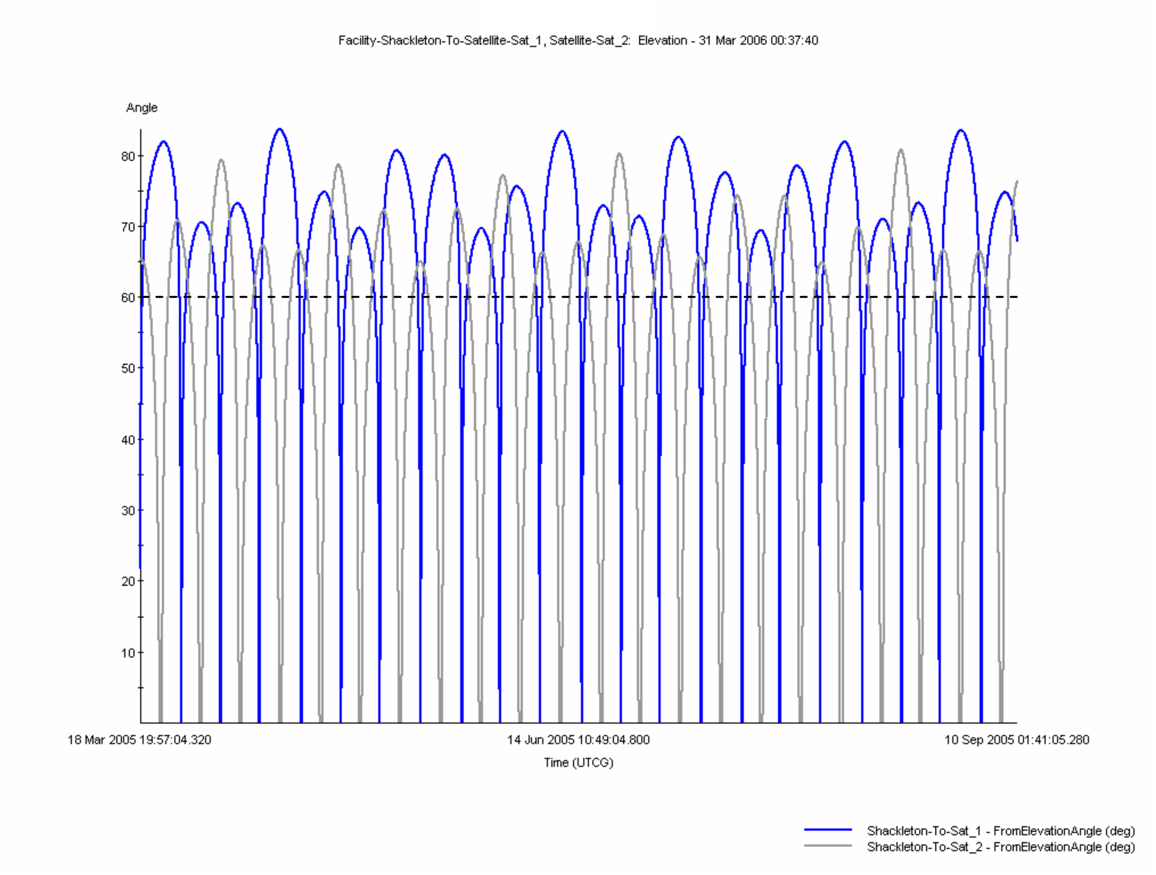

Figure 5.10 Elevation of Each Satellite Above the Horizon as Viewed from the Shackleton Crater Facility for 8-Day L_1 and L_2 Halo Orbit Scenario

Table 5.4

Percent Access Times for 8-Day L_1 and L_2 Halo Orbits

	Facility at Shackleton Crater	Earth	Facility at WSTF
Only L_1 Satellite	98.67%	100.00%	46.13%
Only L_2 Satellite	93.44%	100.00%	47.43%
Both Satellites	92.11%	100.00%	45.46%
Either Satellite	100.00%	100.00%	48.10%
Simulation Time (days)	175.24		

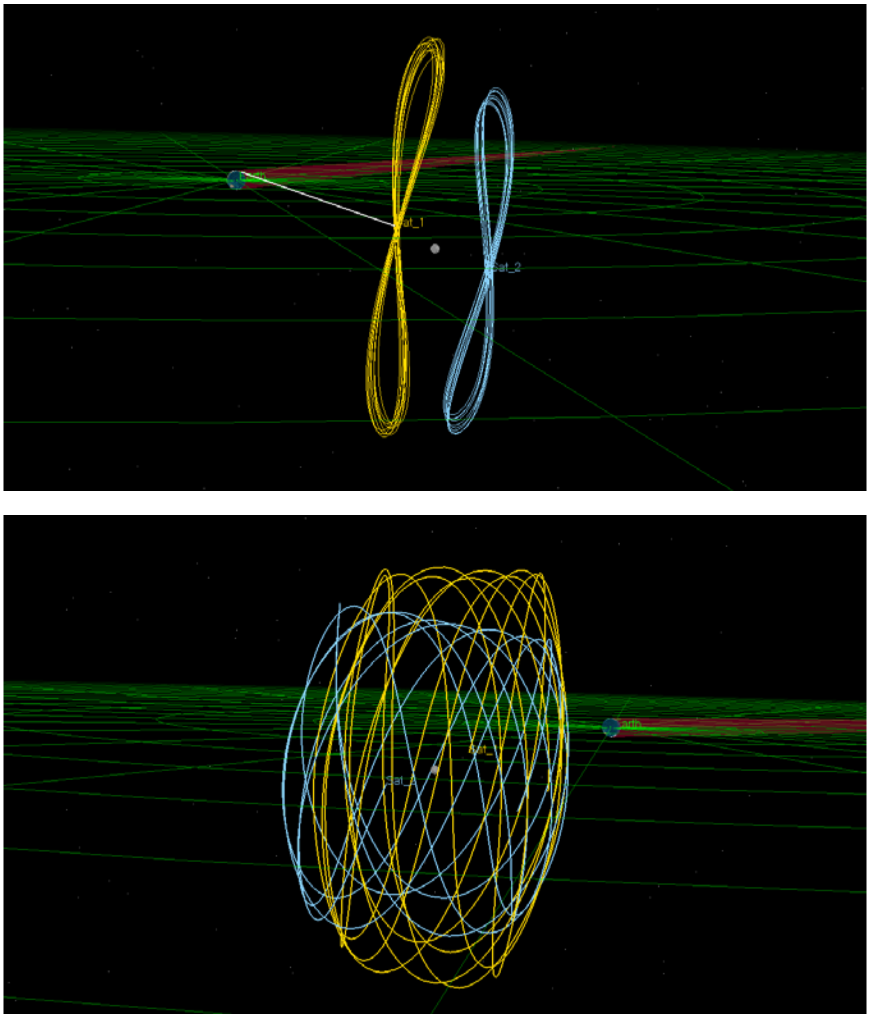

Figure 5.11 STK 16-Day L_1 and L_2 Vertical Orbits:

Moon Centered, Rotating Frame (Top);

Moon Centered, Inertial Frame (Bottom)

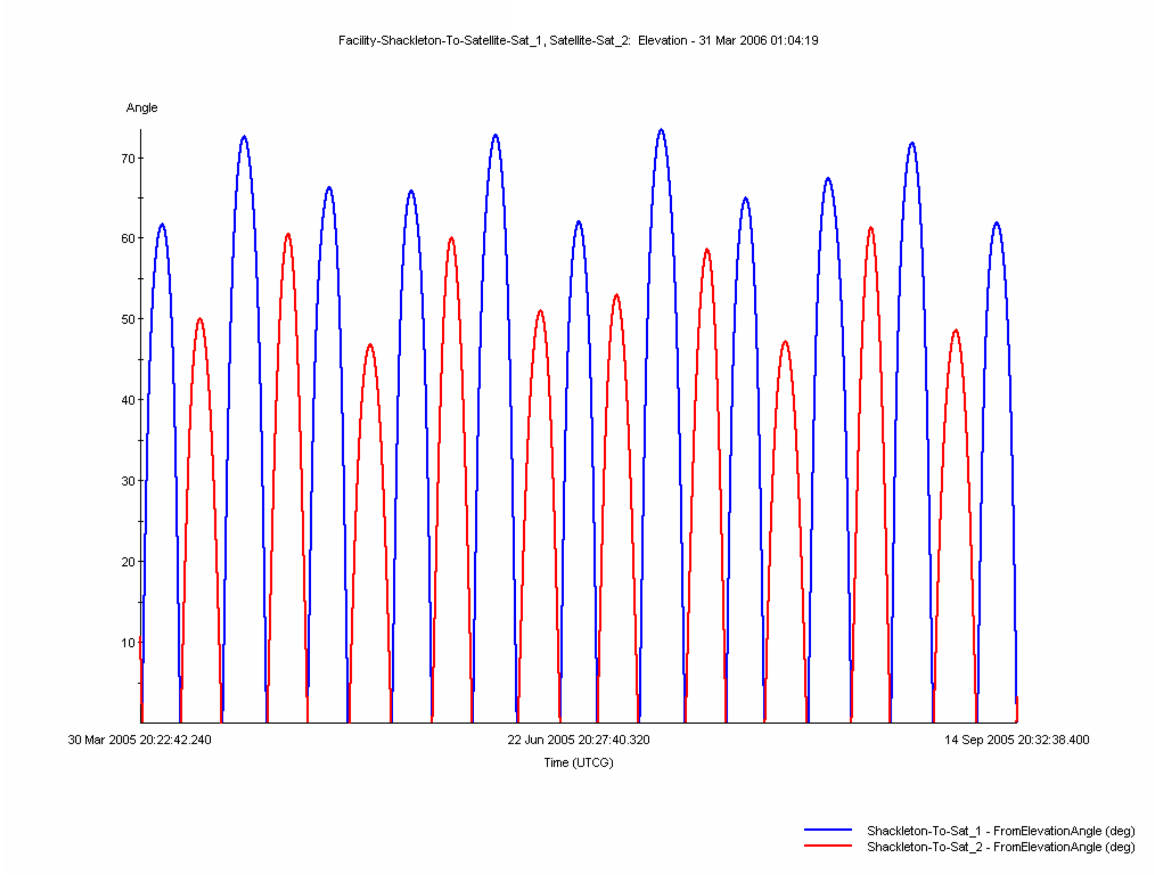

Figure 5.12 Elevation of Each Satellite Above the Horizon as Viewed from the Shackleton Crater Facility for 16-Day L_1 and L_2 Vertical Orbit Scenario

Table 5.5

Percent Access Times for 16-Day L_1 and L_2 Vertical Orbits

	Facility at Shackleton Crater	Earth	Facility at WSTF
Only L_2 Satellite	51.47%	98.27%	49.29%
Only L_1 Satellite	47.02%	100.00%	48.04%
Both Satellites	0.08%	98.27%	45.19%
Either Satellite	98.41%	100.00%	52.14%
Simulation Time (days)	168.01		

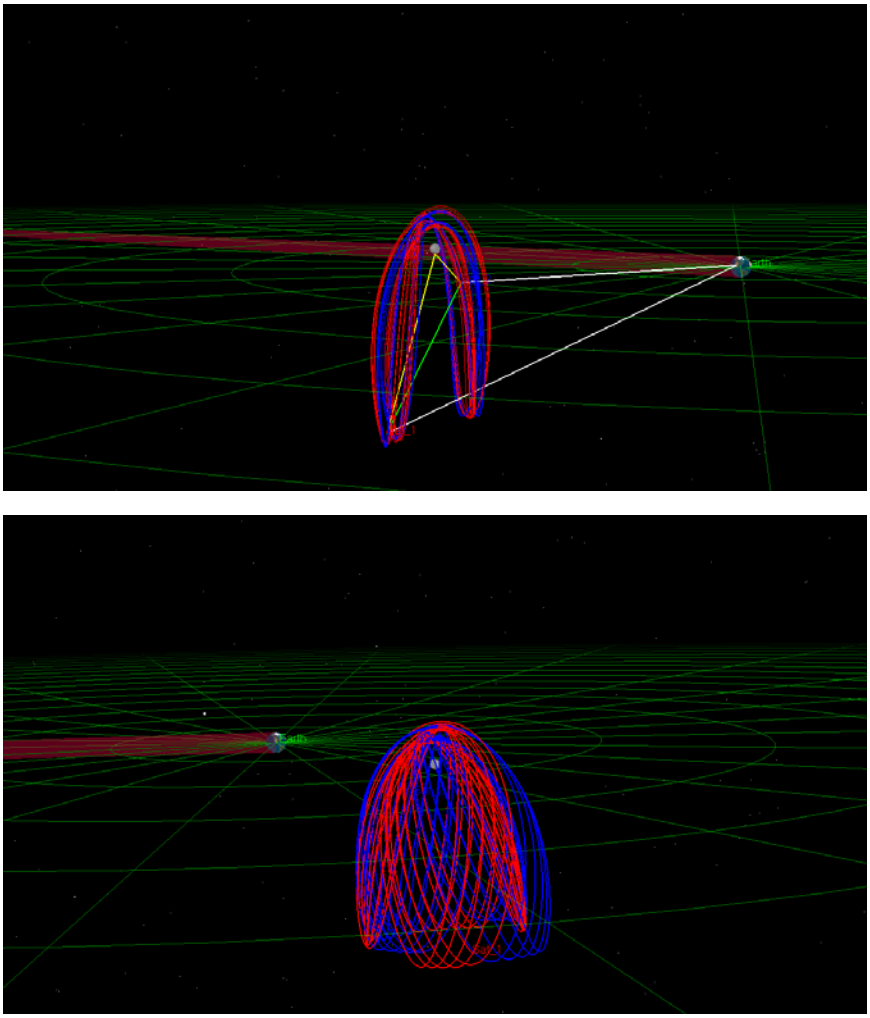

Figure 5.13 STK 14-Day L_2 Butterfly Orbits:
Moon Centered, Rotating Frame (Top);
Moon Centered, Inertial Frame (Bottom)

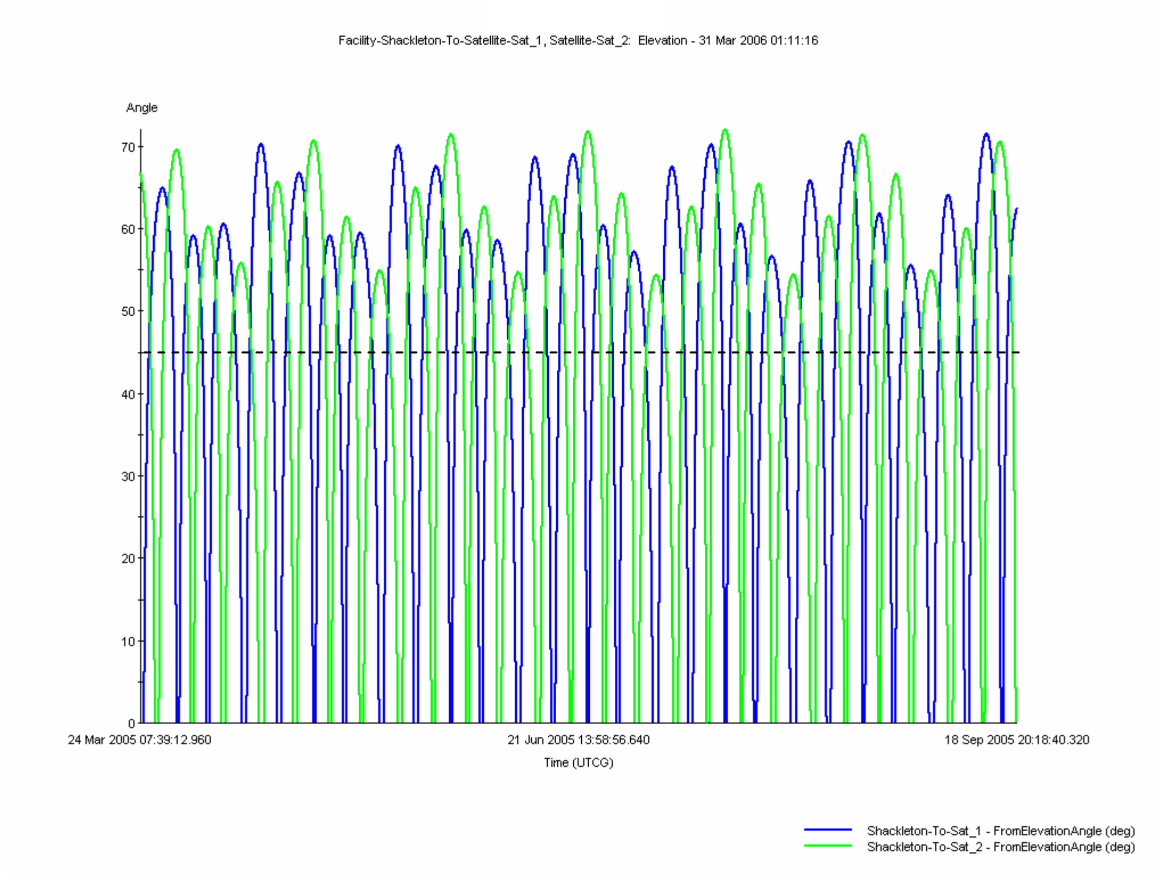

Figure 5.14 Elevation of Each Satellite Above the Horizon as Viewed from the Shackleton Crater Facility for 14-Day L_2 Butterfly Orbit Scenario

Table 5.6

Percent Access Times for 14-Day L_2 Butterfly Orbits

	Facility at Shackleton Crater	Earth	Facility at WSTF
Only Satellite 1	89.10%	99.45%	46.90%
Only Satellite 2	89.15%	99.39%	46.61%
Both Satellites	78.25%	98.89%	45.29%
Either Satellite	100.00%	100.00%	48.21%
Simulation Time (days)	178.53		

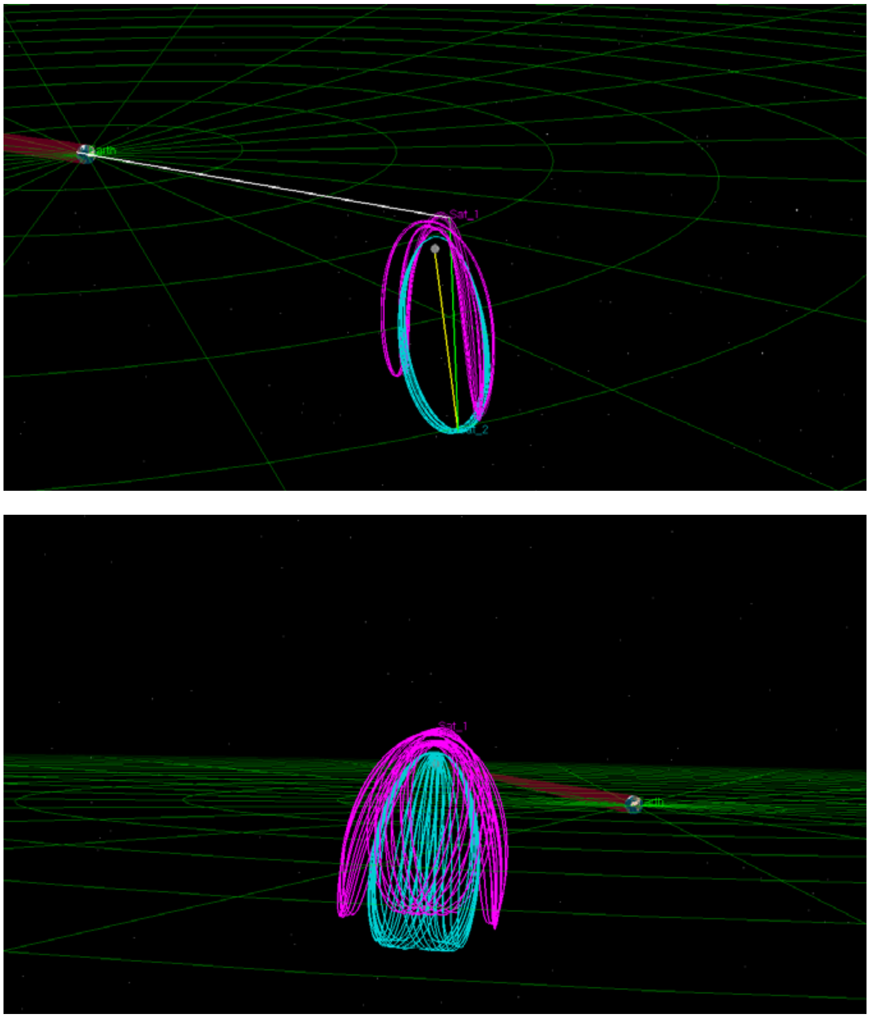

Figure 5.15 STK 7-Day L_2 Halo and 14-Day L_2 Butterfly Orbits:
Moon Centered, Rotating Frame (Top);
Moon Centered, Inertial Frame (Bottom)

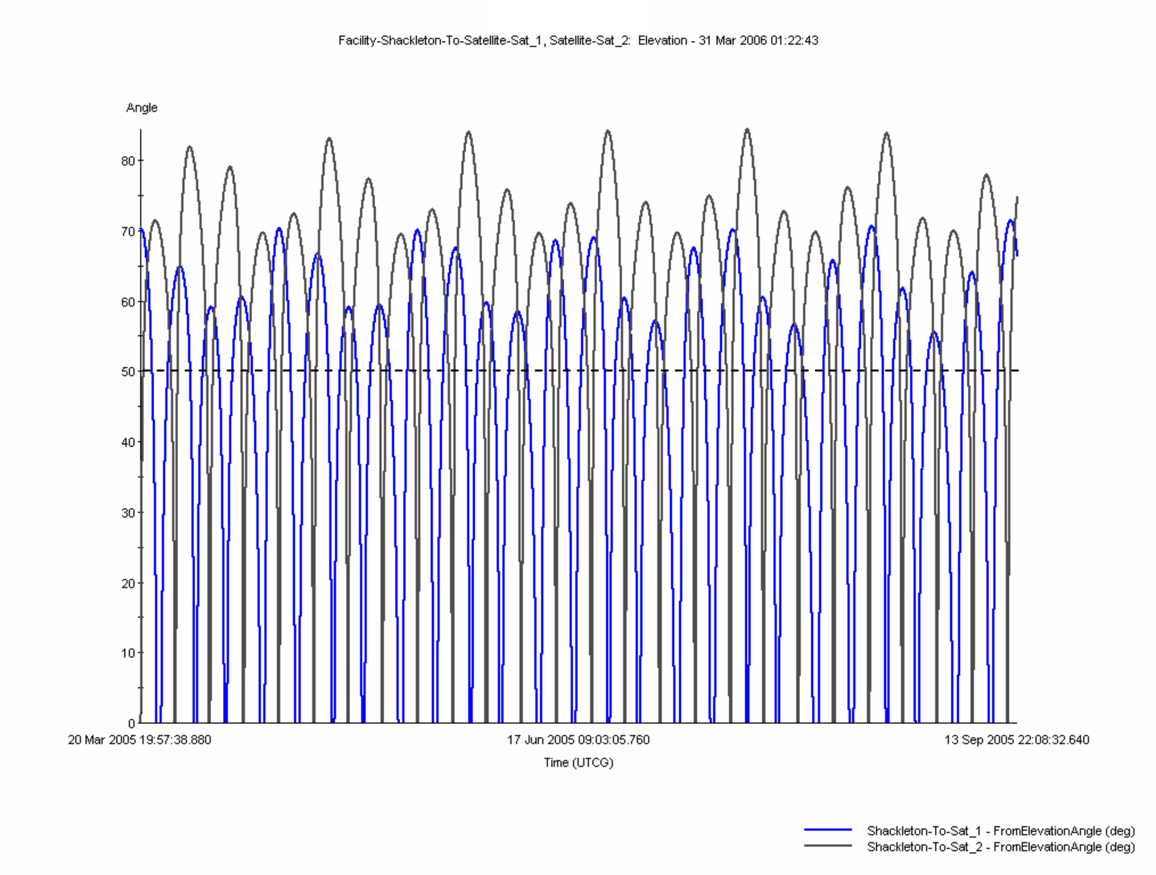

Figure 5.16 Elevation of Each Satellite Above the Horizon as Viewed from the Shackleton Crater Facility for 7-Day L_2 Halo and 14-Day L_2 Butterfly Orbit Scenario

Table 5.7

Percent Access Times for 7-Day L_2 Halo and 14-Day L_2 Butterfly Orbits

	Facility at Shackleton Crater	Earth	Facility at WSTF
Only 14-Day Satellite	89.22%	99.53%	47.18%
Only 7-Day Satellite	96.35%	100.00%	46.86%
Both Satellites	85.85%	99.53%	45.60%
Either Satellite	100.00%	100.00%	48.55%
Simulation Time (days)	177.09		

5.2 Station-Keeping Analysis

Another important factor in determining architectures for lunar south pole coverage is the station-keeping cost associated with each satellite. Once a baseline coverage scenario is constructed, potential station-keeping costs are investigated. The unstable subspace that is available from dynamical systems theory is used to develop a station-keeping strategy. Results are provided for the nine orbits that are defined in Table 4.1.

5.2.1 The Station-Keeping Algorithm

A preliminary station-keeping analysis is constructed by modifying the targeting sequence in Astrogator Connect. A schematic representation the station-keeping algorithm for four patch points appears in Figure 5.17. Note that the green path represents the reference orbit as computed directly from GENERATOR. Along the green path, the GENERATOR patch points are numbered #1– #4 and are defined as the target points in Astrogator. Note that the six-dimensional state vectors are decomposed into three-dimensional position and velocity vectors, i.e., $\vec{q}_i = \left\{ \vec{R}_i^T \quad \vec{V}_i^T \right\}^T$. However, the vehicle is not actually associated with the reference state. Perturbing the satellite into the unstable subspace, and determining the maneuvers necessary to offset the error and maintain the orbit, ultimately yields a good approximation of the maximum station-keeping cost [31-37]. So, the perturbations along the unstable direction are computed from equation (2.66) and appear in magenta as $\left\{ \delta\vec{R}_1^T \quad \delta\vec{V}_1^T \right\}^T$. Recall that position and velocity perturbations are represented by the displacement *d* along the unstable direction in equation (2.66). These perturbations are analogous to navigation errors and the impact of such errors is most significant if they are in the unstable direction. Therefore, the magnitude of *d* is sized to be consistent with the magnitude of some average navigation 3σ position errors; that is, the value might typically cover a range from 2 to 3 km in position. To account for slight differences between the unstable directions from the CR3BP and the full model, a baseline 3σ position error of 5 km is used in this analysis. These perturbations $\left\{ \delta\vec{R}_1^T \quad \delta\vec{V}_1^T \right\}^T$ are added to the initial state and propagation in

Astrogator over the time interval necessary to reach point #2 moves the vehicle along a new actual path (in blue). Of course, the state associated with the satellite at the end of this propagation is actually $\left\{\delta\vec{\tilde{R}}_2^T \quad \delta\vec{\tilde{V}}_2^T\right\}^T$. A correction maneuver, $\Delta\vec{v}_2$, is computed via a targeting sequence in Astrogator to actually reach the next target point #3. This $\Delta\vec{v}_2$ is necessary to offset the error introduced by $\left\{\delta\vec{R}_1^T \quad \delta\vec{V}_1^T\right\}^T$. The $\Delta\vec{v}_2$ from the targeting sequence is adjusted by $\pm 2\%$ to include hot (+) or cold (–) burn errors, i.e., $\delta\Delta\vec{v}_2$. However, to incorporate possible errors, perturbations along the unstable direction are again added. After the adjusted $\Delta\vec{v}_2 + \delta\Delta\vec{v}_2$ is implemented, the satellite is perturbed $\left\{\delta\vec{R}_2^T \quad \delta\vec{V}_2^T\right\}^T$ in the unstable direction and again propagated forward. The process is repeated for a specified time interval, i.e., a pre-determined number of target points. The total station-keeping cost is $\Delta v = \sum_{i=2}^{n-1} \left\|\Delta\vec{v}_i\right\|$ for n target points.

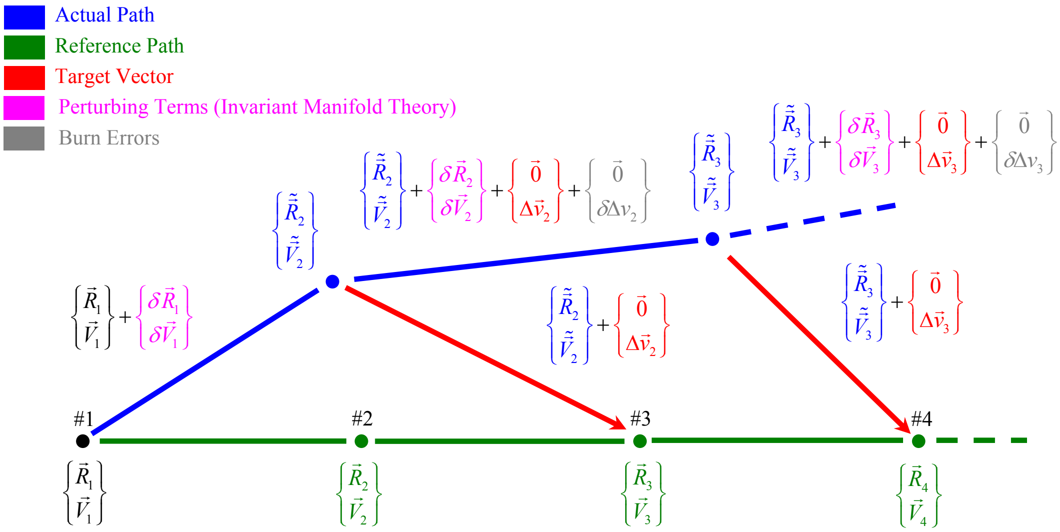

Figure 5.17 Schematic for Station-Keeping Algorithm

5.2.2 Station-Keeping Results

The station-keeping costs are obtained in Astrogator Connect using the algorithm from the previous section. (See Figure 5.17.) Results for each orbit in Table 4.1 are specified in Table 5.8 for one complete year. In general, station-keeping cost increases with stability index. The lowest costs correspond to the 7- and 8-day L_2 near-rectilinear halo orbits while the highest costs are associated with the 14-day L_1 vertical orbit. The algorithm depicted in Figure 5.17 does not compute optimal cost, therefore these costs are not optimized. However, experience suggests that these results are consistent with an impulsive control scheme [33].

Table 5.8

Station-Keeping Results for One Year (~ 24 Revs)

Orbit Type	Libration Point	Period (days)	Avg. 3σ Δv (cm/s)	No. of Maneuvers	Avg. Time Between Maneuvers (days)	Avg. Δv (m/s)	Total Δv (m/s)
Near-Rectilinear Halo	L_2	7.0	2.06	86	4.20	0.057	4.82
Near-Rectilinear Halo	L_1	8.0	1.52	55	6.40	0.101	5.54
Near-Rectilinear Halo	L_2	8.0	2.18	55	6.40	0.086	4.69
Halo	L_1	12.0	3.82	60	6.00	1.106	66.33
Halo	L_2	14.0	2.77	156	2.33	0.183	28.47
Vertical	L_1	14.0	3.13	68	5.25	2.527	171.82
Butterfly	L_2	14.0	9.78	78	4.67	0.409	31.86
Vertical	L_1	16.0	2.81	91	4.00	0.347	31.55
Vertical	L_2	16.0	2.75	60	6.00	1.472	88.32

6. RESULTS AND RECOMMENDATIONS

6.1 Summary of Results

Particular solutions in the CR3BP are available using analytical approximations in the vicinity of the libration points. The solutions are expanded with five different corrections schemes for numerically computing periodic orbits in the CR3BP. Strategies for numerical computation of families of periodic solutions are offered. A method of bisections establishes a means for locating bifurcations within families and mappings to different families.

The numerical techniques establish a basis for the computation of planar, axial, and vertical families emanating from five equilibrium points in the Earth-Moon system. In addition, halo orbit families in the vicinity of the collinear points and a butterfly family in the vicinity of the trans-lunar libration point are computed. The analyses are easily modified for numerical computation of similar solutions in other systems of interest.

Orbits from the halo, vertical, and butterfly families in the vicinity of the Earth-Moon libration points are selected for potential lunar coverage scenarios. Orbits with altitudes between 50 km and 100,000 km are identified as feasible. Nine different orbits with periods ranging from 7 to 16 days are studied in detail. Two phased spacecraft in a single orbit or two spacecraft in a combination of two different orbits, with periods that are commensurate, ensure adequate coverage of the lunar south pole. The orbit with the desired period is determined in the CR3BP from a corrections process with a periodicity constraint. Multiple revolutions are added and the orbit from the CR3BP is transitioned to a full ephemeris model, including solar perturbations.

A complete coverage analysis is available using advanced commercial software. A ground station is positioned at the Shackleton Crater near the lunar south pole and a transmitting station is located at the White Sands Test Facility. Line-of-sight percent access times with the both stations are computed for five potential coverage scenarios. A preliminary station-keeping analysis is available by targeting points along the baseline orbit and perturbing the spacecraft in a direction consistent with the unstable subspace. Complete coverage of the lunar south pole is achieved with two spacecraft in combinations of Earth-Moon libration point orbits.

This work contributes to the continuing evolution of a general baseline strategy for mission design:

1. Computing periodic solutions in the CR3BP
2. Identifying feasible solutions for mission design requirements
3. Transitioning to a full ephemeris model
4. Verifying mission design requirements using advanced software

The general method is applicable to a broad range of mission applications for libration point orbit design.

6.2 Recommendations for Future Work

Analysis continues to obtain transfers from the Earth to such orbits. An example of the stable and unstable manifolds corresponding to a vertical orbit appears in Figure 6.1. In general, the stability index offers information regarding the relative transfer costs to reach these orbits. Moreover, current designs for lunar south pole coverage include "frozen," polar orbits computed using a two-body model, and with third body effects modeled as gravitational perturbations [37-38]. Establishing a connection between these orbits and the orbits computed in this work may identify even more favorable orbits for lunar south pole coverage. In addition, libration point orbits from other families may also render coverage options for the lunar south pole. A further investigation of periodic orbits and the connections between families in the CR3BP may lead to the discovery new families of orbits with smaller lunar altitudes to aid communications with the lunar ground station. Furthermore, a more complete mapping of the solution space in the CR3BP uncovers even more solutions. The nature of the solutions may aid in return to the Moon and ultimately facilitate exploration to Mars.

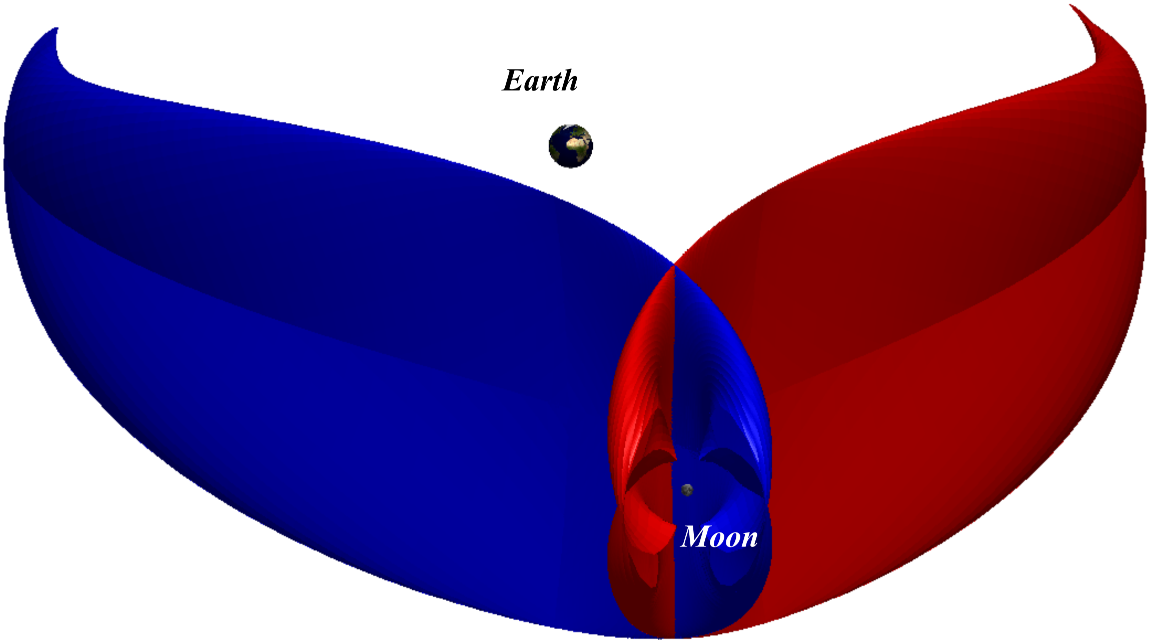

Figure 6.1 Earth-Moon L_1 Vertical Orbit with Associated Unstable (Red) and Stable (Blue) Manifolds

LIST OF REFERENCES

LIST OF REFERENCES

[1] R. Farquhar, "The Flight of ISEE-3/ICE: Origins, Mission History, and a Legacy." Paper No. AIAA 1998-4464, AIAA/AAS Astrodynamics Specialist Conference and Exhibit, Boston, Massachusetts, August 10-12, 1998.

[2] M. Lo, B. Williams, W. Bollman, D. Han, Y. Hahn, J. Bell, E. Hirst, R. Corwin, P. Hong, K. Howell, B. Barden, and R. Wilson, "Genesis Mission Design." Paper No. AIAA 1998-4468, AIAA/AAS Astrodynamics Specialist Conference and Exhibit, Boston, Massachusetts, August 10-12, August 1998.

[3] "The Vision for Space Exploration," National Aeronautics and Space Administration Publication, NP-2004-01-334-HQ, February 2004.

[4] H. Poincaré, *Les Méthodes Nouvelles de la Mécanique Céleste*. Vol. 1, 1892; *New Methods of Celestial Mechanics* (English Translation). Vol. 13, History of Modern Physics and Astronomy, American Institute of Physics, 1993.

[5] F. Moulton (in collaboration with D. Buchanan, T. Buck, F. Griffin, W. Longley, and W. MacMillan), "Periodic Orbits." Carnegie Institute of Washington, Washington D.C., 1920.

[6] M. Hénon, "Exploration Numérique du Problème Restreint. II. Masses égales, stabilité des orbites périodiques." *Annales d'Astrophysique*, Vol. 28, February 1965, pp. 992-1007.

[7] E. Goodrich, "Numerical Determination of Short-Period Trojan Orbits in the Restricted Three-Body Problem." *The Astronomical Journal*, Vol. 71, No. 2, March 1966, pp. 88-93.

[8] T. Bray and L. Goudas, "Doubly Symmetric Orbits about the Collinear Lagrangian Points." *The Astronomical Journal*, Vol. 72, No. 2, March 1967, pp. 202-213.

[9] A. Deprit, J. Henrard, J. Palmore, and J. Price, "The Trojan Manifold in the System Earth-Moon." *Royal Astronomical Society, Monthly Notices*, Vol. 132, April 3, 1967, pp. 311-335.

[10] V. Szebehely, *Theory of Orbits: The Restricted Problem of Three Bodies*. New York: Academic Press, 1967.

[11] M. Hénon, “Vertical Stability of Periodic Orbits in the Restricted Problem.” *Celestial Mechanics*, Vol. 8, 1973, pp. 269-272.

[12] R. Farquhar and A. Kamel, “Quasi-Periodic Orbits About the Translunar Libration Point.” *Celestial Mechanics*, Vol. 7, 1973, pp. 458-473.

[13] D. Richardson and N. Cary, “A Uniformly Valid Solution for Motion about the Interior Libration Point of the Perturbed Elliptic-Restricted Problem.” Paper No. AAS 75-021, AAIA/AAS Astrodynamics Conference, Nassau, Bahamas, July 28-30, 1975.

[14] V. Markellos and A. Halioulias, “Numerical Determination of Asymmetric Periodic Solutions.” *Astrophysics and Space Science*, Vol. 46, 1977, pp. 183-193.

[15] V. Markellos, “Asymmetric periodic orbits in three dimensions.” *Royal Astronomical Society, Monthly Notices*, Vol. 184, 1978, pp. 273-281.

[16] C. Zagouras and P. Kazantzis, “Three-dimensional periodic oscillations generating from plane periodic ones around the collinear Lagrangian points.” *Astrophysics and Space Science*, Vol. 61, No. 2, April 1979, pp. 389-409.

[17] J. Breakwell and J. Brown, “The ‘Halo’ Family of 3-Dimensional Periodic Orbits in the Earth-Moon Restricted 3-Body Problem.” *Celestial Mechanics*, Vol. 20, 1979, pp. 389-404.

[18] I. Robin and V. Markellos, “Numerical Determination of Three-Dimensional Periodic Orbits Generated From Vertical Self-Resonant Satellite Orbits.” *Celestial Mechanics*, Vol. 21, 1980, pp. 395-434.

[19] K. Howell and J. Breakwell, “Almost Rectilinear Halo Orbits.” *Celestial Mechanics*, Vol. 32, No. 1, January 1984, pp. 29-52.

[20] K. Howell, “Three-Dimensional, Periodic, ‘Halo’ Orbits.” *Celestial Mechanics*, Vol. 32, No. 1, January 1984, pp. 53-71.

[21] C. Zagouras, “Three-Dimensional Periodic Orbits about the Triangular Equilibrium Points of the Restricted Problem of Three Bodies.” *Celestial Mechanics*, Vol. 37, June 6, 1984, pp. 28-46.

[22] K. Howell and H. Pernicka, “Numerical Determination of Lissajous Trajectories in the Restricted Three-Body Problem.” *Celestial Mechanics*, Vol. 41, 1988, pp. 107-124.

[23] S. Hughes, D. Cooley, and J. Guzmán, "A Direct Method for Fuel Optimal Maneuvers of Distributed Spacecraft in Multiple Flight Regimes." Paper No. AAS 05-158, Space Flight Mechanics Meeting, Copper Mountain, Colorado, January 23-27, 2005.

[24] B. Marchand and K. Howell, "Aspherical Formations Near the Libration Points in the Sun-Earth/Moon Ephemeris System." Paper No. AAS 04-157, 14th AAS/AIAA Space Flight Mechanics Conference, Maui, Hawaii, February 8-12, 2004.

[25] B. Marchand, K. Howell, and R. Wilson, "A Trajectory Design Strategy in the Multi-Body Regime Including Constraints." (in preparation)

[26] K. Papadakis and C. Zagouras, "Bifurcation Points and Intersections of Families of Periodic Orbits in the Three-Dimensional Restricted Three-Body Problem." *Astrophysics and Space Science*, Vol. 199, No. 2, January 1992, pp. 241-256.

[27] K. Howell and E. Campbell, "Three-Dimensional Periodic Solutions That Bifurcate From Halo Families in the Circular Restricted Three-Body Problem." AAS/AIAA Paper No. 1999-161, AAS/AIAA Space Flight Mechanics Meeting, Breckenridge, Colorado, February 7-10, 1999.

[28] D. Dichmann, E. Doedel, and R. Paffenroth, "The Computation of Periodic Solutions of the 3-Body Problem Using the Numerical Continuation Sofware AUTO." *Libration Point Orbits and Applications,* G. Gómez, M. Lo, J. Masdemont (Editors), Hong Kong, World Scientific, 2003.

[29] E. Doedel, R. Paffenroth, H. Keller, D. Dichmann, J. Galán-Vioque, and A. Vanderbauwhede, "Computation of Periodic Solutions of Conservative Systems with Application to the 3-Body Problem." *International Journal of Bifurcation and Chaos*, Vol. 13, No. 6, 2003, pp. 1353-1381.

[30] R. Farquhar, "The Utilization of Halo Orbits in Advanced Lunar Operations." NASA TND-365, Goddard Spaceflight Center, Greenbelt, Maryland, 1971.

[31] C. Simó, G. Gómez, J. Libre, and R. Martínez, "Station Keeping of a Quasiperiodic Halo Orbit Using Invariant Manifolds." *Proceedings of the Second International Symposium on Spaceflight Dynamics*, Darmstadt, Germany, October 1986, pp. 65-70.

[32] C. Simó, G. Gómez, J. Libre, R. Martínez, and J. Rodríguez, "On the Optimal Station Keeping Control of Halo Orbits." *Acta Astonautica*, Vol. 15, No. 6/7, 1987, pp. 391-197.

[33] K. Howell and H. Pernicka, “Stationkeeping Method for Libration Point Trajectories.” *Journal of Guidance and Control*, Vol. 16, No. 1, 1993, pp. 151–159.

[34] K. Howell and T. Keeter, “Station-Keeping Strategies for Libration Point Orbits: Target Point and Floquet Mode Approaches,” Proceeding of the *AAS/AIAA Spaceflight Mechanics Meeting 1995,* Advances in the Astronautical Sciences, Vol. 89, R. Proulx, J. Liu, P. Seidelmann, and S. Alfano (editors), 1995, pp. 1377-1396.

[35] G. Gómez, K. Howell, J. Masdemont, and C. Simó, “Station-Keeping Strategies for Translunar Libration Point Orbits.” Paper No. AAS 98-168, AAS/AIAA Spaceflight Mechanics Meeting, Monterey, California, February 9-11, 1998.

[36] D. Scheeres, D. Han, and Y. Hou, “The Influence of Unstable Manifolds on Orbit Uncertainty.” *Journal of Guidance, Control, and Dynamics*, Vol. 24, No. 3. May-June 2001, pp. 573-585.

[37] C. Renault and D. Scheeres, “Statistical Analysis of Control Maneuvers in Unstable Orbital Environments.” *Journal of Guidance, Control, and Dynamics*, Vol. 26, No. 5, September-October 2003, pp.758-769.

[38] T. Ely, “Stable Constellations of Frozen Elliptical Inclined Orbits.” *Journal of the Astronautical Sciences*, Vol. 53, No. 3, July-September 2005.

[39] T. Ely and E. Lieb, “Constellations of Elliptical Inclined Lunar Orbits Providing Polar and Global Coverage.” Paper No. AAS 05-158, AAS/AIAA Spaceflight Mechanics Meeting, South Lake Tahoe, California, August 7-11, 2005.

[40] NASA Space Science Enterprise, Strategic Plan. http://spacescience.nasa.gov/admin/pubs/strategy/2000/, Sections 2-3, November 2000.

[41] K. Howell and J. Anderson, *User’s Guide: Purdue Software GENERATOR*, July 2001.

[42] D. Folta and F. Vaughn, “A Survey of Earth-Moon Libration Orbits: Station-Keeping Strategies and Intra-Orbit Transfers.” Paper No. AIAA 04-4741, Proceedings of AAS/AIAA Astrodynamics Specialist Conference, Providence, Rhode Island, 2004.

[43] L. Perko, *Differential Equations and Dynamical Systems*. Springer-Verlag, 3rd ed., 2001.

[44] W. Gautschi, *Numerical Analysis: An Introduction*. Birkhäuser, Boston, 1997, pp. 217-220.

[45] R. Farquhar, “Lunar Communications with Libration-Point Satellites.” *Journal of Spacecraft and Rockets*, Vol. 4, 1967, pp. 1383-1384.

[46] G. Vanderplaats, *Numerical Optimization Techniques for Engineering Design*. Vanderplaats Research & Development, Inc., Colorado Springs, 2001, pp. 250-256.

[47] Information regarding current interest in lunar south pole sites and activities conveyed by José Guzmán, Applied Physics Laboratory, private communication.

VITA

VITA

Daniel J. Grebow received his undergraduate degree in Aeronautical and Astronautical Engineering from Purdue University in May of 2004. He spent the summer of 2005 at NASA Goddard Spaceflight Center. At NASA, under the guidance of David Folta, he participated in a research study concerning lunar coverage using libration point orbits. In collaboration with Martin Ozimek, the results of this work were presented to the Goddard Flight Dynamics branch. He also recently presented the results of the investigation in a paper at the 16th AIAA/AAS Space Flight Mechanics Conference in January, 2006. Additional results have been obtained and a paper, entitled "Multi-Body Orbit Architectures for Lunar South Pole Coverage," is currently in preparation to be submitted for publication in an archival journal. Mr. Grebow anticipates working at NASA Goddard again during summer 2006 and continuing his studies at Purdue University for a Doctoral degree under Dr. Kathleen Howell.